TU Delft

Delft University of Technology

Document Version
Final published version

Citation (APA)
Faragau, A. B. (2023). *Understanding degradation mechanisms at railway transition zones using phenomenological models*. [Dissertation (TU Delft), Delft University of Technology]. https://doi.org/10.4233/uuid:3fc78df4-ddf4-4dad-8ea7-016813d4debc

Important note
To cite this publication, please use the final published version (if applicable).
Please check the document version above.

Copyright
In case the licence states “Dutch Copyright Act (Article 25fa)”, this publication was made available Green Open Access via the TU Delft Institutional Repository pursuant to Dutch Copyright Act (Article 25fa, the Taverne amendment). This provision does not affect copyright ownership.
Unless copyright is transferred by contract or statute, it remains with the copyright holder.

Sharing and reuse
Other than for strictly personal use, it is not permitted to download, forward or distribute the text or part of it, without the consent of the author(s) and/or copyright holder(s), unless the work is under an open content license such as Creative Commons.

Takedown policy
Please contact us and provide details if you believe this document breaches copyrights.
We will remove access to the work immediately and investigate your claim.

This work is downloaded from Delft University of Technology.

Understanding degradation mechanisms at railway transition zones using phenomenological models

Understanding degradation mechanisms at railway transition zones using phenomenological models

Proefschrift

ter verkrijging van de graad van doctor
aan de Technische Universiteit Delft,
op gezag van de Rector Magnificus Prof.dr.ir. T.H.J.J. van der Hagen,
voorzitter van het College voor Promoties,
in het openbaar te verdedigen op woensdag 28 juni 2023 om 10 uur

door

Andrei Bogdan FĂRĂGĂU

civil ingenieur, Technische Universiteit Delft, Nederland
geboren te Cluj-Napoca, Romania.

Dit proefschrift is goedgekeurd door de

promotor: Prof.dr. A.V. Metrikine
promotor: Dr.ir. K.N. van Dalen

Samenstelling promotiecommissie:

Rector Magnificus,	voorzitter
Prof.dr. A.V. Metrikine,	Technische Universiteit Delft, promotor
Dr.ir. K.N. van Dalen,	Technische Universiteit Delft, promotor

Onafhankelijke leden:

Dr.ir. W.T. van Horssen	Technische Universiteit Delft
Prof.dr. A.S.J. Suiker	Technische Universiteit Eindhoven
Prof.dr. G. Degrande	Katholieke Universiteit Leuven, België
Prof.dr. S. Lenci	Università Politecnica delle Marche, Italië
Prof.dr. J. Kaplunov	Keele University, Engeland

This research was supported by the Dutch Technology Foundation TTW (Project 15968), part of the Netherlands Organisation for Scientific Research (NWO), and which is partly funded by the Ministry of Economic Affairs. This research was co-founded by the following industry partners: ProRail, Movares, Deltares, and Tensar.

Keywords:

Printed by: Gildeprint – Enschede

Front & Back:

Copyright © 2023 by A B Fărăgău

ISBN

An electronic version of this dissertation is available at
`https://repository.tudelft.nl/`.

To you all
that do not doubt it is to you.
Because if you doubt it is to you,
then it is not.

Contents

Summary

Due to the current climate crisis, railway transport is receiving increased attention owing to its capability of running fully on electricity, which can be generated from renewable sources. High-speed railway networks and the new concepts, such as Hyperloop, are already competing with road and aviation transport. However, the increased demand on railway transport causes an acceleration in infrastructure degradation leading to an increased frequency of maintenance and repair operations. Consequently, what before was considered normal "wear and tear" of the infrastructure is quickly turning into serious challenges causing disruptions to the normal operation of traffic.

When it comes to track degradation, the so-called *transition zones* require significantly more frequent maintenance than the regular parts of the railway track. Transition zones in railway tracks are areas with substantial variation of track properties (e.g., foundation stiffness) encountered near rigid structures such as bridges, tunnels, culverts, or rail-crossings. The occurrence of differential settlements at transition zones has been known for a long time and a multitude of mitigation measures have been designed to cope with this problem. Nonetheless, the mitigation measures have had just limited success and in some cases have even exacerbated the problem. Although the failure of some mitigation measures stems from inadequate design and poor implementation, overall, the lack of efficiency of mitigation measures can be attributed to the lack of understanding of the main mechanism(s) that drive(s) the differential settlement. Therefore, to design efficient mitigation measures, one needs to *advance the understanding of the physical processes leading to differential settlements at transition zones*. This constitutes the first objective of this dissertation.

The settlement mechanisms are studied in this dissertation through models rather than in-situ measurements or lab experiments. The majority of previous studies have used models to (i) understand and (ii) predict the response of railway tracks at transition zones. Researchers aiming at (i) have usually used simplified phenomenological models in which system characteristics that are not of interest are excluded. More recently, the models' complexity has increased tremendously by incorporating many system characteristics, making these models ideal for (ii), but less ideal for (i) due to the many mechanisms simultaneously at play. This led to the second objective of this dissertation, which is to *investigate the effect of specific characteristics of the railway system on the degradation at transition zones*. In other words, the second objective entails improving the simplified models by incorporating additional characteristics and determining which of these characteristics is of importance and which can be neglected.

Naturally, this dissertation can only focus on a few of the many aspects involved in this complex problem, and the two main constraints are presented in the following. Improving the maintenance operations themselves by employing new technologies could lead to a reduction in the maintenance frequency. However, to develop a long-term solution, one should aim at eliminating the root cause. Therefore, this dissertation investigated the *initiation* phase of the settlement, and not the *accumulation* phase. Furthermore, this dissertation focused on the differential settlement stemming solely from the amplification of stresses and strains that occur at transition zones, which is significant at relatively large train velocities. Consequently, this dissertation has not treated other sources of differential settlements, such as the different rates at which autonomous settlement develops in the open-track and at the man-made structure.

Using a simple phenomenological model representative of the railway track, Chapter 2 demonstrates that the response amplification at transition zones is caused by the interference between the steady-state field and the free field generated by the transition process. Consequently, the more pronounced the free field, the larger the resulting amplification. It also shows that the soft-to-stiff and stiff-to-soft transitions have significantly different behaviour, strongly suggesting the need of different mitigation measure designs for the two types of transition. Finally, the transition radiation energy is shown to be invariant between the soft-to-stiff and stiff-to-soft scenarios, finding which was unexpected considering the above-mentioned difference in behaviour.

Investigating the vehicle-structure interaction, Chapter 4 demonstrates that the amplification of the wheel-rail contact force caused purely by a change in foundation stiffness and damping (i.e., a track without initial imperfections) can be significant. Previous literature studies concluded the opposite; however, these studies considered only quasi-static velocities and small effective changes in foundations properties. The findings presented in this chapter, thus, supplement earlier findings to offer a more complete picture. Nonetheless, even though the vehicle-structure interaction leads to a stronger transition radiation, it leads to a reduction of the response amplification at the critical locations in transition zones where settlement is usually observed.

Chapter 5 identifies three response amplification mechanisms at transition zones in systems that have a periodic nature. The amplification is the product of a system with periodic nature and with a local inhomogeneity, and if one of these characteristics is omitted, the amplification does not occur. While these mechanisms can be influential for the railway over-head wires and for the emerging Hyperloop transportation system, they have a negligible influence in the conventional railway track. Consequently, for investigations focused on transition zones and response amplification at low frequencies, the periodicity of the railway track can be successfully approximated by the equivalent continuously supported one without neglecting influential amplification mechanisms.

Chapter 6 introduces the ballast settlement and investigates its influence on the transition process. It shows that the development of the initial settlement leads to a redistribution

of the transition radiation energy during the transition not only between frequencies, but also between the soft and stiff media. This redistribution is mainly attributed to the separation between the beam and foundation at the settlement location. Consequently, if the developed settlement is not large enough to allow for this separation, the influence of the nonlinear foundation on transition radiation is negligible.

Chapter 8 investigates the influence of the foundation nonlocality on transition radiation. It shows that the nonlocality of the soil layer has an increasingly pronounced effect on the steady-state response with its decreasing shear stiffness. Consequently, modelling the nonlocality of the supporting structure can be important for railway tracks founded on soft soils. Furthermore, for ballasted tracks founded on soft soils, the response amplification at transition zones can be more pronounced in the soil layer than in the ballast layer depending on the transition type. This is caused by the vertical stiffness of the ballast layer can be significantly larger than the one of the soil. This finding suggests that soil settlement should be accounted for if the long-term behaviour is to be correctly represented.

The investigation of several mechanisms of response amplification at transition zones performed in this study has led to a deeper understanding of the mechanisms leading to differential settlement at transition zones in railway tracks. This knowledge can serve future researchers and engineering in designing more efficient mitigation measures.

Samenvatting

Door de huidige klimaatcrisis krijgt het spoorvervoer meer aandacht omdat het volledig kan rijden op elektriciteit, die kan worden opgewekt uit hernieuwbare bronnen. Hogesnelheidsspoornetwerken en de nieuwe concepten, zoals Hyperloop, concurreren nu al met weg- en luchtvaartvervoer. De toegenomen vraag naar spoorwegvervoer veroorzaakt echter een versnelling van de achteruitgang van de infrastructuur, wat leidt tot een hogere frequentie van onderhouds- en reparatiewerkzaamheden. Bijgevolg verandert wat voorheen als normale "slijtage"van de infrastructuur werd beschouwd, snel in serieuze uitdagingen die de normale werking van het verkeer verstoren.

De zogenaamde *overgangszones* vergen beduidend vaker onderhoud dan de reguliere delen van het spoor als het gaat om degradatie van het spoor. Overgangszones in spoorlijnen zijn gebieden met substantiële variatie in spooreigenschappen (bijv. funderingsstijfheid) die men tegenkomt in de buurt van starre constructies zoals bruggen, tunnels, duikers of spoorwegovergangen. Het optreden van zettingsverschillen in overgangszones is al lang bekend en er is een veelheid aan mitigerende maatregelen ontworpen om dit probleem het hoofd te bieden. Desalniettemin hebben de mitigerende maatregelen slechts beperkt succes gehad en in sommige gevallen zelfs het probleem verergerd. Hoewel het mislukken van sommige mitigerende maatregelen het gevolg is van een ontoereikend ontwerp en slechte implementatie, kan het gebrek aan efficiëntie van mitigerende maatregelen over het algemeen worden toegeschreven aan het gebrek aan begrip van de belangrijkste mechanismen die de differentiële afwikkeling aansturen. Daarom moet men, om efficiënte mitigerende maatregelen te ontwerpen, *het begrip vergroten van de fysieke processen die leiden tot differentiële vestigingen in overgangszones*. Dit vormt de eerste doelstelling van dit proefschrift.

De zettingsmechanismen worden in dit proefschrift bestudeerd door middel van modellen in plaats van in-situ metingen of laboratoriumexperimenten. De meeste eerdere studies hebben modellen gebruikt om (i) de respons van spoorlijnen in overgangszones te begrijpen en (ii) te voorspellen. Onderzoekers die zich richten op (i) hebben meestal vereenvoudigde fenomenologische modellen gebruikt waarin systeemkenmerken die niet van belang zijn, worden uitgesloten. Meer recentelijk is de complexiteit van de modellen enorm toegenomen door het incorporeren van veel systeemkenmerken, waardoor deze modellen ideaal zijn voor (ii), maar minder ideaal voor (i) vanwege de vele mechanismen die tegelijkertijd spelen. Dit leidde tot de tweede doelstelling van dit proefschrift, namelijk het *onderzoeken naar het effect van specifieke kenmerken van het spoorwegsysteem op de degradatie in overgangszones*. Met andere woorden, de tweede doelstelling bestaat erin de vereenvoudigde modellen te verbeteren

door aanvullende kenmerken in te bouwen en te bepalen welke van deze kenmerken van belang zijn en welke verwaarloosd kunnen worden.

Uiteraard kan deze dissertatie zich slechts richten op enkele van de vele aspecten die betrokken zijn bij dit complexe probleem, en de twee belangrijkste beperkingen worden in het volgende gepresenteerd. Verbetering van de onderhoudswerkzaamheden zelf door inzet van nieuwe technologieën kan leiden tot een verlaging van de onderhoudsfrequentie. Om een langetermijnoplossing te ontwikkelen, moet men echter streven naar het wegnemen van de onderliggende oorzaak. Daarom onderzocht dit proefschrift de *initiatie*-fase van de vestiging, en niet de *accumulatie*-fase. Verder richtte dit proefschrift zich op de zettingsverschillen die uitsluitend voortkomen uit de versterking van spanningen en rekken die optreden in overgangszones, wat significant is bij relatief hoge treinsnelheden. Bijgevolg heeft dit proefschrift geen andere bronnen van differentiële zettingen behandeld, zoals de verschillende snelheden waarmee autonome zetting zich ontwikkelt in het open spoor en in de door de mens gemaakte structuur.

Met behulp van een eenvoudig fenomenologisch model dat representatief is voor het spoor, laat hoofdstuk 2 zien dat de responsversterking bij overgangszones wordt veroorzaakt door de interferentie tussen het stationaire veld en het vrije veld dat wordt gegenereerd door het overgangsproces. Bijgevolg, hoe meer uitgesproken het vrije veld, hoe groter de resulterende versterking. Het laat ook zien dat de zacht-naar-stijf overgangen en de stijf-naar-zacht overgangen significant verschillend gedrag vertonen, wat sterk suggereert dat er voor de twee soorten overgangen verschillende ontwerpen van mitigerende maatregelen nodig zijn. Ten slotte is aangetoond dat de overgangsstralingsenergie invariant is tussen de scenario's van zacht naar stijf en van stijf naar zacht, wat onverwacht was gezien het bovengenoemde verschil in gedrag.

Hoofdstuk 4, dat de interactie tussen voertuig en constructie onderzoekt, toont aan dat de versterking van de wiel-railcontactkracht, puur veroorzaakt door een verandering in de stijfheid en demping van de fundering (d.w.z. een baan zonder initiële onvolkomenheden), aanzienlijk kan zijn. Eerdere literatuurstudies concludeerden het tegenovergestelde; deze studies beschouwden echter alleen quasi-statische snelheden en kleine effectieve veranderingen in funderingseigenschappen. De bevindingen die in dit hoofdstuk worden gepresenteerd, vullen dus eerdere bevindingen aan om een completer beeld te geven. Desalniettemin leidt de voertuig-constructie-interactie weliswaar tot een sterkere overgangsstraling, maar tot een vermindering van de responsversterking op de kritieke locaties in overgangszones waar zetting gewoonlijk wordt waargenomen.

Hoofdstuk 5 identificeert drie responsversterkingsmechanismen bij overgangszones in systemen die een periodiek karakter hebben. De versterking is het product van een systeem met een periodiek karakter en een lokale inhomogeniteit, en als een van deze kenmerken weggelaten wordt, vindt er geen versterking plaats. Hoewel deze mechanismen van invloed kunnen zijn op de bovenleidingen van het spoor en op het opkomende Hyperloop-transportsysteem, hebben ze een verwaarloosbare invloed op het conventionele

spoor. Bijgevolg kan voor onderzoeken gericht op overgangszones en responsversterking bij lage frequenties de periodiciteit van het spoor met succes worden benaderd door de equivalente continu ondersteunde zonder invloedrijke versterkingsmechanismen te verwaarlozen.

Hoofdstuk 6 introduceert de ballastzetting en onderzoekt de invloed ervan op het transitieproces. Het laat zien dat de ontwikkeling van de initiële zetting leidt tot een herverdeling van de overgangsstralingsenergie tijdens de overgang, niet alleen tussen frequenties, maar ook tussen de zachte en stijve media. Deze herverdeling wordt voornamelijk toegeschreven aan de scheiding tussen de balk en de fundering op de zettingslocatie. Bijgevolg, als de ontwikkelde zetting niet groot genoeg is om deze scheiding mogelijk te maken, is de invloed van de niet-lineaire fundering op de overgangsstraling verwaarloosbaar.

Hoofdstuk 8 onderzoekt de invloed van de non-lokaliteit van de fundering op overgangsstraling. Het laat zien dat de non-lokaliteit van de grondlaag een steeds groter effect heeft op de stationaire respons met zijn afnemende afschuifstijfheid. Bijgevolg kan het modelleren van de non-lokaliteit van de ondersteunende constructie belangrijk zijn voor spoorlijnen die op zachte grond zijn gefundeerd. Bovendien kan voor geballaste sporen op zachte grond de responsversterking bij overgangszones meer uitgesproken zijn in de grondlaag dan in de ballastlaag, afhankelijk van het overgangstype. Dit wordt veroorzaakt doordat de verticale stijfheid van de ballastlaag aanzienlijk groter kan zijn dan die van de grond. Deze bevinding suggereert dat er rekening moet worden gehouden met bodemzetting om het langetermijngedrag correct weer te geven.

Het onderzoek van verschillende mechanismen van responsversterking bij overgangszones uitgevoerd in deze studie heeft geleid tot een beter begrip van de mechanismen die leiden tot differentiële zetting bij overgangszones in spoorlijnen. Deze kennis kan toekomstige onderzoekers en ingenieurs van dienst zijn bij het ontwerpen van efficiëntere mitigatiemaatregelen.

Preface

English poet Alexander Pope wrote a beautiful epitaph for Isaac Newton, which goes like: "Nature and Nature's laws lay hid in night; God said 'Let Newton be!' and all was light". This is something that will never be said about the following pages, which contain a significant part of the research I performed during my doctoral study. But yet again, it is dangerous to aim that high.

From an early age, I found myself naturally drawn to mathematics and some time later to physics, but my early interest in these subjects followed more of a periodic pattern with time rather than an exponential increase. Eventually, I chose to follow a bachelor degree in Civil Engineering, hoping to harmoniously combine the two disciplines. Although this harmony did not materialize during my undergraduate studies, I was lucky enough to have an ideal blend of mathematics and physics during the master's degree at TU Delft. I must confess that I feel less and less of an engineer each day, but I am grateful for the path that brought me to the research group I am currently part of and in which I performed my doctoral study.

To me, the PhD was a journey of discovery in which I found my research direction. Even before embarking on this academic endeavor, I found myself instinctively attracted to the conceptual challenges rather than the more practical ones. This preference has shaped the approach to my doctoral research. I tried to avoid — sometimes consciously and many others unconsciously — complex models which require significant effort to set up and experimental campaigns that are challenging to organize — in my view both are rather practical challenges. Instead, I focused on interpretation of results obtained with somewhat simplified models and aimed at identifying underlying mechanisms (or cause-and-effect connections). Practically oriented readers might perceive this as a weakness of the dissertation, but I believe it to be quite the opposite. While it may not offer a straightforward solution to the industry problem, it goes beyond the boundaries of solely addressing practical concerns — and I firmly believe that academic research should encompasses a broader perspective. What this dissertation offers the reader is in-depth understanding of the physical mechanisms that generally underlie the degradation at railway transition zones.

The end evokes a bittersweet sentiment as I reflect upon the fulfilling journey I have experienced, made possible by the contribution of numerous individuals of the utmost quality whom I would like to express my heartfelt gratitude. First and foremost, I am immensely thankful to my supervisory dream-team, whose guidance and support have been instrumental in making my PhD journey an enjoyable one. Karel, you have been an invaluable mentor, imparting countless valuable research skills throughout our fruitful collaboration spanning over six years, with the hope of many more to come. Your unwavering enthusiasm

to tackle the everyday challenges I encountered along the way has been truly remarkable. Andrei, your valuable research oversight and the consistent generation of relevant questions continues to amaze me. I appreciate you enabling me to embrace the broader research perspective rather than getting entangled in minor obstacles. It is a life's quest to find an exceptional mentor, and I found two!

Furthermore, an integral part of my fulfilling PhD experience was the vibrant research group to which I belong, and I would like to express my gratitude to each member. There was no hurdle that couldn't be overcome with a coffee break, a Bright-minds meeting, a seminar, or the cherished Thursday PSOR drink. Despite the inevitable ebb and flow of individuals from diverse backgrounds and cultures, which is inherent to a research group, the collective spirit was always nurtured. Though I haven't been a part of many research groups, I sense a distinct uniqueness in this particular one, which I strongly believe should be cherished and preserved in the years to come.

Indirect support also came from my friends around the world, with a special mention to those from the Netherlands and Romania. The nature of the PhD makes it encompass your whole life including the personal one. Most of the much needed breaks came in the form of socializing, so I want to express my gratitude for keeping me sane.

I extend my sincere gratitude also to my family. Without your unwavering support in my endeavors far away from home I would not have reached this moment in my journey. While it may often go unnoticed, I am also grateful for your understanding during my occasional extended periods of limited communication when my primary focus was dedicated to my research. Your continuous support and understanding mean a great deal to me. Mulțumesc!

Lastly, my deepest gratitude goes to Paula, my partner in crime (life, I mean). Work-life balance is a vague concept when pursuing a PhD, and your support and encouragement in the difficult moments when focus was primarily channelled towards research is a key factor in the success of this journey. But more importantly, you brought peace into my life, teaching me to cherish the little joys life has to offer. I could not have asked for a better partner!

As I near the completion of this phase of my academic pursuit and reflect back at the journey, the countless moments of frustration barely come to mind. Prevalent in my memory are the engaging interaction with my supervisors and colleagues, the countless philosophically-inclined discussions, and the friendships made along the way which I hope will last a life-time.

Andrei Bogdan Fărăgău
Cluj-Napoca, June 2023

1

Introduction

Cathedral thinking [...] humbly acknowledges that work performed in the present builds on what has been done in the past, while actively engaging with a future that transcends a lifetime and utilitarian gains. It is carried forward with the knowledge and intention that it will outlast the present, and is conducted in a team spirit that spans generations.

Helga Nowotny

Infrastructure networks, such as air, road, and railway transport, are crucial to the well functioning of a society and its economy. On their regular functioning depend millions of commuters, travellers, and businesses worldwide every day. Nevertheless, the transport sector is the second largest emitter of green-house gases (GHG), currently being responsible for around 24 % of the total CO_2 emissions worldwide [1]. Moreover, transport is considered to be the hardest sector to decarbonize [2]. With the increasing risk of climate disaster, the demand for emission free infrastructure networks is growing, and the transportation sector seems to pose a considerable challenge in achieving such a goal.

Among modes of transportation, road and aviation are responsible for the largest part of GHG emission in the transportation sector (see Fig. 1.1). In contrast, rail transport is responsible for the lowest percentage (1.6%) of GHG emission in the transportation sector (see Fig. 1.1). For this reason (among others), railway transport has received increasing attention lately, especially due to its capability of running fully on electricity, which can be generated from green sources. Consequently, governmental bodies (such as EU) have imposed targets for the modal split in freight cargo, basically imposing more freight cargo to be transported by rail (see Fig. 1.2). As for passenger transport, the same trend will be most

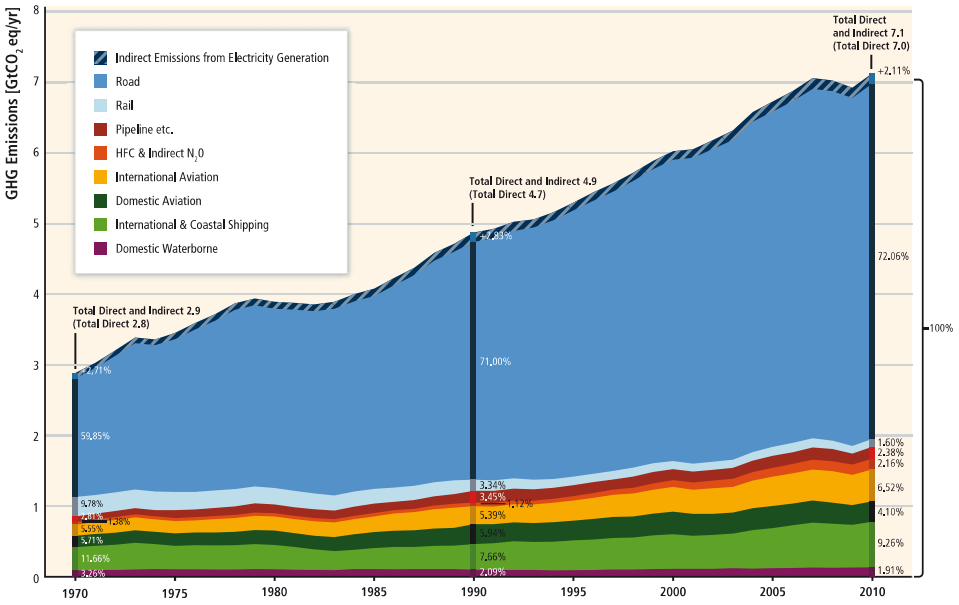

Figure 1.1: Green-house gases (GHG) emissions by mode of transport. Source: Figure 8.1 from IPCC AR5 report [3].

likely imposed. High-speed railway networks and the new concepts, such as Hyperloop, plan to compete (and are already competing) with road and aviation transport (the parts that do not require trans-oceanic voyages).

1.1. Problem statement and motivation

The increased demand on railway transport causes an acceleration in infrastructure degradation leading to an increased frequency of maintenance and repair operations (see Fig. 1.3). On top of that, the increase in railway traffic (more trains per period of time) also reduces the track availability for maintenance operations, thus leading to a negative feedback loop. Consequently, what before was considered normal "wear and tear" of the infrastructure is quickly turning into challenging problems causing disruptions to the normal operation of traffic. The way to overcome these problems is through innovative design and materials, both for the newly built tracks and for the repair and rehabilitation of the already existing tracks. This is an especially big challenge for railway engineers since the design of the classical (and to some extent modern) railway track is based on load-bearing considerations and maintainability [4], and does rarely take into account long-term durability.

A substantial part of the railway infrastructure degradation relates to the vertical position of the track, which changes over time due to ballast and soil settlement. The main reason for losing track geometry is the deformation and densification of the ballast layer, representing 75% of the total track position maintenance [5]. Position correction constituted (in 2007)

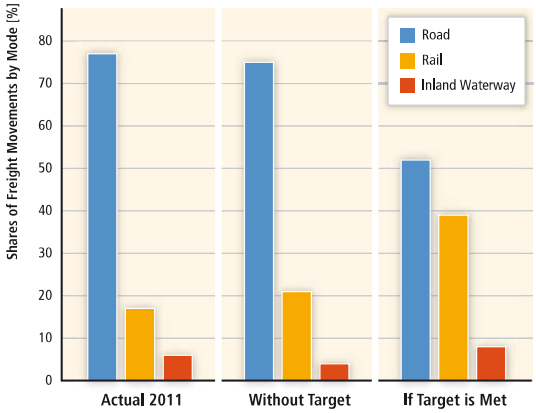

Figure 1.2: Projected freight modal split in the EU-25 in 2030 comparing 2011 shares with future business-as-usual shares without target and with EU White Paper modal split target. Source: Figure 8.8 from IPCC AR5 report [3].

around 40% of maintenance operations on railway infrastructure in the Netherlands [6], with a similar trend also seen in other countries [5]. Consequently, position correction is one of the most important causes of reduced availability of the railway and the subsequent disruption that results.

When it comes to position correction, the so-called *transition zones* require 3–8 times more frequent maintenance than the regular parts of the railway track [5, 6]. Transition zones in railway tracks are areas with substantial variation of track properties (e.g., foundation stiffness) encountered near rigid structures such as bridges, tunnels, culverts, or rail-crossings (see Fig. 1.4). The reason for more frequent maintenance required at transition zones is that differential settlements at these locations are much more pronounced than in the rest of the track (referred to in this thesis as the *open-track*); for example, Nielsen et al. [7] found a strong correlation between the track stiffness inhomogeneity and local irregularities in the vertical track geometry (i.e., differential settlement). Compared to the open-track, significant differences in settlements develop at transition zones over a relatively small distance leading to an even higher variability of the support properties, and in more extreme cases to unsupported sleepers (also known as hanging sleepers [8]). Once the differential settlements exceed a certain threshold, maintenance is (preferably) scheduled in order to avoid limiting the velocity of the train at these locations.

Plenty of causes have been presented in literature for the differential settlements at transition zones. These causes can be divided into two categories, namely the causes leading to the *initiation phase* of the degradation when the track is considered straight and without faults, and the *accumulation phase* in which the track already has differential settlements leading to negative feedback processes that further aggravate the problem. The main degradation processes in the initiation phase of the differential settlement at transition zones are given below:

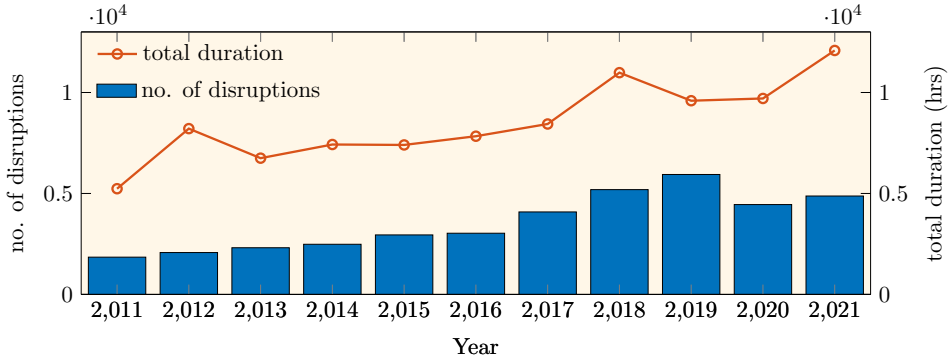

Figure 1.3: Number of disruptions and the total duration of the disruptions in the Dutch railway network between 2011 and 2021. Source: https://www.rijdendetreinen.nl/

a) The difference in mechanical properties (e.g., stiffness, mass, damping, etc.) of the supporting structure at transition zones causes amplification of stresses and strains when the vehicle passes through this location [4, 9, 10]. At the locations where the strains are increased (compared to the open-track), the settlement is amplified, thus leading to differential settlements.

b) Under normal operation conditions, the open-track has a higher settlement rate than the man-made structure, which is usually built such that it does not settle (e.g., founded on piles). This leads, over time, to the supporting structure (soil and sub-ballast) in the open-track to settles more than the man-made structure, thus leading to differential settlements [11].

As for the accumulation phase, the above-mentioned causes continue to be present, and are even amplified. For example, the existence of differential settlements may lead to an even larger difference in mechanical properties of the supporting structure, thus causing a larger amplification of stresses and strains; this is one of the negative feedback processes that are present in the accumulation phase. Other significant causes of degradation in the accumulation phase are presented below:

i) If the profile of differential settlements has a small wavelength and sufficient amplitude, hanging sleepers can occur. Apart from contributing to a negative feedback loop (as explained above), the presence of the hanging sleepers can lead to impact loading of the ballast layer [8] which further exacerbates the degradation.

ii) The differential settlements lead to unlevel rail profile causing an additional amplification of stresses and strains when the vehicle encounters such a fault [13].

Figure 1.4: Different types of transition zones in railway tracks. Culvert (top left; source: https://joewagnergroup.com.au/projects/western-culverts-replacement/), tunnel (top right; source: [12]), bridge (bottom left; source: [4]), and switch (bottom right; source: http://www.railroadpart.com/rail-track-parts/railway-turnout.html).

iii) In the case of hanging sleepers and/or unlevel rail, the redistribution of stresses in the structure can lead to overloading certain components causing ballast particle breakage and sleeper deterioration.

Other site specific causes of degradation in the accumulation phase (e.g., ballast fouling, lateral spreading of ballast, etc.) can be found in literature (e.g., [5, 9, 14]).

Given the plethora of causes for differential settlements at transition zones in railway tracks, it is reasonable to expect that one type of mitigation measure (most likely) cannot be efficient for all scenarios. Consequently, the efficiency of a mitigation measure depends on the ability to identify the governing degradation mechanism(s) in a given scenario.

1.2. Thesis objective

The occurrence of differential settlements at transition zones has been known for a long time and a multitude of mitigation measures have been designed to cope with this problem [5, 14]. Nonetheless, the mitigation measures have had just limited success [14, 15] and in some cases have even exacerbated the problem [9]. Although the failure of some mitigation measures stems from inadequate design and poor implementation [9], overall, the lack of efficiency of mitigation measures can be attributed to the lack of understanding of the main mechanism(s) that drive(s) the differential settlement. To design a successful mitigation measure and/or a maintenance procedure that reduces the subsequent frequency

of maintenance, in the author's view, one needs to first identify the governing degradation mechanism(s) in each specific situation and then tailor the mitigation measure to counteract that mechanism(s). Therefore, one needs a thorough understanding of the physical processes that lead to differential settlements at transition zones.

This leads to the first and main objective of this thesis, which is to *investigate and advance the understanding of the main mechanisms that lead to railway track degradation at transition zones*. Established researchers in this field already generated knowledge about this problem. Therefore, this thesis aims to deepen the understanding that will serve future researchers in designing more efficient mitigation measures.

In previous studies, researchers have investigated the problem of differential settlements at transition zones through field measurements (or lab experiments) and models. Due to the many types of transition zones, railway track designs, environmental factors, and others, the knowledge developed based on field measurements tends to be site specific and it is difficult to generalize. Consequently, the majority of studies have used models to (i) understand and (ii) predict the response of railway tracks at transition zones. Researchers aiming at (i) have usually used simplified phenomenological models in which system characteristics that are not of interest are excluded (e.g., [16–24]). More recently, the models' complexity has increased tremendously by incorporating many system characteristics (e.g., [10, 11, 25–32]), making these models ideal for (ii), but less ideal for (i) due to the many mechanisms simultaneously at play.

This leads to the second objective of this thesis, which is *to investigate the effect of specific characteristics of the railway system on the degradation at transition zones*. In other words, the second objective entails improving the simplified models by incorporating additional characteristics and determining which of these characteristics is of importance and which can be neglected. With the knowledge acquired by fulfilling this objective, the gap between the simplified and complex models can be bridged. It must be emphasized that the second objective is, to some extent, incorporated in the first one because understanding the influence of specific system characteristics can advance the knowledge of the mechanisms that drive settlement at transition zones.

1.3. Scope of the research

The problem of accumulated degradation at transition zones in railway tracks involves many fields of expertise, such as moving-load dynamics, soil dynamics, geotechnical engineering, more applied railway engineering (when it comes to maintenance procedures, for example), behaviour of granular materials (ballast) with multiple time scales (fast time which represents the instantaneous damage, and slow time in which the accumulation of damage occurs over many cycles), mechanical engineering (if one wants to investigate the influence of the vehicle), etc. Naturally, this dissertation can only focus on a few of these aspects, and this sub-section presents the chosen focus.

To mitigate the degradation in the accumulation phase, innovative maintenance techniques should be developed, or the ones that already exist need to be improved. However, to propose a long-term solution, one should aim at fixing the root cause. Therefore, this thesis focuses on the initiation phase. Furthermore, the pronounced differential settlements at transition zones is a damage accumulation process involving many train passages (i.e., many load-unload cycles of the supporting structure). Nonetheless, because this thesis investigates the initiation phase, it thus focuses on the instantaneous residual deformation to one (or a few) passages. The knowledge of the instantaneous residual deformation could be used in a model that accounts for both the fast time (instantaneous residual deformation) and slow time (the accumulation over many cycles); however, this is outside the scope of this thesis.

When it comes to the initiation phase, two main causes have been presented in Section 1.1. After the first train passage, due to cause b), the open-track would have uniformly settled a certain amount that is larger than the track laying on the man-made structure, thus leading to differential settlement. On top of that, the differential settlements in the transition zone are exacerbated due to response amplification (cause a)). While both causes can be influential, this thesis focuses only on the differential settlements caused by cause a) and neglects the settlements caused by cause b). "Find a reason why?" As a consequence of focusing on the initiation phase and on cause a), the investigated system is representative of a railway track in good condition (e.g., after tamping processes), meaning that the system shows (almost) no faults. For amplification of stresses and strains (at transition zones) to occur in such a system, the vehicle needs to travel at a relatively high velocity. Therefore, this thesis focuses on high-speed railway or on normal-speed railway founded on very soft soils (where the critical velocity is low). Furthermore, although some cases have been encountered where the train exceeded the critical velocity (e.g., the Swedish X-2000 high-speed train which runs along the West Coast Line between Gothenburg and Malmö [33]), generally the train velocity is in the sub-critical regime. Consequently, this thesis focuses on velocities close to the critical one, but in the sub-critical regime.

As stated in Section 1.2, this thesis aims to deepen the understanding of the behaviour of railway tracks at transition zones by using simplified models. More specifically, the models formulated in this thesis are phenomenological, meaning that they isolate one (or a few) specific phenomenon to be investigated and neglect the others. Although they represent a distortion of reality, phenomenological models facilitate the understanding of the specific phenomenon it describes and its corresponding mechanisms. In some situations when, for example, specific predictions are required, the interference and interaction of multiple phenomena is important to be taken into account such that the predictions are as close as possible to reality. For this, *predictive* models are best suited (e.g., 3-D finite element models [10, 11, 26, 27, 31]). With predictive models, although not impossible, it is difficult to investigate one (or few) specific phenomenon in great detail because of the difficulty in distinguishing the contribution of each phenomenon that is present in the process and

complex (sometimes unknown) interactions between phenomena. For this reason, phenomenological models are preferred. In this thesis, the phenomenon that the models are designed to investigate is the transition radiation phenomenon (explained thoroughly in Chapter 2). The simplifications compared to predictive models are made mainly with regard to the geometry of the track, soil, and man-made structure, and the vehicle model. More specifically, the 3-D geometry of the track at transition zones is incorporated indirectly by changing stiffness, damping, and mass properties of the 1-D and 2-D phenomenological models. When it comes to the vehicle model, the response under a single wheel is investigated and the influence of the rest of the vehicle is neglected.

Finally, this thesis focuses on the transition radiation phenomenon (explained thoroughly in Chapter 2). In an initially straight track (no differential settlements and no faults) with a transition zone, transition radiation is the phenomenon that is associated to the response amplification in the transition zone. Consequently, some researchers have identified transition radiation as one of the causes of track and foundation degradation [4, 9, 15, 34]. However, other researchers (e.g., [13, 35]) have found that the contribution of transition radiation to the response amplification and, consequently, to track deterioration is insignificant compared to other contributions such as, for example, unlevel rail. Although their findings offer an incomplete picture and are, consequently, slightly misleading (see Section 4.3.5), for the the set of parameters investigated, their findings are correct. The reason this thesis focuses on transition radiation is that, as specified in the previous paragraphs, it focuses on (i) the initiation phase (therefore, none of the feedback processes are considered, such as unlevel rail, hanging sleepers, etc.), and (ii) on the response amplification at transition zones (cause a)).

1.4. Thesis outline

This thesis starts by introducing the phenomenon that leads to amplification of stresses and strains at the transition zones, namely *transition radiation* [36–38]. Transition radiation is demonstrated in its purest form by using a 1-D model consisting of an infinite Euler–Bernoulli beam on Winkler foundation, where the foundation has an abrupt jump in stiffness. The mechanism that causes response amplification is identified and investigated, and the influence of load velocity on the response amplification is addressed. Chapter 2 concludes with the analysis of energy exchange between different components of the system as the load traverses the transition zone.

The third chapter investigates the influence of the critical velocity and its relation to the train velocity on transition radiation and, consequently, on the response amplification at transition zones. Some simplified models of the railway track (e.g., Euler–Bernoulli beam on Winkler foundation) neglect the mass of the ballast and sub-grade causing a serious overestimation of the critical velocity compared to reality. This raises two questions: (i) should the velocity of the load be chosen to match the velocity of the train, or should it be chosen such that the load velocity relative to the critical one matches the real scenario?, and (ii)

what is the influence of over-estimating the critical velocity on the response amplification? Both these questions are addressed in Chapter 3.

Chapter 4 studies of the effect of taking into account the vehicle's own degree of freedom on the response amplification at transition zones. More specifically, the vehicle is modelled as a loaded oscillator in which the mass represents the wheel and the constant load on the mass represents the deadweight of the rest of the carriage. A parametric study is performed by varying the velocity and the properties of the transition zone, and the results are compared to the ones obtained using a moving constant load instead of an oscillator. This chapter addresses not only the second goal of this thesis (determining the influence of certain modelling choices), but also generates some knowledge by showing that the conclusions of some preceding studies are not general, but limited to a quasi-static velocity regime.

In the ballasted railway tracks, the rail is periodically supported by sleepers. The periodicity of the supports causes additional propagating waves in the response generated by the moving load. Chapter 5 investigates if the additional propagating waves are influential for the response amplification at transition zones. The chapter identifies amplification mechanisms that are caused by the combination of (i) the periodicity of the support and (ii) the transition zone, initially for a system representative of catenary wires in railway tracks. Then, these amplification mechanisms are investigated for a system representative of a railway track and, finally, for a system representative of a Hyperloop transportation system. Like Chapter 4, this chapter addresses both aims of this thesis by investigating the influence of including/excluding the sleeper periodicity from the model and determining additional response amplification mechanisms.

Since the degradation/compaction of ballast is a nonlinear process, Chapter 6 introduces a nonlinear supporting structure to a simplified 1-D model. While all previous chapters have studied track degradation indirectly by investigating the response amplification, this chapter investigates the degradation directly. The nonlinear material model represents the instantaneous settlement of the ballast. The degradation after one and few load passages is studied, and the influence of load velocity and some mitigation measures (which are indirectly accounted for) is investigated through a parametric study.

The nonlinear material model introduced in Chapter 6 leads to a more computationally intensive procedure to determine the response of the system. While the computational effort in the case of the 1-D model formulated in Chapter 6 is not too high, the computational effort required for a 2-D model of the track can easily make the problem unfeasible to solve. To this end, Chapter 7 investigates three different solution methods to solve such a nonlinear problem. More specifically, the three solution methods are compared in terms of accuracy, computational efficiency, and feasibility of application to more complex systems (especially to a 2-D one). The comparison in terms of accuracy and computational efficiency is performed quantitatively using the 1-D model formulated in Chapter 6, while the feasibility of application to more complex systems is analysed qualitatively.

There are many significant differences between 1-D and 2-D models of a railway track. The one that is most relevant for this work is the fact that the supporting structure in the 2-D model, unlike in the 1-D model, is frequency-wavenumber dependent, thus making the response of the beam nonlocal in both time and space. To investigate how this influences the response amplification at the transition zones, and using the knowledge gained in Chapter 7, a 2-D model is formulated in Chapter 8. Nonetheless, the 2-D model is kept simple such that the observations made are as general as possible. The degradation is investigated in this system, and it is concluded that the 1-D model (Chapter 7) over-estimates the plastic deformation. Then, the influence of accounting for the nonlocality in both time and space of the supporting structure is investigated by an extensive comparison to equivalent 1-D models.

Finally, the thesis concludes with Chapter 9 which summarizes the conclusions drawn from this research together with several directions for future investigations.

2

Transition radiation in a system representative of a railway track

In fiecare teoretician, se afla un utopist.
Inside every theoretician lies an utopist.

Lucian Boia

The amplification of stresses and strains at transition zones in railway tracks can be associated to the phenomenon of *transition radiation* [38]. Transition radiation is emitted when a source (without an inherent frequency) moves along a straight line with constant sub-critical velocity and acts on or near an inhomogeneous medium [37]. This phenomenon was first analysed by Ginzburg and Frank [36] who described radiation of electromagnetic waves by a charged particle crossing the boundary between an ideal conductor and vacuum. In the early studies it was already apparent that transition radiation was universal from the physical point of view meaning that it occurs irrespective of the nature of the waves. Thus, later on it was also studied in acoustics [39] and mechanics of solids [38].

The first study of transition radiation of elastic waves excited by mechanical objects travelling in inhomogeneous elastic systems was done by Vesnitskii and Metrikine [38]. It occurs, for example, when a train approaches and crosses an inhomogeneity in the railway track (i.e., a transition zone). When this happens, there is an exchange of energy between the train and track [16]. Transition radiation is the radiation caused solely by the inhomogeneity, which is emitted into the railway track in the form of waves. It has been addressed as one of

the primary causes of track and foundation settlement in transition zones due to the often strong amplification of the stress and strain fields [4, 9, 15, 34].

In its purest form, transition radiation is addressed in structures acted upon by a moving constant load. The first study [38], was performed using an elastically supported infinite string subjected to a constant moving load. To also account for the flexural rigidity, Vesnitskii and Metrikin [16] studied a semi-infinite beam subject to a moving mass. Later on, the problem of a beam resting on a piecewise-homogeneous Winkler foundation subjected to a moving constant load was addressed using different solution methods: modal expansion techniques [18, 40] and the moving-element method [35]. To study wave propagation in the ground due to transition radiation, 2-D models of a piecewise-homogeneous continuum acted upon by a moving load [20, 21, 41, 42] as well as 3-D models of the complete track/soil system [27, 29, 30, 43] were analysed.

In this chapter, transition radiation is demonstrated on a system representative of a railway track and its most important characteristics are described. The motivation of this chapter is not its novelty because most results in this chapter have already been presented in literature, but rather to give the reader an introduction to the transition radiation phenomenon, which is beneficial for understanding following chapters. Nevertheless, the current chapter presents some novelty, namely the analysis of the energy balance and its derivation based on the equation of motion (presented in Section 2.4). A similar analysis has previously been performed using a string on Winkler foundation by Vesnitskii and Metrikin [16], while here an Euler–Bernoulli beam is used instead. In the following, a simplified model of a railway track with a transition zone is formulated, the steady-state and transient responses are derived and analysed, after which the analysis of the energy balance is presented. To focus the reader's attention to the qualitative analysis of the transition radiation phenomenon, the figures presented in this chapter mostly omit the x-, y-, and z-axis values. The parameter values used in this chapter are given in Table 6.1 with $k_{\mathrm{d,l}} = k_{\mathrm{d,l}}^{\mathrm{A}}$.

2.1. Model formulation

The system which can demonstrate transition radiation in its purest form and is also representative of a railway track is the infinite Euler-Bernoulli beam resting on Winkler foundation acted upon by a moving constant load (Fig. 2.1). The Winkler foundation has a jump in stiffness at $x = x_{\mathrm{tc}}$ (subscript tc stands for transition centre), dividing the infinite inhomogeneous domain into two semi-infinite homogeneous ones. The equation of motion of the system reads

$$EI\frac{\tilde{\partial}^4 w}{\tilde{\partial} x^4} + \rho\frac{\tilde{\partial}^2 w}{\tilde{\partial} t^2} + k_{\mathrm{d}}(x)\, w = -F_0\,\delta(x - vt), \qquad \forall x, \forall t, \tag{2.1}$$

$$w(x,t) = \begin{cases} w_{\mathrm{l}}(x,t), & x \le x_{\mathrm{tc}}, \\ w_{\mathrm{r}}(x,t), & x \ge x_{\mathrm{tc}}, \end{cases} \qquad k_{\mathrm{d}}(x) = \begin{cases} k_{\mathrm{d,l}}, & x < x_{\mathrm{tc}}, \\ k_{\mathrm{d,r}}, & x \ge x_{\mathrm{tc}}, \end{cases}$$

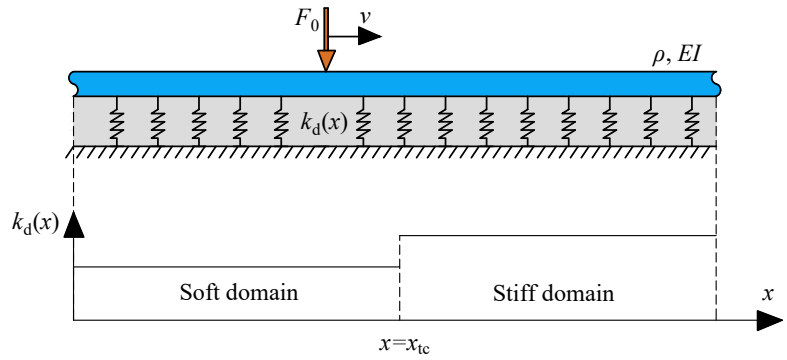

Figure 2.1: Model schematics: infinite Euler–Bernoulli beam resting on a piecewise-homogeneous Winkler foundation, subject to a moving constant load.

where $\frac{\tilde{\partial}}{\partial x}$ and $\frac{\tilde{\partial}}{\partial t}$ represent generalized derivatives with respect to space and time, respectively. Compared to the classical derivatives, the generalized ones can have discontinuities, and are necessary in Eq. (2.1) due to the Dirac delta function $\delta(\dots)$ on the right-hand side, which is a generalized function [44]. EI and ρ are the bending stiffness and mass per unit length of the beam, respectively, while $k_{d,l}$ and $k_{d,r}$ are the (homogeneous) foundation stiffnesses of the left and right semi-infinite domains, respectively. F_0 and v are the magnitude and the velocity of the moving load, while w_l and w_r represent the displacements of the left and right semi-infinite domains, respectively. The space and time dependency of the unknown displacements is omitted from most expressions for brevity. Furthermore, the use of both the $\leq$ and $\geq$ signs in the definition of $w(x,t)$ emphasizes that there is continuity in this quantity at the interface between the two domains (see below).

At the interface between the two domains, continuity in displacement and slope as well as in shear force and bending moment is imposed. Furthermore, the displacements at infinite distance from the moving load should not be infinite (they can be non-zero due to the absence of material damping). The interface and boundary conditions thus read

$$w_l(x_{tc},t) = w_r(x_{tc},t), \qquad w_l'(x_{tc},t) = w_r'(x_{tc},t), \tag{2.2}$$

$$w_l''(x_{tc},t) = w_r''(x_{tc},t), \qquad w_l'''(x_{tc},t) = w_r'''(x_{tc},t), \tag{2.3}$$

$$\lim_{(x-vt)\to-\infty} w_l(x,t) < \infty, \qquad \lim_{(x-vt)\to\infty} w_r(x,t) < \infty, \tag{2.4}$$

where primes denote classical partial derivatives with respect to x.

As the system is infinite and only locally inhomogeneous, the response is assumed to be in the steady state before the load reaches the transition zone. Consequently, initial conditions do not need to be formulated. Thus, Eqs. (2.1) to (2.4) constitute a complete description of the current problem. In the next section, the steady-state solution is derived.

2.2. Steady-state solution

In the limit case $k_{\mathrm{d,l}} = k_{\mathrm{d,r}} = k_{\mathrm{d}}$, the system described above becomes homogeneous and, consequently, its solution is in the steady state for all time moments. Although transition radiation is a transient process, it is of importance to first introduce the steady-state solution, also referred to as the *eigenfield*, because it determines certain characteristics of the transition radiation. This problem was first solved by Timoshenko [45] and many others have reconsidered and extended the problem (e.g., [46–49] among others). The solution is well-known, so only the characteristics important to this thesis are presented.

The equation of motion of the system with homogeneous Winkler foundation reads

$$EI\frac{\tilde{\partial}^4 w}{\tilde{\partial} x^4} + \rho\frac{\tilde{\partial}^2 w}{\tilde{\partial} t^2} + k_{\mathrm{d}} w = -F_0\,\delta(x - vt), \qquad \forall x, \forall t. \tag{2.5}$$

To obtain the steady-state solution to Eq. (2.5), the infinite domain can be divided into two semi-infinite ones, as follows:

$$w(x,t) = \begin{cases} w_{\mathrm{b}}(x,t), & x \le vt, \\ w_{\mathrm{f}}(x,t), & x \ge vt, \end{cases} \tag{2.6}$$

where w_{b} and w_{f} are the solutions behind and in front of the moving load, respectively. At the interfaces between the two domains, continuity in displacement, slope, and bending moment as well as balance of vertical forces is imposed. Furthermore, the displacements at infinite distance from the moving load should not be infinite (similar to the conditions imposed in Eq. (2.4)). The interface and boundary conditions of the homogeneous system thus read

$$w_{\mathrm{b}}(x = vt, t) = w_{\mathrm{f}}(x = vt, t), \qquad w'_{\mathrm{b}}(x = vt, t) = w'_{\mathrm{f}}(x = vt, t), \tag{2.7}$$

$$w''_{\mathrm{b}}(x = vt, t) = w''_{\mathrm{f}}(x = vt, t), \qquad w'''_{\mathrm{f}}(x = vt, t) - w'''_{\mathrm{b}}(x = vt, t) = \frac{F_0}{EI}, \tag{2.8}$$

$$\lim_{(x-vt)\to-\infty} w_{\mathrm{b}}(x,t) < \infty, \qquad \lim_{(x-vt)\to\infty} w_{\mathrm{f}}(x,t) < \infty. \tag{2.9}$$

The resulting equations of motion (of the domains behind and in front of the load) are now homogeneous because the forcing has been transferred from the right-hand-side of Eq. (2.5) to the interface condition expressing the vertical force equilibrium at $x = vt$. Consequently, the solutions of the homogeneous equations of motion can be assumed in the form of harmonic waves, as follows:

$$w_h(x,t) = A_h \mathrm{e}^{\mathrm{i}(\omega t - kx)}, \quad h = \{\mathrm{b}, \mathrm{f}\}, \tag{2.10}$$

where ω is the angular frequency and k the wavenumber of the harmonic wave. Substituting Eq. (2.10) in the homogeneous equations of motion, the *dispersion equation* is obtained, which

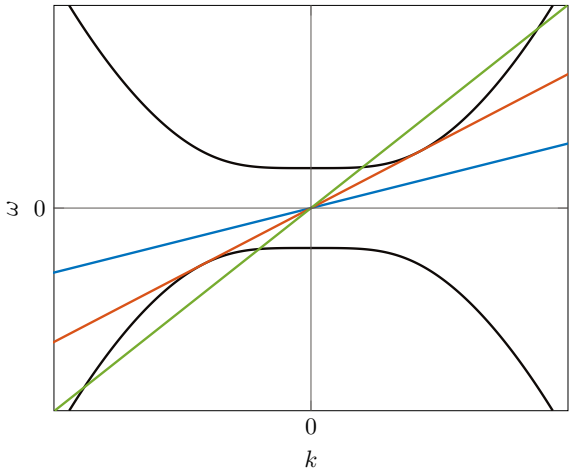

Figure 2.2: Dispersion curves (black) and the kinematic invariant for a sub-critical (blue), the critical (orange), and a super-critical velocity (green).

reads

$$\frac{EI}{\rho} k^4 - \omega^2 + \omega_{\mathrm{co}}^2 = 0, \tag{2.11}$$

where $\omega_{\mathrm{co}} = \sqrt{k_{\mathrm{d}}/\rho}$ is the cut-off frequency. To explicitly determine both ω and k, an additional equation is required; this comes in the form of the *kinematic invariant* that expresses the relation between the wavenumber, frequency, and the velocity of the load. For this system, its expression reads

$$\omega = kv. \tag{2.12}$$

From a physical perspective, the kinematic invariant ensures the phase equality of the generated waves at the point of the moving load. A more detailed derivation of the kinematic invariant is presented in Appendix A.

Solving Eq. (2.11) together with Eq. (2.12) leads to four pairs $(\omega, k) = \left(\omega_{1-4}^{\mathrm{e}}, k_{1-4}^{\mathrm{e}}\right)$, and their nature depends on the load velocity. The superscript e is used to emphasize that these quantities are solutions of the dispersion equation and kinematic invariant, and are no longer more variables. The expressions of the four wavenumbers are given in Appendix B, while the expression of the four frequencies can be obtained from Eq. (2.12).

The dispersion curves and the kinematic invariant are graphically represented in Fig. 2.2. For a velocity below the so-called *critical* velocity, there is no intersection between the kinematic invariant and the dispersion curves leading to complex-valued $(\omega^{\mathrm{e}}, k^{\mathrm{e}})$ pairs. In this scenario, the wave defined in Eq. (2.10) is evanescent for every $(\omega^{\mathrm{e}}, k^{\mathrm{e}})$ pair, meaning that there is no energy radiation away from the load. For a super-critical velocity, the kinematic invariant intersects the two dispersion curves at four locations giving rise to real-valued $(\omega^{\mathrm{e}}, k^{\mathrm{e}})$ pairs. In this scenario, all waves are propagating and energy is radiated away from

the load. At the critical velocity, the kinematic invariant is tangential to the dispersion curves resulting in repeated real-valued $(\omega^{\mathrm{e}}, k^{\mathrm{e}})$ pairs. The repeated nature of the roots is the mathematical condition for resonance (analogous to the single-degree-of-freedom system). From a physical point of view, resonance occurs because energy is being radiated at the critical velocity (real-valued pairs), but the group velocity (graphically represented by the slope of the tangent to the dispersion curve at the point of intersection between the kinematic invariant and the dispersion curves) of the radiated waves is equal to the load velocity, meaning that the radiated waves cannot propagate away from the load. This causes energy build-up leading to resonance. The expression of the critical velocity c_{cr} of this system reads [50]

$$c_{\mathrm{cr}} = \sqrt[4]{\frac{4k_{\mathrm{d}}EI}{\rho^2}}. \tag{2.13}$$

With the known pairs $(\omega^{\mathrm{e}}, k^{\mathrm{e}})$, the solutions are given by the following expression:

$$w_h(x,t) = A_h \mathrm{e}^{-\mathrm{i}k_1^{\mathrm{e}}(x-vt)} + B_h \mathrm{e}^{-\mathrm{i}k_2^{\mathrm{e}}(x-vt)} + C_h \mathrm{e}^{-\mathrm{i}k_3^{\mathrm{e}}(x-vt)} + D_h \mathrm{e}^{-\mathrm{i}k_4^{\mathrm{e}}(x-vt)}, \quad h = \{\mathrm{b}, \mathrm{f}\}. \tag{2.14}$$

It must be emphasized that Eq. (2.14) is not valid for the scenario when $v = c_{\mathrm{cr}}$. The eight unknown amplitudes are determined from the interface and boundary conditions. Throughout this thesis, the wavenumbers of the eigenfield are chosen such that

$$\mathrm{Re}(k_1^{\mathrm{e}}) > 0, \quad \mathrm{Im}(k_1^{\mathrm{e}}) \leq 0, \tag{2.15}$$

$$\mathrm{Re}(k_2^{\mathrm{e}}) > 0, \quad \mathrm{Im}(k_2^{\mathrm{e}}) \geq 0, \tag{2.16}$$

$$\mathrm{Re}(k_3^{\mathrm{e}}) < 0, \quad \mathrm{Im}(k_3^{\mathrm{e}}) \geq 0, \tag{2.17}$$

$$\mathrm{Re}(k_4^{\mathrm{e}}) < 0, \quad \mathrm{Im}(k_4^{\mathrm{e}}) \leq 0. \tag{2.18}$$

Consequently, when applying the boundary conditions at infinite distance from the moving load, the waves with k_2^{e} and k_3^{e} are admissible in the domain that extends to $-\infty$ and the waves with k_1^{e} and k_4^{e} are admissible in the domain that extends to $+\infty$; this leads to $A_{\mathrm{b}} = D_{\mathrm{b}} = B_{\mathrm{f}} = C_{\mathrm{f}} = 0$. The other four amplitudes are determined from the interface conditions Eqs. (2.7)–(2.8), and are presented in Appendix B. The eigenfield, thus, becomes

$$w^{\mathrm{e}}(x,t) = \begin{cases} B_{\mathrm{b}} \mathrm{e}^{-\mathrm{i}k_2^{\mathrm{e}}(x-vt)} + C_{\mathrm{b}} \mathrm{e}^{-\mathrm{i}k_3^{\mathrm{e}}(x-vt)}, & x < vt, \\ A_{\mathrm{f}} \mathrm{e}^{-\mathrm{i}k_1^{\mathrm{e}}(x-vt)} + D_{\mathrm{f}} \mathrm{e}^{-\mathrm{i}k_4^{\mathrm{e}}(x-vt)}, & x \geq vt. \end{cases} \tag{2.19}$$

It must be noted that w^{e} in Eq. (2.19) is real-valued.

This thesis investigates mainly sub-critical velocities, therefore, only this scenario is elaborated in the following. Fig. 2.3 presents the real and imaginary parts of the wavenumber k^{e} and the amplitude of one of the waves (i.e., A_{f}) against the velocity of the load. (Just one wavenumber and amplitude are presented because the other ones differ through just the sign of the real or imaginary parts, and not through their magnitude). The imaginary part

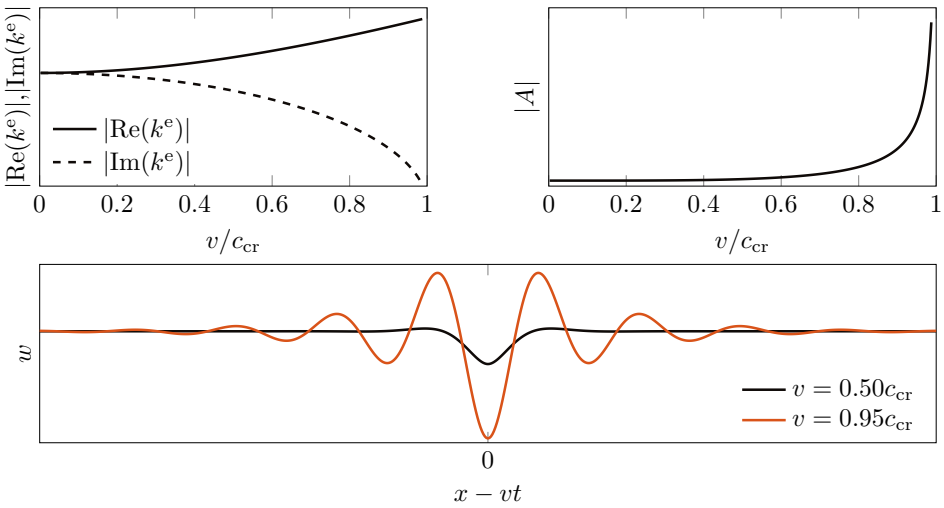

Figure 2.3: The wavenumber (top left panel) and amplitude (top right panel) of the steady-state response against the load velocity and a snap-shot of the eigenfield for two different sub-critical load velocities (bottom panel).

of the wavenumber determines the decay of the eigenfield with distance from the load. As can be seen, the imaginary part of the wavenumber decreases with increasing velocity meaning that the width of the eigenfield increases with increasing velocity. The real part of the wavenumber dictates the wavelength of the eigenfield. For a small load velocity, the wavelength is large, and together with the exponential decay of the eigenfield with distance from the load (dictated by the imaginary part of the wavenumber), this leads to an eigenfield that has a quasi-monotonic decrease away from the load (black line in bottom panel of Fig. 2.3). However, with increasing velocity, the wavelength decreases leading to a more wavy eigenfield. Furthermore, as can be seen from the right panel of Fig. 2.3, the amplitude of the eigenfield increases with increasing velocity, the increase being more pronounced above $v \approx 0.75c_{cr}$; this is the velocity regime on which this thesis focuses.

The bottom panel in Fig. 2.3 presents a snap-shot of the eigenfield for different load velocities. The displacements field in the sub-critical velocity regime moves together with the load and is unchanged in the reference frame that moves with the load (i.e., $\xi = x - vt$); this is due to the fact that the (ω^e, k^e) pairs are complex-valued and there is no wave radiation away from the load. It can be seen that at a larger velocity, the eigenfield is broader, more wavy and has a significantly higher amplitude, confirming the observations made previously.

2.3. Transient solution

The response of the inhomogeneous system described by Eqs. (2.1)–(2.4) can be obtained semi-analytically in various ways (e.g., [51]), but cannot be determined fully analytically. We

choose to apply the Fourier transform* over time and represent the response as a summation of wave modes because we consider this method to be most elegant for this problem. The response obtained in the Fourier domain is analytical and the inverse transform is then performed numerically. The equation of motion in the Fourier domain reads

$$\tilde{w}'''' + k^4(x)\,\tilde{w} = -\frac{F_0}{EI\,v}\mathrm{e}^{-\mathrm{i}\omega\frac{x}{v}}, \tag{2.20}$$

$$k(x) = \begin{cases} k_\mathrm{l} = \sqrt[4]{-\overline{\rho}\omega^2 + \overline{k}_{\mathrm{d,l}}}, & x \le x_\mathrm{tc}, \\ k_\mathrm{r} = \sqrt[4]{-\overline{\rho}\omega^2 + \overline{k}_{\mathrm{d,r}}}, & x \ge x_\mathrm{tc}, \end{cases} \tag{2.21}$$

where the tilde denotes the quantity in the Fourier domain, the overbar indicates that the quantity is scaled by EI, and $\omega \in (-\infty, \infty)$ is the Fourier-domain variable. To determine $\tilde{w}$ from Eq. (2.20), a particular solution is superimposed to the solution of the homogeneous equation. The particular solutions $\tilde{w}_{\mathrm{p,l}}$ and $\tilde{w}_{\mathrm{p,r}}$ are sought for having the same spatial distribution as the forcing and read

$$\tilde{w}_{\mathrm{p,l}}(x,\omega) = -\frac{F_0}{EI}\frac{v^3}{\omega^4 - k_\mathrm{l}^4 v^4}\mathrm{e}^{-\mathrm{i}\omega\frac{x}{v}}, \qquad x \le x_\mathrm{tc}, \tag{2.22}$$

$$\tilde{w}_{\mathrm{p,r}}(x,\omega) = -\frac{F_0}{EI}\frac{v^3}{\omega^4 - k_\mathrm{r}^4 v^4}\mathrm{e}^{-\mathrm{i}\omega\frac{x}{v}}, \qquad x \ge x_\mathrm{tc}. \tag{2.23}$$

The particular solution $\tilde{w}_{\mathrm{p,l}}$ is the frequency-domain eigenfield of a homogeneous system with the properties of the left domain (and analogously for $\tilde{w}_{\mathrm{p,r}}$). In other words, evaluating the inverse Fourier transform of the particular solution (as done through contour integration in [49]) would lead to the eigenfield described in Section 2.2. The complete solutions to Eq. (2.20) (including the solutions of the homogeneous equation) are given as follows:

$$\tilde{w}_\mathrm{l}(x,\omega) = A_\mathrm{l}\mathrm{e}^{-\mathrm{i}k_\mathrm{l}x} + B_\mathrm{l}\mathrm{e}^{\mathrm{i}k_\mathrm{l}x} + C_\mathrm{l}\mathrm{e}^{k_\mathrm{l}x} + D_\mathrm{l}\mathrm{e}^{-k_\mathrm{l}x} + \tilde{w}_{\mathrm{p,l}}(x,\omega), \qquad x \le x_\mathrm{tc}, \tag{2.24}$$

$$\tilde{w}_\mathrm{r}(x,\omega) = A_\mathrm{r}\mathrm{e}^{-\mathrm{i}k_\mathrm{r}x} + B_\mathrm{r}\mathrm{e}^{\mathrm{i}k_\mathrm{r}x} + C_\mathrm{r}\mathrm{e}^{k_\mathrm{r}x} + D_\mathrm{r}\mathrm{e}^{-k_\mathrm{r}x} + \tilde{w}_{\mathrm{p,r}}(x,\omega), \qquad x \ge x_\mathrm{tc}. \tag{2.25}$$

The four branches of k_h (where $h = \{\mathrm{l}, \mathrm{r}\}$) are all complex valued when ω is below the cut-off frequency $\omega_{\mathrm{co},h} = \sqrt{k_{\mathrm{d},h}/\rho}$ and when $\omega > \omega_{\mathrm{co},h}$, there are two real-valued and two imaginary-valued branches. Throughout this thesis, the branches of k_h are chosen such that the imaginary part is negative and the real part is positive. This choice leads to $A_\mathrm{l} = D_\mathrm{l} = B_\mathrm{r} = C_\mathrm{r} = 0$ when the boundary conditions imposing a finite displacement at infinite distance from the load are applied, leading to the following expression for the displacement:

$$\tilde{w}(x,\omega) = \begin{cases} B_\mathrm{l}\mathrm{e}^{\mathrm{i}k_\mathrm{l}x} + C_\mathrm{l}\mathrm{e}^{k_\mathrm{l}x} + \tilde{w}_{\mathrm{p,l}}(x,\omega), & x \le x_\mathrm{tc}, \\ A_\mathrm{r}\mathrm{e}^{-\mathrm{i}k_\mathrm{r}x} + D_\mathrm{r}\mathrm{e}^{-k_\mathrm{r}x} + \tilde{w}_{\mathrm{p,r}}(x,\omega), & x \ge x_\mathrm{tc}. \end{cases} \tag{2.26}$$

*Throughout this thesis we use $\mathrm{e}^{-\mathrm{i}\omega t}$ as the kernel for the forward transform and $\mathrm{e}^{\mathrm{i}\omega t}$ for the inverse transform.

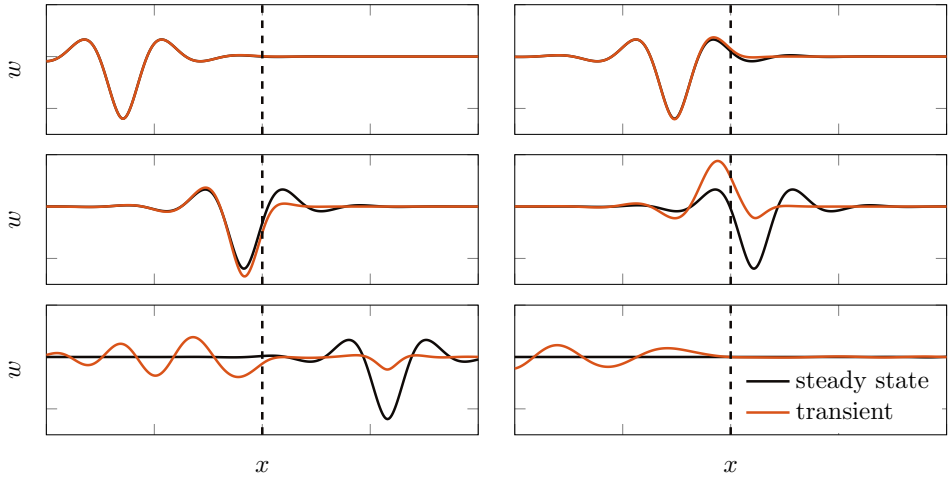

Figure 2.4: Snapshots of the displacement field at different time moments for the system with a jump in foundation stiffness; the vertical dashed line indicates the location of the jump in stiffness.

The remaining four amplitudes are determined from the interface conditions (Eqs. (2.2) and (2.3)). Their expressions are not given here for brevity, but can be obtained straightforwardly by using a symbolic mathematical software (e.g., Maple or Mathematica). To obtain the solution in the time domain, the inverse Fourier transform is applied numerically.

Fig. 2.4 presents the transient response in the time domain together with the eigenfield (of an homogeneous system with the properties of the left domain) for comparison. Far away from the transition zone, the two responses are practically identical (theoretically they are identical only at $t \to -\infty$). When the moving load is close to the transition, the transient response is distorted in comparison to the eigenfield. In the process of the load passing the transition, waves are radiated; the most noticeable are propagating in negative x-direction, although the wave radiation occurs in both directions. Furthermore, evanescent waves that remain in the vicinity of the transition zone are also excited. It can also be observed that the wave propagation still occurs even when the load has left the transition zone (provided that the damping in the system is small).

For certain time moments, amplification of the response can be observed in the vicinity of the load, both downwards and upwards (e.g., the two middle panels in Fig. 2.4). This is the amplification of stresses and strains that can be associated with the differential settlements at transition zones (although Fig. 2.4 presents displacements, the force in the foundation is obtained when multiplying the displacement by $k_\mathrm{d}(x)$). The response amplification is caused by the interference of the incoming eigenfield and the reflected wave-field at the transition, referred to as the *free field*. Mathematically, the free field is nothing else than the homogeneous solution (see Eq. (2.26)) that is necessary to satisfy the interface conditions. It becomes obvious that the more pronounced the free field is compared to the eigenfield, the

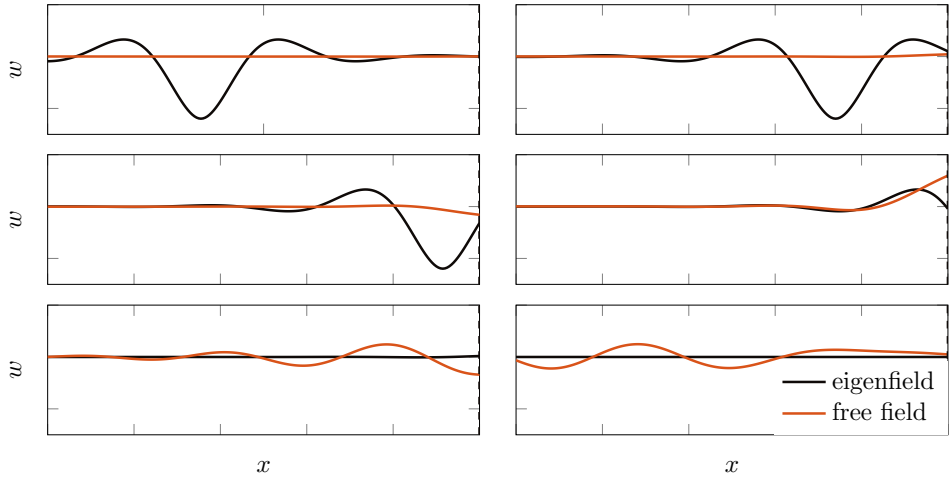

Figure 2.5: Snapshots of the eigenfield and free field in the left domain at different time moments for the system with a jump in foundation stiffness; the vertical dashed line indicates the location of the jump in stiffness.

larger the amplification (the amplification is always relative to the approaching eigenfield). The two fields (eigenfield and free-field) are represented separately for the soft domain in Fig. 2.5. The free-field is excited once the eigenfield is close enough to the jump in stiffness. This implies that the broader the approaching eigenfield, the more interference between the two fields, potentially leading to a larger zone over which the amplification occurs.

The left panel in Fig. 2.6 presents the displacement evaluated under the moving load for two load velocities. As shown in the previous section, the eigenfield width increases with increasing velocity (see bottom panel in Fig. 2.3). The wider eigenfield leads to a larger zone over which the response amplification occurs, confirming the statement made in the previous paragraph. Furthermore, the maximum amplification increases with increasing velocity, as presented in Fig. 2.8 (blue lines).

Fig. 2.7 presents the amplitude spectra of the eigenfield (i.e., $\tilde{w}_{\mathrm{p,l}}$) and of the free field (i.e., $\tilde{w}$ without $\tilde{w}_{\mathrm{p,l}}$) evaluated close to the jump in stiffness and far away to its left. It can be seen that far away from the transition, the free field is non-zero only above the cut-off frequency because the evanescent waves decay before reaching this location. Meanwhile, the amplitude spectrum of the free field close to the transition is non-zero both below and above the cut-off frequency of the soft domain; this shows that the transition radiation process generates both evanescent and propagating waves. For a large load velocity, most of the spectrum content in the near field is located above the cut-off frequency. Consequently, quantities evaluated in the far field (e.g., energy flux) can be good indicators of the amplification that occurs due to the transition. However, for lower velocities, there is content both below and above the cut-off frequency meaning that analysing solely quantities in the far field is not representative of the amplification that occurs in the near field. In this case,

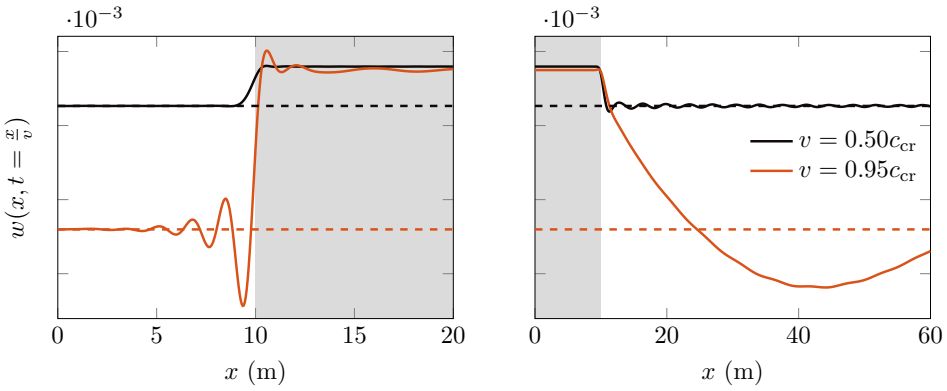

Figure 2.6: The transient response evaluated under the moving load in the soft-to-stiff scenario (left panel) and stiff-to-soft one (top right panel). The stiff domain is represented through the grey background, while the horizontal dashed lines indicate the maximum steady-state displacement in the soft domain.

other quantities (e.g., power input by the load) that include information about the near field need to be included in the investigation. These quantities are addressed in Section 2.4.

Soft-to-stiff vs stiff-to-soft transition

Although the soft-to-stiff and stiff-to-soft transitions seem to poses a certain symmetry, their responses are quite distinct. This has also been observed in field measurements where the settlement profile was different in the two situations. In this sub-section, we investigate the cause of the different behaviour between the soft-to-stiff and stiff-to-soft transitions.

Fig. 2.6 presents a comparison of the two transition scenarios. The displacement evaluated under the moving load is presented for a quasi-static load velocity and one close to the critical velocity. To highlight the response amplification, the steady-state displacement under the moving load in the soft domain is also presented through the horizontal dashed lines; only the one in the soft domain is presented because we are interested in the response amplification before (soft-to-stiff) and after (stiff-to-soft) the stiff zone. It can be seen that for a relatively small load velocity, the results in the two scenarios are similar, even though the amplification in the stiff-to-soft scenario is slightly larger than in the soft-to-stiff one. More importantly, the amplification in both scenarios for the small velocity is significantly lower compared to the large velocity. For the large velocity, the responses in the two scenarios are different. In the soft-to-stiff scenario, the eigenfield travelling in positive x-direction interferes with the free-field travelling in negative x-direction, leading to the response under the moving load to oscillate with a high frequency. In the stiff-to-soft scenario, both interfering fields (eigenfield and free field) travel in positive x-direction, and for the large load velocity ($v = 0.95c_{\mathrm{cr}}$), they have similar travelling velocities. This leads to their constructive interference to occur over a much larger distance (as seen in the different domain length scales between the left and top panels), and to a low frequency oscillation

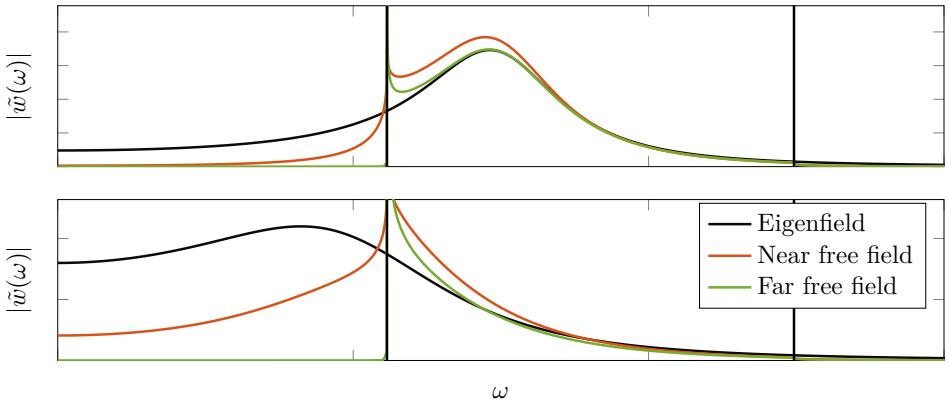

Figure 2.7: The frequency spectra of the response for a high velocity (top panel; $v = 0.95c_{cr}$) and lower velocity (bottom panel; $v = 0.7c_{cr}$). The near/far field corresponds to a location close to/far away from the jump in stiffness.

of the response under the moving load. This implies that, for a relatively large velocity, the settlement in the soft-to-stiff scenario will occur close to the stiff zone and will have a small wavelength, while the opposite is true for the stiff-to-soft scenario.

Although the maximum response amplification in both scenarios is similar in magnitude, this is only the case for the system without material damping. Once damping is accounted for in the foundation, the free field decays with distance from the transition. This causes the amplification in the stiff-to-soft scenario, which occurs at a large distance from the transition, to decrease considerably even when prescribing a small amount of damping. This is shown in Fig. 2.8 that presents the maximum amplification in both scenarios versus relative load velocity (v/c_{cr}), for a small (top panel) and a large (bottom panel) amount of damping. The addition of damping causes the maximum amplification in the stiff-to-soft case to decrease at large relative velocities to values even smaller than at low relative velocities, while the presence or amount of damping does not significantly influence the amplification trend in the soft-to-stiff case (it does affect the magnitude, but not the trend). It is important to note that, at low to medium relative velocities, the maximum amplification in the stiff-to-soft scenario can be larger than in the soft-to-stiff one, but the velocity range over which this occurs decreases the higher the damping is.

To better understand the results presented in Figs. 2.6 and 2.8, we investigate each of the two waves that compose the free field and their individual contribution to the response amplification. We also study the influence of the foundation viscous damping on the two waves. The viscous foundation damping is given by an additional term ($+c_d\dot{w}$) in the equation of motion (Eq. 2.1), where the viscous damping coefficient c_d is define through a damping ratio ζ, which throughout this thesis is defined similarly to that of a single-degree-of-freedom system, and reads

$$c_d(x) = 2\zeta\sqrt{\rho\, k_d(x)}. \tag{2.27}$$

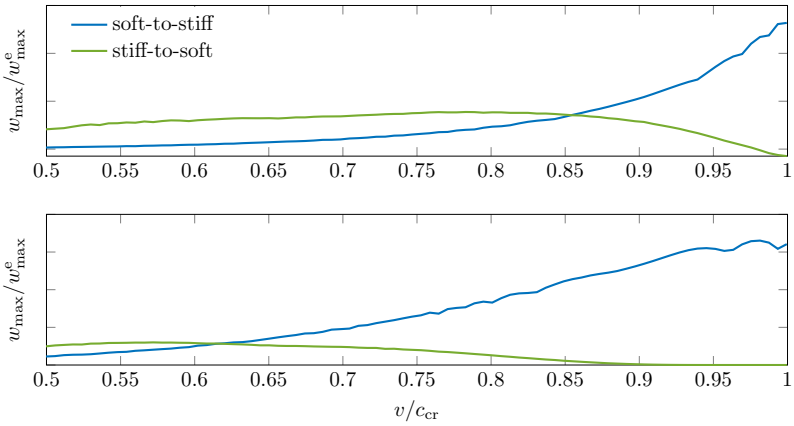

Figure 2.8: The maximum amplification versus velocity of the moving load for a small amount (top panel) and a large amount (bottom panel) of foundation damping for both soft-to-stiff and stiff-to-soft scenarios.

As can be seen, the damping coefficient in the two domain is chosen such that the damping ratio is kept constant.

Figs. 2.9 and 2.10 present the individual waves in the time domain (i.e., the time-domain counterparts of the free waves from Eq. (2.26)) in the soft-to-stiff and stiff-to-soft scenarios, respectively. Because the maximum downward response amplification generally occurs under the moving load, the waves are evaluated at $x = vt$. The left panels present the wave with argument $\pm \mathrm{i}k_{\mathrm{l,r}}x$ which we refer hereafter as the propagating wave, and the right panels show the wave with argument $\pm k_{\mathrm{l,r}}x$ referred to as the evanescent wave. Although both waves have a continuous frequency spectrum meaning that both are evanescent at frequencies under the cut-off one, we refer to them as aforementioned because one has a stronger propagation component while the other has the opposite. Finally, these waves are presented for three velocities (low, medium, and large relative velocity) and for varying amount of foundation damping. The way to interpret these plots is to understand that each wave in the left panel is superimposed with its counterpart from the right panel to obtain the full free field under the moving load; the full free field is superimposed with the eigenfield (which has a constant value under the moving load) to obtain the full transient response. Note that the downward response amplification is of interest throughout this analysis.

The soft-to-stiff scenario presented in Fig. 2.9 shows that for relatively low (top panels) and medium (middle panels) velocities, the propagating wave enables the downward amplification while the evanescent wave reduces the amplification because it has mostly positive values. For the large velocity (bottom panels), while both waves contribute to the amplification, the propagating one has a much larger overall contribution. Interestingly, the increase of damping leads to a magnitude decrease of the evanescent wave (i.e., a smaller reduction in the amplification) for the low and medium relative velocities, while it does not cause a sig-

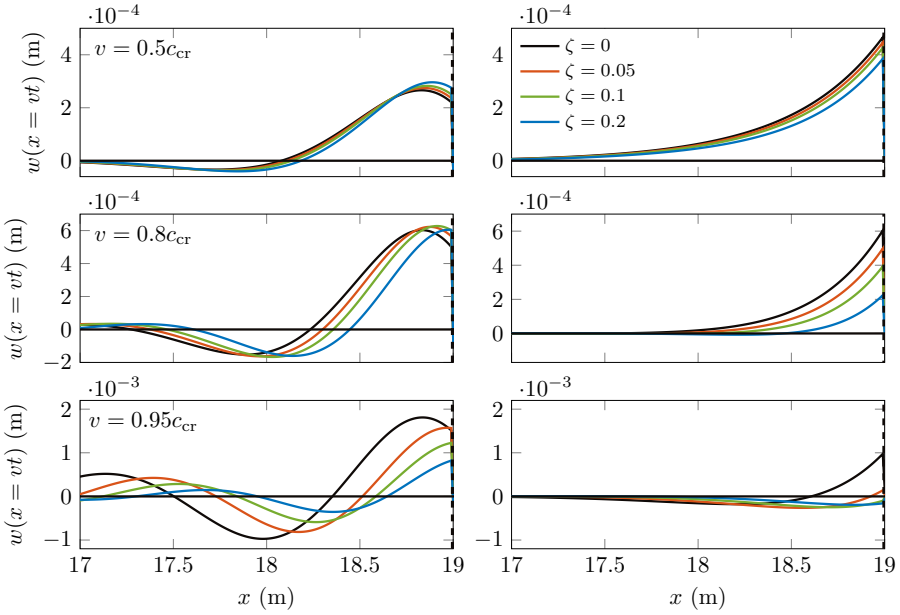

Figure 2.9: The propagating (left panels) and evanescent (right panels) free waves evaluated at $x = vt$ for different values of the foundation viscous damping. The soft-to-stiff transition is presented and $x_{\mathrm{tc}} = 19$ m.

nificant change to the propagating wave. This leads, in other words, to a more pronounced amplification with increasing foundation damping, which is counter-intuitive. For the large velocity, increasing the damping leads to a reduction in the downward displacement of both the propagating and evanescent waves, and, thus, to a diminishing amplification. Finally, it is interesting to note that increasing the damping leads to the maximum amplification to shift closer to the stiff zone for all load velocities, but especially at large velocities.

The behaviour is considerably different in the stiff-to-soft scenario presented in Fig. 2.10. At low relative velocity (top panels), both waves contribute to the amplification and their downward maximum occurs at approximately the same location (i.e., they are in phase). For medium velocity (middle panels), the two waves are out of phase. Close to the stiff zone, the large upward displacement of the propagating wave cancels out the downward displacement of the evanescent wave. Further away from the stiff zone, the evanescent wave has decayed almost completely while the propagating one reaches its maximum downward displacement, thus governing the downward amplification. At large velocity and non-zero damping, the propagating wave decreases monotonically from positive values to zero (even for small damping ratios) meaning that it damps out before reaching a downward maximum, and although the evanescent wave has a downward maximum, it is cancelled out by the much larger magnitude of the propagating wave. It is important to remember that the wave is evaluated under the moving load ($x = vt$), and at the large velocity considered

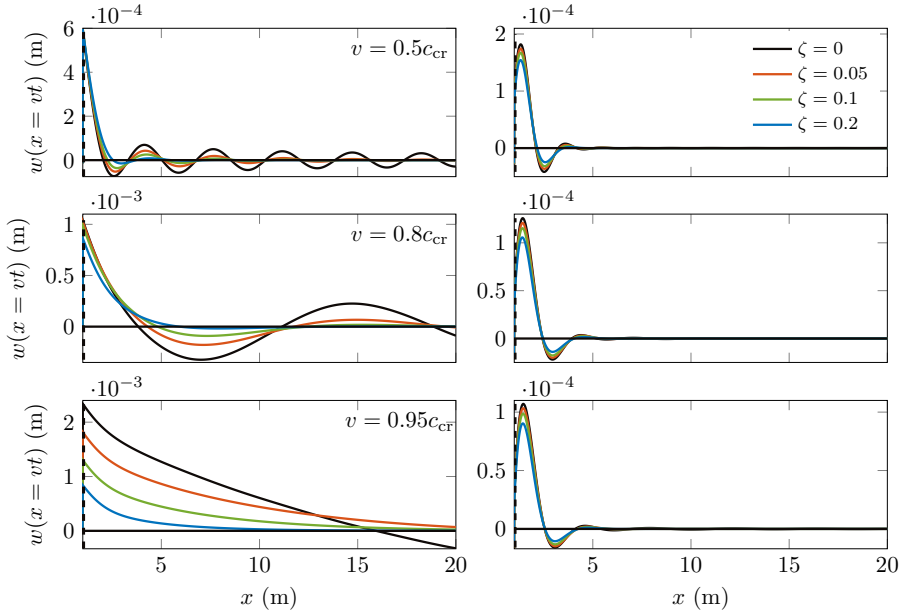

Figure 2.10: The propagating (left panels) and evanescent (right panels) free waves evaluated at $x = vt$ for different values of the foundation viscous damping. The stiff-to-soft transition is presented and $x_{tc} = 0$ m.

($v = 0.95c_{cr}$), the reference frame moves almost together with the wave (both the load and the wave propagate in positive x-direction in the stiff-to-soft scenario). This means that if the reference frame moves together with the crest of the wave, for example, we would solely observe a decrease in amplitude due to dispersion and damping, explaining the lack of oscillations seen in the propagating wave. Finally, from the damping point of view, it can be seen that its increase has a positive effect on reducing the amplification for all velocity regimes.

The analysis of the effect of individual waves on the amplification under the moving load has explained more in depth the results obtained in Figs. 2.6 and 2.8. Together with those results, it becomes clear that the characteristics of the transient process are significantly different between the soft-to-stiff and stiff-to-soft transitions. The wave types that contribute positively and negatively to the downward amplification are different in the two scenarios and increasing the foundation damping can have negative effects on the amplification in the soft-to-stiff case while having a beneficial effect in the stiff-to-soft case. This strongly suggests that for a mitigation measure to be efficient, it should be designed differently for the two types of transition.

2.4. Energy analysis

In this section, the transition radiation process is analysed from an energy perspective and the exchange of energy between different system components is investigated. To this end, the equation of motion (Eq. (2.1)) is rewritten as follows:

$$EI\frac{\tilde{\partial}^4 w}{\tilde{\partial} x^4}+\rho\frac{\tilde{\partial}^2 w}{\tilde{\partial} t^2}+k_{\mathrm{d,l}}\,w H(x_{\mathrm{tc}}-x)+k_{\mathrm{d,r}}\,w H(x-x_{\mathrm{tc}})=-F_0\,\delta(x-v t), \tag{2.28}$$

where $H(\ldots)$ is the Heaviside function. To obtain an equation expressing the energy balance from one that expresses equilibrium of forces per unit length, the whole equation is multiplied by the velocity and integrated over space and time. We firstly multiply by the velocity $\dot{w}$ and integrate over space to obtain the equilibrium of power, which, after some mathematical manipulations, reads

$$\begin{aligned} EI\big(w'''\dot{w}-w''\dot{w}'\big)\Big|_{x\to-\infty}^{x\to+\infty}+\int_{-\infty}^{+\infty}\frac{\partial}{\partial t}\frac{1}{2}\Big(EIw''^2+\rho\dot{w}^2+k_{\mathrm{d,l}}w^2H(x_{\mathrm{tc}}-x) \\ +k_{\mathrm{d,r}}w^2H(x-x_{\mathrm{tc}})\Big)\mathrm{d}x=-F_0\frac{\partial w}{\partial t}\Big|_{x=vt}, \end{aligned} \tag{2.29}$$

where the overdots represent classical derivatives with respect to time. To obtain the equation expressing the energy balance, Eq. (2.29) is integrated over time, as follows:

$$\begin{aligned} EI\int_{-\infty}^{+\infty}\big(w'''\dot{w}-w''\dot{w}'\big)\Big|_{x\to-\infty}^{x\to+\infty}\mathrm{d}t+\int_{-\infty}^{+\infty}\frac{1}{2}\Big(EIw''^2+\rho\dot{w}^2+k_{\mathrm{d,l}}w^2H(x_{\mathrm{tc}}-x) \\ +k_{\mathrm{d,r}}w^2H(x-x_{\mathrm{tc}})\Big)\Big|_{t\to-\infty}^{t\to+\infty}\mathrm{d}x=-F_0\int_{-\infty}^{+\infty}\frac{\partial w}{\partial t}\Big|_{x=vt}\mathrm{d}t. \end{aligned} \tag{2.30}$$

The right-hand side term represents the energy input E^{in} by the moving load and can further be decomposed into two components. To this end, a variable change is performed by introducing a coordinate $\xi=x-vt$ moving with the load. The resulting expression reads

$$E^{\mathrm{in}}=E^{\mathrm{hf}}+\big(W_{\mathrm{l}}^{\mathrm{F}}-W_{\mathrm{r}}^{\mathrm{F}}\big), \tag{2.31}$$

$$E^{\mathrm{hf}}=F_0\,v\int_{-\infty}^{+\infty}\frac{\partial w}{\partial\xi}\Big|_{\xi=0}\mathrm{d}t, \tag{2.32}$$

$$W_{\mathrm{l}}^{\mathrm{F}}=F_0\,w(\xi=0)\Big|_{t\to-\infty},\qquad W_{\mathrm{r}}^{\mathrm{F}}=F_0\,w(\xi=0)\Big|_{t\to+\infty}, \tag{2.33}$$

where E^{hf} is the energy introduced into the system by the horizontal force ensuring the constant velocity of the moving load (although not explicitly prescribed, this force is implicitly assumed to act on the system if a constant load velocity is imposed [16]) and $\Delta W^{\mathrm{F}}=W_{\mathrm{r}}^{\mathrm{F}}-W_{\mathrm{l}}^{\mathrm{F}}$ is the work done by the moving load at $t\to+\infty$ and $t\to-\infty$.

To emphasize the radiation energy, Eq. (2.30) is rewritten as follows:

$$E_{\mathrm{l}}^{\mathrm{rad}} + E_{\mathrm{r}}^{\mathrm{rad}} = E^{\mathrm{hf}} + \left(W_{\mathrm{l}}^{\mathrm{F}} - W_{\mathrm{r}}^{\mathrm{F}}\right) + \left(E_{\mathrm{l}}^{\mathrm{e}} - E_{\mathrm{r}}^{\mathrm{e}}\right), \tag{2.34}$$

$$E_{\mathrm{l}}^{\mathrm{rad}} = -EI \int_{-\infty}^{+\infty} \left(w''' \dot{w} - w'' \dot{w}'\right)\Big|_{x\to-\infty} \mathrm{d}t, \tag{2.35}$$

$$E_{\mathrm{r}}^{\mathrm{rad}} = EI \int_{-\infty}^{+\infty} \left(w''' \dot{w} - w'' \dot{w}'\right)\Big|_{x\to+\infty} \mathrm{d}t, \tag{2.36}$$

$$E_{\mathrm{l}}^{\mathrm{e}} = \int_{-\infty}^{+\infty} \frac{1}{2}\left(EIw''^2 + \rho\dot{w}^2 + k_{\mathrm{d,l}} w^2\right)\Big|_{t\to-\infty} \mathrm{d}x, \tag{2.37}$$

$$E_{\mathrm{r}}^{\mathrm{e}} = \int_{-\infty}^{+\infty} \frac{1}{2}\left(EIw''^2 + \rho\dot{w}^2 + k_{\mathrm{d,r}} w^2\right)\Big|_{t\to+\infty} \mathrm{d}x, \tag{2.38}$$

where $E_{\mathrm{l}}^{\mathrm{rad}}$ and $E_{\mathrm{r}}^{\mathrm{rad}}$ represent the energy-flux through cross-sections at $x \to -\infty$ and $x \to +\infty$, respectively, and $\Delta E^{\mathrm{e}} = E_{\mathrm{r}}^{\mathrm{e}} - E_{\mathrm{l}}^{\mathrm{e}}$ is the difference in eigenfield energy between $t \to +\infty$ and $t \to -\infty$. Eq. (2.34) expresses the energy balance in the system and shows that the transition radiation energy $E^{\mathrm{rad}} = E_{\mathrm{l}}^{\mathrm{rad}} + E_{\mathrm{r}}^{\mathrm{rad}}$ is composed of the difference in eigenfield energy between the right and left domains, the work done by the moving load to develop these eigenfields (at $t \to \pm\infty$), and the energy spent by the horizontal force to maintain the constant velocity of the moving load. Next, we take each term separately and investigate its influence on the transition radiation energy.

Eigenfield energy and the work done by the moving load

The energy of the eigenfield can be obtained by substituting Eq. (2.19) in Eq. (2.37) and evaluating the integral, which can be done analytically. Considering the current model, the eigenfield energy depends on four system parameters, namely v, k_{d}, ρ, and EI. Here, we focus on the variation of the eigenfield energy with respect to v and k_{d}. Although ρ and EI can vary in the transition zone, their variation is known less than the variation of k_{d}.

The left panel in Fig. 2.11 presents the variation of the eigenfield energy with increasing foundation stiffness. It must be emphasized that the load velocity is chosen such that the relative velocity $v = 0.5c_{\mathrm{cr}}$ is maintained. This is done to eliminate the influence of the different relative velocity on the eigenfield energy, thus focusing only on the influence of the foundation stiffness. Consequently, v changes with each value of k_{d} (see Eq. (2.13)). Results show that the higher the foundation stiffness, the lower the energy of the eigenfield; in the limit of the foundation stiffness going to infinity, the response is trivial and does not contain energy. Also, the nonlinear dependency of the eigenfield energy on foundation stiffness means that the contribution ΔE^{e} to the radiation energy does not depend only on the difference in stiffness $\Delta k_{\mathrm{d}} = k_{\mathrm{d,r}} - k_{\mathrm{d,l}}$, but also on the magnitudes of $k_{\mathrm{d,r}}$ and $k_{\mathrm{d,l}}$. A better indicator of ΔE^{e} is the stiffness ratio $p = \frac{k_{\mathrm{d,r}}}{k_{\mathrm{d,l}}}$, and is, therefore, used throughout the thesis.

The influence of the relative velocity on the eigenfield energy is presented in the right panel of Fig. 2.11. It can be seen that the closer it is to the critical one, the larger the energy

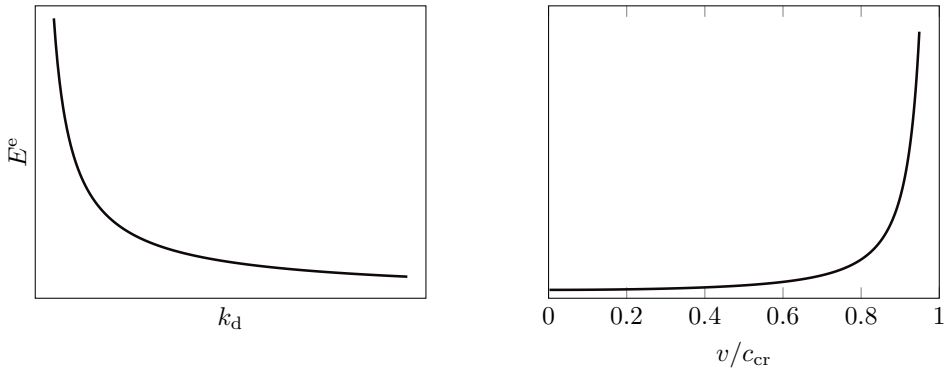

Figure 2.11: The energy of the eigenfield for different spring stiffness (left panel) and different load velocity (right panel); the load velocity in the left panel is different for each value of the spring stiffness such that the relative velocity $v = 0.5c_{\mathrm{cr}}$ is maintained.

in the eigenfield. The energy tends to infinity as the load velocity tends to the critical one because resonance occurs at $v = c_{\mathrm{cr}}$ and the response at resonance is infinite due to the lack of damping.

Fig. 2.12 presents the difference in eigenfield energy ΔE^{e} for different load velocities and stiffness ratios. The absolute value of ΔE^{e} is presented in Fig. 2.12 because its sign depends if the transition in stiffness is soft-to-stiff or stiff-to-soft. In the soft-to-stiff scenario, $-\Delta E^{\mathrm{e}}$ (as it appears on the right-hand side of the energy balance equation, Eq. (2.34)) has a positive value while for the stiff-to-soft it has a negative value. This means that in the soft-to-stiff scenario, the difference in eigenfield energy adds to the radiated energy while in the stiff-to-soft scenario, the opposite is true.

The difference in eigenfield energy is influenced by two factors: (i) the relative velocity $\frac{v}{c_{\mathrm{cr}}}$ changes because v is constant while c_{cr} changes with the change in foundation stiffness, and (ii) the stiffness ratio. At low relative velocities, the main contribution to ΔE^{e} comes from the stiffness ratio because the response is quasi-static in both left and right domains. As the relative velocity increases, the difference in eigenfield energy increases significantly, especially as the load velocity approaches the critical one. At large relative velocities (relative to the critical velocity in the left domain $c_{\mathrm{cr,l}}$), ΔE^{e} is dominated by the change in relative velocity when the load passes the transition.

As for the work ΔW^{F} done by the load, one can verify that it has qualitatively the same behaviour as the difference in eigenfield energy. Therefore, for brevity, these results are not presented here.

Energy input from the horizontal force

The existence of a horizontal force can seem controversial because there is no explicit horizontal force in the system described by Eq. (2.1). However, by prescribing a constant load

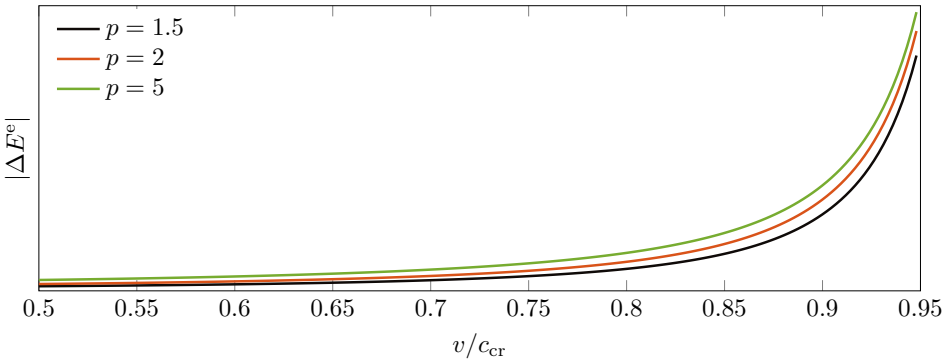

Figure 2.12: The absolute value of the difference in eigenfield energy for different relative load velocities (c_{cr} corresponds to the soft domain) and stiffness ratios $p = \frac{k_{\mathrm{d,r}}}{k_{\mathrm{d,l}}}$.

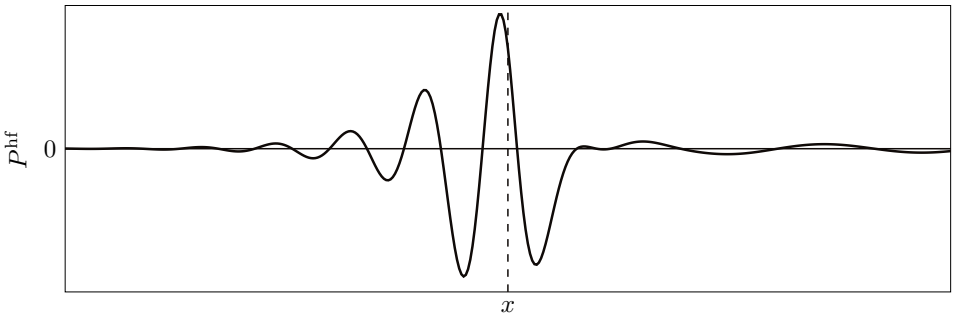

Figure 2.13: The power input by the horizontal force in the soft-to-stiff scenario; the horizontal dashed line indicates the location of the jump in stiffness.

velocity, the horizontal force is implicitly imposed to maintain the constant velocity of the load [16]. The energy input by this force represents the energy a train (or other vehicle) needs to spend to maintain its constant velocity.

Fig. 2.13 presents the power input by the horizontal force as it passes through the transition zone. Far away from the transition zone where the response is in the steady state, the power input is zero because, in the absence of damping, there is no mechanism to absorb energy. As the load passes through the transition zone, the power input fluctuates. It can be seen that at some locations it introduces power into the system (positive power input) and at other it takes away power from the system (negative power input). Also, the maximum power input into the system seems to occur right before the jump in stiffness where also the maximum response amplification occurs.

Fig. 2.14 presents the energy input (the power input integrated over time) by the horizontal force for different load velocities and different stiffness ratios. In the soft-to-stiff scenario, the energy input for most velocities and stiffness ratios is negative, meaning that

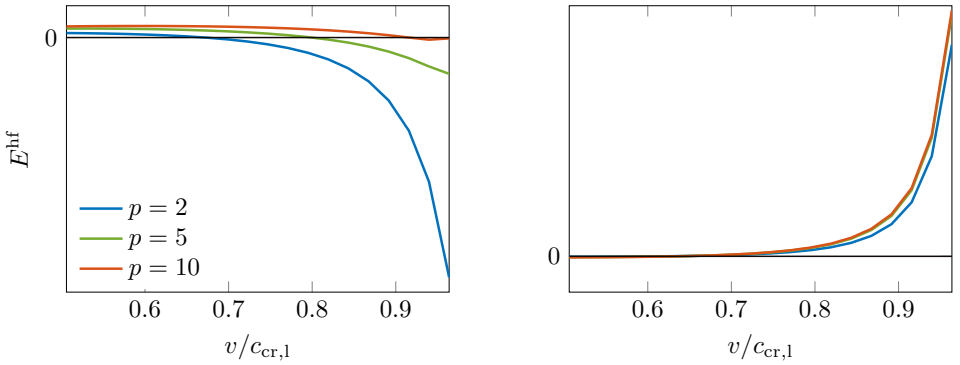

Figure 2.14: The energy input by the horizontal force versus load velocity for different stiffness ratios; soft-to-stiff scenario (left panel) and stiff-to-soft scenario (right panel). In the right panel, the green and red lines overlap.

the energy goes from the structure to the load, and not the other way around, which is, to some degree, counter intuitive. This can be explained by the fact that in the soft-to-stiff scenario, the response goes from high-energy state (soft domain) to low-energy state (stiff domain); part of the difference in eigenfield energy is radiated (transition radiation), but part goes back to the load. Fig. 2.14 shows that the higher the velocity, meaning a larger difference in eigenfield energy (see Fig. 2.12), the more energy goes back to the load (except for very high stiffness ratios). To conclude, for most large load velocities and realistic stiffness ratio (e.g., 1-5), the energy input from the horizontal force in the soft-to-stiff scenario is negative; this means that instead of adding to the energy radiated, the horizontal force takes away energy. The opposite is true for the stiff-to-soft scenario where the horizontal force needs to input energy in the system to develop the high-energy eigenfield. The fact that the energy input by the horizontal force is always larger for the stiff-to-soft case is demonstrated in the next section.

Energy radiation

The energy radiated is the energy of the free field that passes the cross-sections at $x \to \pm\infty$. At this location, the free field and eigenfield are completely separated, allowing us to use the free-field quantities in Eqs. (2.35) and (2.36). To investigate the frequencies present in the radiation field, the power spectral density $\tilde{P}^{\mathrm{rad}}$ of the radiated field is investigated. Its expression can be derived from the energy of the radiated field (Eqs. (2.35) and (2.36)) as follows [16, 17, 20]

$$\begin{aligned} E_{\mathrm{l}}^{\mathrm{rad}} &= -EI \int_{-\infty}^{+\infty} \left(w_{\mathrm{f}}''' \dot{w}_{\mathrm{f}} - w_{\mathrm{f}}'' \dot{w}_{\mathrm{f}}' \right) \Big|_{x \to -\infty} \mathrm{d}t \\ &= -\frac{EI}{\pi} \int_{0}^{\infty} \mathrm{Re}\left(\tilde{w}_{\mathrm{f}}''' \tilde{v}_{\mathrm{f}}^{*} - \tilde{w}_{\mathrm{f}}'' \tilde{v}_{\mathrm{f}}^{*\prime} \right) \Big|_{x \to -\infty} \mathrm{d}\omega, \end{aligned} \tag{2.39}$$

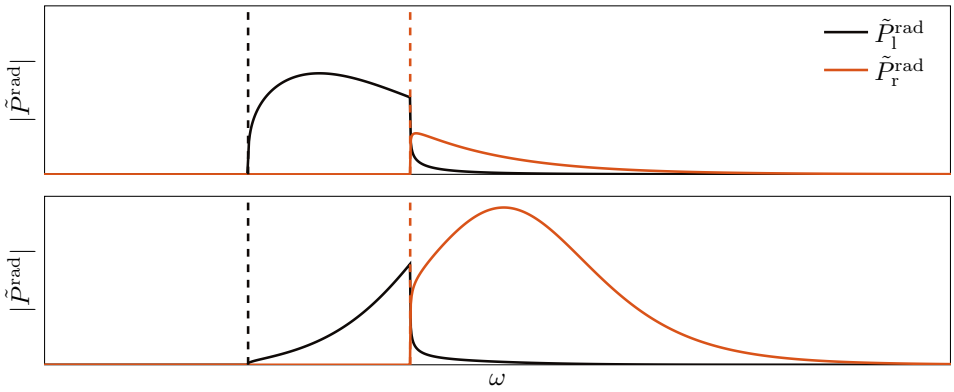

Figure 2.15: The power spectral density of the radiation for the soft-to-stiff scenario for $v = 0.7c_{\mathrm{cr,l}}$ (top panel) and $v = 0.95c_{\mathrm{cr,l}}$ (bottom panel).

where $\tilde{v}_{\mathrm{f}} = \mathrm{i}\omega\tilde{w}_{\mathrm{f}}$ is the Fourier-domain velocity, * represents the complex-conjugate of the quantity, and subscript f represents the free-field quantity. The expression under the integral is the power spectral density.

Fig. 2.15 presents the power spectral density of the radiated field to the left and to the right. It can be seen that, as in Fig. 2.7, there is no energy content below the corresponding cut-off frequency of each domain because wave propagation does not occur below this frequency and no energy reaches the cross-sections at $x \to \pm\infty$. The energy radiated to the left drops significantly above the cut-off frequency of the right domain because energy transmission into the right domain can occur above this frequency and, consequently, less energy is reflected to the left domain. This shows that the energy of the free field in the left domain is mostly composed of frequencies between the cut-off frequencies of the two domains. Furthermore, it can be seen that the radiation in the soft domain is stronger than in the stiff domain, but this is not always the case as found by van Dalen et al. [20]. If most energy content of the approaching eigenfield lies below the cut-off frequency of the stiff domain, then most energy is radiated in the soft domain. However, for high velocities and low stiffness ratios, most energy content of the eigenfield is above both cut-off frequencies (see bottom panel of Fig. 2.15). This can result in most energy being radiated in the stiff domain, as can be seen in the bottom left panel of Fig. 2.16.

Fig. 2.16 presents the energy radiated for different stiffness ratios. In the soft-to-stiff scenario (left panels), it can be seen that for a relatively low velocity ($v = 0.7c_{\mathrm{cr,l}}$), the energy radiated in the soft zone is larger than the one in the stiff zone for all stiffness ratios. However, for a high velocity ($v = 0.95c_{\mathrm{cr,l}}$) and low stiffness ratios, the radiation in the stiff zone is larger and can be explained using the same rationale as in the previous paragraph. Nonetheless, once the stiffness ratio increases, the radiation in the soft zone becomes

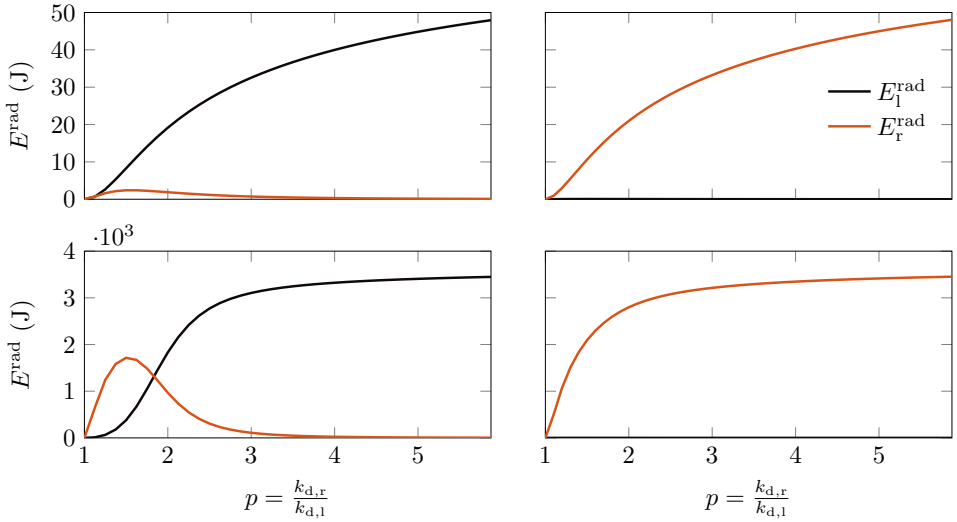

Figure 2.16: The energy radiated for different stiffness ratios in the soft-to-stiff (left panels) and stiff-to-soft (right panels) scenarios for $v = 0.7c_{\mathrm{cr,l}}$ (top panels) and $v = 0.95c_{\mathrm{cr,l}}$ (bottom panels); note that the vertical scale of the left and right panels are the same.

dominant. When it comes to the stiff-to-soft scenario (right panels), almost all the energy radiated is in the soft domain irrespective of load velocity and stiffness ratio.

It is interesting to note that the energy radiation has very similar magnitudes in both the soft-to-stiff and stiff-to-soft scenarios. After a closer inspection, it seems that the total energy radiated is invariant for the two scenarios (i.e., soft-to-stiff and stiff-to-soft). This is shown in Fig. 2.17, where the relative difference in radiated energy between the two scenarios (relative to the energy radiated in the soft-to-stiff scenario) is almost null; the small values are caused by numerical integration and an extremely small damping added to the foundation. This result means that the free-field propagating waves carry the same amount of energy in both scenarios, which is unexpected (at least for the author).

Since the total radiated energy $E_{\mathrm{t}}^{\mathrm{rad}} = E_{\mathrm{l}}^{\mathrm{rad}} + E_{\mathrm{r}}^{\mathrm{rad}}$ is invariant for the two scenarios, and ΔE^{e} as well as ΔW^{F} differ only in sign (not in magnitude) between the two scenarios, the following relations can be written for the energy input by the horizontal force:

$$E_1^{\mathrm{hf}} = E_{\mathrm{t}}^{\mathrm{rad}} - |\Delta E^{\mathrm{e}}| - |\Delta W^{\mathrm{F}}|, \tag{2.40}$$

$$E_2^{\mathrm{hf}} = E_{\mathrm{t}}^{\mathrm{rad}} + |\Delta E^{\mathrm{e}}| + |\Delta W^{\mathrm{F}}|, \tag{2.41}$$

where subscripts 1 and 2 stand for soft-to-stiff and stiff-to-soft, respectively. It is clear from Eq. (2.41) that the energy input by the horizontal force in the stiff-to-soft scenario is always greater than the one in the soft-to-stiff scenario, as indicated in the previous section.

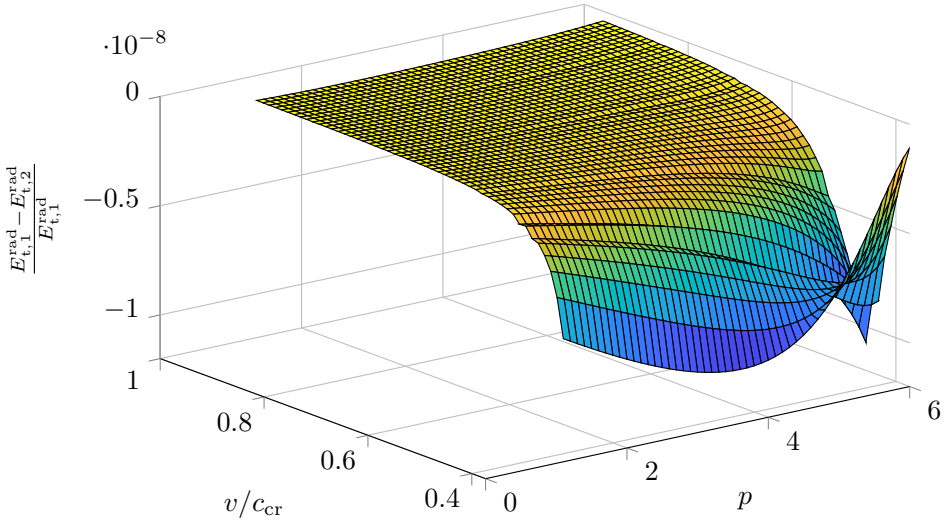

Figure 2.17: The relative difference in total energy radiated $E_t^{rad} = E_l^{rad} + E_r^{rad}$ between the soft-to-stiff (subscript 1) and stiff-to-soft (subscript 2) scenarios for different relative velocities and stiffness ratios. As can be seen, the relative difference is almost null.

2.5. Conclusions

The goal of this chapter was to offer the reader an introduction to the transition radiation phenomenon and present some of its important characteristics that are referred to in next chapters. To this end, a simplified model of a railway track with a transition zone was formulated; more specifically, the model consists of an Euler–Bernoulli beam resting on a Winkler foundation with a piecewise-homogeneous stiffness in space, acted upon by a moving constant load.

It was shown that the response amplification at transition zones is caused by the interference between the steady-state field (eigenfield) and the free field generated during the transition process. Consequently, the more pronounced the free field compared to the eigenfield, the larger the resulting amplification. The frequency spectrum of the free field showed that, depending on the load velocity, the evanescent waves excited during the transition radiation process can have a strong influence on the response amplification and, therefore, the investigation of the quantities in the far field should be supplemented with ones from the near field.

The different behaviour of the system in the soft-to-stiff and stiff-to-soft scenarios was also investigated in depth. For the soft-to-stiff transition, the response amplification has been observed to be significant at load velocities between 75% and 100% of the critical one, and it increases considerably as the load velocity approaches the critical one. Also, the broader the approaching eigenfield (which occurs with increasing velocity of the load) the larger the zone over which the amplification occurs. For the stiff-to-soft transition, the

strongest response amplification occurs at lower velocities than for the soft-to-stiff ones, namely between 50% and 80% of the critical velocity, after which the amplification decreases. To understand the causes of these differences, the individual waves composing the free field have been studied. It was shown that the waves contributing positively or negatively to the response amplification are different between the two scenarios. Furthermore, the increase in foundation damping can have negative effects on the response amplification in the soft-to-stiff case (which is counter intuitive) while having a beneficial effect in the stiff-to-soft case. These results strongly suggests that for a mitigation measure to be efficient, it should be designed differently for the two types of transition.

The analysis of the energy balance showed that the transition radiation energy is composed of the difference in eigenfield energy between the right and left domains, the work done by the moving load to develop these eigenfields, and the energy input by the horizontal force that maintains the constant velocity of the moving load. It was shown that the maximum positive power input by the horizontal force occurs at the same location where the maximum response amplification is observed, suggesting a link between maximum power input and degradation. Furthermore, results show that, in the soft-to-stiff scenario, for most large load velocities and realistic stiffness ratio, the energy input from the horizontal force is negative meaning that it takes away energy from the system. The opposite is true for the stiff-to-soft scenario where the horizontal force needs to input energy in the system to develop the high-energy eigenfield. When it comes to the transition radiation energy, the spectral energy density in each domain lies above the cut-off frequency of the corresponding domain. Furthermore, in the left (soft) domain, the majority of the spectral energy density lies below the cut-off frequency of the right (stiff) domain (i.e., it lies between the cut-off frequencies of the two domains). It was also shown that for relatively large velocities and low stiffness ratios, the transition radiation into the stiff domain is more energetic, while for all other cases the one into the soft domain is dominating. Finally, results show that the total energy radiated in the soft-to-stiff and stiff-to-soft scenarios is invariant, result which was unexpected.

3

Transition radiation–importance of load velocity relative to the critical one

The great menace to progress is not ignorance, but illusion of knowledge.

Daniel Boorstin

The model formulated in Chapter 2, namely an Euler-Bernoulli beam on Winkler foundation (EBW), is a phenomenological model. Its aim is to accurately represent one phenomenon, namely transition radiation (and consequently the response amplification at transition zones), while neglecting others. The parameter values in a phenomenological model are chosen according to the phenomenon it represents. For example, depending on the phenomenon of interest, the beam's mass in the EBW model can represent the mass of the rail (e.g., in problems where noise emission is of interest [52]), it can represent the mass of the rail and sleepers (e.g., modelling the system response to high-frequency excitation cause by rail corrugation [53]), or the mass of the whole system (including soil) activated by the vehicle. Consequently, the question arises what values should the parameters have to accurately represent transition radiation?

In literature, studies employing 1-D phenomenological models that investigate the behaviour of railway tracks at transition zones use small alterations of the EBW model [10, 19, 25, 35] as well as models with multiple layers [13, 22, 54]. The values of parameters used in these studies vary significantly (depending on the scenario being modelled), but there is one

common feature in most studies. The load velocity is chosen as the realistic train velocity while the critical velocity of the model is not explicitly tuned to match the critical velocity in the field. This could be problematic since the Winkler foundation is known to significantly overestimate the critical velocity of the railway track, and as seen in Chapter 2, transition radiation and the response amplification at transition zones is strongly influenced by the v/c_{cr} ratio.

From Eq. (2.13), it is clear that the critical velocity depends on the bending stiffness EI, support stiffness k_{d}, and mass ρ. While EI is mostly given by the rail, and many studies have investigated the values to be attributed to k_{d}, the choice of value for the mass per unit length of the beam is less clear. If one chooses realistic values for EI and k_{d} (see Table 4.1 for the values), and represents the mass of the rail and of the sleepers through ρ (as done by Grassie et al. [53]; the values is given in Table 4.1), the critical velocity is $c_{\mathrm{cr}} \approx 410$ m/s (i.e., 1475 km/h). This is much higher than the measured critical velocity of railway tracks in areas with soft soils, where the so-called Rayleigh wave velocity (which usually is the critical velocity) can be, in extreme cases, as low as 40–50 m/s (i.e., 150–180 km/h) [33, 55]. Therefore, choosing a realistic value for the load velocity (e.g., 100–200 km/h) together with the Winkler model that overestimates the critical velocity will lead to a quasi-static response equivalent to the train velocity of 20 km/h on a track with realistic minimum critical velocity of 180 km/h. This combination can lead to wrong conclusions.

The reason why the Winkler model overestimates the critical velocity is that it neglects the part of the supporting structure mass (ballast, sub-ballast, soil, etc.) activated by the vehicle. Models in literature that consider multiple layers of masses [13, 22, 54], although accurately representing the critical velocity is not their aim, do predict much more realistic critical velocities. However, the critical velocity can also be tuned to match the measured ones in the EBW model by artificially increasing the beam's mass. Yet another alternative is to keep the values unchanged and consider a load velocity that leads to a realistic v/c_{cr} ratio (i.e., artificially increase load velocity). This chapter compares these three modelling choices and investigates their effect on the response when it comes to model transition radiation and response amplification at transition zones.[*] The structure of this chapter is similar to the one in the previous chapter. Firstly, the two-layer model is formulated and the steady-state and transient responses are derived. Then, the three models are compared in terms of dispersion curves, frequency spectra of responses, time-domain responses, and energy associated to the transition process.

3.1. Model formulation and solution

The model formulated in this section is a two-layer (TL) model. It consists of an infinite Euler-Bernoulli beam with bending stiffness EI and mass per unit length ρ_{t} and a continuously distributed layer of mass per unit length ρ_{b} (the layer of distributed mass can also be seen

[*] Part of this chapter is based on the MSc thesis of Bilal Ouchene [56] supervised by the author.

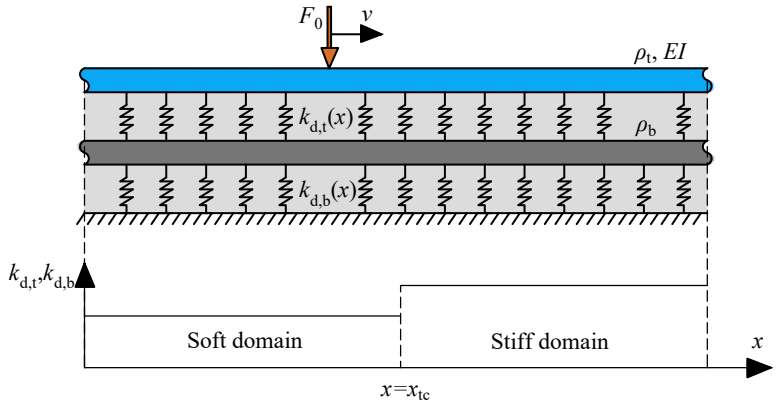

Figure 3.1: Model schematics of the two-layer model. The top layer is the Euler-Bernoulli beam while the bottom layer is a distributed mass layer.

as a beam without bending stiffness). The two are connected through a layer of springs with stiffness $k_{d,t}$, while the layer of distributed mass is resting on a Winkler foundation of stiffness $k_{d,b}$. (The subscripts t and b stand for top and bottom.) As in Chapter 2, there is a jump in stiffness at $x = x_{tc}$, in both layers of springs. The system is depicted in Fig. 3.1 and its equations of motion read

$$EI\frac{\tilde{\partial}^4 w}{\tilde{\partial} x^4} + \rho_t \frac{\tilde{\partial}^2 w}{\tilde{\partial} t^2} + k_{d,t}(x)(w-u) = -F_0\,\delta(x-vt), \tag{3.1}$$

$$\rho_b \frac{\tilde{\partial}^2 u}{\tilde{\partial} t^2} + k_{d,t}(x)(u-w) + k_{d,b}(x)u = 0, \tag{3.2}$$

$$w(x,t) = \begin{cases} w_l(x,t), & x \le x_{tc}, \\ w_r(x,t), & x \ge x_{tc}, \end{cases} \qquad u(x,t) = \begin{cases} u_l(x,t), & x \le x_{tc}, \\ u_r(x,t), & x \ge x_{tc}, \end{cases}$$

$$k_{d,t}(x) = \begin{cases} k_{d,t,l}, & x < x_{tc}, \\ k_{d,t,r}, & x \ge x_{tc}, \end{cases} \qquad k_{d,b}(x) = \begin{cases} k_{d,b,l}, & x < x_{tc}, \\ k_{d,b,r}, & x \ge x_{tc}, \end{cases}$$

where w and u are the displacements of the beam and of the mass layer, respectively.

The interface conditions reveal a particularity of the considered system. On the one hand, the transient problem requires the same interface conditions $x = x_{tc}$ as in Section 2.1, namely continuity in displacement and slope as well as in shear force and bending moment (Eqs. (2.2) and (2.3)). Furthermore, the conditions applied to the beam at infinite distance from the moving load are also the same as in Section 2.1 (Eq. (2.4)). For the layer of mass, no interface or boundary conditions are imposed since, not having bending or shear stiffness, it does not to allow for direct transfer of information between neighbouring cross-sections; i.e., each distinct cross-section of the mass layer is coupled to other cross-

sections only through the beam, so satisfying the beam's interface and boundary conditions is sufficient for the transient problem. On the other hand, to determine the eigenfield (i.e., homogeneous system) using the approach from Section 2.2, six interface conditions are required at $x = vt$ (two additional equations to Eqs. (2.7) and (2.8)). The additional interface conditions at $x = vt$ are continuity in displacement and slope of the mass layer. It is important to emphasize that there is no inconsistency since the two sets of interface conditions are distinct, one expresses conditions at $x = vt$ for a homogeneous system and the other expresses conditions at $x = x_{\mathrm{tc}}$ for an inhomogeneous system. The different number of interface conditions originates from the fact that the considered system allows, as shown in Sections 3.2 and 3.3, for four free-field waves and for six eigenfield waves. This particularity vanishes once bending or shear stiffness is attributed to the mass layer.

Similar to the situation in Section 3.1, the initial conditions do not influence the response in the vicinity of the transition zone. Therefore, Eqs. (3.1) and (3.2) together with Eqs. (2.2)–(2.4) constitute a complete description of the problem. Next, the steady-state and transient responses are derived and investigated.

3.2. Steady-state response

When the two layers of springs have constant stiffness throughout the infinite domain, the model is homogeneous and the response to the moving load is in the steady state. The characteristics of the steady-state solution, as seen in Chapter 2, help in understanding the transient response. Consequently, the steady-state response is derived first. The analysis is similar to the one in the work of Erofeev et al. [57], where they have used a string instead of a beam.

To obtain the solution in this scenario, we use the same approach described in Section 2.2, which is to divide the infinite domain into two semi-infinite ones, namely behind and in front of the moving load. As in Section 2.2, the solutions of the homogeneous equations of motion can be assumed in the form of harmonic waves, as follows:

$$w_h(x,t) = A_h \mathrm{e}^{\mathrm{i}(\omega t - kx)}, \qquad u_h(x,t) = B_h \mathrm{e}^{\mathrm{i}(\omega t - kx)}, \quad h = \{\mathrm{b},\mathrm{f}\}, \tag{3.3}$$

where subscripts b and f stand for behind and front, respectively. After substituting the assumed solutions in the equations of motion, in order to obtain non-trivial solutions, the determinant of the system matrix is set to zero, resulting in the dispersion equation of the system:

$$EIk^4 - \rho_{\mathrm{t}}\omega^2 + k_{\mathrm{d,t}} - \frac{k_{\mathrm{d,t}}^2}{-\rho_{\mathrm{b}}\omega^2 + k_{\mathrm{d,t}} + k_{\mathrm{d,b}}} = 0. \tag{3.4}$$

The dispersion curves are graphically presented in Fig. 3.2. The two-layer system has four dispersion curves (two for positive frequencies and two for negative ones; Fig. 3.2 presents only the curves for positive frequencies), unlike the beam on elastic foundation which has two dispersion curves. The additional curves appear because the dispersion equation has a

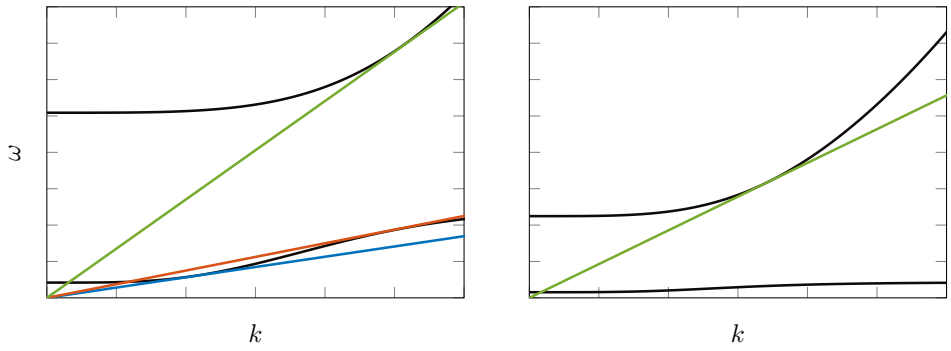

Figure 3.2: The dispersion curves (black lines) and the possible kinematic invariants that lead to critical velocities (orange, blue, and green lines) in the two-layer system. The parameter values are chosen such that there are three critical velocities in the left panel and only one critical velocity in the right panel.

term proportional to ω^4, while in the previous case the highest power of ω in the dispersion equation is two. The lower dispersion branch tends to a flat plateau (finite value of ω) as k increases. This is a consequence of not attributing any bending and/or shear stiffness to the additional mass layer, which causes its reaction to be purely local (similar to the Winkler model). Once the layer has non-zero bending and/or shear stiffness, the lower dispersion branch does not any more tend to a flat plateau, but increases with increasing k (e.g., [58]). The flat plateau of the lower branch leads to this system always having at least one intersection between the kinematic invariant and the dispersion curves, meaning that for any velocity different from zero, there is always one propagating wave. This outcome is an artefact of this system and does not have any physical root. Nonetheless, the amplitude of this propagating wave is generally small compared to the other waves and does not significantly influence the response.

Fig. 3.2 presents two qualitatively different scenarios; one with a low value of the additional mass layer (left panel), and one with a high value of the same quantity (right panel). The qualitatively different behaviour of the two scenarios lies in the amount of critical velocities they present. The one with low additional mass has three critical velocities (velocities at which the kinematic invariant is tangential to the dispersion curves), while the scenario with high additional mass presents only one. This is caused by the shape of the lower dispersion curve and is elaborated in the next few paragraphs.

Substituting the kinematic invariant, Eq. (2.12), into the dispersion equation, a polynomial of order six in k is obtained. Compared to the system in Chapter 2 (which has a polynomial of order four, see Eq. (2.11) together with Eq. (2.12)), the system with an additional mass layer has two additional solutions for the wavenumber, meaning that its solution is composed of six waves instead of four. Similar to the classical system, the type of waves in the system with the additional mass layer depends on the velocity of the load. Unlike the classical system, the nature of the waves in the current system also depends on the value of

the additional mass (as hinted from the two scenarios presented in Fig. 3.2). To determine the types of waves, we first need to solve the system of equations consisting of the dispersion equation and the kinematic invariant for k. The polynomial of order six can be reduced to a polynomial of order three by making the substitution $y = k^2$, and the resulting polynomial reads

$$ay^3 + by^2 + cy + d = 0, \tag{3.5}$$

$$a = -EIv^2\rho_\mathrm{b}, \quad b = v^4\rho_\mathrm{t}\rho_\mathrm{b} + EI(k_{\mathrm{d,t}} + k_{\mathrm{d,b}}), \tag{3.6}$$

$$c = -v^2\big((\rho_\mathrm{t} + \rho_\mathrm{b})k_{\mathrm{d,t}} + k_{\mathrm{d,b}}\rho_\mathrm{t}\big), \quad d = k_{\mathrm{d,t}}k_{\mathrm{d,b}}. \tag{3.7}$$

The nature of the roots depends on the sign of the discriminant D of this polynomial. If the discriminant is positive, all roots y are distinct and real-valued, meaning that the kinematic invariant intersects the dispersion curves at three distinct locations. If the discriminant is negative, one root is real-valued and the other two are complex conjugates, meaning that the kinematic invariant intersects the dispersion curves at only one location. This change in the nature of the roots marked by the change in sign of the discriminant, marks the change from sub- to super-critical velocity regime (i.e., sub-critical regime is marked by negative discriminant while the super-critical one is marked by positive discriminant). Although in this system there always is one propagating wave, we do not consider this as a super-critical regime because, then, the critical velocity would be 0. As was discussed above, this is an anomaly of this system.

The boundary between the two regimes lies at $D = 0$. Fig. 3.3 presents the position of this boundary in the v and ρ_b space. In the limit of $\rho_\mathrm{b} \to 0$, the system is equivalent to a beam on Winkler foundation with the equivalent stiffness of $k_{\mathrm{d,t}}$ and $k_{\mathrm{d,b}}$ assembled in series. The critical velocity in this limit case is given by Eq. (2.13) with the appropriate parameter values and is represented in Fig. 3.3 by $c_{\mathrm{cr},0}$. In the limit of $\rho_\mathrm{b} \to \infty$, the system is equivalent to a beam on Winkler foundation with stiffness $k_{\mathrm{d,t}}$ because it would require infinite energy to mobilize the infinite inertia of the mass layer. Also in this limit case, the critical velocity $c_{\mathrm{cr},\infty}$ is given by Eq. (2.13). It is obvious that $c_{\mathrm{cr},\infty} \geq c_{\mathrm{cr},0}$ because the equivalent stiffness of two springs in series is always smaller than or equal to the stiffness of one of them. Fig. 3.3 also shows that, like in Fig. 3.2, depending on the value of ρ_b, there is one scenario in which three critical velocities are observed, and one in which there is only one critical velocity. The transition between these two distinct scenarios occurs at $\rho_\mathrm{b} = \rho_{\mathrm{b,cr}}$, situation in which there are two critical velocities. It can be seen that above $\rho_{\mathrm{b,cr}}$, the addition of the mass layer leads to a slight increase in the critical velocity of the system compared to that of the beam on Winkler foundation (i.e., $c_{\mathrm{cr},\infty}$), a finding which is counter-intuitive. Since the purpose of the additional mass in this chapter is to lower the critical velocity, we focus on the values of $\rho_\mathrm{b} < \rho_{\mathrm{b,cr}}$.

Once the wavenumbers k_n^e and the corresponding eigenvectors $\mathbf{q}_n^\mathrm{e}$ (where $n = 1, \ldots, 6$) are determined from the dispersion equation (Eq. (3.4)) with the kinematic invariant substi-

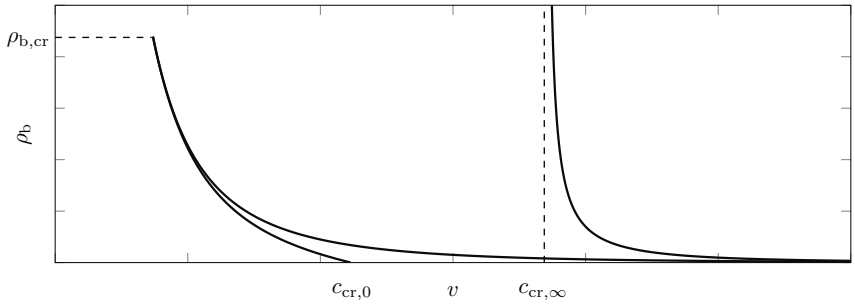

Figure 3.3: The curves where the discriminant of the dispersion equation (with the kinematic invariant substituted) is zero.

tuted, the 12 unknown amplitudes need to be determined from the interface and boundary conditions.

Since we limit our investigation to sub-critical velocities and to $\rho_{\mathrm{b}} < \rho_{\mathrm{b,cr}}$, it means that there are four complex-valued wavenumbers and two real-valued ones in each of the domains in front and behind the moving load. Eq. (2.9) eliminates two waves out of the four corresponding to the complex-valued wavenumbers in each domain. However, when it comes to the waves corresponding to the two real-valued wavenumbers, the choice is not straightforward. The two propagating waves have a very small group velocity (the group velocity is given by the tangent to the dispersion curve at the location of the intersection with the kinematic invariant) because the intersection between the kinematic invariant and lower dispersion branch occurs at locations where the dispersion curve is quite flat. Also, one wave propagates in positive x-direction while the other in negative x-direction. When it comes to the domain in front of the load, the wave propagating in negative x-direction is eliminated because nothing can propagate from $-\infty$, while also the wave propagating in positive x-direction is eliminated because its group velocity is smaller than the load velocity, thus it cannot exist in front of the load. The domain behind the load allows for both waves to exist. Therefore, the domain behind the load has four waves (two propagating and two evanescent), while the domain in front of the load has two evanescent waves. The solutions read

$$w^{\mathrm{e}}(x,t) = \begin{cases} A_2 \mathrm{e}^{-\mathrm{i}k_2^{\mathrm{e}}(x-vt)} + A_3 \mathrm{e}^{-\mathrm{i}k_3^{\mathrm{e}}(x-vt)} + A_5 \mathrm{e}^{-\mathrm{i}k_5^{\mathrm{e}}(x-vt)} + A_6 \mathrm{e}^{-\mathrm{i}k_6^{\mathrm{e}}(x-vt)}, & x < vt, \\ A_1 \mathrm{e}^{-\mathrm{i}k_1^{\mathrm{e}}(x-vt)} + A_4 \mathrm{e}^{-\mathrm{i}k_4^{\mathrm{e}}(x-vt)}, & x \geq vt, \end{cases} \tag{3.8}$$

$$u^{\mathrm{e}}(x,t) = \begin{cases} B_2 \mathrm{e}^{-\mathrm{i}k_2^{\mathrm{e}}(x-vt)} + B_3 \mathrm{e}^{-\mathrm{i}k_3^{\mathrm{e}}(x-vt)} + B_5 \mathrm{e}^{-\mathrm{i}k_5^{\mathrm{e}}(x-vt)} + B_6 \mathrm{e}^{-\mathrm{i}k_6^{\mathrm{e}}(x-vt)}, & x < vt, \\ B_1 \mathrm{e}^{-\mathrm{i}k_1^{\mathrm{e}}(x-vt)} + B_4 \mathrm{e}^{-\mathrm{i}k_4^{\mathrm{e}}(x-vt)}, & x \geq vt. \end{cases} \tag{3.9}$$

It must be noted that the amplitudes A and B are related through the eigenvectors as follows: $B_n = A_n q_{n,2}^{\mathrm{e}}$, where $n = 1, \ldots, 6$ and $q_{n,2}^{\mathrm{e}}$ represents the second entry in the corresponding

*n*th eigenvector. This means that there are, in fact, six remaining unknown amplitudes that are determined from the interface conditions.

The interface conditions imposed to the beam, namely Eqs. (2.7) and (2.8), need to be supplemented with additional ones for the distributed mass layer, which express the continuity in displacement and slope at $x = x_{\mathrm{tc}}$. These continuity conditions are a consequence of the spatially continuous distribution of the external load by the beam, which together with the homogeneity of the spring layers leads to a spatially continuous force acting on the mass layer; such a force must lead to a continuous displacement and slope of the mass layer. The additional conditions read

$$u_{\mathrm{b}}(x = vt, t) = u_{\mathrm{f}}(x = vt, t), \qquad u'_{\mathrm{b}}(x = vt, t) = u'_{\mathrm{f}}(x = vt, t), \tag{3.10}$$

The six unknown amplitudes can be determined from these interface conditions. The expressions are not given here for brevity, but can be obtained straightforwardly by using a symbolic mathematical software (e.g., Maple or Mathematica). It must also be mentioned that the responses in Eqs. (3.8) and (3.9) are real-valued.

3.3. Transient response

To obtain the response of the inhomogeneous system, the same approach as in Section 2.3 is used here. After applying the Fourier transform to Eqs. (3.1) and (3.2) and some mathematical manipulations, the following result is obtained:

$$\tilde{w}'''' - k^4(x)\,\tilde{w} = -\frac{F_0}{EI\,v}\mathrm{e}^{-\mathrm{i}\omega\frac{x}{v}}, \tag{3.11}$$

$$\tilde{u} = \frac{k_{\mathrm{d,t}}(x)}{-\rho_{\mathrm{b}}\omega^2 + k_{\mathrm{d,t}}(x) + k_{\mathrm{d,b}}(x)}\,\tilde{w}, \tag{3.12}$$

$$k(x) = \begin{cases} k_{\mathrm{l}} = \sqrt[4]{-\overline{\rho}\omega^2 + \overline{k}_{\mathrm{d,t,l}} - \dfrac{k^2_{\mathrm{d,t,l}}}{EI\left(-\rho_{\mathrm{b}}\omega^2 + k_{\mathrm{d,t,l}} + k_{\mathrm{d,b,l}}\right)}}, & x \le x_{\mathrm{tc}}, \\ k_{\mathrm{r}} = \sqrt[4]{-\overline{\rho}\omega^2 + \overline{k}_{\mathrm{d,t,r}} - \dfrac{k^2_{\mathrm{d,t,r}}}{EI\left(-\rho_{\mathrm{b}}\omega^2 + k_{\mathrm{d,t,r}} + k_{\mathrm{d,b,r}}\right)}}, & x \ge x_{\mathrm{tc}}. \end{cases} \tag{3.13}$$

As can be seen from Eqs. (3.11) and (3.12), the equation of motion of the mass layer has become an algebraic equation in the Fourier domain, and the expression of $\tilde{u}$ as a function of $\tilde{w}$ has been replaced in the equation of motion of the beam, thus reducing it to the same shape as in Section 2.3 with just the expression of the wavenumber being different (compare Eq. (3.13) to Eq. (2.21)). This means that the same expressions from Section 2.3 are valid here with the the wavenumbers from Eq. (3.13). The solution in the Fourier domain (after

applying the boundary conditions at infinity), thus, reads

$$\tilde{w}(x,\omega) = \begin{cases} B_{\mathrm{l}}\mathrm{e}^{\mathrm{i}k_{\mathrm{l}}x} + C_{\mathrm{l}}\mathrm{e}^{k_{\mathrm{l}}x} + \tilde{w}_{\mathrm{p,l}}(x,\omega), & x \leq x_{\mathrm{tc}}, \\ A_{\mathrm{r}}\mathrm{e}^{-\mathrm{i}k_{\mathrm{r}}x} + D_{\mathrm{r}}\mathrm{e}^{-k_{\mathrm{r}}x} + \tilde{w}_{\mathrm{p,r}}(x,\omega), & x \geq x_{\mathrm{tc}}. \end{cases} \tag{3.14}$$

The unknown amplitudes are obtained from the interface conditions (Eqs. (2.2) and (2.3)). The response of the mass layer is obtained from Eq. (3.12), and the solutions in the time domain are obtained by numerically evaluating the inverse Fourier transforms.

One could be confused by the expectation that, as derived in the previous section, the addition of the mass layer should lead to two additional waves to be present in the system (a total of six waves) while in Eq. (3.14) there are only four waves present. The apparent discrepancy comes from the fact that the two additional waves appear only in the eigenfield while the four waves in Eq. (3.14) are free waves. In true fact, Eq. (3.14) contains 10 waves: the six waves in the eigenfield present in the particular solutions $\tilde{w}_{\mathrm{p},h}$ and the four free waves. It can also be seen that six wavenumbers are obtained from the dispersion equation only after the kinematic invariant is substituted, leading to wavenumbers corresponding to waves in the eigenfield; if one does not substitute the kinematic invariant in the dispersion equation, with largest power of ω being four, four frequency-dependent wavenumbers are obtained representing the four free waves in Eq. (3.14).

Both steady-state and transient solutions are now determined. In the next section, the three approaches discussed in the introduction of this chapter are compared.

3.4. Model comparison

In this section, we compare the two options to incorporate the mass of the supporting structure into the 1-D model formulated in Chapter 2. As explained in the chapter introduction, the two options investigated here are (i) to incorporate the additional mass by artificially increasing the mass of the beam (EBW+M model) and (ii) to add a separate layer of distributed mass (TL model, where TL stands for two layers), model that is formulated in the previous section (see also Fig. 3.1). These two options are compared also to the model formulated in Chapter 2 (EBW model) without accounting for the additional mass of the supporting structure to investigate if the additional mass has a significant influence on the response and if simply considering a realistic relative velocity v/c_{cr} is sufficient when it comes to modelling transition radiation. The comparison is made in terms of the transition radiation and, more specifically, in terms of the response amplification at the transition zone.

The parameters of the model with the additional mass layer are chosen such that the beam accounts for the mass of the rail and distributed mass of the sleepers while the additional mass layer accounts for the mass of the ballast. Furthermore, the the top layer of springs corresponds to the rail-pads while the lower layer of springs represents the equivalent stiffness of the ballast and soil. An alternative is to represent the stiffness of the rail-pads

and the ballast through the top layer of springs, while considering the stiffness of the soil in the lower layer of springs. Both these scenarios lead to similar qualitative behaviour because in both cases the stiffness of the top layer of springs is significantly larger than the one of the bottom layer. The results presented in this section adopt the first option.

To draw fair conclusions from this investigation, the parameters of the EBW+M system are tuned to the TL model. More specifically, the stiffness of the Winkler layer is chosen to match the static stiffness in the TL model. Furthermore, the artificially increased mass of the beam is chosen such that the critical velocities in the two models match. For a meaningful comparison, the load velocity relative to the critical one is kept constant between models. This means that the load velocity in the TL and EBW+M models is the same, while it is higher in the EBW model. The parameters used to compute the results in this section are given in Table 3.1.

Table 3.1: Parameter values for the three systems: two-layer (TL) model, and Euler-Bernoulli beam with/without artificially increased mass on Winkler foundation (EBW+M/EBW, respectively).

Model	Parameter	Symbol	Value	Unit
TL	Bending stiffness	EI	$6.4{\cdot}10^6$	Nm^2
	Mass per unit length of beam	ρ_t	268.3	kg/m
	Mass per unit length of layer	ρ_t	810	kg/m
	Stiffness of top layer	$k_\mathrm{d,l,t}$	$208 \cdot 10^6$	$\mathrm{N/m}^2$
	Stiffness of bottom layer	$k_\mathrm{d,l,b}$	$7.6{\cdot}10^6$	$\mathrm{N/m}^2$
	Dead weight	F_0	$80 \cdot 10^3$	N
EBW+M	Mass per unit length	ρ	1062	kg/m
	Winkler stiffness	$k_\mathrm{d,l}$	$7.3{\cdot}10^6$	$\mathrm{N/m}^2$
EB	Mass per unit length	ρ	268.3	kg/m
	Winkler stiffness	$k_\mathrm{d,l}$	$7.3{\cdot}10^6$	$\mathrm{N/m}^2$

3.4.1. Dispersion curves and frequency spectra

Fig. 3.4 presents the dispersion curves (only for positive frequencies) of the three models. It can be seen that the cut-off frequencies of the TL and EBW+M systems are the same while the cut-off frequency of the EBW presents is higher. This is expected since the static stiffness in all three models is the same while the mass in the third model is lower than in the other two. The dispersion curves of the two models with additional mass is very similar for low wavenumbers and low frequencies. This indicates that free waves excited at the transition zone in this range of wavenumbers and frequencies will, most likely, lead to similar quantitative results. However, once the wavenumber increases, the lower dispersion branch of the TL model tends to a plateau while the dispersion curve of the EBW+M continues to increase in frequency, leading to a significant difference between the two models. For high frequencies, the dispersion of the EBW model is more similar to the TL model because, for high frequencies, the mass layer is barely activated. Finally, one significant qualitative

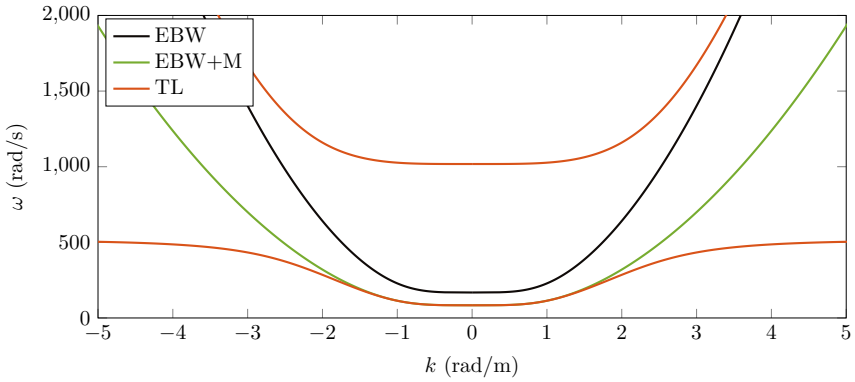

Figure 3.4: The dispersion curves of two-layer (TL) model, and Euler-Bernoulli beam with/without artificially increased mass on Winkler foundation (EBW+M/EBW, respectively).

difference between the TL model and the one-layer models is that the former has a range of frequencies between the plateau of the lower branch and the cut-off frequency of the upper branch in which wave propagation is not possible; this zone is called a *stop band*.

The left panel in Fig. 3.5 presents the dispersion curves and kinematic invariants corresponding to the three models (remember that the load velocity is different in the three models in order to maintain the same relative velocity). It can be clearly seen that the critical velocity has decreased in the systems with additional mass. The middle panel of Fig. 3.5 presents the displacement spectra evaluated at a position to the left of x_{tc} while the right panel presents the free-field spectra evaluated at $x = 0$. It can be seen that the two models with additional mass predict a very similar behaviour while the model without additional mass has the energy content at higher frequencies. This makes sense because even if the wavenumber content is the same in the three models (which is the case in the quasi-static regime due to the tuning of the models), the energy content in the system without additional mass needs to be at higher frequencies simply because the velocity of the load is higher. Therefore, even if one tunes the time-domain response fields to be quantitatively similar, the frequency spectrum in the system without additional mass will have energy content at higher frequencies.

3.4.2. Time-domain response

Fig. 3.6 presents the time-domain displacement field computed with the three models in the scenario with a transition zone. For the model without additional mass, the velocity of the load is chosen such that the ratio $v/c_{\text{cr,l}}$ is the same for all models, resulting in an increased v. Consequently, the time moments at which the displacement field snap-shots are presented in Fig. 3.6 is adjusted such that the load is at the same location in all three models.

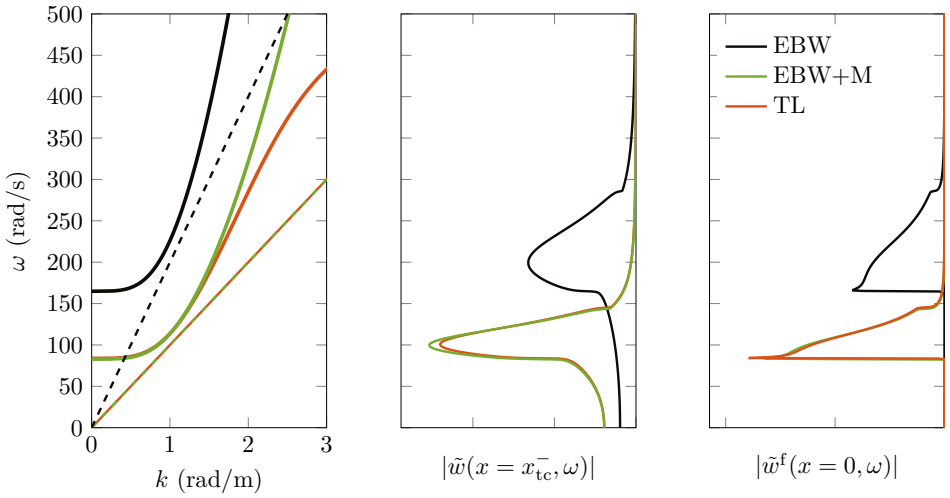

Figure 3.5: The dispersion curves (solid lines) and kinematic invariants (dashed lines) (left panel), the frequency spectra of the transient displacement (middle panel), and free-field displacement (right panel), corresponding to the three models.

From the top left panel can be seen that the eigenfields of all three models match very well. The very good match between the results of all three models is unchanged throughout the transition process. It can be observed, especially in the bottom two panels, that also the wave radiation predicted by all three models is, from a practical point of view, the same. The same good match is observed at other velocities (e.g., quasi-static or even $v \approx 0.95 c_{\mathrm{cr,l}}$), but the results are not presented here for brevity.

3.4.3. Energy analysis

The top panel in Fig. 3.7 presents the power input by the horizontal force in all three models (see Section 2.4 for a detailed discussion about power input). While the two models with additional mass show a very good agreement, the power input exhibited in the EBW model is twice as big. Looking at Eq. (2.32), it becomes clear why this is the case; while the response (velocity) under the moving load matches very well in all three models (can be deduced from the good response agreement observed in Fig. 3.6), the load velocity in the EBW system is about twice as big as the one in the models with additional mass to ensure the same ratio v/c_{cr}. This leads to the difference in power input, and when this is normalized by the load velocity, the agreement between all three models is very good, as can be seen in the bottom panel of Fig. 3.7. This shows that while all three models predict the same qualitative behaviour, quantitatively there are differences when it comes to the power input by the moving load.

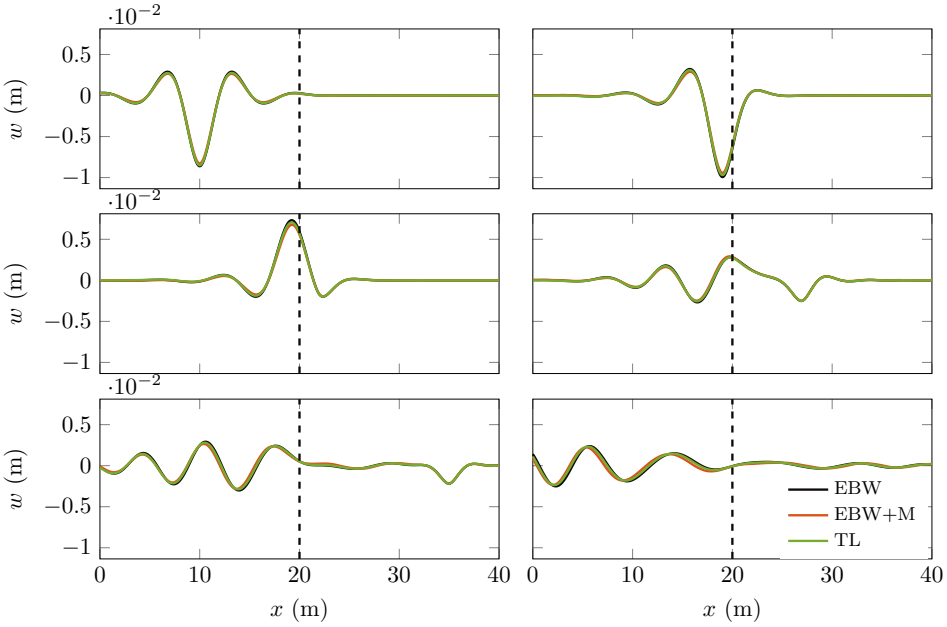

Figure 3.6: Snapshots of the transient displacement field at different time moments for the three models; the vertical dashed line indicates the location of the jump in stiffness. $v \approx 0.9c_{\mathrm{cr,l}}$.

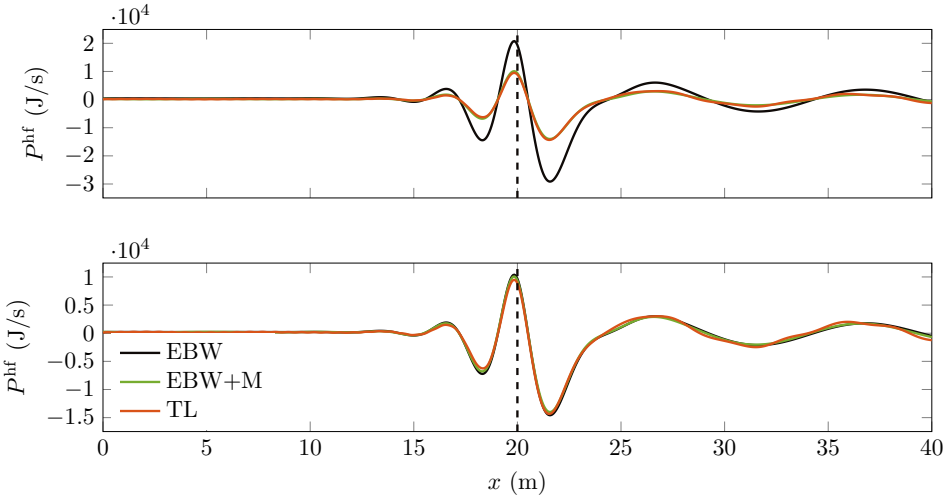

Figure 3.7: The power input by the horizontal force in the three models; the horizontal dashed line indicates the location of the jump in stiffness.

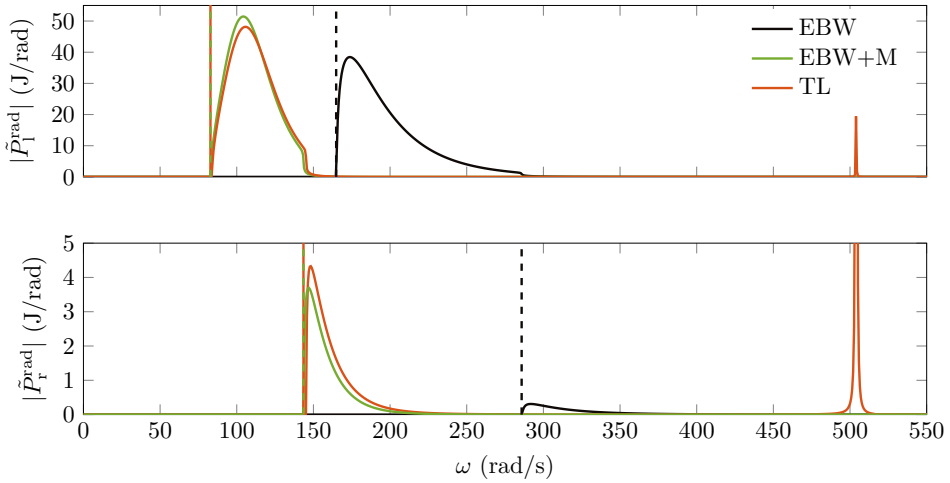

Figure 3.8: The power spectral density of the radiation to the left (top panel) and to the right (bottom panel). The vertical dashed lines indicate the cut-off frequency corresponding to each model. Note that the power input in the EBW model has been multiplied by a factor of 500.

Fig. 3.8 presents the power spectral density of transition radiation. The two models with additional mass show a good agreement, although there is a small difference in the distribution of the energy radiated to the left and right. The power spectral density in the TL model exhibits an infinite peak. This peak corresponds to the propagating wave in the eigenfield present only in the TL model, leading to infinite amount of energy radiated from the load at that frequency. As discussed in the previous section, this is an artefact of the TL model and does not have a physical relevance. Furthermore, similar to the displacement in the frequency domain (see Fig. 3.5), the power spectrum in the model without additional mass is located at higher frequencies. More importantly, the results presented in Fig. 3.8 for the EBW model are multiplied by a factor 500. This shows that the quantitative predictions of the EBW system significantly underestimate the quantity of energy radiated. Moreover, the results are also qualitatively different because the distribution of the energy to the radiation left and right is different compared to the other two models.

3.5. Conclusions

This chapter compared three modelling approaches to ensure a realistic ratio v/c_{cr}, which is of paramount importance when studying the response amplification at transition zones. The three approaches are (i) to formulate a two-layer model where the additional structure mass is included in the bottom layer (see Fig. 3.1), (ii) artificially increase the beam's mass in the 1-D model formulated in Chapter 2, and (iii) artificially increase the load velocity. The comparison of the models was done in view of the transition radiation process and the associated response amplification at transition zones.

The formulated two-layer system showed a number of characteristics different to those of the classical beam on Winkler foundation (formulated in Chapter 2). More specifically, it has four dispersion curves instead of two, causing the system to have one, two, or three critical velocities depending on the mass of the additional layer. The two additional dispersion curves also lead to the formation of an additional stop-band in which waves cannot propagate in the system. Furthermore, it was shown that above a specific value of the additional mass layer, an increase in this quantity leads to an increase in the critical velocity, which is counter-intuitive. Finally, due to the lack of bending or shear stiffness of the additional layer, there is at least one intersection between the kinematic invariant and the lower dispersion branch for any non-zero load velocity. This means that the steady-state response always presents at least one propagating wave, which is an artefact of the model.

Results show that the two models with additional mass have a very good agreement for all quantities investigated. This shows that the additional mass layer is not necessary to be included, at least not for studying transition radiation. The model without the additional mass, but with artificially increased velocity showed a very good agreement, both qualitatively and quantitatively, in the time-domain response, but less so in the response spectra. In the latter, the larger load velocity leads to the response having higher frequencies than the other two models, but with a similar qualitative behaviour. When it comes to the power spectral density, the neglect of the additional mass leads to a gross underestimation of this quantity as well as to a different distribution of the energy radiated left and the one radiated to the right.

To conclude, the investigation in this chapter showed that all three approaches lead, in general, to the same qualitative, and sometimes, quantitative behaviour. For investigating the time-domain response, all three approaches can be used, while for the energy analysis, the predictions of the model without additional mass should be trusted only quantitatively.

4

Influence of vehicle-structure interaction on transition radiation

It is through science that we prove, but through intuition that we discover.

Henri Poincaré

In order to improve the design of transition zones and develop successful mitigation measures, the underlying mechanisms leading to soil and ballast differential settlement need to be better understood. To this end, a significant amount of studies focus on modelling ballast [e.g., 24, 59–63] and its settlement [e.g., 26]. Most of these ballast settlement models relate the amount of settlement to the magnitude of the force applied on the ballast. As showed in Chapter 2, the response is amplified at transition zones, thus indicating indirectly an increase in ballast settlement. However, the vehicle-track interaction, which was neglected in Chapter 2, could influence the response amplification at the transition zone. This chapter investigates the influence of the vehicle-structure interaction on transition radiation and the corresponding response amplification.*

In its purest form, transition radiation is addressed in structures acted upon by a moving constant load, as presented in Chapter 2. However, modelling the vehicle as a moving constant load has obvious limitations, such as neglecting the vehicle inertia, the absence of the corresponding interaction between the vehicle and the supporting structure, and the impossibility of unstable motions of the vehicle. For that reason, researchers included

* This chapter is based on one of the author's publications [64] and it presents slight modifications to the original publication.

the interaction between the vehicle with its own degrees of freedom and the supporting structure in studies on transition radiation. Lei and Mao [13] found that the contact force is not greatly influenced by the magnitude of the stiffness jump (i.e., stiffness dissimilarity), but that it is mostly influenced by the angle of the rail elevation after differential settlements have occurred. Also Banimahd et al. [65] concluded that the so-called faults in the track (i.e., differential settlements) influence the contact force much more than the stiffness variation does. Moreover, the findings of Ang and Dai [35] are in agreement with the conclusions of Lei and Mao [13] and of Banimahd et al. [65]. However, Germonpré et al. [31] found that at large velocities, the contact force in the case of an abrupt transition significantly increases compared to the smooth transition. Transition radiation was also studied using complex multiple-degrees-of-freedom vehicles interacting with inhomogeneous 1-D supporting structures [10, 25, 66], and with inhomogeneous 2-D and 3-D supporting structures [e.g., 27, 28, 67], confirming that the inertia of the vehicle can play an important role in the transition radiation phenomenon and in the track-geometry degradation.

To study the transition radiation phenomenon, detailed models of finite and inhomogeneous systems that interact with complex vehicle models are available in the literature, as explained above. However, more fundamental studies using simplified models of transition zones in infinite systems interacting with a moving oscillator, similar to system stability studies [e.g., 68–75], are scarce. This motivates the aim of the current chapter, which is to formulate a 1-D model of an infinite Euler-Bernoulli beam on a smoothly inhomogeneous Kelvin foundation, interacting with a moving oscillator, in order to study the effect of accounting for the vehicle's internal degree of freedom on transition radiation. The solution can be obtained by means of the Green's-function method [76] because the supporting structure is assumed to behave linearly. To this end, the response of the beam to the moving vehicle, which is modelled as a loaded oscillator, is expressed through a convolution integral in terms of the unknown contact force and the known time-domain Green's function of the beam-foundation sub-system. Then, the contact relation (i.e., integral equation) is solved iteratively for the contact force. Moreover, the finite difference method is used for the spatial discretization to accommodate the smoothly inhomogeneous foundation. The infinite extent of the system is accounted for through a set of non-reflective boundary conditions, and through the initial conditions based on the steady-state response of a beam with homogeneous foundation subject to a moving load (the steady state is assumed to have developed prior to reaching the transition).

The novelty of the current chapter lies in studying the influence of the degree of freedom of the vehicle on the transition radiation in an infinite and smoothly inhomogeneous structure by comparing it to the situation in which the vehicle action is approximated by its dead weight. Furthermore, two possible indicators of the transition-zone performance are identified. The current chapter has some similarities to the works of Lei and Mao [13] and of Ang and Dai [35], but is distinct in the following ways. Firstly, the vehicle models in both studies are more complex than the one used in the current chapter, making the observations

difficult to relate/compare to the case of a single moving constant load. Secondly, both works are limited to piecewise-homogeneous foundations, while the current chapter addresses a smooth stiffness and damping variation of the supporting structure. Thirdly, the infinite extent of the system is properly accounted for in the present work. Finally, the extent of the parametric study presented in both previous works is considerably enlarged in the current study, and thus, more general observations of the system's behaviour can be made, relevant for engineering practice.

Modelling the railway track as a 1-D system (with frequency-independent parameters) has its shortcomings. For example, the wave propagation in the vertical direction as well as surface waves are not captured by this model, aspects which can influence the dynamic response. However, the qualitative observations and the mechanisms identified with this simplified model will be present in a more comprehensive model. Therefore, for the purpose of studying the influence of the vehicle's own degree-of-freedom on the transition radiation phenomenon, the 1-D model is sufficient. It must be emphasized that this chapter focuses on transition radiation as the process of energy emission, which is characterized by the energy flux through a boundary that encompasses the emitter, with no emphasis on the type of waves that are generated (propagating and/or evanescent).

4.1. Model formulation

In this section, a 1-D model is formulated, consisting of an infinite Euler-Bernoulli beam resting on a smoothly inhomogeneous Kelvin foundation, interacting with a moving one-mass loaded oscillator (Fig. 4.1). Apart from the different vehicle model and the addition of foundation damping, compared to the system in Chapter 2, the system in this chapter allows the transition in stiffness to be smooth (actually, it allows for any arbitrary shape), not only abrupt. Consequently, the infinite system is divided into three domains: the *computational domain* $\left(x \in [0, L]\right.$ as can be seen in Fig. 4.1$\left.\right)$ that contains the entire inhomogeneity of the supporting structure and its vicinity, and two homogeneous semi-infinite domains, one at each boundary of the computational domain. The initial position (at $t = 0$) of the moving oscillator is at $x = 0$ and its oscillations are restricted to the computational domain, such that the vehicle can be approximated by a moving load in the two semi-infinite domains. The equation of motion for the three domains reads

$$EI\frac{\tilde{\partial}^4 w}{\tilde{\partial} x^4} + \rho\frac{\tilde{\partial}^2 w}{\tilde{\partial} t^2} + c_{\mathrm{d}}(x)\frac{\tilde{\partial} w}{\tilde{\partial} t} + k_{\mathrm{d}}(x)\, w = -F(t)\,\delta(x - vt), \qquad \forall x, \forall t, \tag{4.1}$$

$$w(x,t) = \begin{cases} w_{\mathrm{l}}(x,t), & x \le 0, \\ w_{\mathrm{c}}(x,t), & 0 \le x \le L, \\ w_{\mathrm{r}}(x,t), & x \ge L, \end{cases} \qquad F(t) = \begin{cases} F_0, & t \le 0, \\ F_{\mathrm{c}}(t), & 0 \le t \le \frac{L}{v}, \\ F_0, & t \ge \frac{L}{v}, \end{cases}$$

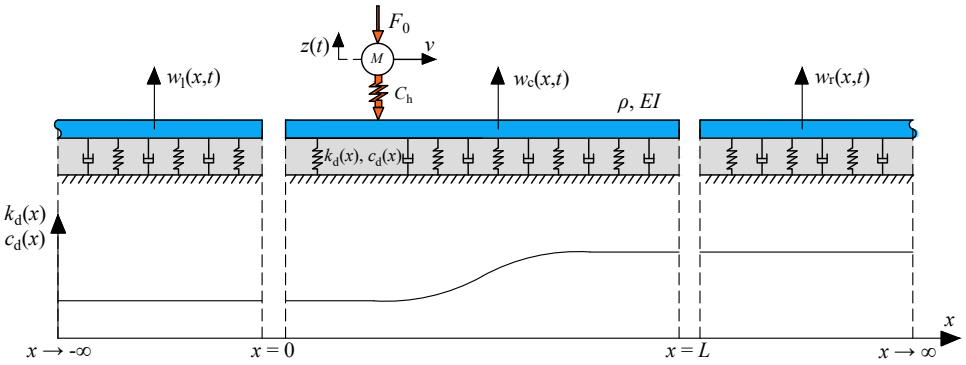

Figure 4.1: Schematization of the model: infinite Euler-Bernoulli beam continuously supported by a smoothly inhomogeneous Kelvin foundation, interacting with a moving loaded oscillator.

$$k_d(x) = \begin{cases} k_{d,l}, & x \le 0, \\ k_{d,c}(x), & 0 \le x \le L, \\ k_{d,r}, & x \ge L, \end{cases} \qquad c_d(x) = \begin{cases} c_{d,l}, & x \le 0, \\ c_{d,c}(x), & 0 \le x \le L, \\ c_{d,r}, & x \ge L, \end{cases}$$

where $c_{d,l}$ and $c_{d,r}$ are the (homogeneous) foundation damping of the left and right semi-infinite domain, respectively; $k_{d,c}(x)$ and $c_{d,c}(x)$ are the foundation stiffness and foundation damping of the computational domain, respectively. $F_c(t)$ is the time-dependent contact force in the computational domain. Finally, w_c is the unknown displacement of the computational domain. Moreover, by adopting $\le$ and $\ge$ signs in the definition of $w(x,t)$, $F(t)$, $k_d(x)$, and $c_d(x)$ for all domains it is emphasized that there is continuity in these quantities at the interfaces between the three domains.

In this formulation, the vehicle is modelled as a loaded one-mass oscillator (i.e., loaded mass-spring system), where the constant dead load F_0 (which includes the dead weight of the wheel) corresponds to the vehicle weight on the wheel, the mass M represents the wheel of the vehicle and the spring represents the contact elasticity between the wheel and the rail. The car body and the bogies could be modelled by additional suspended masses. However, the frequencies at which these suspended masses oscillate are much lower than the oscillation frequency of the wheel in the interaction with the rail. Therefore, the degrees of freedom of the suspended masses of the car body and bogies are neglected. In the remainder of the chapter, the term oscillator is used to denote the loaded one-mass oscillator. The equation of motion for the oscillator reads

$$M\ddot{u} = F(t) - F_0, \tag{4.2}$$

where u is the displacement of the mass. The interaction between the oscillator and the beam-foundation sub-system is described by the Hertzian contact law, where the possibility

of contact loss is incorporated as presented in the following equation:

$$\left(\frac{F(t)}{C_{\mathrm{H}}}\right)^{\frac{2}{3}} = \big(u(t) - w(vt,t)\big)\, H\big(u(t) - w(vt,t)\big), \tag{4.3}$$

where C_{H} is Hertz's constant and $H(\ldots)$ denotes the Heaviside function. It must be noted that for large transition lengths, the inertia of the suspended masses may have a non-negligible effect on the behaviour due to the low frequencies of the interaction [67].

From Eq. (4.1) it can be deduced that the shear force is continuous everywhere except under the moving load where the force is discontinuous. This discontinuity is accounted for in the equation of motion (Eq. (4.1)), for all time moments, due to the presence of the generalized derivatives. Consequently, as interface conditions between the domains, continuity in displacement and slope, as well as in shear force and bending moment is imposed. The set of boundary conditions is completed by imposing that, due to the presence of damping, the displacements of the left and right domains are zero at infinite distance from the moving oscillator:

$$w_{\mathrm{l}}(0,t) = w_{\mathrm{c}}(0,t), \qquad w_{\mathrm{c}}(L,t) = w_{\mathrm{r}}(L,t), \tag{4.4}$$

$$w'_{\mathrm{l}}(0,t) = w'_{\mathrm{c}}(0,t), \qquad w'_{\mathrm{c}}(L,t) = w'_{\mathrm{r}}(L,t), \tag{4.5}$$

$$w''_{\mathrm{l}}(0,t) = w''_{\mathrm{c}}(0,t), \qquad w''_{\mathrm{c}}(L,t) = w''_{\mathrm{r}}(L,t), \tag{4.6}$$

$$w'''_{\mathrm{l}}(0,t) = w'''_{\mathrm{c}}(0,t), \qquad w'''_{\mathrm{c}}(L,t) = w'''_{\mathrm{r}}(L,t), \tag{4.7}$$

$$\lim_{|x-vt|\to\infty} w_{\mathrm{l}}(x,t) = 0, \qquad \lim_{|x-vt|\to\infty} w_{\mathrm{r}}(x,t) = 0. \tag{4.8}$$

The computational domain could be made very large such that the influence of the initial conditions on the response dies out before the oscillator reaches the transition zone. However, for computational efficiency, $x = 0$ should be as close as possible to the inhomogeneity (i.e., the computational domain should be as small as possible), meaning that the choice of initial conditions affects the response in the transition zone. Prior to reaching a transition zone, the response caused by a train can generally be considered to be in the steady state. Consequently, the initial conditions must be chosen such that the system reaches the steady-state regime instantaneously at the start of the simulation, and are thus based on the eigenfield of the approaching load. For the considered problem, in the steady state, the moving oscillator is equivalent to a moving constant load where the magnitude of the force is equal to F_0, and the eigenfield w^{e} for such a system is given by Eq. (2.19) (with the addition of the damping term which appears in the expression of the wavenumbers).

The initial conditions based on the eigenfield are correct only if the initial fields (i.e., displacement and velocity fields) are not disturbed by the inhomogeneity because the eigenfield relates to a *homogeneous* Kelvin foundation. Consequently, $x = 0$ should be positioned such that the initial fields based on the eigenfield are negligibly small at the inhomogeneity (they cannot be precisely zero due to the eigenfield's exponential decay in space). The ini-

tial conditions of the left domain are imposed as the eigenfield part behind the oscillator, the ones of the computational domain are imposed as the eigenfield part in front of the oscillator, and the initial conditions of the right domain are trivial:

$$w_\mathrm{l}(x,t=0) = w^\mathrm{e}(x,t=0), \qquad \dot{w}_\mathrm{l}(x,t=0) = \dot{w}^\mathrm{e}(x,t=0), \qquad -\infty < x < 0, \tag{4.9}$$

$$w_\mathrm{c}(x,t=0) = w^\mathrm{e}(x,t=0), \qquad \dot{w}_\mathrm{c}(x,t=0) = \dot{w}^\mathrm{e}(x,t=0), \qquad 0 \le x \le L, \tag{4.10}$$

$$w_\mathrm{r}(x,t=0) \approx 0, \qquad \dot{w}_\mathrm{r}(x,t=0) \approx 0, \qquad L < x < \infty. \tag{4.11}$$

The initial conditions of the oscillator should be chosen such that it also reaches the steady state instantaneously at the start of the simulation. Considering that the contact force is constant and equal to F_0 in the steady state, the initial conditions for the oscillator are given as follows:

$$u(t=0) = \left(\frac{F_0}{C_\mathrm{H}}\right)^{\frac{2}{3}} + w^\mathrm{e}(0,0), \qquad \dot{u}(t=0) = 0. \tag{4.12}$$

Eqs. (4.1) to (4.12) constitute a complete description of the problem. Next, the solution method is presented.

4.2. Solution method

The system described in Section 4.1 is nonlinear due to the nonlinear contact relation (Eq. (4.3)). However, the beam-foundation sub-system behaves linearly. This allows to obtain the solution using the time-domain Green's-function method [76] which is explained next.

4.2.1. General procedure

The goal of the Green's-function method is to express the displacement of the beam at the contact point in terms of the unknown contact force $F(t)$. The obtained displacement can be substituted in the contact relation (Eq. (4.3)). Then, the displacement of the mass can be expressed in terms of the contact force, and the resulting expression can be substituted in the equation of motion of the mass. The resulting integro-differential equation can then be solved for the unknown contact force numerically. This approach is suited for any type of vehicle model. However, taking advantage of the linearity of the vehicle model used in this chapter (except for the contact spring), the displacement of the vehicle is expressed in terms of the unknown contact force through the Green's-function method too. Then, the contact relation reduces to an integral equation for the contact force, and is solved iteratively.

To express the displacement of the beam in terms of the contact force, the forward Laplace transform is applied over time to the equation of motion of the computational domain, resulting in the following expression:

$$EI\,\hat{w}_\mathrm{c}'''' + \left[\rho\, s^2 + c_\mathrm{d,c}(x)\, s + k_\mathrm{d,c}(x)\right] \hat{w} = \hat{f}_\mathrm{c}^\mathrm{ML} + \hat{f}_\mathrm{c}^\mathrm{IC}, \tag{4.13}$$

where $\hat{w}_c$ represents the unknown Laplace-domain displacement of the computational domain, and $s = \sigma + i\omega$ is the Laplace variable, with σ a small and positive real number and ω the angular frequency. Furthermore, $\hat{f}_c^{ML}$ represents the Laplace-domain moving-load forcing of the computational domain, and $\hat{f}_c^{IC}$ represents the Laplace-domain initial-conditions forcing of the computational domain, which are given by

$$\hat{f}_c^{ML}(x,s) = -\tfrac{1}{v}\hat{F}_c\left(\tfrac{x}{v}\right)e^{-s\frac{x}{v}}, \tag{4.14}$$

$$\hat{f}_c^{IC}(x,s) = \left(\rho s + c_{d,c}(x)\right) w_c(x,t=0) + \rho\, \dot{w}_c(x,t=0), \tag{4.15}$$

where $\hat{F}_c$ represents the Laplace-domain contact force in the computational domain. It must be noted that the contact force $\hat{F}_c$ is yet unknown, while the initial-conditions forcing is completely determined (Eq. (4.10)). It is therefore chosen to determine the response caused by the moving load and the response generated by the initial conditions separately, using different approaches. The displacement $\hat{w}_c^{IC}$ generated by the initial conditions can be determined in the Laplace domain and the procedure is elaborated in Section 4.2.2. The displacement caused by the unknown contact force can be obtained in the time domain by means of the Green's-function method. To this end, the Laplace-domain displacement $\hat{w}_c^{ML}$ caused by the unknown contact force is expressed in terms of the Green's function as follows:

$$\hat{w}_c^{ML}(x,s) = \int_0^L \hat{g}(x,\xi,s)\, \hat{f}_c^{ML}(\xi,s)\mathrm{d}\xi, \tag{4.16}$$

where ξ represents the spatial variable of integration and $\hat{g}(x,\xi,s)$ represents the Laplace-domain Green's function of the inhomogeneous and infinite beam-foundation system which is determined in Section 4.2.2. To obtain the time-domain displacement w_c^{ML}, Eq. (4.16) is expressed in the time domain using a convolution integral:

$$\begin{aligned} w_c^{ML}(x,t) &= \int_0^L \int_0^t g(x,\xi,t-\tau)\, F_c(\tau)\delta(\xi - v\tau)\mathrm{d}\tau\mathrm{d}\xi \\ &= \int_0^t g(x,v\tau,t-\tau)\, F_c(\tau)\, H(L-v\tau)\mathrm{d}\tau, \qquad t \geq 0, \end{aligned} \tag{4.17}$$

where g represents the time-domain Green's function and is obtained by applying the inverse Laplace transform to $\hat{g}$, as shown in Section 4.2.2.

The total displacement of the beam in the time domain is a superposition of the displacement caused by the moving load and the displacement generated by the initial conditions:

$$w_c(x,t) = \int_0^t g(x,v\tau,t-\tau)\, F_c(\tau)\, H(L-v\tau)\mathrm{d}\tau + w_c^{IC}(x,t) + w_c^{L}(x,t), \tag{4.18}$$

where w_c^L represents the displacement of the computational domain caused by the oscillator continuing its movement in the right domain, and $w_c^L \sim H(vt - L)$ meaning that w_c^L is non-zero only after the oscillator has entered the right domain. Because the oscillator is

assumed to be in the steady state when it enters the right domain, w_c^L depends on the steady-state contact force F_0 and not on the unknown contact force $F_c(t)$. Therefore, w_c^L is obtained using the same procedure employed for obtaining w_c^{IC}, which is elaborated in Section 4.2.2.

The displacement of the beam has now been expressed in terms of the unknown contact force, as seen in Eq. (4.18). Taking advantage of the linearity of the vehicle model (except for the contact spring), the same procedure is applied for obtaining the displacement of the mass as a function of the unknown contact force. The Laplace-domain displacement of the mass $\hat{u}$ reads

$$\hat{u}(s) = -\frac{F_0}{Ms^3} + \frac{\hat{F}_c}{Ms^2} + \frac{u(t=0)}{s} + \frac{\dot{u}(t=0)}{s^2}. \tag{4.19}$$

The time-domain displacement u of the mass is obtained by evaluating the inverse Laplace transform of Eq. (4.19) analytically, and its expression reads

$$u(t) = -\frac{F_0}{2M}t^2 + \frac{1}{M}\int_0^t (t-\tau)\,F_c(\tau)\mathrm{d}\tau + u(t=0) + \dot{u}(t=0)\,t, \qquad t \geq 0. \tag{4.20}$$

Both the displacement of the mass and that of the beam are now expressed in terms of the unknown contact force. The contact force $F_c(t)$ is solved for iteratively at each time moment such that the contact relation is satisfied. The procedure for obtaining the contact force is thoroughly explained in [72], and is briefly summarized here. Outside the computational domain, the contact force is assumed to be constant and equal to F_0. Therefore, the contact force needs to be determined only in the time interval when the oscillator is inside the computational domain. Upon evaluating the displacement of the beam at $x = vt$, both displacements (Eqs. (4.18) and (4.20)) are substituted in the contact relation (Eq. (4.3)), resulting in the following integral equation:

$$\left(\frac{F_c(t)}{C_H}\right)^{\frac{2}{3}} = R(t)\,H\big(R(t)\big), \qquad 0 \leq t \leq \frac{L}{v}, \tag{4.21}$$

where $H\big(R(t)\big)$ denotes the Heaviside function with argument $R(t)$, which reads

$$\begin{aligned} R(t) = &-\frac{F_0}{2M}t^2 + \frac{1}{M}\int_0^t (t-\tau)\,F_c(\tau)\mathrm{d}\tau + u(t=0) + \dot{u}(t=0)\,t \\ &-\int_0^t g(vt, v\tau, t-\tau)\,F_c(\tau)\mathrm{d}\tau + w_c^{IC}(vt, t). \end{aligned} \tag{4.22}$$

Considering the time discretization $t_0, t_1, \ldots, t_n$, with $t_0 = 0$, $t_n = t$ (the present time moment) and $\Delta t = t_i - t_{i-1}$ where $i = \{1, \ldots, n\}$, Eq. (4.21) becomes

$$\left(\frac{F_c(t_n)}{C_H}\right)^{\frac{2}{3}} = R_n\,H(R_n), \qquad 0 \leq t_n \leq \frac{L}{v}, \tag{4.23}$$

$$R_n = -\frac{F_0}{2M} t_n^2 + \sum_{i=1}^{n} \frac{1}{M} \int_{t_{i-1}}^{t_i} (t_n - \tau)\, F_c(\tau) \mathrm{d}\tau + u(t=0) + \dot{u}(t=0)\, t_n$$
$$- \sum_{i=1}^{n} \int_{t_{i-1}}^{t_i} g(v t_n - v\tau, t_n - \tau)\, F_c(\tau) \mathrm{d}\tau + w_c^{IC}(v t_n, t_n).$$

It must be emphasized that although Eqs. (4.21) and (4.23) are valid only for $0 \leq t_n \leq \frac{L}{v}$, the simulation is not limited to this time interval provided that the oscillations of the mass have stopped before the oscillator reaches the right boundary $x = L$.

Assuming that both the Green's function of the beam-foundation system and the contact force have a linear variation during the time interval $\tau \in [t_{i-1}, t_i]$, the integrals in Eq. (4.23) are evaluated analytically, resulting in a nonlinear algebraic equation which can be solved iteratively for the unknown contact force at present time t_n. Once the time history of the contact force has been obtained, the response of the mass and that of the beam can be computed by substituting the determined contact force in Eqs. (4.18) and (4.20).

At this point, the Green's functions g of the inhomogeneous and infinite beam-foundation sub-system, the displacement w_c^{IC} caused by the initial conditions, and the displacement w_c^{L} generated by the oscillator continuing its movement in the right domain are not determined. This is done in the next sub-section.

4.2.2. The beam-foundation Green's functions, the response to initial conditions and the response caused by the oscillator continuing its movement in the right domain

Due to the spatial variation of the foundation stiffness and damping (as seen in Eq. (4.13)), the Green's functions $\hat{g}$ of the beam-foundation sub-system, the displacement $\hat{w}_c^{IC}$ caused by the initial conditions, and the displacement $\hat{w}_c^{L}$ generated by the oscillator continuing its movement in the right domain cannot be solved analytically for all stiffness and damping profiles. Therefore, the finite difference method (central difference scheme of $O(\Delta x^2)$) is used to spatially discretize Eq. (4.13). Upon discretization of the computational domain, the Laplace-domain equation of motion describing the beam-foundation sub-system subjected to initial conditions reads

$$\left[\hat{K}_{ij} + (\rho s^2 + c_{d,c,i}\, s + k_{d,c,i}) I_{ij}\right] \hat{w}_{c,j}^{IC} = \hat{f}_{c,i}^{IC} + \hat{f}_{c,i}^{B}, \tag{4.24}$$

where $\hat{K}_{ij}$ represents the bending-stiffness matrix of the beam, $\hat{f}_{c,i}^{B}$ represents a force exerted by the semi-infinite domains at the boundaries and is derived in Section 4.2.3, and I_{ij} is the identity matrix. The time-domain displacement is obtained by left multiplying Eq. (4.24) with the inverse of the dynamic stiffness matrix (i.e., the expression in the square brackets) and by evaluating the inverse Laplace transform numerically. However, the Laplace-domain spectrum of $\hat{w}_{c,j}^{IC}$ exhibits a poor decay due to the applied non-zero initial conditions. Consequently, the numerical integration must in principle be performed up to very high

frequencies leading to a significant computational effort. A method of incorporating the high frequencies without increasing the computational effort is presented in [77] and is also applied here to accurately obtain $w^{\mathrm{IC}}_{\mathrm{c},j}$.

The same procedure used for obtaining $w^{\mathrm{IC}}_{\mathrm{c}}$ is used to obtain $w^{\mathrm{L}}_{\mathrm{c}}$. For this case, the Laplace-domain equation of motion reads

$$\left[\hat{K}_{ij} + (\rho\, s^2 + c_{\mathrm{d,c},i}\, s + k_{\mathrm{d,c},i}) I_{ij}\right] \hat{w}^{\mathrm{L}}_{\mathrm{c},j} = \hat{f}^{\mathrm{L}}_{\mathrm{c},i}, \tag{4.25}$$

where $\hat{f}^{\mathrm{L}}_{\mathrm{c},i}$ represents a boundary-forcing vector exerted at the right boundary by the oscillator as it continues its movement in the right domain, and is derived in Section 4.2.3.

To obtain the Laplace-domain Green's functions $\hat{g}$ needed in Eq. (4.16), the right-hand side of Eq. (4.13) is replaced by a Dirac delta function in space $\delta(x-\xi)$. Upon spatial discretization, the Laplace-domain equation of motion that describes the impulse response reads

$$\left[\hat{K}_{ij} + (\rho\, s^2 + c_{\mathrm{d,c},i}\, s + k_{\mathrm{d,c},i}) I_{ij}\right] \hat{g}_j = \hat{f}^{\delta}_{\mathrm{c},i}. \tag{4.26}$$

The discretised Dirac delta function is a vector with a single non-zero entry at $x = \xi$, and its expression is given as follows:

$$\hat{\mathbf{f}}^{\delta} = \left[0, 0, \ldots, \frac{1}{\Delta x}, \ldots, 0, 0\right]^{\mathrm{T}}. \tag{4.27}$$

It must be noted that Eq. (4.26) has to be solved individually for each position of the impulse $\xi \in [0, L]$. Consequently, the Green's functions are stored in a matrix $\hat{g}_{ij}$ where i indicates the discretized excitation variable ξ_i and j the discretized observation variable x_j. In addition, the length of the discrete element at the boundaries is $\Delta x/2$, which has to be accounted for in Eq. (4.27) when $\xi_i = 0$ or $\xi_i = L$.

Special attention should be given to the numerical evaluation of the inverse Laplace transform of the Green's functions. Firstly, in order to evaluate the Green's functions at $x_j = v\,t_j$ and $\xi_i = v\tau_i$ (required in Eq. (4.21)), the sampling requirements $\Delta x = v\,\Delta t$ and $\Delta\xi = v\,\Delta\tau$ need to be satisfied. Furthermore, depending on the required maximum frequency of integration $\omega_{\max}$, the time step can become very small leading to an unrealistically small spatial step. To fulfill the above-mentioned requirements, a spatial interpolation scheme is used for $\hat{g}_{ij}$. Secondly, for the total response w_{c} to instantaneously reach the steady state at $t = 0$, the Green's functions must satisfy trivial initial conditions at $t = \tau$, especially close to $t = 0$. To this end, the causal character of the response is employed and the *imaginary-part approach* is selected since it automatically satisfies the trivial initial conditions even if the inverse Laplace integral is truncated. Consequently, the time-domain Green's functions are computed as

$$g_{ij} = -\frac{2\, e^{\sigma(t_j-\tau_i)}}{\pi} \int_0^{\omega_{\max}} \mathrm{Im}(\hat{g}_{ij}) \sin\big(\omega(t_j-\tau_i)\big)\mathrm{d}\omega, \qquad i = 1,\ldots,j;\ j = 1,\ldots,n. \tag{4.28}$$

At this point, the only unknowns are the boundary conditions of the computational domain. Upon application of the finite difference scheme, the boundary conditions are incorporated in the stiffness matrix of the beam $\hat{K}_{ij}$ and in the boundary-forcing vectors $\hat{f}^{\mathrm{B}}_{\mathrm{c},i}$ and $\hat{f}^{\mathrm{L}}_{\mathrm{c},i}$. The non-reflective boundary conditions are determined in the next sub-section.

4.2.3. Non-reflective boundary conditions

The procedure in this sub-section is based on the formulation described thoroughly in [77], and is summarized in the following. As boundary conditions for the computational domain, the reaction forces of the semi-infinite domains at the interfaces with the computational domain are imposed. The goal is to express the interface reaction forces (bending moment and shear force) of the left and right domains as functions of the unknown displacement and slope of the computational domain at the corresponding interfaces. To this end, the forward Laplace transform is applied over time to the equations of motion of the two semi-infinite domains, (Eq. (4.1) for $x \in (-\infty, 0]$ and $x \in [L, \infty)$), leading to

$$\hat{w}_{\mathrm{l}}'''' - k_{\mathrm{l}}^4\, \hat{w}_{\mathrm{l}} = \tfrac{1}{EI}\hat{f}_{\mathrm{l}}^{\mathrm{IC}}, \qquad \hat{w}_{\mathrm{r}}'''' - k_{\mathrm{r}}^4\, \hat{w}_{\mathrm{r}} = \tfrac{1}{EI}\hat{f}_{\mathrm{r}}^{\mathrm{ML}}, \tag{4.29}$$

where $\hat{w}_{\mathrm{l}}$ and $\hat{w}_{\mathrm{r}}$ represent the unknown Laplace-domain displacements of the left and right domains, respectively; k_{l} and k_{r} represent the wavenumbers of the two semi-infinite domains and read

$$k_h = \sqrt[4]{-\overline{\rho} s^2 - \overline{c}_{\mathrm{d},h} s - \overline{k}_{\mathrm{d},h}}, \qquad h = \{\mathrm{l}, \mathrm{r}\}, \tag{4.30}$$

where the overline denotes that the quantity has been scaled by EI. The branches of the complex-valued wavenumbers are chosen such that $\mathrm{Im}(k_h) < 0$ and $\mathrm{Re}(k_h) > 0$. Furthermore, $\hat{f}_{\mathrm{l}}^{\mathrm{IC}}$ and $\hat{f}_{\mathrm{r}}^{\mathrm{ML}}$ represent the Laplace-domain initial-conditions forcing of the left domain and the Laplace-domain moving-load forcing acting on the right domain, respectively, and their expressions are the same as Eqs. (4.14) and (4.15), but with F_0 instead of $F_{\mathrm{c}}\left(\frac{x}{v}\right)$ and with the initial conditions of the left domain (Eq. (4.9)) instead of those of the computational domain. As for the boundary conditions, the zero-displacements condition (the Laplace-domain counterpart of Eq. (4.8)) is imposed at infinity, while the unknown Laplace-domain displacement and slope of the computational domain (the Laplace-domain counterparts of Eqs. (4.4) and (4.5)) are prescribed at the interfaces.

The Laplace-domain displacements $\hat{w}_{\mathrm{l}}$ and $\hat{w}_{\mathrm{r}}$ can be obtained analytically by solving Eq. (4.29) with the above-discussed boundary conditions. The interface reaction forces of the two semi-infinite domains are then expressed as functions of the prescribed displacements and slopes, and they read

$$\begin{pmatrix} \hat{w}_{\mathrm{l}}'''(0,s) \\ \hat{w}_{\mathrm{l}}''(0,s) \end{pmatrix} = \begin{pmatrix} \hat{k}_{\mathrm{l,V\upsilon}} & \hat{k}_{\mathrm{l,V\phi}} \\ \hat{k}_{\mathrm{l,M\upsilon}} & \hat{k}_{\mathrm{l,M\phi}} \end{pmatrix} \begin{pmatrix} \hat{w}(0,s) \\ \hat{w}'(0,s) \end{pmatrix} - \hat{\mathbf{b}}_{\mathrm{l}}^{\mathrm{IC}}, \tag{4.31}$$

$$\begin{pmatrix} \hat{w}_{\mathrm{r}}'''(L,s) \\ \hat{w}_{\mathrm{r}}''(L,s) \end{pmatrix} = \begin{pmatrix} \hat{k}_{\mathrm{r,V\upsilon}} & \hat{k}_{\mathrm{r,V\phi}} \\ \hat{k}_{\mathrm{r,M\upsilon}} & \hat{k}_{\mathrm{r,M\phi}} \end{pmatrix} \begin{pmatrix} \hat{w}(L,s) \\ \hat{w}'(L,s) \end{pmatrix} - \hat{\mathbf{b}}_{\mathrm{r}}^{\mathrm{ML}}, \tag{4.32}$$

where the entries of the matrices represent the dynamic stiffness coefficients associated with boundary forces proportional to the unknown displacement and slope at the interfaces; subscript V stands for shear force, M for bending moment, υ for translation, and ϕ for rotation. The dynamic stiffness coefficients read

$$\hat{k}_{h,\mathrm{V}\upsilon} = (-1+\mathrm{i})\,k_h^3, \qquad \hat{k}_{h,\mathrm{V}\phi} = \mathrm{i}k_h^2, \tag{4.33}$$

$$\hat{k}_{h,\mathrm{M}\phi} = (1+\mathrm{i})\,k_h, \qquad \hat{k}_{h,\mathrm{M}\upsilon} = \mathrm{i}k_h^2, \quad h = \{\mathrm{l},\mathrm{r}\}. \tag{4.34}$$

In addition, vector $\hat{\mathbf{b}}_{\mathrm{l}}^{\mathrm{IC}}$ incorporates the influence of the initial conditions on the reaction forces, giving rise to boundary forces independent of the unknown displacement and slope of the computational domain, which are accounted for in Eq. (4.24) through $\hat{f}_{\mathrm{c},i}^{\mathrm{B}}$. Due to the fact that in Section 4.2.1 the response $\hat{w}_{\mathrm{c}}^{\mathrm{IC}}$ caused by the initial conditions (Eq. (4.24)) and the response $\hat{w}_{\mathrm{c}}^{\mathrm{ML}}$ caused by the moving oscillator are treated separately, vector $\hat{\mathbf{b}}_{\mathrm{l}}^{\mathrm{IC}}$ is only incorporated in the boundary condition for the determination of the response caused by the initial conditions. The vector is given by the following expression:

$$\hat{\mathbf{b}}_{\mathrm{l}}^{\mathrm{IC}} = \begin{pmatrix} \hat{w}'''_{\mathrm{l,p}}(0,s) \\ \hat{w}''_{\mathrm{l,p}}(0,s) \end{pmatrix} + \begin{pmatrix} \hat{k}_{\mathrm{l,V}\upsilon} & \hat{k}_{\mathrm{l,V}\phi} \\ \hat{k}_{\mathrm{l,M}\upsilon} & \hat{k}_{\mathrm{l,M}\phi} \end{pmatrix} \begin{pmatrix} \hat{w}_{\mathrm{l,p}}(0,s) \\ \hat{w}'_{\mathrm{l,p}}(0,s) \end{pmatrix}, \tag{4.35}$$

where $\hat{w}_{\mathrm{l,p}}(0,s)$ is the particular solution that accounts for $\hat{f}_{\mathrm{l}}^{\mathrm{IC}}$ in Eq. (4.29). It can be obtained as follows:

$$\hat{w}_{\mathrm{l,p}}(0,s) = \int_{-\infty}^{0} \hat{g}_{\mathrm{l}}(x-\xi,s)\Big|_{x=0} \hat{f}_{\mathrm{l}}^{\mathrm{IC}}(\xi,s)\,\mathrm{d}\xi, \tag{4.36}$$

where $\hat{g}_{\mathrm{l}}$ is the Laplace-domain Green's function of a homogeneous and infinite beam-foundation system with the properties of the left domain, and its expression is given by Eq. (6.38). The integral in Eq. (4.36) can be computed analytically, but the solution is not presented here for brevity.

Similar to $\hat{\mathbf{b}}_{\mathrm{l}}^{\mathrm{IC}}$, vector $\hat{\mathbf{b}}_{\mathrm{r}}^{\mathrm{ML}}$ contains the contribution of the moving load to the reaction forces at the right boundary, and reads

$$\hat{\mathbf{b}}_{\mathrm{r}}^{\mathrm{ML}} = \begin{pmatrix} \hat{V}^{\mathrm{L}}(s) \\ \hat{M}^{\mathrm{L}}(s) \end{pmatrix}, \tag{4.37}$$

where $\hat{V}^{\mathrm{L}}$ and $\hat{M}^{\mathrm{L}}$ are the shear force and bending moment, respectively, exerted by the moving oscillator on the right boundary after it has entered the right semi-infinite domain, and their expressions read

$$\hat{V}^{\mathrm{L}}(s) = \frac{\mathrm{i}F_0\left(s+(1+\mathrm{i})\,k_{\mathrm{r}}v\right)}{(k_{\mathrm{r}}v+s)(k_{\mathrm{r}}v-\mathrm{i}s)}\,\mathrm{e}^{-s\frac{L}{v}}, \qquad \hat{M}^{\mathrm{L}}(s) = \frac{-\mathrm{i}F_0 v}{(k_{\mathrm{r}}v+s)(k_{\mathrm{r}}v-\mathrm{i}s)}\,\mathrm{e}^{-s\frac{L}{v}}. \tag{4.38}$$

It must be noted that Eq. (4.38) is correct only if the oscillations of the vehicle have stopped before reaching $x = L$ (as assumed in Section 4.1 and explained in Section 4.2.1), such that the contact force is again constant and equal to F_0; this represents the criterion for choosing L. Also, Eq. (4.38) is used in the boundary conditions only for determining the displacement $\hat{w}_{\mathrm{c}}^{\mathrm{L}}$ generated by the oscillator continuing its movement in the right domain, and not for determining $\hat{w}_{\mathrm{c}}^{\mathrm{IC}}$, nor for determining $\hat{g}$. It must also be mentioned that for the results presented in Section 4.3, Eq. (4.38) is not used because the simulations are performed only until the moving oscillator reaches the right boundary. However, according to the problem statement in Section 4.1, if a certain analysis is concerned with the response of the computational domain after the moving oscillator has entered the right domain (i.e., free vibration), Eq. (4.38) must be incorporated. Moreover, the presented solution method can handle unstable vibrations of the oscillator onset by the inhomogeneity (e.g., breaking the wave-velocity barrier when going from the stiff domain to the soft one). However, for such a scenario, the maximum time of the simulation is limited to the moment the load reaches the right boundary of the computational domain because Eq. (4.38) is only valid for a constant contact force.

Eqs. (4.31) and (4.32) represent the non-reflective boundary conditions which are prescribed to the computational domain through the Laplace-domain image of Eqs. (4.6) and (4.7). The term $\hat{\mathbf{b}}_{\mathrm{l}}^{\mathrm{IC}}$ is accounted for through the boundary-forcing vector $\hat{f}_{\mathrm{c},i}^{\mathrm{B}}$ while $\hat{V}^{\mathrm{L}}$ and $\hat{M}^{\mathrm{L}}$ are accounted for through the boundary-forcing vector $\hat{f}_{\mathrm{c},i}^{\mathrm{L}}$, because they are not proportional to the unknown displacement and are thus considered as external forces. The remaining parts of Eqs. (4.31) and (4.32) are accounted for in the beam's stiffness matrix $\hat{K}_{ij}$. The application of these boundary conditions ensures that the behaviour of the finite computational domain is not influenced by artificial boundaries and that the infinite extent of the model is respected in an exact manner.

4.3. Results and discussion

In this section, the proposed solution is firstly validated by considering two limit cases and comparing the obtained results to a benchmark solution. Then, the time-domain response of the wheel and of the rail under the wheel are presented for two specific cases, and the influence of the oscillator on the response at the contact point is highlighted. Subsequently, the influence of the oscillator on the power input into the beam-foundation system is discussed. From these results, two indicators of potential damage caused to the supporting structure are identified, namely the maximum contact force and the energy/power input. Finally, the influence of the transition length, oscillator velocity, and stiffness ratio on the two indicators is assessed through a parametric study.

To investigate the influence of the transition length l_{t} on the maximum contact force and the energy/power input, the spatial profile of the foundation stiffness is chosen based

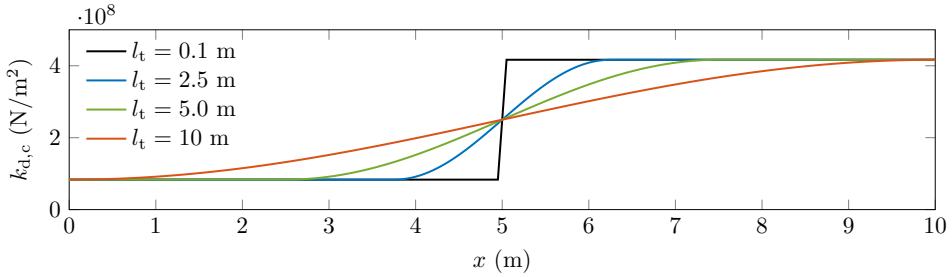

Figure 4.2: The spatial profile of the foundation stiffness given by Eq. (4.39) for different transition lengths l_t; the centre of the transition $x_{tc} = 5$ m and the stiffness ratio $p = 5$.

on a sine squared (depicted in Fig. 4.2) as follows:

$$k_{d,c}(x) = \begin{cases} k_{d,l}, & 0 \le x < x_{tc} - \frac{l_t}{2}, \\ k_{d,l}\left(1 + \sin\left[\left(\frac{x - x_{tc}}{l_t} + \frac{1}{2}\right)\frac{\pi}{2}\right]^2 (p-1)\right), & x_{tc} - \frac{l_t}{2} \le x \le x_{tc} + \frac{l_t}{2}, \\ k_{d,r}, & x_{tc} + \frac{l_t}{2} < x \le L, \end{cases} \tag{4.39}$$

where x_{tc} represents the location of the centre of the transition and p is the stiffness ratio between the stiff and soft domains. The location of the transition zone inside the computational domain is dictated by the spatial extent of the initial conditions, as discussed in Section 4.1, while the value of L is chosen such that the oscillations of the moving mass have stopped before it reaches the position $x = L$, as discussed in Section 4.2.3. In addition, the spatial variation of the foundation damping is chosen such that the damping ratio ζ, defined similarly to that of a single-degree-of-freedom system, is kept constant. The relation between the damping coefficient and damping ratio is given in Eq. (2.27).

4.3.1. Parameter values

The choice of two parameters, namely the stiffness ratio p and the velocity v of the oscillator, requires special attention. In this work, the stiffness ratio $p = \frac{k_{d,stiff}}{k_{d,soft}}$ is the stiffness ratio between the stiff and soft domains of the supporting structure (i.e., not including the beam's stiffness). This is different from the ratio q of the vertical stiffness of the track (including the beam's stiffness), which is the difference in stiffness experienced by the vehicle. The two are related (in static or quasi-static conditions) through the following expression [78]:

$$q \approx p^{\frac{3}{4}}. \tag{4.40}$$

Several researchers have measured the vertical track stiffness in areas with soft soils and have reported differences in the vertical track stiffness at transition zones between $q \approx 1.5$–3 [4, 15, 79, 80], which corresponds to $p \approx 1.5$–4.5. For most of the results in the remainder of the

chapter, $p = 5$ is chosen. Although the chosen value is on the high end, it is not unrealistically high. The value was chosen to accentuate the transition radiation mechanisms such that they are easier to identify. In Section 4.3.3, $p = 10$ (i.e., $q = 5.6$) is chosen to illustrate the wheel-rail separation. Moreover, in Section 4.3.5, $p = 1{-}20$ (i.e., $q = 1{-}9.5$); although above $p = 5$ the values are less realistic (or even not at all realistic close to $p = 20$), they are presented in order to observe the overall trend.

The maximum design velocity of trains in areas with soft soils is around 60–70% of the minimum critical velocity in the track. However, in extreme cases, trains have even exceeded the critical velocity (e.g., the Swedish X-2000 high-speed train which runs along the West Coast Line between Gothenburg and Malmö [33]). In this chapter, for Sections 4.3.3 and 4.3.4, the oscillator velocity is chosen as 90–95% of c_{cr}; although these velocities are high for regular train operation, they are chosen to once more accentuate the transition radiation mechanisms such that they are easier to identify. It must be emphasized that the identified mechanisms are present also for lower velocities, but they are just harder to observe. For Section 4.3.5, the oscillator velocity is varied between 13–110% of c_{cr}. Again, although super-critical velocities are rarely observed in practice, the wide range of velocities is given to analyse the overall trend in behaviour.

The parameters which are kept constant throughout the presented results are given in Table 4.1. The bending stiffness corresponds to the UIC 60 rail and the mass per unit length includes the rail mass per meter and the contribution of the (concrete) sleepers uniformly distributed along the rail [53], such that the model captures the track response at low frequencies (including its first natural frequency).

Table 4.1: Values of the system parameters.

Parameter	Symbol	Value	Unit
Bending stiffness	EI	$6.42{\cdot}10^{6}$	Nm^2
Mass per unit length	ρ	268.33	kg/m
Dead weight	F_0	$80 \cdot 10^{3}$	N
Foundation stiffness	$k_{\text{d,l}}$	$83.33{\cdot}10^{6}$	N/m^2
Foundation damping ratio	ζ	0.25	
Wheel mass	M	750	kg
Hertz's constant	C_{H}	$1.1864{\cdot}10^{11}$	$\text{N/m}^{3/2}$

4.3.2. Verification and convergence

To verify the solution derived in Section 4.1, two limit cases are considered and are compared to a benchmark solution. Firstly, to validate the Green's functions of the beam-foundation structure and the suppression of initial transients through the applied initial conditions, the limit case of a moving constant load is considered, where the magnitude of the load is equal to F_0. In this limit case, the degree of freedom of the mass and the contact equation

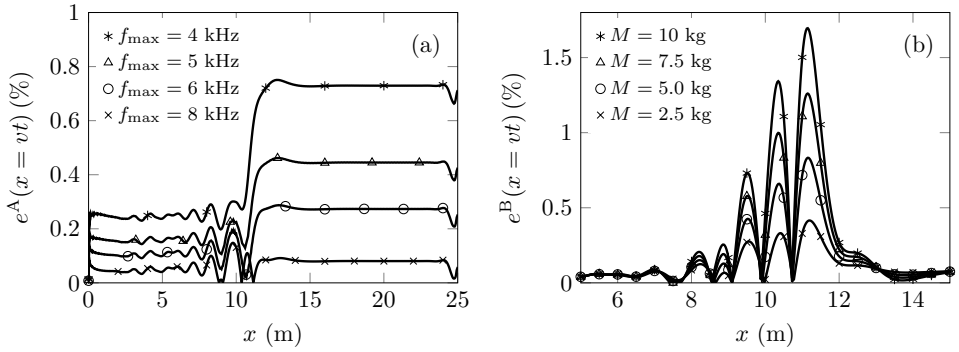

Figure 4.3: Error under the moving load for different maximum frequencies (panel (a)) and for different values of the wheel's mass (right panel); the abrupt transition is at $x_{\mathrm{tc}} = 10\,\mathrm{m}$, $v = 0.95\,c_{\mathrm{cr,l}}$, and $p = 5$; $f_{\max} = 8$ kHz (panel (b)).

vanish, while the time-domain displacement of the beam (Eq. (4.18)) simplifies to

$$w^{\mathrm{A}}_{\mathrm{lim}}(vt, t) = F_0 \int_0^t g(vt, v\tau, t-\tau)\,\mathrm{d}\tau + w^{\mathrm{IC}}_{\mathrm{c}}(vt, t). \tag{4.41}$$

Secondly, to incorporate the iterative scheme of solving the contact equation in the verification, the same limit case is considered (moving constant load) by taking the limit of the wheel's mass going to zero. However, the wheel's mass cannot be set to zero because it leads to a singularity in the expression of the wheel's displacement, as can be seen in Eq. (4.20). Therefore, the wheel's mass is gradually decreased to study the convergence of the second limit-case solution $w^{\mathrm{B}}_{\mathrm{lim}}$ as the mass goes to zero. The foundation is considered as piecewise homogeneous for both cases (i.e., $l_{\mathrm{t}} = \Delta x$). Both limit-case responses $w^{\mathrm{A}}_{\mathrm{lim}}$ and $w^{\mathrm{B}}_{\mathrm{lim}}$ are compared to the semi-analytical transient solution derived in Section 2.3.

The errors e^{A} and e^{B} presented in Fig. 4.3, corresponding to the first and second limit cases, respectively, are defined as follows:

$$e^{h}(x = vt) = \frac{|w_{\mathrm{bench}}(x = vt, t) - w^{h}_{\mathrm{lim}}(x = vt, t)|}{|w_{\mathrm{bench}}(x = vt, t)|}, \quad h = \{\mathrm{A}, \mathrm{B}\}, \tag{4.42}$$

where w_{bench} is the benchmark solution given by the inverse Fourier transform of Eq. (2.26). To study the convergence of the presented solution, the truncation frequency for the inverse Laplace transform in the first limit case is varied, while a constant truncation frequency of $f_{\max} = 16$ kHz is used for the benchmark solution. Note that by changing the maximum frequency in the limit case, according to the Nyquist sampling rule, the time stepping also changes.

Panel (a) of Fig. 4.3 shows that the first limit-case solution converges to the semi-analytical one as the maximum frequency is increased. The error in the soft domain is

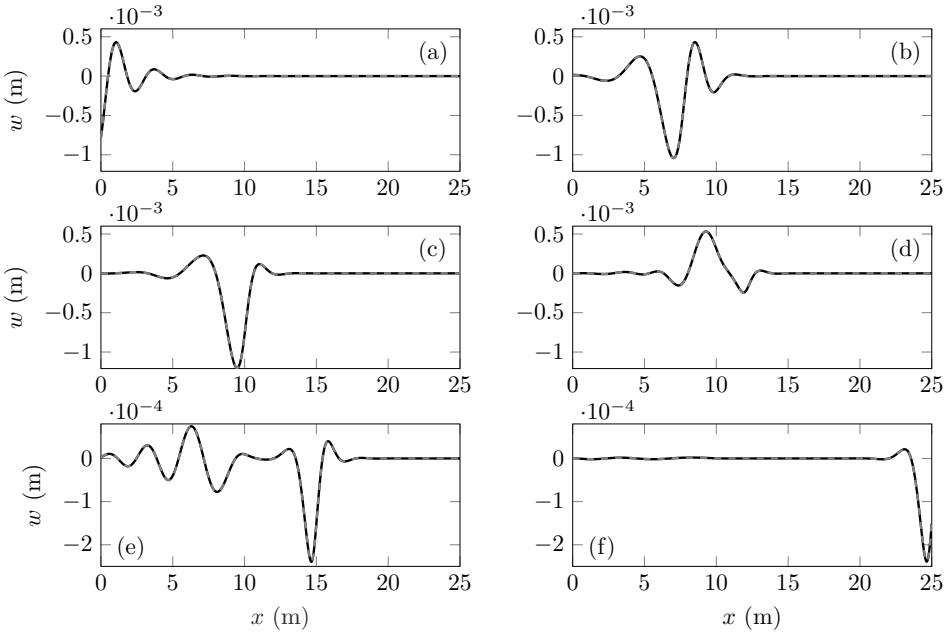

Figure 4.4: The displacement field for the moving constant load obtained in the limit case A (black-continuous line) and with the semi-analytical approach (grey-dashed line) for different time moments: (a) $t = 0$ s, (b) $t = 0.0187$ s, (c) $t = 0.0246$ s, (d) $t = 0.0299$ s, (e) $t = 0.0368$ s, (f) $t = 0.0618$ s; the abrupt transition is at $x_{\text{tc}} = 10$ m, $v = 0.95\, c_{\text{cr,l}}$, and $p = 5$; $f_{\text{max}} = 8$ kHz.

smaller than the one in the stiff domain because the higher foundation stiffness leads to smaller displacements and, thus, to a higher relative error. The error e^{A} is mainly caused by two factors, namely the truncation (in frequency) of the inverse Laplace integral (Eq. (4.28)) and the spatial discretization introduced by the finite difference method. Also, to satisfy $\Delta x = v\Delta t$ (discussed in Section 4.2.2), the spatial step size Δx can become unrealistically small depending on the time step Δt. To this end, a spatial step size which leads to accurate results is chosen ($\Delta x = 0.05$ m), and to satisfy $\Delta x = v\Delta t$ an interpolation scheme is used. However, the error caused by the interpolation scheme is negligible. It can be observed in Fig. 4.3 that for truncation frequency $f_{\text{max}} = 8$ kHz, the error is less than 0.5%, which is more than satisfactory. A higher maximum frequency leads to smaller error; however, the computational effort increases significantly. For all other results presented in this section, the maximum frequency was therefore chosen as 8 kHz. anything about the error in the cases studied further, where the inertia of the wheel is significant.

In panel (b) of Fig. 4.3, the second limit-case solution $w^{\text{B}}_{\text{lim}}$ is observed to converge to the benchmark solution for the wheel's mass tending to zero. Moreover, the errors in the steady-state regimes are the same for all mass values and are equal to the errors in the first limit case e^{A}. This suggests that the error introduced by iterative solver is negligible. It must

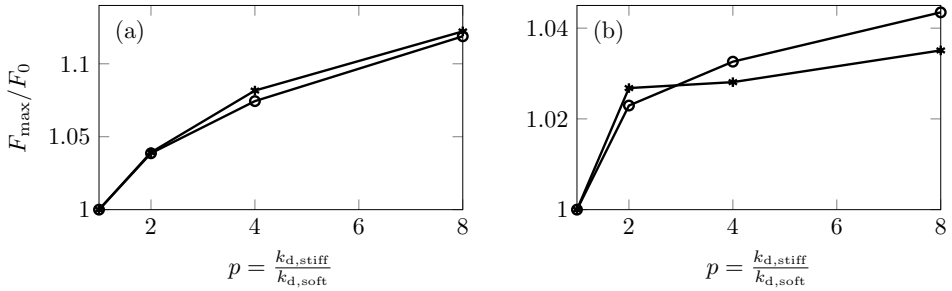

Figure 4.5: The normalized maximum contact force obtained with the loaded one-mass oscillator (asterisks) compared to the results obtained by Ang and Dai [35] with the three-mass oscillator (circles) for $v = 90$ m/s (panel (a)) and $v = 70$ m/s (panel(b)); the parameters used are the ones from Ang and Dai [35].

be noted that error e^{B} in the area of the transition zone is mainly due to the incapability of considering the true limit case ($M = 0$), and does not imply

To verify the response throughout the domain and not just at the contact point, the full displacement field in the limit case A (i.e., Eq. (4.41), but not limited to $x = vt$) is presented for different time moments in Fig. 4.4, and is compared to the benchmark solution $w_{\mathrm{bench}}(x, t)$. It can be seen from Fig. 4.4 that the results agree very well from the fact that the two lines are indistinguishable. In panel (a) it can be seen that the initial transients have been successfully suppressed through the implementation of the correct initial conditions (i.e., the response is in the steady-state regime); here it can also be clearly observed why the initial conditions based on the eigenfield must decay before reaching the inhomogeneity ($x_{\mathrm{tc}} = 10$ m in this case). Moreover, in panel (e), the fact that the two solutions agree very well demonstrates that all waves generated inside the computational domain propagate away from the transition with no reflection at the boundaries. Also, in panel (f) it can be seen that the eigenfield passes to the right domain without any disturbance. Therefore, it can be concluded that the solution derived in Section 4.1 is correct.

Finally, a validation of the vehicle model employed in this chapter is presented in Fig 4.5. More specifically, the suitability of the loaded one-mass oscillator for studying the wheel-rail interaction is investigated. The normalized maximum contact force obtained with the loaded one-mass oscillator is compared to the one obtained with a more comprehensive vehicle model, namely the three-mass oscillator used by Ang and Dai [35]. For the higher velocity (panel (a)), the results agree very well, while for the lower velocity (panel (b)), the results present some differences, but not major ones. This can be explained by the fact that the lower the velocity, the lower the frequencies of interaction, which leads to the sprung masses having a more significant influence. Overall, the results agree well rendering the loaded one-mass oscillator suitable for studying wheel-rail interaction at transition zones. Nonetheless, it must be noted that a vehicle model with multiple contact points can influence the results more significantly. Also, for large transition lengths, the inertia of the suspended masses may have a more pronounced influence due to the low frequencies of interaction.

4.3.3. Time-domain responses

To study the interaction between the moving oscillator and the beam-foundation structure, the displacement of the mass and that of the beam at the contact point, as well as the contact force are presented in Fig. 4.6. Two specific cases are considered: the oscillator moving from the soft domain to the stiff one and that moving from the stiff domain to the soft one. For both scenarios, the velocity is chosen as 90% of the critical velocity in the soft domain ($c_{\mathrm{cr,l}}$ for the soft-to-stiff case and $c_{\mathrm{cr,r}}$ for the stiff-to-soft case), and the transition length l_{t} is chosen as 0.1 m, which is close to the piecewise-homogeneous case. To ensure that the initial displacement and velocity fields do not interact with the inhomogeneity, the centre of the transition zone x_{tc} is positioned at $x = 19$ m for the soft-to-stiff case and at $x = 11$ m for the stiff-to-soft case. It is clear from Fig. 4.6 that the response reaches the steady state instantaneously as the oscillator enters the computational domain and thus, that the initial transients have been suppressed. Note that this initial plateau is only depicted in Fig. 4.6 to demonstrate that the initial transients have been suppressed, and is omitted in the following figures since it does not provide any information about the interaction.

In the soft-to-stiff case (left panels in Fig. 4.6), the displacement of both the mass and the beam (at the contact point) exhibit significant oscillations (panel (a) in Fig. 4.6). The oscillations are caused by the interaction of the moving oscillator with the inhomogeneous elastic structure, where three mechanisms play a role:

1. Bending waves are excited as the load approaches and passes the transition due to the eigenfield interacting with the inhomogeneity (i.e., transition radiation phenomenon).

2. A vibration of the mass (i.e., variation of the vertical momentum) induced by bending waves that kinematically excite the moving oscillator at the contact point.

3. A vibration of the mass induced by a parametric variation of the system properties as experienced by the moving oscillator (i.e., varying foundation stiffness).

The three mechanisms described above are coupled as follows. The first and second mechanisms are completely interdependent; stronger wave radiation introduces stronger oscillations at the contact point, leading to a stronger vibration of the mass, which in turn influences the wave radiation. In addition, although stronger vibration of the mass leads to stronger wave radiation, implying that the third mechanism influences the first one, stronger wave radiation does not lead to stronger parametric variation, meaning that the first mechanism does not influence the third one. Furthermore, the first mechanism is considered to be the primary one, as it also takes place in the case of a moving constant load (as observed in Chapter 2), while the second and third mechanism are characteristic of the moving oscillator.

The stronger radiation caused by the oscillation of the mass has a clear influence on the variation of the contact force (panel (c) in Fig. 4.6). In the considered case, the maximum

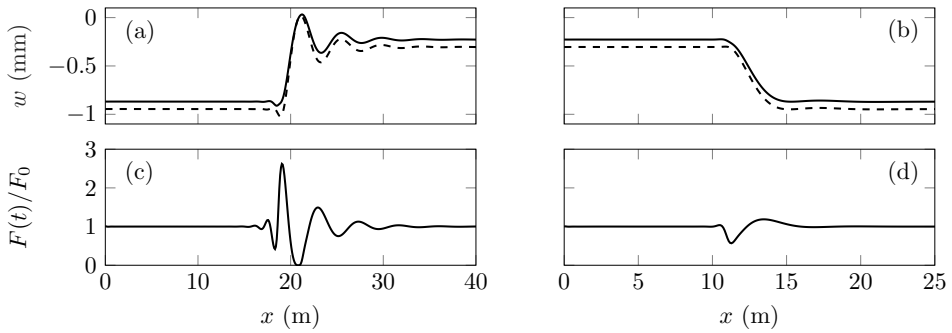

Figure 4.6: Displacement of the mass (dashed line) and of the beam at the contact point (solid line) (panels (a) and (b)), and the normalized contact force (panels (c) and (d)); $l_t = 0.1$ m, $x_{tc} = 19$ m and $v = 0.90\, c_{cr,l}$ for the soft-to-stiff case (left panels); $l_t = 0.1$ m, $x_{tc} = 11$ m and $v = 0.90\, c_{cr,r}$ for the stiff-to-soft case (right panels); $p = 5$.

contact force is almost three times larger than in the steady state. Moreover, the maximum peak in the contact force is followed by a decrease in contact force which in this case reaches the value of zero for a short time interval. This means that the wheel loses contact with the rail. The loss of contact between the wheel and the rail is discussed more thoroughly in Section 4.3.3. The large variation in the contact force could be one of the factors leading to degradation of the foundation in the vicinity of transition zones. Therefore, the maximum contact force is selected in Section 4.3.5 as an indicator of the damage in the supporting structure and thus of the performance of the transition zone.

In the stiff-to-soft case (right panels in Fig. 4.6), the displacement of both the mass and the beam (at the contact point) exhibit smaller oscillations compared to the soft-to-stiff case, which is in agreement with other findings in the literature [35, 77]. This can be explained based on the mechanism described previously:

a The smaller in amplitude and less broad eigenfield turns out to yield weaker bending-wave excitation at the inhomogeneity and the excited large-amplitude waves propagate into the soft domain (related to the first mechanism).

b Smaller oscillations at the contact point lead to smaller vibrations of the mass (related to the second mechanism), which in turn introduce weaker additional waves in the beam (related to the first mechanism).

c As the oscillator passes the transition, the displacement at the contact point increases due to lower foundation stiffness; however, the inertia of the mass keeps it (initially) at the same level. Consequently, in the stiff-to-soft case, the inertia force points upwards while the dead load points downwards, partially cancelling each other (related to the third mechanism).

The effect of items b) and c) are clearly visible in the lower variation of the contact force in the stiff-to-soft case (panel (d) in Fig. 4.6).

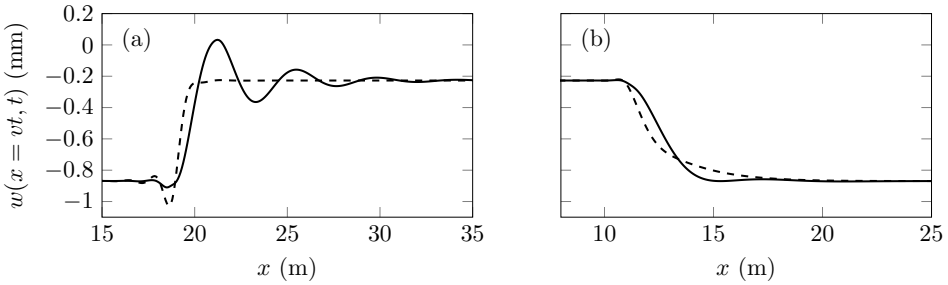

Figure 4.7: Beam displacement under the moving constant load (dashed line) and under the moving oscillator (solid line); $l_t = 0.1$ m, $x_{tc} = 19$ m and $v = 0.90\, c_{cr,l}$ for the soft-to-stiff case (panel (a)); $l_t = 0.1$ m, $x_{tc} = 11$ m and $v = 0.90\, c_{cr,r}$ for the stiff-to-soft case (panel (b)); $p = 5$.

It is important to note that the stiff-to-soft case analyzed in this chapter assumes that the system initially is in the steady state. In reality, the system reaches the steady state in the stiff domain (e.g., a bridge) only if it is long enough. For a short stiff domain embedded in a soft domain (e.g., a culvert [25]), the response might not reach the steady state, leading to different behaviour in the stiff-to-soft transition.

To highlight the influence of the moving oscillator on the vibrations at the contact point, the displacement of the beam at the contact point is compared to the displacement of the beam under a moving constant load in Fig. 4.7. The steady-state responses are the same in both cases (oscillator vs. constant load) because the vertical acceleration of mass is zero in this regime. The differences arise once the eigenfields start to interact with the inhomogeneity. In the soft-to-stiff case (panel (a) of Fig. 4.7), due to the decrease in contact force (panel (c) in Fig. 4.6), a smaller response amplification is observed at the contact point before the transition ($x \approx 18$ m). The contact force is lower because the free field destructively interferes with the eigenfield, thus unloading the contact between the wheel and the rail. In this case, accounting for the vehicle-structure interaction can have a beneficial influence on the response amplification at transition zones. However, once the moving vehicle has entered the stiff domain, significant vibrations are observed in the oscillator case. Moreover, the larger oscillations could lead to more significant rearrangements of the ballast particles, potentially leading to differential settlements. In the stiff-to-soft case, the difference between the moving oscillator and the moving constant load is significantly smaller. This could have been anticipated from the smaller variation in the contact force presented in panel (d) of Fig. 4.6.

Loss of contact between the wheel and the rail

For certain values of the oscillator velocity, stiffness ratio and transition length, the wheel can loose contact with the rail. This has been identified in studies of transition radiation [e.g., 35], of oscillators interacting with bridges [e.g., 81], and in studies of stability of moving vehicles [e.g., 74]. The loss of contact has been observed in the previous section

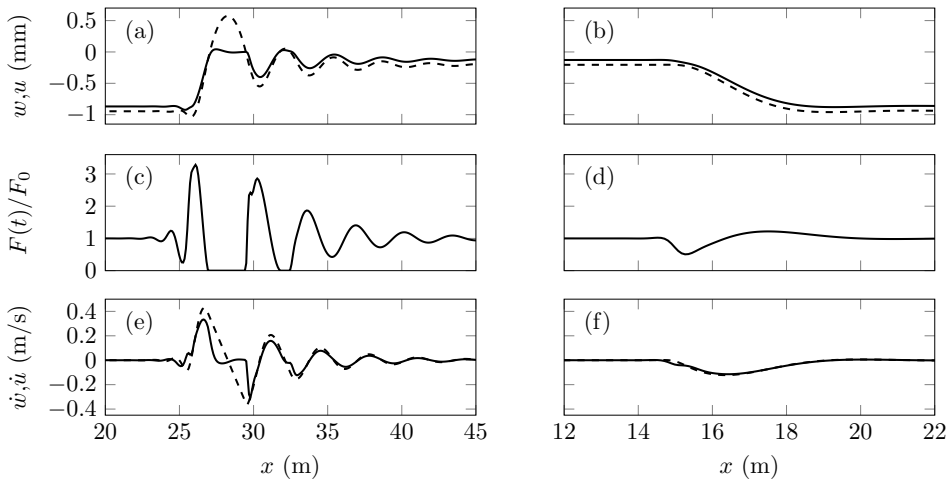

Figure 4.8: Displacement of the mass (dashed line) and of the beam at the contact point (solid line) (panels (a) and (b)), the normalized contact force (panels (c) and (d)), and the velocity of the mass (dashed line) and of the beam at the contact point (solid line) (panels (e) and (f)); $l_t = 0.1$ m, $x_{tc} = 26$ m and $v = 0.90\, c_{cr,l}$ for the soft-to-stiff case (left panels); $l_t = 0.1$ m, $x_{tc} = 15$ m and $v = 0.90\, c_{cr,r}$ for the stiff-to-soft case (right panels); p=10.

(soft-to-stiff transition in Fig. 4.6), but for a very short duration. To highlight it, the stiffness ratio is increased to $p = 10$ for the results presented in this section.

The left panels in Fig. 4.8 clearly present the loss of contact between the wheel and the rail, which occurs when the contact force (panel (c) in Fig. 4.8) is zero. In the considered case, there are even two loss-of-contact events. This can also be observed in the displacements (panel (a) in Fig. 4.8) and velocities (panel (e) in Fig. 4.8). When the displacement and velocity of the beam at the contact point have similar patterns as the displacement and velocity of the mass, respectively, there is contact between the two. Once the contact is lost, the behaviour of the beam and the mass become considerably different. This is due to the different forces acting on the two sub-systems when there is loss of contact; the beam is subject to the restoring forces of the foundation and of the bending resistance of the beam, while the mass is acted upon by the dead load F_0. The loss-of-contact and the impact after it lead to strong oscillations in the response and large variation in the contact force, potentially causing damage in the supporting structure and/or in the rail.

The right panels in Fig. 4.8 show that the loss of contact between the wheel and the rail does not occur in the stiff-to-soft case. This fact can be explained by the same reasoning as employed in the previous section. Although not all parameter combinations have been investigated, for the ones that have been, loss of contact was not observed in the stiff-to-soft scenario, showing that this is less likely to occur than in the soft-to-stiff scenario.

4.3.4. Energy considerations

In this section, the vehicle-structure interaction is studied from the energy point of view, which offers additional insight into the influence of the oscillator on the transition radiation and thus into the potential damage of the supporting structure. The energy emitted by the vehicle into the track that is dissipated in the ballast layer can be directly related to the damage in the supporting structure [23]. The higher the energy emitted (i.e., energy input) into the track, the stronger the degradation. Consequently, reducing the energy input represents an important aim for damage reduction in the supporting structure. The current model cannot be used to identify the amount of energy dissipated in the ballast layer. However, the proposed model can provide the energy input into the track, which can be an estimate of the energy dissipated in the ballast layer, and thus an indicator of potential damage in the supporting structure. To highlight the influence of the oscillator on the energy input, the oscillator is compared to the moving constant load.

The energy input per unit time (i.e., power input) provided by the moving oscillator $P^{\text{in}}_{\text{osc}}$ and by the moving constant load $P^{\text{in}}_{\text{const}}$ are given by the following expressions (equivalent to Eq. (2.31)):

$$P^{\text{in}}_{\text{osc}}(t) = F(t)\,\frac{\partial w}{\partial t}\Big|_{x=vt}, \qquad P^{\text{in}}_{\text{const}}(t) = F_0\,\frac{\partial w_0}{\partial t}\Big|_{x=vt}, \tag{4.43}$$

where w_0 is the displacement of the beam in the moving constant load case. The total energy spent by the moving oscillator and the moving constant load can be obtained by integrating the power inputs in Eq. (4.43) over the whole time domain. However, these integrals are not convergent due to the damping in the foundation, which requires continuous power input to maintain the constant velocity. For that reason, the differential power input between the moving oscillator and the moving constant load can be integrated instead (done below and in Section 4.3.5), to offer information about the difference in energy input.

In addition, one can look at the spectrum of the differential-power input, which gives insight into the frequency content of the additional energy exchange between the oscillator and the supporting structure. The spectrum $\Delta\tilde{P}^{\text{in}}$ can be computed by taking the forward Fourier transform of the differential-power input, as given in the following expression:

$$\Delta\tilde{P}^{\text{in}} = \int_{-\infty}^{\infty} \left(P^{\text{in}}_{\text{osc}} - P^{\text{in}}_{\text{const}}\right) \mathrm{e}^{-\mathrm{i}\omega t}\,\mathrm{d}t. \tag{4.44}$$

Note that $\Delta\tilde{P}^{\text{in}}$ is different to the power spectral density of the radiation presented in Section 2.4.

Fig. 4.9 presents the power input for the two vehicle models and the amplitude spectra of the differential-power input. Since the inertia of the mass is not activated in the steady-state regime, the power input is initially the same for the two vehicle models. When the eigenfields interact with the inhomogeneity, the power inputs fluctuate significantly before reaching the steady-state regime in the right domain. Overall, the power input in the soft-to-stiff case appears to be significantly amplified by the presence of the oscillator, thus showing that

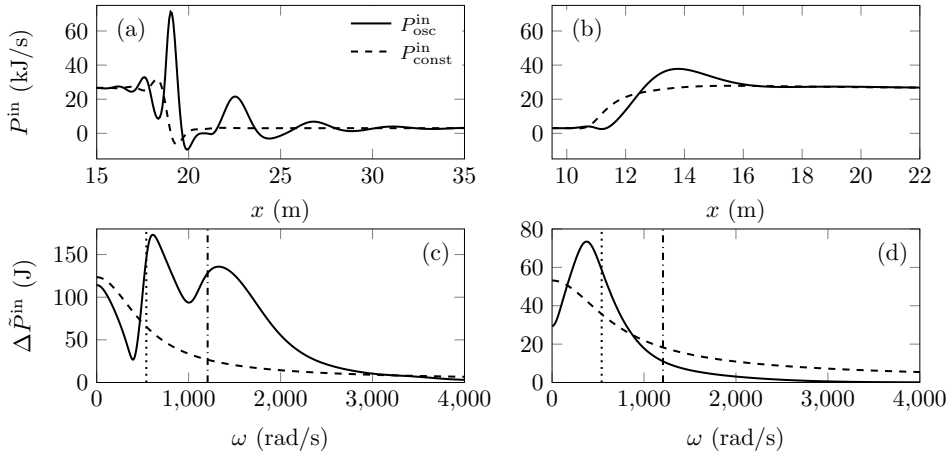

Figure 4.9: Power input (top panels) and amplitude spectrum of the differential-power input (bottom panels); the dashed line in the bottom panels represents the amplitude spectrum of the eigenfield's power flux in the left domain; the vertical lines in the bottom panels indicate the cut-off frequency of the soft domain (dotted line) and of the stiff domain (dash-dotted line); $l_{\text{t}} = 0.1$ m, $x_{\text{tc}} = 19$ m and $v = 0.90\, c_{\text{cr,l}}$ for the soft-to-stiff case (left panels); $l_{\text{t}} = 0.1$ m, $x_{\text{tc}} = 11$ m and $v = 0.90\, c_{\text{cr,r}}$ for the stiff-to-soft case (right panels); $p = 5$.

the presence of the oscillator can lead to stronger transition radiation. For the stiff-to-soft scenario, the influence of the oscillator is less drastic.

As can be seen from the amplitude spectra of the differential-power input (bottom panels of Fig. 4.9), a significant part of the additional energy exchange in the soft-to-stiff case is at frequencies larger than both cut-off frequencies (of the soft and stiff domains). For the stiff-to-soft scenario, the additional energy exchange lies in similar amounts below and above the cut-off frequency of the soft domain. To give a reference, the amplitude spectrum of the eigenfield's power flux in the left domain is included in the bottom panels of Fig. 4.9. It can be seen that for the soft-to-stiff case, the additional power exchange between the oscillator and the supporting structure is significantly larger than the spectrum of the eigenfield's power flux while for the stiff-to-soft case they are of similar magnitude.

4.3.5. Parametric study

In Sections 4.3.3 and 4.3.4, two indicators of potential damage caused to the supporting structure have been identified, namely the maximum contact force and the difference in energy input. In this section, these two indicators are addressed as functions of the oscillator velocity, the transition length and the stiffness ratio through a parametric study. The three parameters chosen to be varied are the most influential ones for the transition radiation phenomenon. Furthermore, these parameters can be adjusted in the design stage to minimize damage in the supporting structure. It must be noted that, while the maximum contact force offers insight into the magnitude of the transition radiation (as a whole),

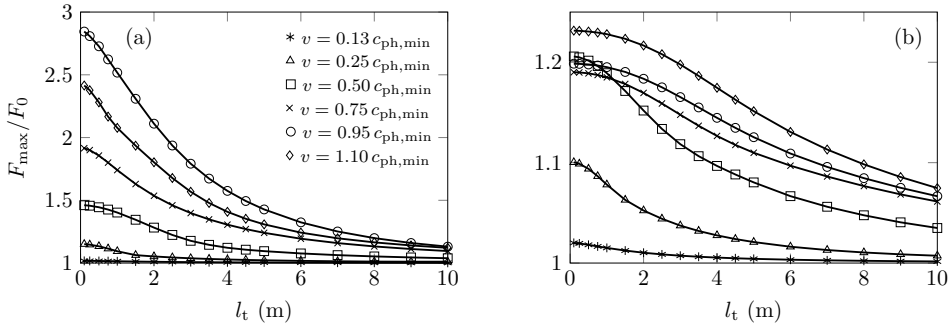

Figure 4.10: Maximum contact force normalized by the dead load versus transition length for different oscillator velocities; soft-to-stiff case (panel (a)) and stiff-to-soft case (panel (b)); in the legend, c_{cr} represents $c_{\mathrm{cr,l}}$ for the soft-to-stiff case and $c_{\mathrm{cr,r}}$ for the stiff-to-soft case; $p = 5$.

the difference in energy input provides information only into the *additional* effect of the vehicle-structure interaction on the transition radiation.

Variation of the transition length

Here, the transition length l_t is varied and the response for different oscillator velocities is investigated in terms of the maximum contact force $F_{\max}$ and in terms of the difference in energy input. It must be emphasized that in the present study the transition length refers to the zone over which the stiffness (and damping) of the supporting structure varies, and that the rail is considered completely straight (i.e., no differential settlements) when it is at rest, while in some other studies (e.g., Lei and Mao [13]) the transition length/angle refers to the zone where the rail exhibits some slope due to differential settlements.

Figure 4.10 presents the maximum contact force versus transition length for different oscillator velocities. In the soft-to-stiff case (panel (a) in Fig. 4.10) the maximum contact force decreases nonlinearly with increasing transition length for all velocities considered. The decrease is most significant for the velocities close to the critical velocity. However, even for operational speeds of conventional trains (e.g., $v = 0.5\, c_{\mathrm{cr}}$), the maximum contact force can be significantly minimized by choosing a transition length of 4–6 m. Increasing the transition length even more does not lead to a considerable improvement of the transition zone performance. In the stiff-to-soft case (panel (b) in Fig. 4.10), the maximum contact force decreases as well with increasing transition length, but much less pronounced than in the stiff-to-soft case. Nonetheless, for small transition lengths, the maximum contact force can be 20–25% larger than the steady-state one for relatively high velocities, and the maximum contact force can be reduced by 10–15% when increasing the transition length to 6–10 m.

Fig. 4.11 presents the difference in energy input between the moving oscillator and the moving constant load versus transition length for different velocities. A similar behaviour

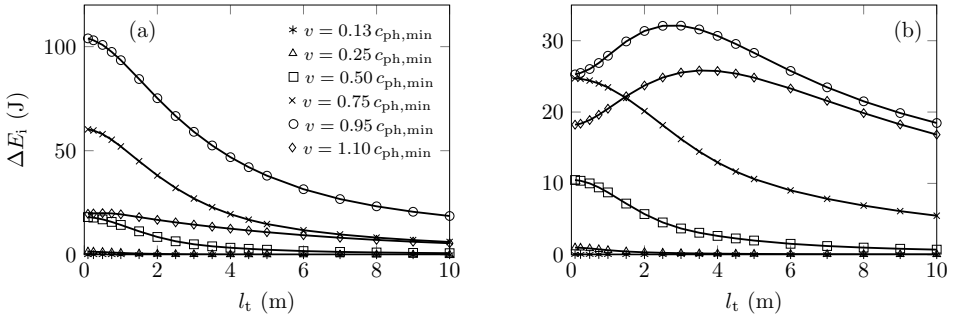

Figure 4.11: Difference in energy input versus transition length for different oscillator velocities; the soft-to-stiff case (panel (a)) and the stiff-to-soft case (panel (b)); in the legend, c_{cr} represents $c_{cr,l}$ for the soft-to-stiff case and $c_{cr,r}$ for the stiff-to-soft case; $p = 5$.

as for the maximum contact force is observed in the soft-to-stiff case (panel (a) in Fig. 4.11). The difference in the energy input decreases nonlinearly with increasing transition length and the decrease is drastic for relatively high velocities, about a factor 2–5 in going from $l_t = 0.1$ m to $l_t = 10$ m. For velocities up to $v = 0.75\,c_{cr}$, the behaviour in the stiff-to-soft case (panel (b) in Fig. 4.11) is similar to the soft-to-stiff case. However, for larger velocities (e.g., $v = 0.95\,c_{cr}$ and $v = 1.10\,c_{cr}$), the difference in the energy input exhibits a behaviour totally different from the soft-to-stiff case and from the maximum contact force. A peak in the difference of energy input is identified between $l_t = 2$ m and $l_t = 6$ m. This means that in this range, although most can be gained in terms of the maximum contact force decrease (see panel (b) of Fig. 4.10), the energy input increases compared to the constant load case. This could be one of the reasons why similar amount of damage is observed in front and behind a transition zone consisting of a soft-to-stiff transition directly followed by a stiff-to-soft one (for one-way tracks), where mitigation measures to create a gradual transition are employed (e.g., approach slabs). In the case of an approach slab of 2–4 m, there is a substantial decrease in the difference of energy input before the transition (compared to the abrupt case), while there is a substantial increase in the difference of energy input after the transition. This finding is not obvious from studying solely the observables such as contact force, displacements and velocities.

Variation of the velocity

In this section, the maximum contact force and the difference in energy input are presented as functions of the velocity of the moving oscillator. Three transition lengths are considered: $l_t = 0.1$ m, $l_t = 5$ m and $l_t = 10$ m. Fig. 4.12 presents the maximum contact force results. In the soft-to-stiff case (panel (a) in Fig. 4.12), the maximum contact force increases nonlinearly with the increasing velocity up to a value close to the critical velocity $c_{cr,l}$, and it decreases beyond that. For an abrupt transition, the increase of the maximum contact force is significant, but it reduces with increasing transition length. This is in accordance with

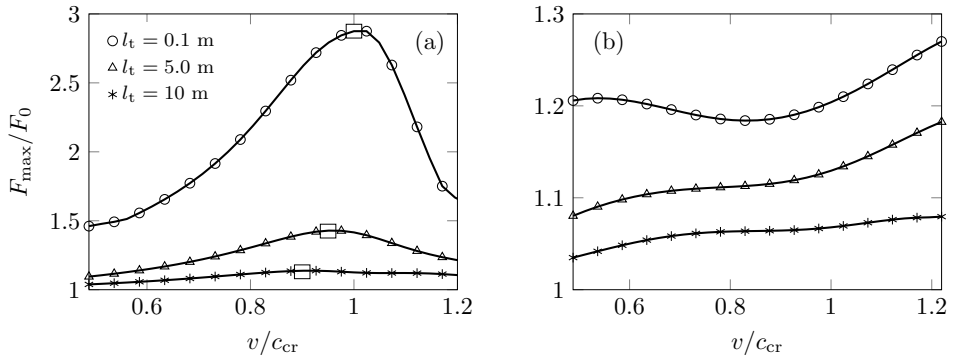

Figure 4.12: Maximum contact force normalized by the dead load versus velocity of the moving oscillator for different transition lengths; soft-to-stiff case (panel (a)) and stiff-to-soft case (panel (b)); the rectangles indicate the location of the maximum for each curve (panel (a)); $p = 5$.

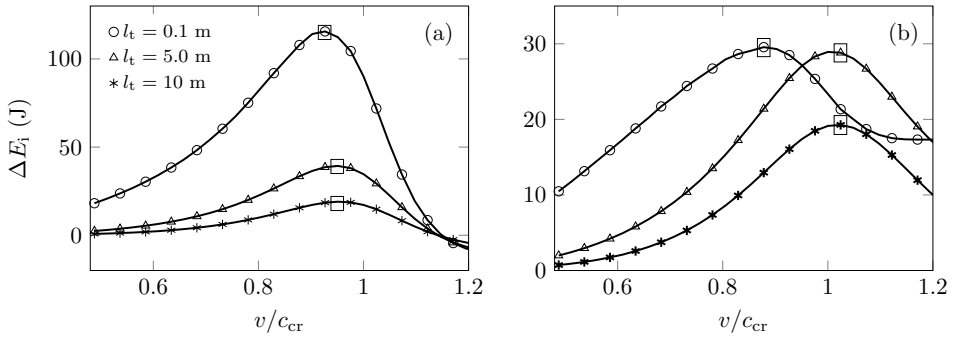

Figure 4.13: Difference in energy input between the moving oscillator and the constant moving load versus velocity for different transition lengths; soft-to-stiff case (panel (a)) and stiff-to-soft case (panel (b)); the rectangles indicate the location of the maximum for each curve; $p = 5$.

the findings in Section 4.3.5 (Fig. 4.10). Furthermore, the critical velocity for the maximum contact force (marked with rectangles in Fig. 4.12) is observed to decrease with increasing transition length. For $l_t = 0.1$ m the critical velocity is close to $c_{cr,l}$, while in the case of $l_t = 10$ m the critical velocity has decreased to $0.9\, c_{cr,l}$. A different behaviour is observed for the stiff-to-soft cases (panel (b) in Fig. 4.12). A local peak in the maximum contact force is observed at relatively low velocities, after which an almost linear increase is observed with increasing load velocity. The location of the local peak shifts to higher velocities for increasing transition length. Also, compared to the soft-to-stiff case, the change in maximum contact force with increasing load velocity is much smaller.

The difference in energy input for the soft-to-stiff case (panel (a) of Fig. 4.13) exhibits a similar behaviour to the one observed for the maximum contact force (panel (a) in Fig. 4.12). However, the critical velocity for the difference of energy input shifts much less with

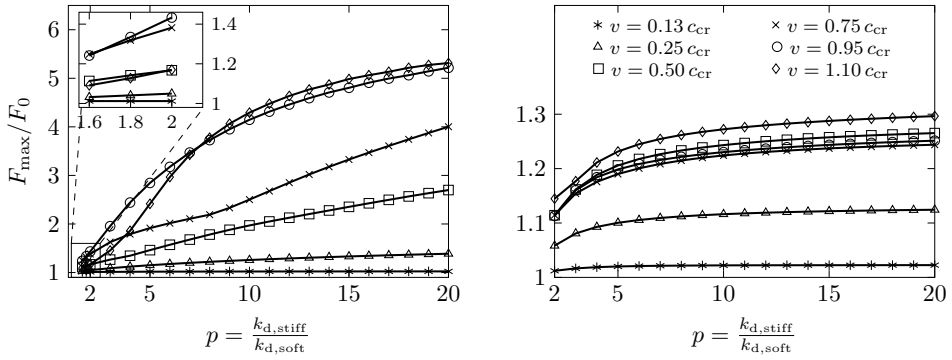

Figure 4.14: Maximum contact force normalized by the dead load versus stiffness ratio for the soft-to-stiff case (left panel) and for the stiff-to-soft case (right panel); $l_{\mathrm{t}} = 0.1$ m; in the legend, c_{cr} represents $c_{\mathrm{cr,l}}$ for the soft-to-stiff case and $c_{\mathrm{cr,r}}$ for the stiff-to-soft case.

the variation of the transition length. Moreover, the difference in energy input becomes negative at certain supercritical velocities, meaning that the moving oscillator inputs less energy into the beam-foundation system than the moving constant load. In the stiff-to-soft case (panel (b) of Fig. 4.13), the difference in energy input exhibits a behaviour different from the one observed for the maximum contact force (panel (b) in Fig. 4.12). The difference in energy input increases with increasing transition length, with a peak around $c_{\mathrm{cr,r}}$, beyond which it decreases. The critical velocity exhibits some peculiar shifts with the variation of transition length. Moreover, the transition length increase does not seem to have such a considerable impact on the reduction of the difference in energy input compared to the soft-to-stiff case.

Variation of the stiffness ratio

In this section, the maximum contact force and the difference in energy input are presented as functions of the stiffness ratio p. Lei and Mao [13] found that the influence of the stiffness ratio on the maximum contact force is minimal. In their study, the supporting structure was modelled as two Kelvin-foundation layers in series (similar to the model formulated in Chapter 3); the bottom layer represents the sub-soil and is piecewise homogeneous while the top layer represents the ballast and is homogeneous. Although the stiffness jump prescribed in the bottom layer is significant ($n = 10$ and $n = 100$, where $n = k_{\mathrm{lower}}^{\mathrm{stiff}} / k_{\mathrm{lower}}^{\mathrm{soft}}$), the equivalent single-layer Kelvin foundation has a small stiffness ratio and a limited variation range ($p \approx 1.6$ for $n = 10$ and $p \approx 1.8$ for $n = 100$, while $p = 5$ can be observed in areas with soft soils [4, 79, 80]). Moreover, Ang and Dai [35] found that for a smooth surface of the rail the increase in the maximum contact force with increasing stiffness ratio is negligible. However, the load velocities considered in their study are much lower than the critical velocity in the soft domain, namely around 13% and 18%. Here, the velocity and the stiffness-ratio ranges

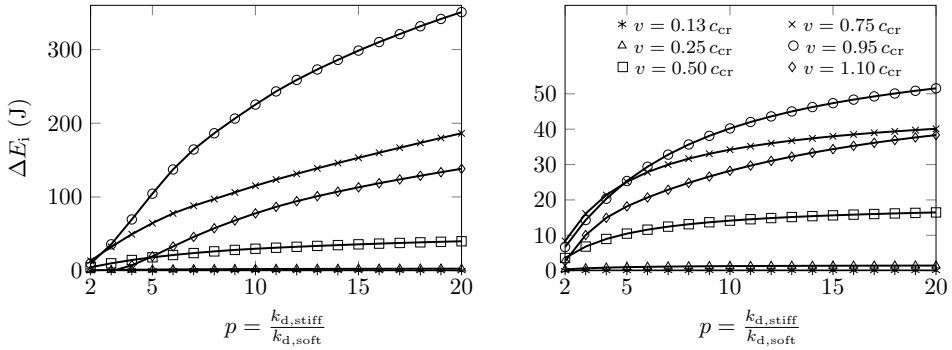

Figure 4.15: Difference in energy input between the moving oscillator and the moving constant load versus stiffness ratio for the soft-to-stiff case (left panel) and for the stiff-to-soft case (right panel); in the legend, c_{cr} represents $c_{cr,l}$ for the soft-to-stiff case and $c_{cr,r}$ for the stiff-to-soft case.

are extended such that more general observations can be made about the influence of the stiffness ratio on the maximum contact force.

Fig. 4.14 presents the maximum contact force versus stiffness ratio p for different oscillator velocities. In both cases (soft-to-stiff and stiff-to-soft), the maximum contact force increases with increasing stiffness ratio, tending to a specific value which is obtained in the limit case of $k_{d,stiff} \to \infty$. Although the qualitative behaviour in the two cases is similar, the increase of the maximum contact force is much more significant in the soft-to-stiff case. In the soft-to-stiff case, the lines of $v = 0.95\, c_{cr}$ and of $v = 1.10\, c_{cr}$ intersect, implying that the critical velocity for the maximum contact force is also dependent on the stiffness ratio (next to transition length, discussed in Section 4.3.5). In the stiff-to-soft case, the line of $v = 0.50\, c_{cr}$ lies above the lines of $v = 0.75\, c_{cr}$ and of $v = 0.95\, c_{cr}$, which is in agreement with the results presented in panel (b) of Fig. 4.12. Furthermore, Fig. 4.15 presents the difference in energy input versus stiffness ratio p for different velocities. The behaviour exhibited by the difference in energy input is very similar to the one observed for the maximum contact force (Fig. 4.14).

As can be seen in the left panel of Fig. 4.14, for small oscillator velocities (e.g, $v = 0.13\, c_{cr}$), the increase in maximum contact force with increasing stiffness ratio is negligible, a result which is in agreement with the findings of Ang and Dai. (It must be mentioned that there is a difference between this agreement in findings and the one presented in Section 4.3.2; in Fig. 4.5, the results are obtained using the same parameters as in Ang and Dai to validate the choice of the vehicle model, while here, the findings agree also for the parameter values adopted in the current paper.) Also, for stiffness ratio between 1.6–1.8, the change in maximum contact force is insignificant (less than 1% for small oscillator velocities and up to 4% for oscillator velocities close to the critical velocity), results which are in agreement with the conclusions of Lei and Mao. However, for larger velocities and wider stiffness-ratio range, the maximum contact force increases drastically, reaching a dynamic amplification

factor greater than 5 for velocities close the the critical velocity. Moreover, even for oscillator speeds of 25–50% of the critical velocity, which represent operational speeds of conventional trains, the dynamic amplification factor can reach values of 1.4–2.5 (for very large stiffness dissimilarities). Therefore, even if the rail is completely straight (i.e., no differential settlements have occurred), which is assumed in this paper, the stiffness variation alone can lead to a significant increase in the maximum contact force for large enough oscillator velocities and considerable stiffness-ratio values. This increase in the maximum contact force can lead to the onset of degradation in the form of differential settlements, which generally cause additional increase in the maximum contact force as has been found by Ang and Dai and Lei and Mao, aggravating the degradation. To conclude, these findings confirm that uneven stiffness, next to initial imperfection (as studied by others [e.g., 13, 35]), is one of the main causes for the onset of degradation.

4.4. Conclusions

In this chapter, the influence of accounting for the interaction between the vehicle and the supporting structure on the transition radiation phenomenon has been studied. To this end, a one-dimensional model has been formulated, consisting of an infinite Euler-Bernoulli beam resting on a locally inhomogeneous Kelvin foundation, interacting with a moving loaded oscillator that has a nonlinear Hertzian spring. The linear behaviour of the individual sub-systems, namely the moving mass and the supporting structure, allows to obtain the solution by means of the Green's-function method. The finite difference method has been used for the spatial discretization of the finite computational domain to accommodate the smoothly inhomogeneous foundation. Furthermore, the infinite extent of the system has been accounted for through a set of non-reflective boundary conditions derived by replacing the semi-infinite domains adjacent to the computational domain with their response at the interfaces, and through appropriate initial conditions. The solution has been validated by comparing the obtained results to a benchmark solution for two limit cases in which the problem simplifies to a moving constant load, and by comparing the obtained results with findings in the literature.

Accounting for the interaction between the moving oscillator and the supporting structure generally leads to stronger transition radiation, caused by the variation of the vertical momentum of the moving mass. Results show that the interaction causes a variation of the contact force and the maximum contact force exhibits a significant increase compared to the moving constant load case. However, the maximum contact force decreases nonlinearly with increasing transition length. Furthermore, for oscillator velocities close to the minimum phase velocity, the maximum contact force increases significantly with increasing stiffness ratio, implying that the stiffness ratio is an important factor in minimizing the maximum contact force. This finding supplements the existing literature where limited velocity and stiffness-ratio ranges have been considered, while the present work provides a more com-

plete picture about the influence of the velocity and stiffness ratio on the maximum contact force.

The influence of the oscillator on the transition radiation has also been investigated from an energy point of view. Results show that the power input by the oscillator into the supporting structure can be significantly larger than that of the moving constant load. Meanwhile, the difference in energy input between the moving oscillator and the moving constant load shows a significant decrease with increasing transition length for the soft-to-stiff transition. For the stiff-to-soft transition, the maximum difference in energy input does not necessarily occur for the minimum transition length, which is a peculiarity of this problem. Furthermore, the difference in energy input increases with increasing stiffness ratio following a similar trend to the one exhibited by the contact force.

Finally, in most scenarios investigated in this chapter, accounting for the vehicle-structure interaction led to a reduced amplification at transition zones. More specifically, at the locations which have been identified in Chapter 2 to have the maximum response amplification, accounting for the vehicle-structure interaction led to a reduction of the maximum amplification compared to the moving constant load model. This finding suggests that modelling the vehicle as a moving constant load can be conservative when it comes to settlement at transition zones.

5

Influence of system periodicity on transition radiation

Nothing in life is to be feared, it is only to be understood.
Now is the time to understand more, so that we may fear less.

Marie Curie

Periodic systems under the action of moving loads have attracted the attention of researchers in the past century. These problems pose academic challenges and are of high practical relevance due to their application in railway, road, and bridge engineering, among others. Despite the numerous studies on periodic systems, few investigations are dedicated to the influence of transition zone on the dynamic response of such systems. This chapter is based on Ref. [82] and aims at investigating if the combination of (i) a transition zone and (ii) the periodic nature of the structure can lead to undesired response amplification that is otherwise not observed in systems that neglect either (i) or (ii).

The study of periodic structures goes back to Newton who investigated the velocity of sound in air by using a lattice of point masses; for an interesting historical background of wave propagation in periodic *lumped* structures, see [83]. Rayleigh studied for the first time a *continuous* periodic structure [84], considering a string with a periodic and *continuous variation* of density along its length. When it comes to a periodic and *discrete* variation in *continuous* structures, Mead [85–87] was among the pioneers that studied free wave propagation in such systems. Concerning moving loads on such structures, Jezequel [88] and Cai et al. [89] were among the first to study periodically and discretely supported beams acted upon

by a moving load. Vesnitskii and Metrikin [16, 70] offered an extensive investigation into the behaviour of a periodically and discretely supported string acted upon by a moving load. More recently, there have been numerous studies of periodic guideways acted upon by vehicles, for example [63, 76, 90–94], and also numerous studies focusing on the vehicle instability caused by the periodic nature of the guideway (i.e., parametric instability or sometimes called parametric resonance), for example [95, 96].

Studies using complex models containing periodic structures and transition zones are present in literature, for example [22, 24, 26, 31]; however, these studies concentrate on predicting the transient response in the vicinity of the transition zone and do not treat specifically the influence of the discrete and periodic supports on these results. Moreover, with increased model complexity the identification and investigation of particular/isolated phenomena becomes very difficult, if not impossible. Therefore, this chapter focuses on the identification and investigation of a response amplification phenomenon that arises due to the combination of periodicity and local inhomogeneity in a system acted upon by a moving load. The local inhomogeneous region is itself periodic too, but with different parameters than the rest of the structure.

This chapter starts by introducing the general theory of periodic continuous systems by using a system consisting of a discretely supported string. With the same system, the solution method is described and three mechanisms that cause response amplification are identified (see Sections 5.1.4, 5.1.5, 5.1.6). Then, the identified mechanisms are investigated in a system consisting of a discretely supported beam with the properties of a railway track. Finally, the beam model is used to investigate the amplification mechanisms in a Hyperloop transportation system.

5.1. Discretely supported string – identification of amplification mechanisms

To study the amplification phenomenon in its purest form, in this section, a 1-D model is formulated consisting of a constant moving load acting on an infinite string periodically supported by discrete springs and dashpots, with a finite domain in which the stiffness and damping of the supports is larger than for the rest of the infinite domain. The novelty of this section lies in the identification and investigation of three amplification mechanisms arising from the combination of periodicity and local inhomogeneity in a system acted upon by a moving load; they have not been yet reported in the literature. The three mechanisms are described in detail in Sections 5.1.4, 5.1.5, and 5.1.6, respectively. Although these mechanisms are identified in this simple model, they are intrinsic to any periodic system with a local inhomogeneity, and, thus, can help understand the potential response amplification in more complex systems that incorporate these two characteristics. Finally, as this model is representative of a catenary system (overhead wires in railway tracks), the three identified

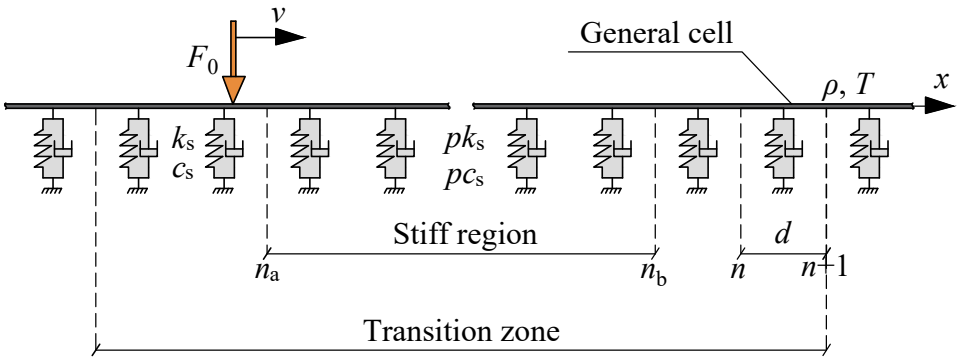

Figure 5.1: Model schematics: infinite tensioned string discretely supported by an inhomogeneous foundation, subjected to a moving constant load. The positive displacement of the string is considered upwards.

mechanisms can help understand the fatigue and wear of the catenary systems close to transition zones as well as wear in the energy collector system.*

5.1.1. Model description

The system studied in this section consists of an infinite string with distributed mass per unit length ρ that is under tension T; the string is discretely supported by springs with stiffness $k_s(x)$ and dashpots with damping coefficient $c_s(x)$; the generic cell is defined at $x \in [nd, (n+1)d]$ where n is the cell number and d is the cell width, and the spring-dashpot element is located in the middle of the cell at $x = \bar{n}d$ with $\bar{n} = n + \frac{1}{2}$; this system is acted upon by a moving constant load of amplitude F_0 and velocity v. The stiffness and damping of the supports varies in space in such a way that there is a zone of length l in which the stiffness and damping of the supports is p times larger than for the rest of the infinite domain; the region in the close vicinity to the stiff zone is called the transition zone. Fig. 5.1 presents a visual schematic of the system while its equation of motion reads

$$\rho \frac{\tilde{\partial}^2 w}{\tilde{\partial} t^2} - T \frac{\tilde{\partial}^2 w}{\tilde{\partial} x^2} + \sum_{n=-\infty}^{\infty} \left(k_s(x) + c_s(x) \frac{\partial}{\partial t} \right) w \delta(x - \bar{n}d) = -F_0 \delta(x - vt), \tag{5.1}$$

The supports stiffness is a piecewise function in space and is defined as follows:

$$k_s(x) = \begin{cases} k_s, & x < x_a, \\ p\,k_s, & x_a \leq x \leq x_b, \\ k_s, & x > x_b. \end{cases} \tag{5.2}$$

*This section of the chapter is based on one of the author's publications [82] and it presents few alterations to the original publication.

For simplicity, the spatial distribution of the damping is assumed to be the same as that of the stiffness. The values for the parameters are taken from Metrikine [97]; they represent the parameters for a realistic catenary system.

In the remainder of the chapter, *homogeneous* system is used to refer to the system without transition zone while *inhomogeneous* system is used for the system with a transition zone, even though both systems are inherently inhomogeneous due to the discrete supports. Important to note, *transition zone* does not refer only to the stiff region, but to the stiff region and its vicinity, as can be seen in Fig. 5.1.

5.1.2. Homogeneous system

In this section we present the characteristics of the periodic system without the transition zone. The goal here is to introduce the solution method used throughout this chapter, to highlight important characteristics of the periodic and continuous system, and to present the steady-state response to a moving constant load. Note that the system without damping is considered here for clarity in the derivation. To this end, we aim at writing an expression linking the states (displacement and slope) at the two boundaries of a generic cell. Firstly, we apply the forward Fourier transform over time to the equation of motion (Eq. (5.1)), thus obtaining the following expression:

$$\tilde{w}'' + \left(\frac{\omega^2}{c^2} - \sum_{n=-\infty}^{\infty} \frac{k_s}{T}\delta(x - \bar{n}d)\right)\tilde{w} = \frac{F_0}{Tv} e^{-i\omega\frac{x}{v}}, \tag{5.3}$$

where the tilde is used to denote the quantity in the Fourier domain and $c = \sqrt{\frac{T}{\rho}}$ is the wave velocity in the unsupported string. We can limit our investigation to a generic cell $x \in [nd, (n+1)d]$ and split this cell into two domains, with $\tilde{w}_1$ to the left of the support and $\tilde{w}_2$ to the right of it. This allows us to write the solutions in the two domains as follows:

$$\tilde{w}_1(x,\omega) = C_1 e^{-i\gamma x} + C_2 e^{i\gamma x} + \tilde{w}_p(x,\omega), \qquad nd \le x \le \left(n+\tfrac{1}{2}\right)d, \tag{5.4}$$

$$\tilde{w}_2(x,\omega) = D_1 e^{-i\gamma x} + D_2 e^{i\gamma x} + \tilde{w}_p(x,\omega), \qquad \left(n+\tfrac{1}{2}\right)d \le x \le (n+1)d, \tag{5.5}$$

$$\tilde{w}_p(x,\omega) = \frac{F_0}{T}\frac{v}{\gamma^2 v^2 - \omega^2} e^{-i\omega\frac{x}{v}}, \tag{5.6}$$

where $\gamma = \frac{\omega}{c}$ is the wavenumber in the unsupported string. Note that $\tilde{w}_p$ is the steady-state solution of an unsupported string acted upon by a moving constant load. The interface conditions between the two domains at $x = \bar{n}d$ represent displacement continuity and vertical force equilibrium, and read

$$\begin{aligned} \tilde{w}_1 &= \tilde{w}_2, \\ \tilde{w}_2' - \tilde{w}_1' &= \frac{k_s}{T}\tilde{w}_1. \end{aligned} \tag{5.7}$$

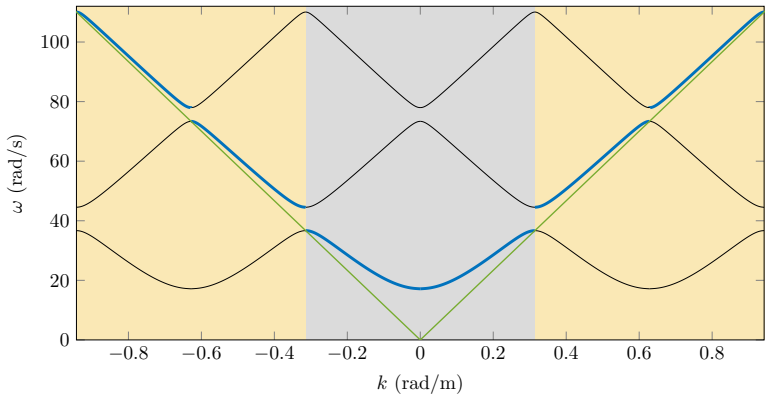

Figure 5.2: Dispersion curves of the periodic system in three Brillouin zones (black and blue lines) and the dispersion curve of the unsupported string (green line); the different Brillouin zones are indicated through different background colour. The primary dispersion curve is displayed with the thick blue lines while the secondary ones with thin black lines.

Using the two interface conditions, D_1 and D_2 can be expressed in terms of C_1 and C_2. Also, we express C_1 and C_2 in terms of the state at $x = nd$ (i.e., displacement $\tilde{w}_n$ and slope $\tilde{w}'_n$). The resulting state inside the generic cell reads

$$\begin{pmatrix} \tilde{w}(x,\omega) \\ \tilde{w}'(x,\omega) \end{pmatrix} = \begin{pmatrix} f_{1,1}(x-nd) & f_{1,2}(x-nd) \\ f_{2,1}(x-nd) & f_{2,2}(x-nd) \end{pmatrix} \begin{pmatrix} \tilde{w}_n \\ \tilde{w}'_n \end{pmatrix} + \begin{pmatrix} \tilde{w}^{\mathrm{ML}}(x,\omega) \\ \tilde{w}^{\mathrm{ML}\prime}(x,\omega) \end{pmatrix}, \quad nd \le x \le (n+1)d, \tag{5.8}$$

where $f_{1,1}$, $f_{1,2}$, $f_{2,1}$, and $f_{2,2}$ are piecewise defined functions that relate the state inside the cell to the state at the left boundary ($x = nd$) while $\tilde{w}^{\mathrm{ML}}$ and $\tilde{w}^{\mathrm{ML}\prime}$ are piecewise defined functions that include the influence of the particular solution on the state inside the cell; their expressions are not given for brevity, but they can easily be obtained using a symbolic mathematical software (e.g., Maple). To express the state at $x = (n+1)d$ in terms of the state at $x = nd$, one has to evaluate Eq. (5.8) at $x = (n+1)d$. The resulting relation is

$$\tilde{\mathbf{w}}_{n+1} = \mathbf{F}\tilde{\mathbf{w}}_n + \tilde{\mathbf{w}}^{\mathrm{ML}}_{n+1}, \tag{5.9}$$

where matrix $\mathbf{F}$ is called the Floquet (or monodromy) matrix. Relation (5.9) is a discrete function that relates the information at the interfaces of an arbitrary cell.

To investigate the propagation characteristics of the system, we momentarily focus on the system without the moving load, and it would become clear that the following expression links the state at $x = nd$ to the one at $x = 0$:

$$\tilde{\mathbf{w}}_n = \mathbf{F}^n \tilde{\mathbf{w}}_0. \tag{5.10}$$

To reveal specific characteristics of the periodic system, we perform an eigenvalue (α) and eigenvector ($\mathbf{u}$) analysis of $\mathbf{F}$. One can express the solution using the so-called Floquet wavenumbers $k^{\mathrm{F}} = \frac{\mathrm{i}\ln(\alpha)}{d}$ and it, thus, reads

$$\tilde{\mathbf{w}}_n = a_1 \mathrm{e}^{-\mathrm{i}k_1^{\mathrm{F}} nd}\mathbf{u}_1 + a_2 \mathrm{e}^{-\mathrm{i}k_2^{\mathrm{F}} nd}\mathbf{u}_2, \tag{5.11}$$

where a_1 and a_2 are unknown amplitudes that can be obtained from the two boundary conditions that need to be imposed to the system. To determine the Floquet wavenumbers k^{F}, the dispersion equation (obtained from the eigenvalue analysis of $\mathbf{F}$; it is presented in Ref. [16] and a mathematical derivation is given in Appendix A) needs to be solved for k^{F}; the dispersion equation reads

$$\cos(k^{\mathrm{F}} d) = \frac{k_{\mathrm{s}} c}{2T\omega} \sin\left(\frac{\omega d}{c}\right) + \cos\left(\frac{\omega d}{c}\right). \tag{5.12}$$

As can be seen from Eq. (5.12), the dispersion relation for the discretely supported string is a transcendental equation. This means that there are infinitely many wavenumbers k^{F} linked to one specific frequency ω and the distance between subsequent wavenumbers is $\frac{2\pi}{d}$. These repeating zones are called Brillouin zones [83]. For discrete systems, all dispersion information is contained in the first Brillouin zone $\left(\left[-\frac{\pi}{d}, \frac{\pi}{d}\right]\right)$ because waves of wavenumber larger than $\frac{\pi}{d}$ cannot propagate. As the Floquet wavenumbers are derived from a discrete function (Eq. (5.10)), they are limited to the first Brillouin zone $\left(\text{i.e., } k^{\mathrm{F}} \in \left[-\frac{\pi}{d}, \frac{\pi}{d}\right]\right)$. However, the system considered here is a continuous one and waves with all wavenumbers can propagate. Consequently, the response $\bar{w}(x, \omega)$ will contain wavenumbers from all Brillouin zones and the continuous wavenumber reads $k = k^{\mathrm{F}} + m\frac{2\pi}{d}$ with $m = \pm 1, \pm 2, \ldots$. A repetition occurs also with increasing ω; however here, the repetition is not exact due to the presence of ω in the denominator of the sine term. This causes the dispersion curve of the periodic system to tend to the one of the unsupported string as ω tends to infinity.

The dispersion curve is presented in Figure 5.2. Three Brillouin zones are presented and it may seem that the repetition from one zone to the next is exact. However, the branches closest to the dispersion curve of the unsupported string give rise to waves with more energy compared to all the other branches; these branches form the *primary* dispersion curve. From a physical perspective, the energy propagated from cell to cell is governed by the Floquet wavenumbers k^{F} and no distinction can be made between different Brillouin zones; however, the propagation inside the cells is governed by the string and wavenumbers from all Brillouin zones can be present dictated by the dispersion equation of the free string. Therefore, the propagation in the continuous and periodic system is a combination of the two, dictating that the waves with wavenumber k closest to γ receives most amount of energy. This is demonstrated mathematically in Appendix C. Also, we can observe that the discrete system exhibits multiple (actually infinitely many [83]) frequency ranges where no propagation is possible; these frequency ranges are called *stop bands*, while the frequency ranges in which

propagation is possible are called *pass bands*. For comparison, in a continuously supported system the only frequency range in which wave propagation is not possible is below the cut-off frequency. Strictly speaking, stop bands (as well as pass bands) only exist if the system does not have dissipation; however, for small values of dissipation, the stop bands strongly attenuate wave propagation in these frequency ranges.

Returning to the problem with the moving load, we still need to impose two boundary conditions to have a fully determined solution. Because we are searching for the steady-state response, we can make use of the so-called *periodicity condition* [16]. For the considered system (the load does not have an inherent frequency), the response inside each cell is exactly the same as in the previous one but shifted in time by $\frac{d}{v}$. The two boundary conditions, therefore, read

$$\begin{aligned} \tilde{w}_1(x = nd)e^{-\mathrm{i}\omega\frac{d}{v}} &= \tilde{w}_2(x = (n+1)d), \\ \tilde{w}_1'(x = nd)e^{-\mathrm{i}\omega\frac{d}{v}} &= \tilde{w}_2'(x = (n+1)d). \end{aligned} \tag{5.13}$$

Using Eqs. (5.13), we can determine the remaining two unknown amplitudes C_1 and C_2 (their expressions can be found in [16]). The steady-state solution in the Fourier domain is now determined. To obtain the time-domain solution, the inverse Fourier transform is performed numerically (for which to work efficiently, a small amount of damping is introduced.)

For a continuously supported string, the steady-state response does not exhibit any wave propagation away from the load (we only consider sub-critical velocities). For the discretely supported string, however, waves are excited from the load every time it passes a support. In the case of a single support, the load generates a continuous wave spectrum when it passes it; this is *transition radiation* as described in Chapter 2. In the periodic system, the waves generated at each support interfere (constructively for some frequencies and destructively for others) leading to a discrete frequency spectrum of the radiated waves; this phenomenon is sometimes called *resonance* transition radiation [37] because the constructive interference of the radiated waves leads to resonance for some system parameters. More specifically, resonance occurs when the group velocity of one generated wave is equal to the load velocity. From Fig. 5.10, we can identify the velocities at which resonance occurs (consider only the black line). As it can be seen, the system has many velocities at which resonance occurs, but some velocities lead to stronger resonance than others. Strong resonance occurs at low frequencies of the generated harmonic and at high velocities of the load [16].

To determine the frequency/wavenumbers of the waves generated by the moving load, next to the dispersion curve we need another equation that expresses a relation between the frequency, wavenumber, and the load velocity, namely the kinematic invariant. For this system, the kinematic invariant can be determined from the following equation [16] (a

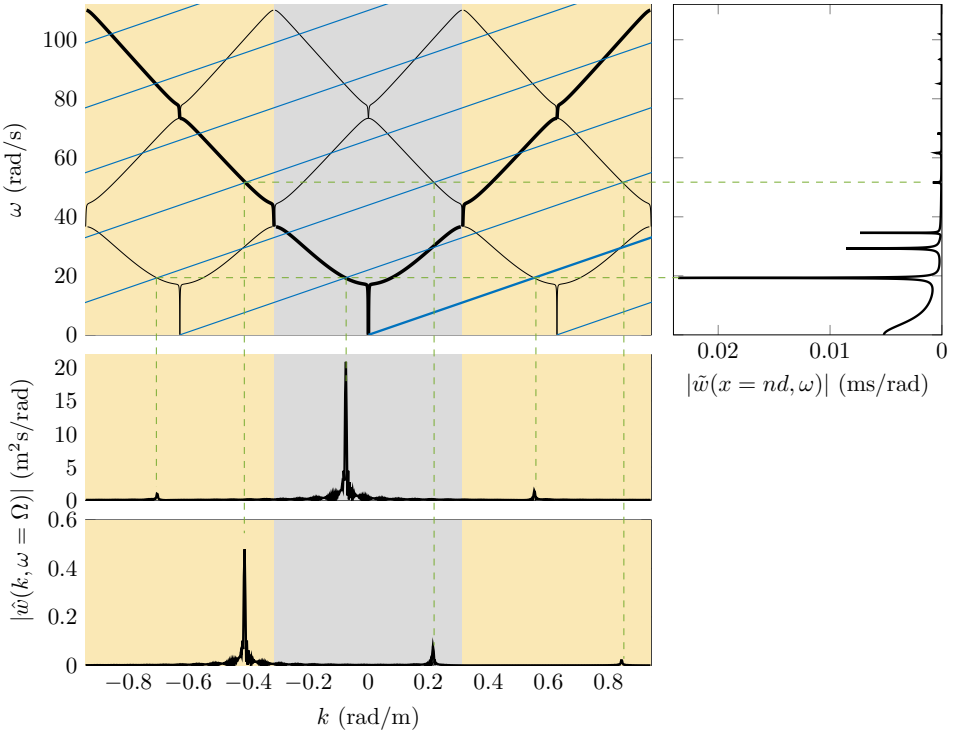

Figure 5.3: The dispersion curve (black solid lines) and the kinematic invariants (blue solid lines) (top left panel; $v \approx 0.25c$), the frequency spectrum of the steady-state displacement (top right panel), and the wavenumber spectra of the steady-state displacement (bottom panels) evaluated at $\Omega = 19$ and $\Omega = 51$ rad/s (indicated by the horizontal dashed lines).

mathematical derivation of the kinematic invariants is given in Appendix A):

$$\cos(kd) = \cos\left(\frac{\omega d}{v}\right). \tag{5.14}$$

Eq. (5.14) shows that there are infinitely many kinematic invariants. The 0th-order kinematic invariant is given by $\omega = kv$ that relates to a constant moving load while the higher order kinematic invariants are given by $\omega = kv + m\frac{2\pi v}{d}$ with $m = \pm 1, \pm 2, \ldots$, and are related to moving harmonic loads of frequency $m\frac{2\pi v}{d}$.

Figure 5.3 presents the dispersion curve together with the kinematic invariants of the current problem. The dispersion curve is slightly different compared to the one in Fig. 5.2 due to the presence of damping. It can be seen that there is no intersection point between the 0th order kinematic invariant (thick blue line) and primary dispersion curve (thick black line) because the considered load velocity is subcritical; nonetheless, there are intersection points between higher order components. The intersections between one of the kinematic invariants and the dispersion curve represent propagating waves emitted by the moving

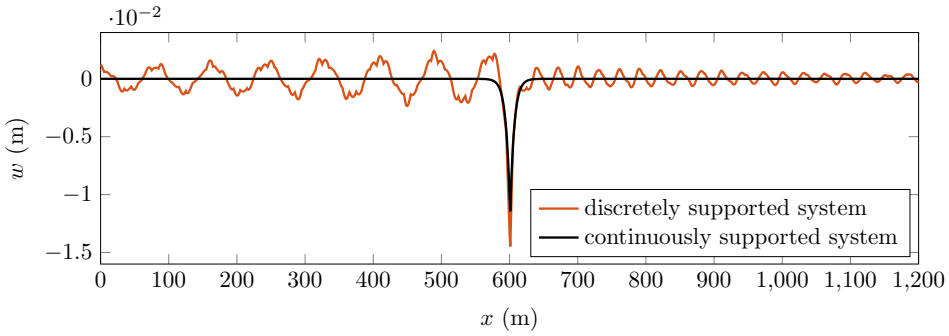

Figure 5.4: Snapshot of the time-domain displacement field for the discretely and continuously supported systems.

load in the steady state. Moreover, it is important to observe in Fig. 5.3 that the emitted waves form a discrete frequency spectrum, as expected, and that all generated waves have frequencies in the pass bands of the system.

Moreover, it is clear from the wavenumber spectrum that the wave pack with frequency ω (e.g., $\omega = 19$ or $\omega = 51$ rad/s depicted in Fig. 5.3 through the dashed green lines) is composed of infinitely many discrete harmonic waves. The reason is that the harmonic wave is not an eigen-solution of the equation of motion; consequently, the eigenfunction is represented as a superposition of infinitely many harmonic waves. Some of these harmonic waves have a negative phase velocity while others have a positive one. Nonetheless, the wave pack ($\omega = 19$ or $\omega = 51$ rad/s) has a negative group velocity meaning that it travels in negative x direction. Also, the main contribution to the wave pack can be seen to come from the intersection of one of the kinematic invariants with the *primary* dispersion curve, as explained previously.

Figure 5.4 presents a time-domain snapshot of the steady-state displacement field. It can be observed that in front of the load, the wave is mainly governed by one frequency-wavenumber pair while behind more pairs seem to be influential; also, the amplitude of the wave behind the load is larger than the one in front. The wave in front of the load is mainly governed by the second peak in the frequency spectrum which is associated with a positive group velocity larger than the load speed (so it travels in front of the load; see top plots in Fig. 5.3) while the one behind the load is governed by the first and third peaks which are associated with negative group velocities; this explains the difference in amplitude as well as the frequency-wavenumber content of the waves.

5.1.3. Inhomogeneous system

In this section, the periodic system with a transition zone (as depicted in Fig. 5.1) is considered. The solution is obtained using a Green's function approach (in some ways similar to the one in Chapter 4); the moving load is first assumed to act inside only one cell and the response of this system is determined. To obtain the response of the system to the moving load acting on all cells, the individual solutions are superimposed. The drawback of this

approach is that the load cannot act from $t \to -\infty$ since this would imply obtaining and adding infinitely many solutions. Nonetheless, if the load enters far away to the left of the transition zone and if the system has damping, the response in the transition zone should be in the steady state. (This shortcoming could be avoided by imposing the steady state as initial conditions of the system, as done in Chapter 4; this is not done here because the computational cost of the above-mentioned procedure is very low.)

The solution procedure starts, as previously, by applying the Fourier transform over time to Eq. (5.1). Then, the loading obtained is only considered for one cell; the solution procedure is demonstrated for the situation in which the load is applied to the left of the stiff zone, but the same procedure needs to be followed when it acts inside the stiff zone or to the right of it. The obtained equation of motion is divided in 5 domains: (1) left of the loaded cell, (2) the loaded cell, (3) right of the loaded cell and left of the stiff zone, (4) inside the stiff zone, and (5) to the right of the stiff zone. Their solutions can be written as done in the previous section and read

$$\tilde{\mathbf{w}}_{1,n,n_\xi} = a_2 \mathrm{e}^{-\mathrm{i}k_2^{\mathrm{F}} nd}\mathbf{u}_2, \qquad n < n_\xi, \tag{5.15}$$

$$\tilde{\mathbf{w}}_{2,n,n_\xi} = b_1 \mathrm{e}^{-\mathrm{i}k_1^{\mathrm{F}} nd}\mathbf{u}_1 + b_2 \mathrm{e}^{-\mathrm{i}k_2^{\mathrm{F}} nd}\mathbf{u}_2 + \tilde{\mathbf{w}}_n^{\mathrm{ML}}, \qquad n = n_\xi, \tag{5.16}$$

$$\tilde{\mathbf{w}}_{3,n,n_\xi} = c_1 \mathrm{e}^{-\mathrm{i}k_1^{\mathrm{F}} nd}\mathbf{u}_1 + c_2 \mathrm{e}^{-\mathrm{i}k_2^{\mathrm{F}} nd}\mathbf{u}_2, \qquad n_\xi < n < n_{\mathrm{a}}, \tag{5.17}$$

$$\tilde{\mathbf{w}}_{4,n,n_\xi} = d_1 \mathrm{e}^{-\mathrm{i}\overline{k}_1^{\mathrm{F}} nd}\overline{\mathbf{u}}_1 + d_2 \mathrm{e}^{-\mathrm{i}\overline{k}_2^{\mathrm{F}} nd}\overline{\mathbf{u}}_2, \qquad n_{\mathrm{a}} \leq n < n_{\mathrm{b}}, \tag{5.18}$$

$$\tilde{\mathbf{w}}_{5,n,n_\xi} = e_1 \mathrm{e}^{-\mathrm{i}k_1^{\mathrm{F}} nd}\mathbf{u}_1, \qquad n \geq n_{\mathrm{b}}. \tag{5.19}$$

where n is the left interface of the observation cell, n_ξ is the left interface of the loaded cell (i.e., the excitation cell), and the overbar indicates that the quantity is associated to the stiff zone; n_{a} and $n_{\mathrm{b}} - 1$ are the left interfaces of the first and last cells, respectively, in the stiff zone. The boundary conditions at infinity have already been accounted for in these solutions. Also, the signs of the wavenumbers have been chosen as $\mathrm{Im}(k_1^{\mathrm{F}}) < 0$ and $\mathrm{Im}(k_2^{\mathrm{F}}) > 0$. To determine the unknown amplitudes, interface conditions are imposed between the domains in the form of continuity in displacements and forces. The total solution (for the moving load acting on all considered cells) becomes

$$\tilde{\mathbf{w}}_n = \sum_{n_\xi = N_{\mathrm{left}}}^{N_{\mathrm{right}}} \tilde{\mathbf{w}}_{n,n_\xi}, \tag{5.20}$$

where $\tilde{\mathbf{w}}_{n,n_\xi} = [\tilde{\mathbf{w}}_{1,n,n_\xi}, \tilde{\mathbf{w}}_{2,n,n_\xi}, \tilde{\mathbf{w}}_{3,n,n_\xi}, \tilde{\mathbf{w}}_{4,n,n_\xi}, \tilde{\mathbf{w}}_{5,n,n_\xi}]$ is the solution for all the cells when the load is applied at n_ξ, N_{left} is the first cell on which the load acts (at $t = 0$) and N_{right} represents the last cell. N_{left} needs to be chosen sufficiently to the left of the transition zone such that the response is in the steady state in the transition zone. N_{right} can be chosen based on the maximum time of the simulation and it does not introduce any unwanted transients in the response. It must be mentioned that the domain for which the response is determined

can be and, for computational efficiency, should be smaller than the domain over which the load is applied. In other words, if N_{left} is chosen far to the left of the transition zone, there is no need to determine the response there; we can restrict our domain of interest (i.e., observation) in the transition zone.

The solution is now determined at the interfaces between cells. To determine the solution inside the cells, one simply needs to use Eq. (5.8). In the following, three mechanisms are described and investigated that occur due to the combination of periodicity with the local inhomogeneity and lead to response amplification.

5.1.4. Wave interference mechanism

Fig. 5.3 shows that, in the case of a homogeneous system, the frequencies of all emitted waves lie inside the pass bands. However, once there is a change in stiffness of the supporting structure (i.e., a transition zone), the locations of the stop bands are different for the different parts of the infinite domain. Consequently, the frequencies of waves excited by the load in the soft regions can be in the stop band of the stiff zone. This causes the waves to be reflected almost completely by the stiff zone and to interfere with the wave field travelling with the load. This wave interference can lead to amplifications of the response in the transition zone.

For this mechanism to be pronounced, the amplitude of the waves that are in the stop band of the stiff zone should be significant. This criterion is met when the velocity is close to a resonance velocity. In Fig. 5.10, the strongest resonance in the soft region occurs at a velocity $v \approx 26$ m/s; consequently, for this investigation a velocity slightly higher than this one is chosen (i.e., $v = 28$ m/s). This is done because the excited wave needs to propagate faster than the load such that it has time to reflect from the stiff region. (At resonance, the group velocity of the generated wave equals the load velocity; for a load velocity slightly larger than resonance velocity, the generated wave of interest travels slightly faster than the load.)

There are two situations which lead to amplification of the response in the transition zone. Firstly, the forward propagating wave is reflected at the stiff region and propagates backwards interfering with the wave field close to the load. This amplification should be observable at the left of the stiff region. Secondly, when the load has passed the stiff region, the backward propagating wave is reflected at the stiff zone and propagates forward interfering with wave field close to load. This amplification should be observable to the right of the stiff zone.

Firstly, we investigate the region to the left of the stiff zone. The response is evaluated at approximately 5 m to the left of x_a (see Figure 5.1); the frequency and wavenumber spectra of the transient response are compared to the steady-state ones in Fig. 5.5. On the one hand, the second peak in the frequency spectrum, corresponding to the forward propagating wave, is amplified in the transient response; because the frequency of this wave is in the stop band of the stiff zone, the wave is reflected almost in its entirety (not completely due

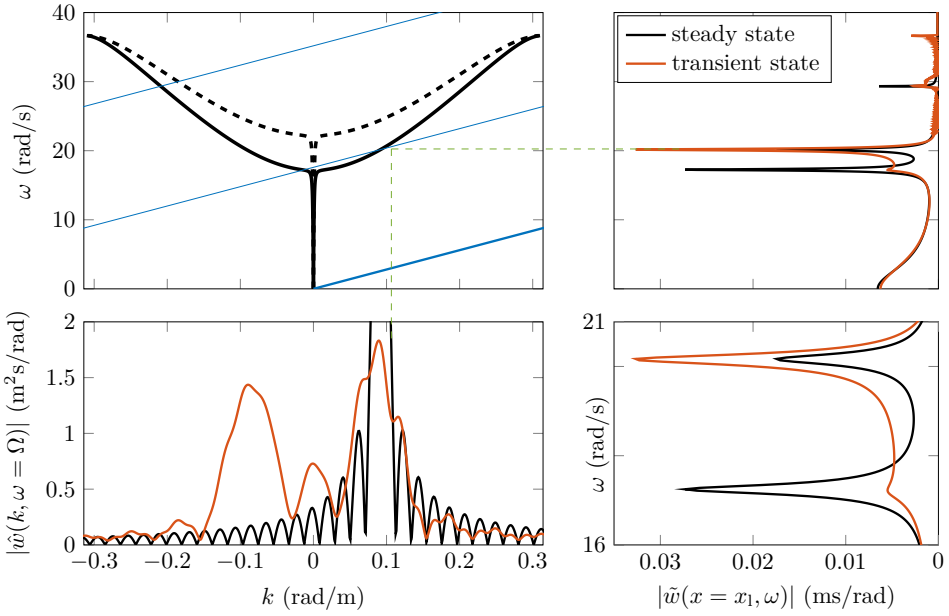

Figure 5.5: The primary dispersion curves for the soft (black solid line) and stiff (black dashed line) regions and the kinematic invariants (blue lines) (top left panel; $v = 28$ m/s), the frequency spectra of the displacements at a position $x_1 = x_a - 5$ m to the left of and near the stiff zone (top right panel), and the wavenumber spectra of the displacements (bottom left panel) evaluated at $\Omega = 20.2$ rad/s (indicated by the horizontal green dashed line); the bottom right panel is a zoom in of the top right panel.

to damping and transmission to the right of the stiff region). Moreover, unlike the steady-state response, the wavenumber spectrum of the transient response exhibits an additional wave with wavenumber equal in magnitude but opposite in sign (i.e., opposite direction of propagation) to that of the forward propagating wave, confirming the wave reflection. On the other hand, we can see that the first peak in the frequency spectrum, corresponding to backward propagating wave, is almost completely eliminated; the fact that the response is evaluated very close to the stiff zone (to its left) implies that less time is available to generate this wave (in the stiff zone, this wave is no longer generated), which explains the lower amplitude.

When looking to the right of the stiff zone, the opposite is occurring. Figure 5.6 shows that the first peak in the frequency spectrum is amplified while the second peak is almost completely eliminated in the transient response. A similar reasoning as above can be used to explain these observations. A general picture is obtained when looking at the time-domain response under the moving load, presented in Fig. 5.7. The transient response is amplified significantly to the left and right of the stiff region.

The response for the equivalent continuously supported system with a transition zone is also presented to show, that in that case, there is no visible amplification (due to the relatively

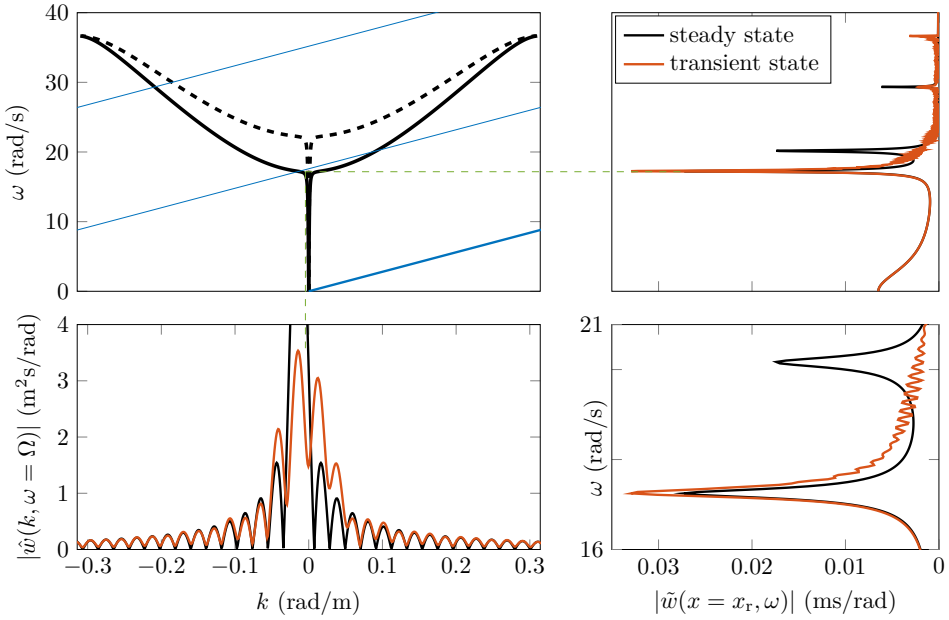

Figure 5.6: The primary dispersion curves for the soft (black solid line) and stiff (black dashed line) regions and the kinematic invariants (blue lines) (top left panel; $v = 28$ m/s), the frequency spectra of the displacements at position $x_\mathrm{r} = x_\mathrm{b} + 15$ m to the right of and near the stiff zone (top right panel), and the wavenumber spectra of displacements (bottom left panel) evaluated at $\Omega = 17.2$ rad/s (indicated by the horizontal green dashed line); the bottom right panel is a zoom in of the top right panel.

low velocity). It is now clear that this significant amplification is caused by the periodicity of the system together with the transition zone; if any of these two characteristics are removed, the amplification vanishes.

The question arises how this mechanism is affected by the length of the stiff zone. If the stiff zone has a very short length, the tunnelling effect (similar to the quantum tunnelling [98]) can occur leading to energy being tunnelled to the soft domain to the right of the stiff zone. As a short investigation, we consider the same system, but an incident wave coming from the left is used instead of the moving load. The solution to that problem (cf. Eqs. (5.15)–(5.19)) reads

$$\tilde{\mathbf{w}}_{1,n} = A_\mathrm{i}\mathrm{e}^{-\mathrm{i}k_1^\mathrm{F}(n-n_\mathrm{a})d}\mathbf{u}_1 + A_\mathrm{r}\mathrm{e}^{-\mathrm{i}k_2^\mathrm{F}(n-n_\mathrm{a})d}\mathbf{u}_2, \qquad n < n_\mathrm{a}, \tag{5.21}$$

$$\tilde{\mathbf{w}}_{2,n} = A_1\mathrm{e}^{-\mathrm{i}\overline{k}_1^\mathrm{F}(n-n_\mathrm{a})d}\overline{\mathbf{u}}_1 + A_2\mathrm{e}^{-\mathrm{i}\overline{k}_2^\mathrm{F}(n-n_\mathrm{a})d}\overline{\mathbf{u}}_2, \qquad n_\mathrm{a} \leq n < n_\mathrm{b}, \tag{5.22}$$

$$\tilde{\mathbf{w}}_{3,n} = A_\mathrm{t}\mathrm{e}^{-\mathrm{i}k_1^\mathrm{F}(n-n_\mathrm{b})d}\mathbf{u}_1, \qquad n \geq n_\mathrm{b}. \tag{5.23}$$

where A_i, A_r, and A_t are the amplitudes of the incident, reflected and transmitted waves, respectively; A_1 and A_2 are the amplitudes of the waves inside the stiff zone. Eq. (5.23) together

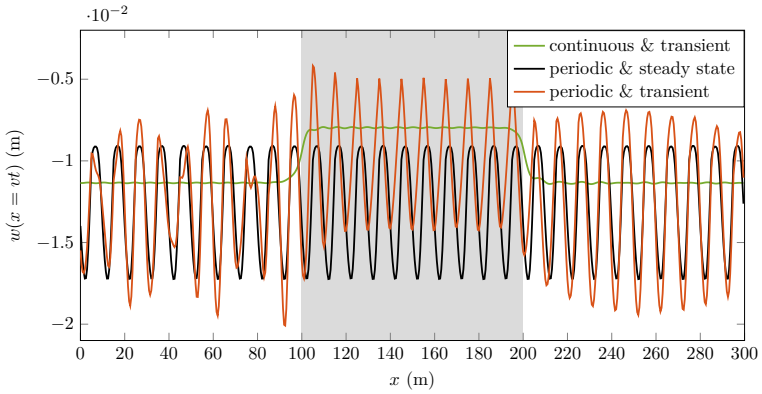

Figure 5.7: The displacement evaluated under the moving load for the wave-interference mechanism; the location of the stiff zone is indicated by the grey background.

with the continuity conditions at the interfaces of the three domains can be used to express the amplitudes of all waves in terms of the amplitude of the incident wave A_i. This allows us to study the reflected and transmitted waves depending on the frequency/wavenumber of the incoming wave and on the length of the stiff zone.

Fig. 5.8 presents the coefficients $|A_{\mathrm{r,t}}|^2$ of the reflected and transmitted waves, respectively, for three lengths of the stiff zone, where the length of the stiff zone is defined as $l = rd$ (i.e., an integer number of cells). (The coefficients $|A_{\mathrm{r,t}}|^2$ are presented and not the amplitudes themselves because $|A_\mathrm{r}|^2 + |A_\mathrm{t}|^2 = |A_\mathrm{i}|^2$ in the absence of damping [98].) Both coefficients are very small for frequencies below the cut-off frequency of the soft zone; in this frequency range, the incoming wave is evanescent, leading to no energy input. For frequencies in the pass band of both domains, the coefficient of the transmitted wave is dominant while that of the reflected one is low. In the frequency range between the cut-off frequencies of the two domains, the outcome depends highly on the length of the stiff zone. For a large r, the coefficient of the transmitted wave is zero while the reflected one is almost 1 (it is not exactly 1 due to the presence of damping). For a smaller r, energy is tunnelled to the right side and the transmission increases while the reflection decreases. The energy tunnelling to the right domain can be observed in the top panel of Fig. 5.9.

Returning to the problem with the moving load, the frequencies of the two dominant waves excited by the moving load (in the scenario studied previously; see Fig. 5.5) are both in between the cut-off frequencies of the two domains. For a large r, both waves experience almost full reflection, and thus, the significant amplification observed previously. For $r = 1$, the forward propagating wave will not any more fully reflect, as can be inferred from the right panel of Fig. 5.8 (the forward propagating wave is indicated through the top green dashed line), while the backward propagating wave is still almost fully reflected (the backward propagating wave is indicated through the bottom green dashed line). This scenario should lead to a smaller amplification to the left of the stiff zone and the same amplification to

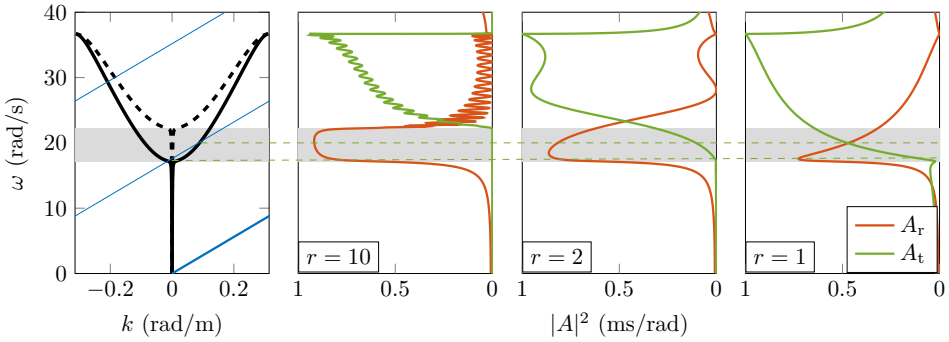

Figure 5.8: The primary dispersion curves for the soft (black solid line) and stiff (black dashed line) regions and the kinematic invariants (blue lines) (left panel; $v = 28$ m/s), and the coefficients of the reflected and transmitted waves (the 3 panels on the right) for 3 lengths of the stiff region; the frequency range between the cut-off frequencies of the two domains is indicated by the grey background.

the right of the stiff zone. This is confirmed in the bottom panel of Fig. 5.9, where the amplification to the left of the stiff zone is slightly smaller for $r = 1$ than for $r = 10$, while the amplification to the right of the stiff zone is almost the same (there is a shift in time and space due to the different lengths of the stiff zone, so one needs to compare peaks at 115 m (orange) and 205 m (green)). Nonetheless, the amplification to the left of the stiff zone can be clearly seen even for $r = 1$.

It is important to mention that the wave interference mechanism is not sensitive to the stiffness difference between the stiff and soft domain, provided that the generated waves are in the pass band of the stiff zone. Simulations have been performed also for $p = 5$ instead of $p = 2$ and the amplification turned out to be very similar in magnitude. Also, it must be mentioned that the wave-interference mechanism occurs also in the continuously supported system subject to a moving constant load, leading to amplification of the response as shown for a beam in [77]; however, for a continuously supported system subject to a moving constant load, this mechanism is influential only for velocities close to the critical velocity while here it can lead to a significant response amplification for much lower velocities of the load.

5.1.5. Passing from non-resonance velocity to a resonance velocity

As discussed in Section 5.1.2, there are several load velocities that can lead to resonance in the periodic system. When designing the catenary system, its properties should be chosen such that these resonance velocities are far away from operational velocities of trains. However, even if the operational velocity is far from resonance velocities outside transition zones, it can be close to a resonance velocity inside the stiff region of the transition zone if this is not designed having this criterion in mind. In this section, the situation is investigated in which the load passes from non-resonance velocity in the soft region to a resonance velocity

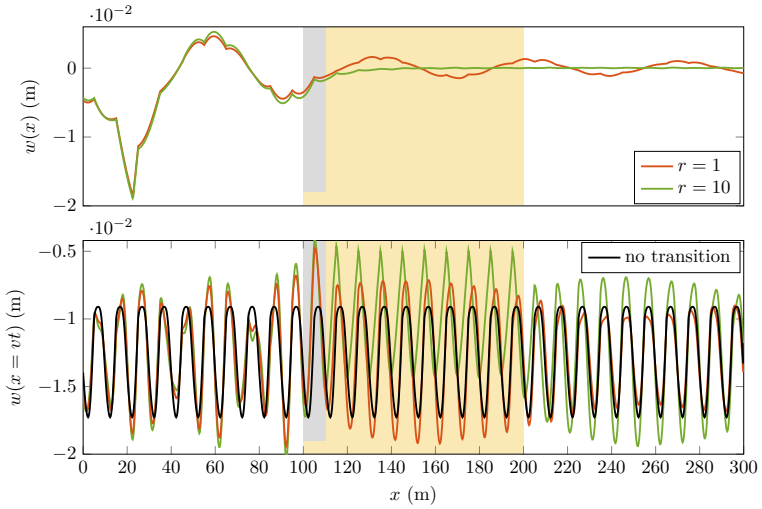

Figure 5.9: Snapshot of the displacement fields (top panel) and the displacements under the moving load (bottom panel) for a short stiff zone ($r = 1$; the position of the stiff zone is indicated through the grey background) and a long one ($r = 10$; the position of the stiff zone is indicated through the yellow background).

inside the stiff region. Note that the velocity of the load is kept constant and just the velocity at which resonance occurs changes due to a change of the support stiffness.

Fig. 5.10 presents the resonance velocities for the soft and stiff regions (here the stiffness ratio is $p = 2$). For a load velocity of $v = 33.5$ m/s, the response is non-resonant in the soft region while in the stiff region it is expected to get amplified due to the occurrence of resonance. The fact that this velocity causes resonance in the stiff region can also be seen in the dispersion curve presented in Fig. 5.11; one kinematic invariant (the first-order one) is tangential to the dispersion curve of the stiff region meaning that the group velocity of the generated wave is equal to the load velocity, which leads to resonance. The amplification of the response in the stiff zone can be observed in both the frequency spectrum and wavenumber spectrum. Moreover, the frequency and wavenumber spectra exhibit additional large peaks at the frequency and wavenumber, respectively, corresponding to the wave generated inside the stiff zone.

Fig. 5.12 presents the displacement under the moving load. The amplification in the stiff zone is observed clearly with a drastic increase compared to the response in the soft region. The increase in response requires a few cell lengths to develop, characteristic to resonance; for short stiff zones, resonance might not have time to develop, but for longer ones strong response amplification can develop. It is important to mention that the mechanism of passing to resonance velocity has an equivalent in the continuously supported system subject to a moving constant load, but there are important distinctions. Firstly, in the continuous system, resonance can only occur at the critical velocity (the boundary between sub-critical and super-critical velocities) that usually is much larger than the operational train velocities.

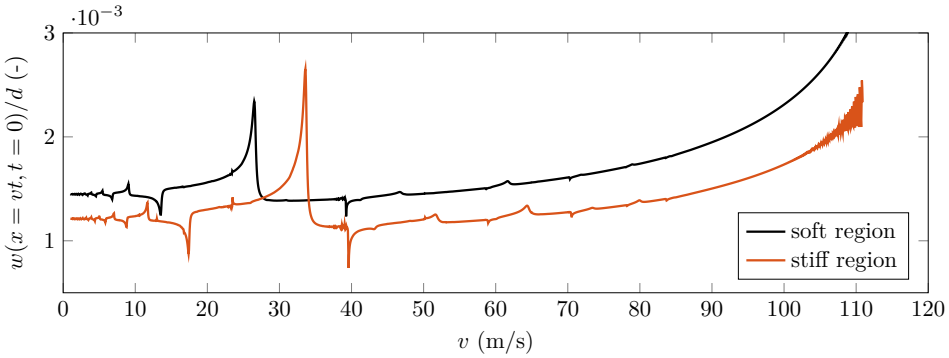

Figure 5.10: Load velocities that lead to resonance in the soft and stiff regions: normalized displacement under the moving load at $t = 0$ versus velocity.

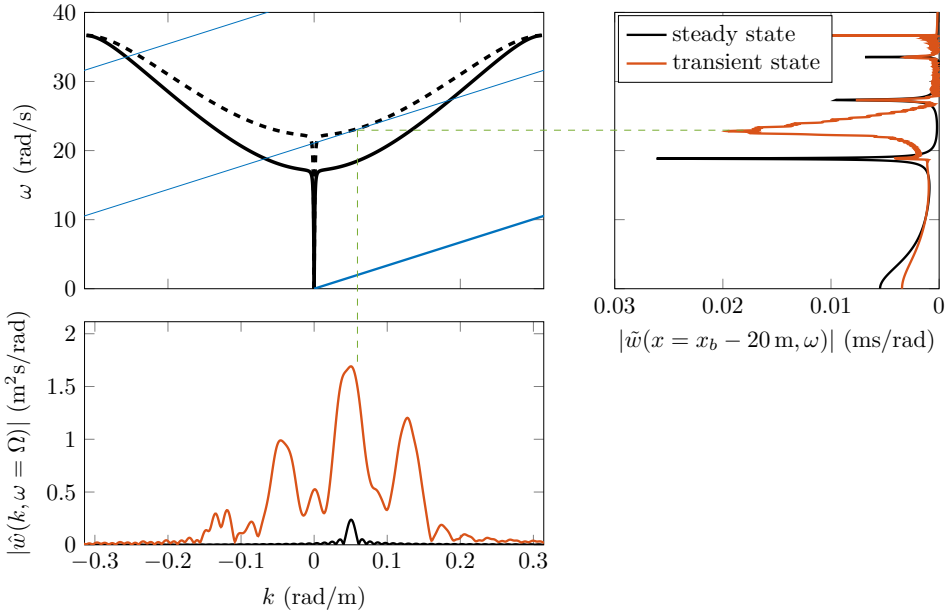

Figure 5.11: The primary dispersion curves for the soft (black solid line) and stiff (black dashed line) regions and the kinematic invariants (blue lines) (top left panel; $v = 33.5$ m/s), the frequency spectra of the displacements at a position inside the stiff zone (top right panel), and the wavenumber spectra of displacements (bottom left panel) evaluated at $\Omega = 23$ rad/s (indicated by the horizontal green dashed line).

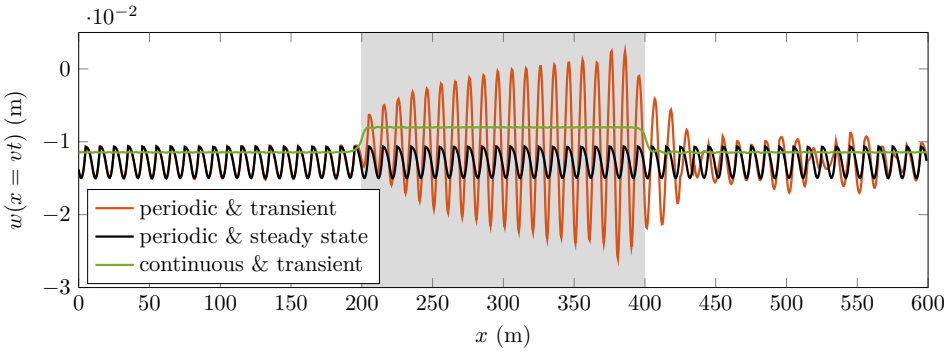

Figure 5.12: The displacements evaluated under the moving load for the resonance velocity in the stiff zone; the location of the stiff zone is indicated by the grey background.

For example, the continuous system equivalent to the periodic one considered in this section has a critical velocity of around 115 m/s while the velocity that leads to the considered resonance in the stiff region is 33.5 m/s. Secondly, to go from sub-critical to critical velocity, the stiffness of the supporting structure needs to decrease (if all other parameters are kept constant); this is much less common in practice because transition zones are usually regions with stiffer structures.

5.1.6. Wave trapping inside the stiff zone

The stiff zone has a finite length l, and consequently the incoming waves generated by the moving load in the soft region could get trapped inside. Wave trapping could lead to response amplification inside the stiff zone even when the moving load is relatively far away. To mathematically derive the conditions for wave trapping, a system without damping is used, while in the graphical results a small amount of damping is present; however, the change in the wave-trapping conditions caused by a small amount of damping is negligible. The amount of damping imposed in this subsection is one quarter of that used in the rest of the chapter to be able to present this mechanism in its purest form; for larger amounts of damping, although the mechanism can still be seen, it is less pronounced.

An approximate condition for wave trapping is that q half-wavelengths of the wave inside the stiff zone is an integer fraction of l. Mathematically this can be written as

$$q\frac{1}{2}\lambda = l = rd, \qquad q \in \mathbb{N}, \quad r \in \mathbb{N}, \tag{5.24}$$

where λ is the wavelength. This would only be exact if the stiff zone was simply supported at both ends, which is not the case for the considered system. An exact condition for the considered system can be derived by using the phase-closure principle (see [99]) to determine

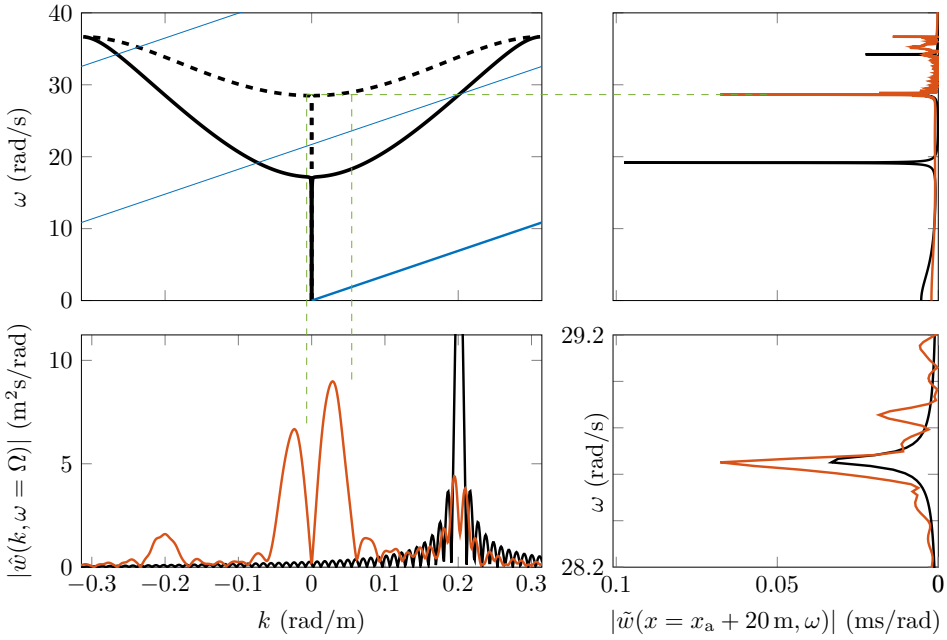

Figure 5.13: The primary dispersion curves for the soft (black solid line) and stiff (black dashed line) regions and the kinematic invariants (blue lines) (top left panel; $\nu = 34.5$ m/s), the frequency spectra of the displacements at a position inside the stiff zone (top right panel), and the wavenumber spectra of displacements (bottom left panel) evaluated at $\Omega = 28.6$ rad/s (indicated by the horizontal green dashed line); the bottom right panel is a zoom in of the top right panel.

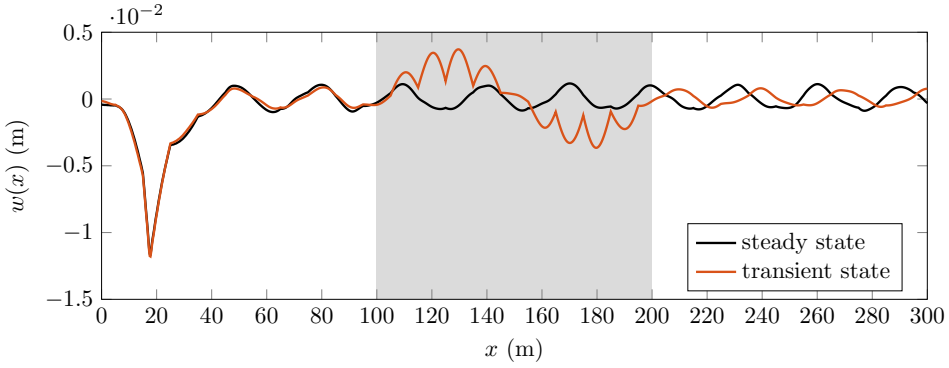

Figure 5.14: Snapshot of the time-domain displacements for the situation when the wave is trapped in the stiff zone; the stiff zone is indicated by the grey background.

the modes of vibration of the stiff zone. However, this exceeds the purpose of the chapter and the approximate condition is sufficient to observe the mechanism.

From relation (5.24) the wavenumber k_{tr} for the wave to be trapped is determined and it reads

$$k_{\mathrm{tr}} = \frac{q\pi}{rd}. \tag{5.25}$$

In order to find the corresponding frequency, the wavenumber in the first Brillouin zone is chosen because the waves with most energy generated by the moving load are located in the first pass band (the higher harmonics have significantly less energy) and the first Brillouin zone. The frequency ω_{tr} corresponding to k_{tr} can be found by numerically solving the dispersion equation for ω_{tr}

$$\cos\left(\frac{q\pi}{r}\right) = \frac{(pk_{\mathrm{s}})c}{2T\omega_{\mathrm{tr}}}\sin\left(\frac{\omega_{\mathrm{tr}}d}{c}\right) + \cos\left(\frac{\omega_{\mathrm{tr}}d}{c}\right). \tag{5.26}$$

A wave with wavenumber k_{tr} given by Eq. (5.25) and frequency ω_{tr} would be trapped inside the stiff zone. The wavenumber $k_{\mathrm{tr},2}$ of the generated wave in the soft region (the frequency remains the same ω_{tr}) reads

$$k_{\mathrm{tr},2} = \frac{1}{d}\arccos\left(\frac{1}{p}\cos\left(\frac{q\pi}{r}\right) + \frac{p-1}{p}\cos\left(\frac{\omega_{\mathrm{tr}}d}{c}\right)\right). \tag{5.27}$$

Clearly, the wave with wavenumber $k_{\mathrm{tr},2}$ and frequency ω_{tr} generated in the soft region will give rise to a wave in the stiff region that is trapped. One can easily check this by considering the system with a harmonic load (acting at a location in the open track) instead of a moving one, in which case the wave trapping can be clearly observed (this result is not presented here for conciseness). To observe the same behaviour for the moving load, one first needs to determine the velocity of the load at which this wave (wavenumber $k_{\mathrm{tr},2}$ and frequency ω_{tr}) is generated. To this end, we substitute $k = k_{\mathrm{tr},2}$ and $\omega = \omega_{\mathrm{tr}}$ in the kinematic invariant, Eq. (5.14). Because subcritical velocities are considered, the 0th-order kinematic invariant cannot intersect the primary dispersion curve; therefore, we look at the 1st-order kinematic invariant, and the velocity of the load corresponding to this situation reads

$$v_{\mathrm{tr}} = \frac{\omega_{\mathrm{tr}}d}{k_{\mathrm{tr},2}\,d + 2\pi}. \tag{5.28}$$

The frequency and wavenumber spectra evaluated at a position inside the stiff zone are presented in Fig. 5.13. The frequency spectrum of the transient response exhibits a large peak at ω_{tr} corresponding to the trapped wave. Moreover, the wavenumber spectrum shows that the wave in the soft region with wavenumber $k_{\mathrm{tr},2}$ (represented by the black line) is transformed in the stiff region into two peaks at k_{tr} and $-k_{\mathrm{tr}}$ that represent the trapped (standing) wave inside the stiff zone. The two peaks are not equal in magnitude as would be the case for a *true* standing wave. One reason is that, as the source is on the left of the stiff

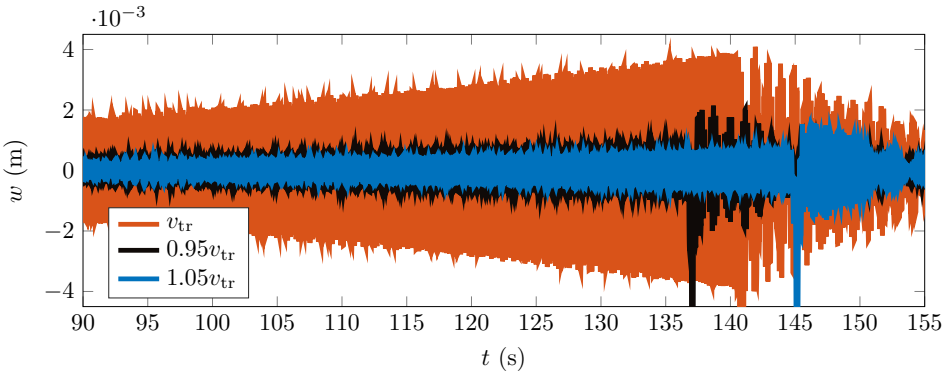

Figure 5.15: Displacement time history evaluated inside the stiff zone for slightly different load velocities.

region, the wave travelling in negative x direction (which is a reflection of the wave travelling in positive x direction) is damped more; another reason is that energy is transmitted to the right of the stiff domain. Fig. 5.14 presents a snapshot of the displacement field where the trapped wave can be clearly observed. The amplification is not drastic, but it is clear. In Fig. 5.14 can also be seen that energy is transmitted to the right domain, meaning that even in the absence of damping, the amplification in the stiff domain will not be infinite. Moreover, it is important to realize that only the wave corresponding to the second peak (in the frequency domain) is trapped; all other waves can pass through. Finally, the amplification disappears for slightly different velocities, as can be seen in Fig. 5.15, or different lengths of the stiff zone (provided that it is not another multiple of the wavelength).

5.1.7. Relation to the continuously supported system with a harmonic moving load

An easier problem to solve that could also capture the three mechanisms discussed in Section 5.1.3 is the continuously supported string subject to a moving harmonic load. The solution of this problem can be obtained by applying the Fourier transform over time to the governing equations and solving the resulting ordinary differential equation in the Fourier-space domain. This has been done in, for example, [49, 77] for a moving constant load and can easily be extended to a moving harmonic load.

The frequency of the harmonic load can be chosen such that the first two peaks in the frequency spectrum (e.g., Fig. 5.3) are accurately represented; by choosing $\Omega = \frac{2\pi v}{d}$, the kinematic invariant in the continuously supported system coincides with the 1st-order kinematic invariant from the periodic system. Moreover, for the responses of the two systems to match, the moving load must have two components: a constant one (zero frequency) and a harmonic one; this way, the response is not symmetric with respect to the zero displacement line, but is shifted downwards as seen in Fig. 5.7. Thus, the expression for the moving

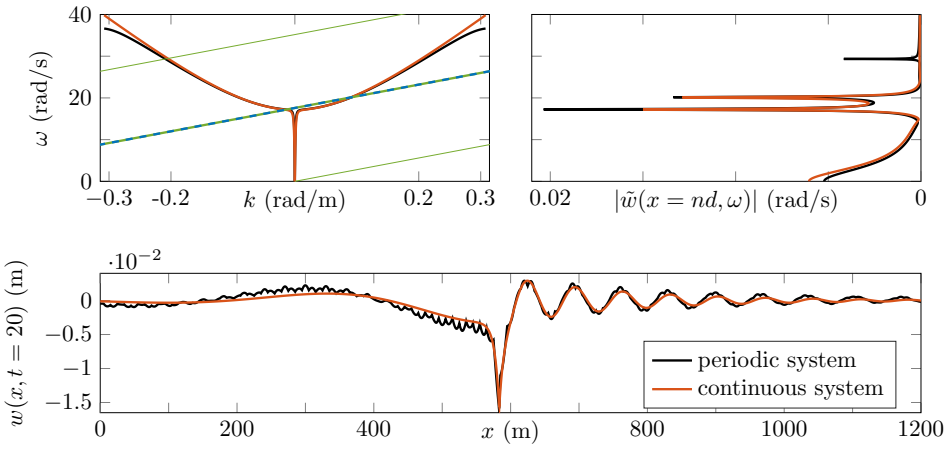

Figure 5.16: Comparison of the periodic system and continuous one; the dispersion curves and the kinematic invariants (top left panel), the frequency spectra of the steady-state displacements (top right panel), and a snapshot of the time-domain displacements (bottom panel).

harmonic load reads $-F_0\big(p_1 + p_2\cos(\Omega t)\big)\delta(x - vt)$, where p_1 and p_2 need to be tuned such that the overall steady-state displacement field matches the one of the periodic system.

Fig. 5.16 presents the comparison of the periodic and continuous systems. It can be seen that the frequency spectra of the two systems agree well for the first two peaks, and the continuous system does not exhibit more peaks than these two. One can introduce more peaks in the response of the continuous system by imposing multiple harmonic components to the moving load (i.e., $p_3\cos(2\Omega t)$, etc.). The bottom panel in Fig. 5.16 shows that the time-domain displacement fields also agree well. For this set of parameters, $p_1 = 1$ and $p_2 = 0.1$ lead to the best fit overall; it must be emphasized that these tuning parameters change with system properties (e.g., load velocity, support spacing, support stiffness, etc.) and they cannot be determined without the response of the periodic system.

Firstly, when it comes to the wave-interference mechanism, Fig. 5.17 shows that the transient response of the continuous system exhibits qualitatively the same behaviour as the periodic one. However, the response in the stiff region differs considerably between the two systems because parameters p_1 and p_2 have been chosen such that the responses match in the soft region, not in the stiff one. This is one drawback of the equivalent model if one is interested in the response inside the stiff region. Also, the wave-interference mechanism can be reproduced in the continuous system only if the waves (in the periodic system) with most energy are located in the first stop band of the stiff region; if these waves were in the second stop band, then they would be able to propagate through the stiff zone of the continuous system because, unlike the periodic one, it only has one stop band. When it comes to the tunnelling effect, this can also occur in the continuously supported system

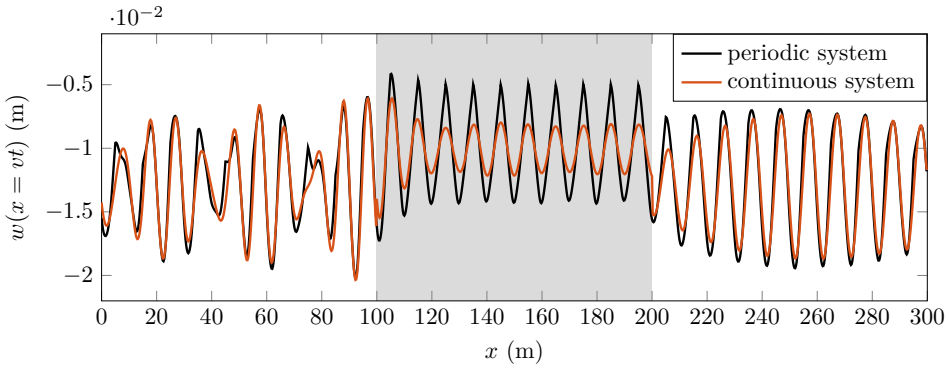

Figure 5.17: Displacements evaluated under the moving load; the position of the stiff region is indicated by the grey background.

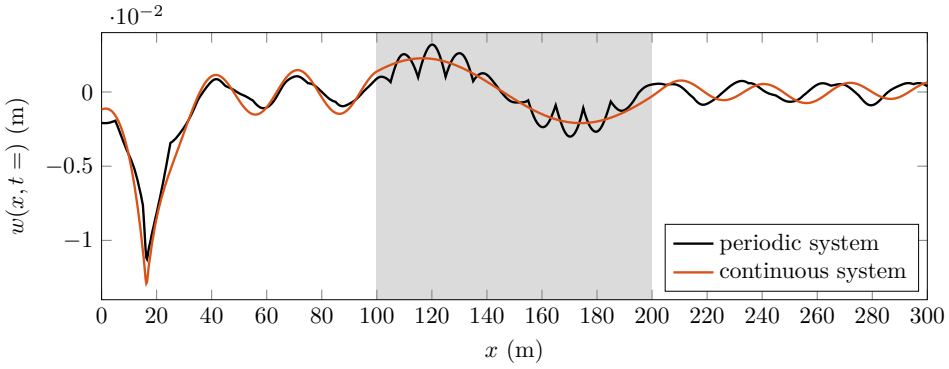

Figure 5.18: Snapshot of the time-domain displacements for the situation when the wave is trapped in the transition zone; the position of the stiff region is indicated by the grey background.

and will lead to a decrease in the response amplification caused by the wave-interference mechanism.

Secondly, for the wave-trapping mechanism, Fig. 5.18 shows that the continuous system exhibits a similar behaviour as the periodic one, and the agreement between the two is very good. If one wants to investigate this mechanism in detail, the continuous system can be an option. The fit between the transient responses can be further improved by changing the scaling factors p_1 and p_2, but this would require to have the transient response of the periodic system in advance, defeating the purpose of using the continuous system.

Finally, for passing from non-resonance velocity to resonance velocity, the continuous system cannot be used at all. The continuous system has one resonance velocity, the critical velocity; the value of that critical velocity is much higher than the one leading to resonance in Section 5.1.5. Consequently, this mechanism can only be investigated in the periodic system.

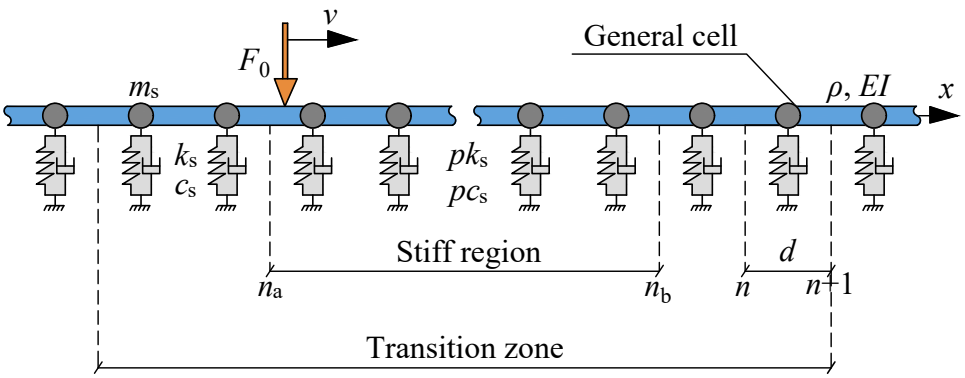

Figure 5.19: Model schematics: infinite Euler-Bernoulli beam discretely supported by an inhomogeneous foundation, subjected to a moving constant load. The positive displacement of the beam is considered upwards.

5.2. System representative of a railway track

Here we investigate the mechanisms identified in Section 5.1 for a system representative of a railway track. To this end, the 1-D model formulated in this section differs from the one in Section 5.1 in the following ways: (i) the tensioned string is replaced by an Euler-Bernoulli beam (under zero tension), (ii) the beam has a small amount of internal damping (incorporated through the damping factor ξ_{EI}), and (iii) point masses m_{s} are added at the supports to represent the sleepers and part of the mass of the ballast. Fig. 5.19 visually describes the system, while its equation of motion reads

$$EI\left(1+\xi_{\mathrm{EI}}\frac{\tilde{\partial}}{\tilde{\partial}t}\right)\frac{\tilde{\partial}^4 w}{\tilde{\partial}x^4}+\rho\frac{\tilde{\partial}^2 w}{\tilde{\partial}t^2}+\sum_{n=-\infty}^{\infty}\left(m_{\mathrm{s}}\frac{\tilde{\partial}^2}{\tilde{\partial}t^2}+c_{\mathrm{s}}(x)\frac{\tilde{\partial}}{\tilde{\partial}t}+k_{\mathrm{s}}(x)\right)w\delta(x-\bar{n}d)=-F_0\delta(x-vt). \tag{5.29}$$

The stiffness $k_{\mathrm{s}}(x)$ and damping $c_{\mathrm{s}}(x)$ have the same spatial distribution as in Section 5.1. The damping in the soft regions is defined similarly to Eq. (2.27) and reads

$$c_{\mathrm{s}}=2\zeta_{\mathrm{s}}\sqrt{k_{\mathrm{s}}m_{\mathrm{s}}}, \tag{5.30}$$

where ζ_{s} is the damping ratio.

The parameters chosen for this system are similar to the ones in Chapter 4, but with some differences. Since the sleepers are accounted through the point masses m_{s}, their mass is no longer distributed along the beam; consequently, the mass of the beam accounts for just the mass of the rail in this model. Also, since the beam is discretely supported, the support stiffness is no longer distributed along the beam. The parameters used for this section are given in Table 5.1.

The method to determine the solution to the system without the transition zone is the same as in Section 5.1.2. The only difference is that the state vector $\tilde{\mathbf{w}}$ contains two more components, namely the bending moment and the shear force. Consequently, the

Table 5.1: Parameter values for the system representative of a railway track.

Parameter	Symbol	Value	Unit
Bending stiffness	EI	$6.42{\cdot}10^{6}$	Nm^2
Mass per unit length	ρ	60	kg/m
Dead weight	F_0	$80 \cdot 10^{3}$	N
Support mass	m_s	125	kg
Support stiffness	k_s	$50 \cdot 10^{6}$	N/m
Support damping ratio	ζ_s	0.05	
Material damping factor	ξ_EI	$5 \cdot 10^{-6}$	s
Support spacing	d	0.6	m

interface conditions at the location of the support $x = \bar{n}d$ contain besides the continuity in displacement and slope also equilibrium of the moments and forces. In the Fourier domain they read

$$\begin{aligned} \tilde{w}_1'' &= \tilde{w}_2'', \\ EI\left(\tilde{w}_2''' - \tilde{w}_1'''\right) &= \left(-k_\mathrm{s}\omega^2 + \mathrm{i}c_\mathrm{s}\omega + k_\mathrm{s}\right)\tilde{w}_1. \end{aligned} \tag{5.31}$$

Furthermore, the Floquet matrix $\mathbf{F}$ is a 4x4 matrix. After performing the eigenvalue decomposition of $\mathbf{F}$, the solution to the system without the transition zone is obtained and reads

$$\tilde{\mathbf{w}}_n = a_1 e^{-\mathrm{i}k_1^\mathrm{F} nd}\mathbf{u}_1 + a_2 e^{-\mathrm{i}k_2^\mathrm{F} nd}\mathbf{u}_2 + a_3 e^{-\mathrm{i}k_3^\mathrm{F} nd}\mathbf{u}_3 + a_4 e^{-\mathrm{i}k_4^\mathrm{F} nd}\mathbf{u}_4 + \tilde{\mathbf{w}}_n^\mathrm{ML}, \tag{5.32}$$

where now there are four waves with unknown amplitudes a_{1-4} and Floquet wavenumbers k_{1-4}^F. For the system with a transition zone, the procedure is the same as in Section 5.1.3, with the difference that Eqs. (5.15) and (5.19) have two waves each while Eqs. (5.16)–(5.18) have 4 waves each.

The dispersion characteristics of the system without the transition zone are presented in Fig. 5.20. The shape of the dispersion curves is different compared to the one of the string (see Fig. 5.3) because the dispersion equation of the beam model is quartic while the one of the string model is quadratic. Also, the significant amount of damping present in the beam model (the railway track has larger damping than the overhead wires) makes the delimitation between stop and pass bands unclear (the indication of stop/pass bands in Fig. 5.20 is approximate). Most importantly, it can be seen that, for the parameter values representative of a railway track, both the dispersion curves and the steady-state response spectrum are very similar to the ones of the equivalent continuously supported system; the only noticeable differences occur at large frequencies, and even these ones are not considerable. This is an indication that the periodic nature of the railway track does not influence its response in a significant way. The justification for this is that the periodic variation in properties of the

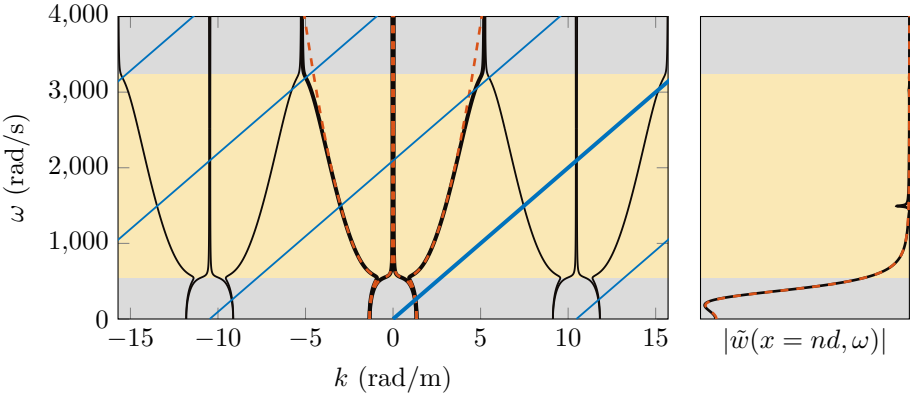

Figure 5.20: The dispersion curves in three Brillouin zones (black lines) and the kinematic invariants (blue lines) (left panel), and the frequency spectrum of the steady-state displacement (right panel); the grey/yellow background represents a stop/pass band. The orange dashed lines are the dispersion curves and frequency response of the equivalent continuously supported system.

supporting structure as felt by the moving load is not considerable due to the large bending stiffness of the rail.

The three mechanisms that lead to amplifications of the response in the transition zone identified in Section 5.1 have been investigated in the system representative of a railway track. However, the amplification observed in any of the three mechanisms is negligible. For brevity, the results are not presented here. For the wave-interference (see Section 5.1.4) and wave-trapping mechanisms (see Section 5.1.6), the fact that the amplitude of the free waves (e.g., the small peak at high frequencies in Fig. 5.20) generated by the moving load is negligible in comparison to the amplitude of the response in the vicinity of the moving load (the large peak at low frequencies in Fig. 5.20), leads to the response amplification in the transition zone to be insignificant. When it comes to passing to a resonance velocity (see Section 5.1.5), the amplification of the response at one of these resonance velocities (except for the one separating the sub- and super-critical regimes, which is very large) is negligible too.

Finally, we also investigated a *worst-case* scenario in which the ballasted track is replaced by a slab-track (i.e., increased support stiffness) combined with an axial compressive force in the beam (to simulate compressive forces in the rail that appear when its temperature increases due to hear) that causes effectively a lowering of the beam's bending stiffness. These two modifications cause an increase in the periodic variation of the support stiffness as felt by the moving load. However, also in this scenario, none of the three amplification mechanisms are influential. Therefore, we can conclude that in the system representative of a railway track (both ballasted- and slab-track), the amplification mechanisms studied in Section 5.1 can be neglected because they do not lead to significant amplification of the response. Furthermore, for investigations focused on transition zones and response amplification

at low frequencies (e.g., not valid when studying noise emission), the periodicity of the railway track can be successfully approximated by the equivalent continuously supported one without neglecting influential amplification mechanisms.

5.3. System representative of a Hyperloop transportation system

Hyperloop is a new emerging transportation system that is in the development stage. Its design minimises the air resistance by having the vehicle travel inside a de-pressurised tube (near vacuum) supported by columns. This design may lead to a strong periodic variation of the stiffness experienced by the vehicle. Moreover, along its route, it will cross bodies of water or come across junctions/switches, all of which are transition zones.

The current section investigates the potential response amplification in a Hyperloop system that results from the combination of (i) a transition zone and (ii) the structure having a periodic nature. More specifically, the three mechanisms identified in Section 5.1 are investigated using a model representative for a Hyperloop transportation system. Accounting for these mechanisms in the design can help prevent degradation of the Hyperloop tube close to transition zones as well as fatigue and wear of the transportation pod.[†]

5.3.1. Parameter values for the Hyperloop system

The system adopted in this section is exactly the same as the one in Section 5.2, but with different values for the parameters which are given in the following.

There are multiple designs of the Hyperloop transportation system; here, a typical Hyperloop design is considered. The steel tube has a thickness of 19 mm and an inner diameter of 2.5 m, leading to $\rho = 1331$ kg/m (a 10% increase was considered to account for additional equipment) and $EI = 2.5 \times 10^{10}$ Nm^2. The support stiffness is tuned using a FEM analysis of the 3D structure (excluding the soil) such that the displacement at the location of the supports match when a static load is applied in the middle of the span. Note that the displacement is at the rail level which is located at the top of the tube (the vehicle is suspended from the top in this design); therefore, the stiffness of the support (in our phenomenological model) accounts not only for the stiffness of the column, but also for the flexibility of the connection between the tube and the rail and, most importantly, for the flexibility introduced by the ovalization of the tube. The concrete columns supporting the tube have a spacing of $d = 16$ m and are assumed to be of 1.5 m diameter and 5 m height; the point mass in the model represents the mass of the columns that is activated by the vehicle and is chosen here as 10% of the overall mass of the column $m_s = 2332$ kg (such a small value is chosen because most flexibility at the supports comes from the ovalization of the tube and thus, the columns are not deformed much). When it comes to the damping, a very small amount is assumed to be conservative, namely $\xi_{EI} = 5 \times 10^{-6}$ s and $c_s = 10$ kNs/m. Although the damping seems small, it originates mostly from the tube itself and not from the soil

[†]This section of the chapter is based on one of the author's publications [100] and it presents few alterations to the original publication.

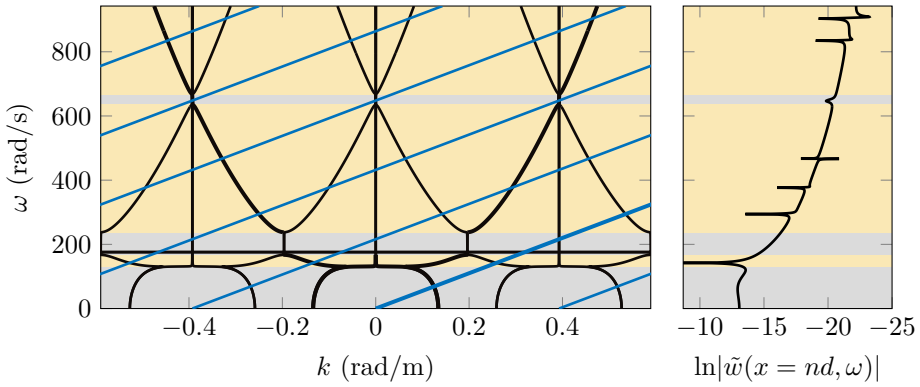

Figure 5.21: The dispersion curves in three Brillouin zones (black lines) and the kinematic invariants (blue lines) (left panel), and the frequency spectrum of the steady-state displacement (right panel); the grey/yellow background represents a stop/pass band.

(since the columns are not deformed much) and the metal tube is not expected to have high damping. The parameters used for this section are given in Table 5.2.

Table 5.2: Parameter values for the system representative of a Hyperloop.

Parameter	Symbol	Value	Unit
Bending stiffness	EI	$2.5{\cdot}10^{10}$	Nm^2
Mass per unit length	ρ	1330	kg/m
Dead weight	F_0	$30 \cdot 10^3$	N
Support mass	m_s	2330	kg
Support stiffness	k_s	$44 \cdot 10^7$	N/m
Support damping	c_s	$10 \cdot 10^3$	Ns/m
Material damping factor	ξ_EI	$5 \cdot 10^{-6}$	s
Support spacing	d	16	m

The solution method is exactly the same as in Section 5.2; consequently, it is not repeated here. The dispersion characteristics of the system without the transition zone are presented in Fig. 5.21. It can be seen that the first pass band is very narrow (i.e., the second stop band is very close to the first one). This indicates that the discretely supported system is significantly different to the continuously supported one, unlike for the system representative of a railway track (see Section 5.2).

Next, the three mechanisms that lead to amplifications of the response in the transition zone are investigated in the Hyperloop scenario.

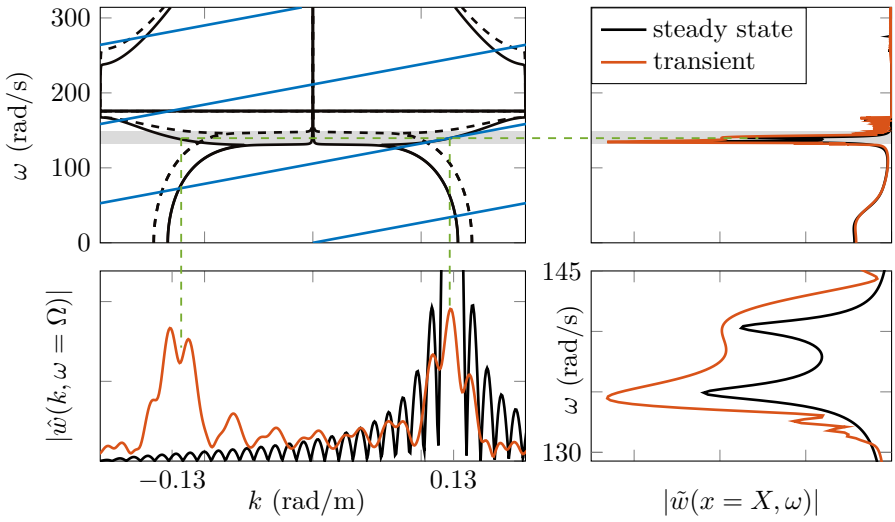

Figure 5.22: The dispersion curves for the soft (black solid line) and stiff (black dashed line) regions and the kinematic invariants (blue lines) (top left panel), the displacements frequency spectra to the left of the stiff zone (top right panel; $X = x_a - 5$ m), and the wavenumber spectra of the displacements (bottom left panel) evaluated at $\Omega = 140$ rad/s (indicated by the horizontal green dashed line); the bottom right panel is a zoom in of the top right panel; the grey background indicates the overlapping region of the pass-band of the soft zone and the stop-band of the stiff one; $p = 1.3$ and $v = 269$ m/s.

5.3.2. Results

Wave interference mechanism

The frequency-domain response in Fig. 5.22 shows that there are two harmonics of large amplitude generated in the steady state, which are in one of the stop-bands of the stiff zone. These waves are, as can be seen, amplified in the transient response (at the left of the stiff zone) due to the wave interference between the incoming and reflected waves. The reflection of one of the two harmonics (the one at $\omega = 140$ rad/s) can be seen in the wavenumber-domain response through the presence of an additional peak (compared to the steady state) at wavenumber equal in magnitude but opposite in sign (i.e., opposite direction of propagation) to that of the forward propagating wave.

To quantify the amplification, the time-domain response under the moving load is presented in Fig. 5.23. The response is evaluated under the moving load because it is governing. A considerable amplification can be observed at the left of the stiff zone that, at its maximum, is of about 20%. The response of the equivalent continuously supported system with a transition zone is also presented to show that, in that case, there is no visible amplification. Clearly, this significant amplification is caused by the periodicity of the system together with the transition zone; if any of these two characteristics are removed, the amplification vanishes.

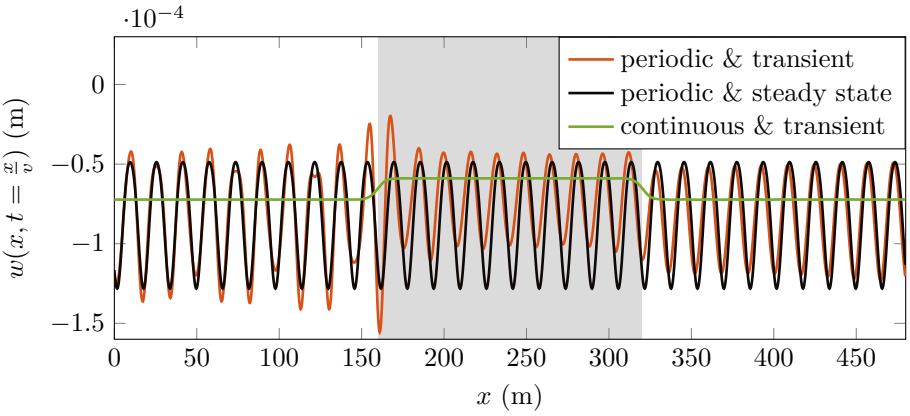

Figure 5.23: The displacement evaluated under the moving load for the wave-interference mechanism; the location of the stiff zone is indicated by the grey background.

It is important to note that a larger difference in stiffness p does not cause a significant increase in the amplification; the important factor for this mechanism is that p is such that the generated harmonics are in one of the stop bands of the stiff zone. Also, even though the velocity is in the operational range for Hyperloop, it is chosen specifically for this mechanism to occur (see Section 5.1.4 for the choice of velocity); for other velocities, the generated waves are either of low amplitude or inside the pass-bands of the stiff zone, making this mechanism not to occur. Finally, the larger the damping (especially the tube's internal damping), the smaller the amplification observed because the generated waves cannot propagate sufficiently far before being attenuated.

Passing from non-resonance velocity to a resonance velocity

The properties of the Hyperloop system should be chosen such that these resonance velocities are far away from operational speeds. However, even if the operational velocity is far from resonance velocities outside transition zones, it can be close to a resonance velocity inside it. In this section, we investigate the situation in which the load passes from non-resonance velocity in the soft region to a resonance velocity inside the stiff region.

The top panel in Fig. 5.24 presents the resonance velocities for the soft and stiff regions. For $v \approx 288$ m/s, the stiff zone resonates while the soft one does not. The bottom panel in Fig. 5.24 presents the displacement under the moving load for $v = 288$ m/s. The amplification in the stiff zone is clearly observed with a drastic increase compared to the steady state. At its maximum, the amplification of the displacement is of more than 20% while the amplification of the bending moment (not presented here for brevity) is more than 25%. The increase in response requires many cell lengths to develop, characteristic to resonance; for short stiff zones, resonance might not have time to develop, but for longer ones strong response

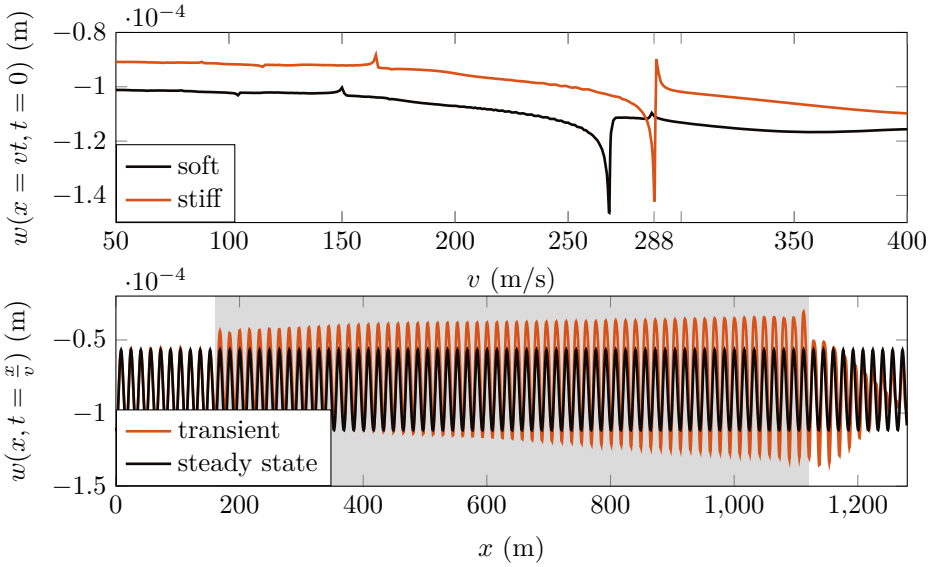

Figure 5.24: Response under the load vs velocity in the soft and stiff regions (top panel) and the displacements evaluated under the moving load for resonance in the stiff zone (bottom panel); the stiff zone is marked by the grey background; $p = 1.3$.

amplification can develop. It must be mentioned that increasing the damping diminishes the amplification, as expected for resonance.

Wave trapping inside the stiff zone

Wave trapping could lead to response amplification inside the stiff zone even when the moving load is relatively far away. The conditions for a wave to get trapped in the stiff zone are described in detail in Section 5.1.6 and are summarized in the following. An approximate condition for wave trapping is that q half-wavelengths of the wave inside the stiff zone is equal to or an integer fraction of l. From this conditions, the wavenumber k_{tr} of the wave trapped in the stiff zone can be determined, and from the dispersion curves (Fig. 5.21 with the properties of the stiff zone), the corresponding frequency ω_{tr} can be obtained. The incoming wave from the soft zone needs to have the same frequency ω_{tr} and the corresponding wavenumber $k_{\text{tr},2}$ can be determined from the dispersion curves with the properties of the soft zone. So, the incoming wave from the soft zone with wavenumber $k_{\text{tr},2}$ and frequency ω_{tr} will lead to a wave of wavenumber k_{tr} and frequency ω_{tr} in the stiff zone that will get trapped. The load velocity that excites a wave of wavenumber $k_{\text{tr},2}$ and frequency ω_{tr} can be obtained from the kinematic invariant expression.

The top panel in Fig. 5.25 presents a snapshot of the displacement field where the trapped wave can be clearly observed even though the load is relatively far away. The bottom panel in Fig. 5.25 presents the displacement time-history at a point inside the stiff zone. The

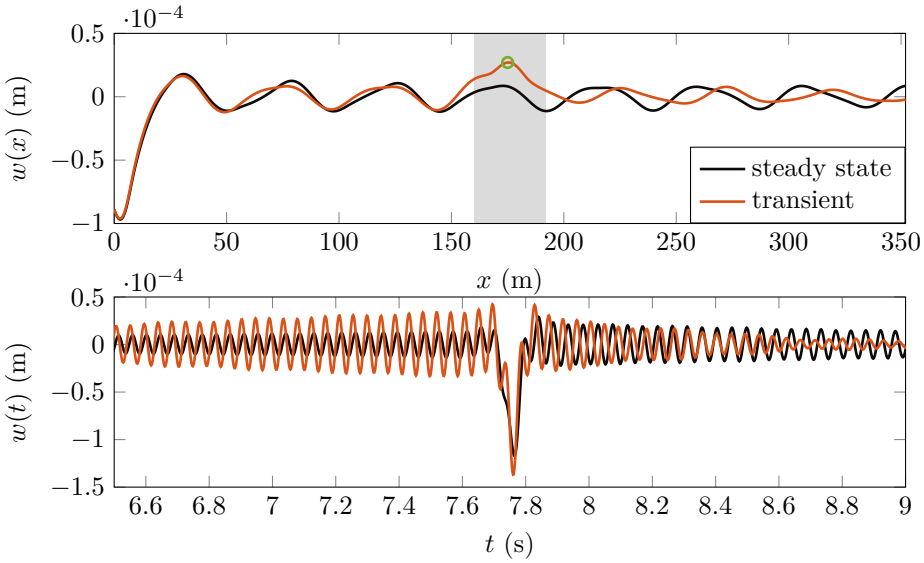

Figure 5.25: Snapshot of the time-domain displacements (top panel) and the displacements time-history at the point marked by the green circle (bottom panel) for the situation when the wave is trapped in the stiff zone; the stiff zone is indicated by the grey background; $p = 1.2$ and $v = 270$ m/s.

amplitude inside the stiff zone is more than double the one of the steady state when the load is relatively far away from the transition zone; under the moving load, at its maximum, the amplification is around 17%. For slightly different velocities or different lengths of the stiff zone (except for integer fractions of half the wavelength), the amplification vanishes.

5.4. Conclusions

This chapter investigated three mechanisms that can lead to response amplification in a continuous and periodic system with a transition zone described by an increase in support stiffness. These mechanisms were investigated using an infinite string/beam periodically supported by discrete springs and dashpots, acted upon by a moving constant load; the two models are representative of a catenary system in railway tracks (string) and of a railway track or a Hyperloop transportation system (beam). Nonetheless, the mechanisms described in this chapter can occur also in other continuous and periodic systems. The amplification is the product of a system with periodic nature and with a local inhomogeneity, and if one of these characteristics is omitted, the amplification will not occur.

The first mechanism is the wave interference that can lead to response amplification to the left and to the right of the stiff region. The waves generated by the moving load outside the transition zone are reflected almost entirely by the stiff region if one of the frequencies of the waves are located in a stop band of the stiff region. This almost complete reflection leads

to wave interference close to the moving load, which in turn leads to response amplification. Results show that this mechanism is of importance when the velocity of the load is slightly higher than one of the resonance velocities in the soft regions. Furthermore, for small lengths of the stiff zone energy can be tunnelled to the soft domain causing a reduction in the reflection coefficient which in turn leads to a reduced amplification.

The second mechanism is the passing from non-resonance velocity in the soft region to a resonance velocity in the stiff region. This causes resonance to occur inside the stiff region leading to a drastic amplification of the response mainly inside the stiff region. Results show that this mechanism leads to the biggest response amplification between the three mechanisms (both in the catenary and Hyperloop systems), but requires the stiff zone to be sufficiently long such that resonance can build up.

The third mechanism is the wave trapping inside the stiff region. For specific values of the wavenumber and frequency of the waves generated in the soft region, waves can get trapped inside the stiff zone potentially leading to response amplification around and inside the stiff zone. Results show that this mechanism leads to amplification inside the stiff region even when the moving load is relatively far away from it. However, for reasonable values of damping, this mechanism is not as pronounced as the other two.

The possibility of capturing these mechanisms using a simpler model, a continuously supported string acted upon by a moving harmonic load, was also studied. The wave-interference and wave-trapping mechanisms observed in the periodic system can be seen in the continuous system too, while the resonance mechanism cannot be replicated using the continuous model. To obtain similar results for the continuous system, the moving load needs to be altered by including harmonic components next to the static one. The static and harmonic force components need to be tuned to the steady-state response of the periodic system. Once this tuning is satisfactory, the transient responses match quite well and the two mechanisms are qualitatively well captured. However, the tuning parameters, in principle, are not known before-hand and need to be updated for each change of the system properties, which makes it difficult to use the continuous system in practical situations.

These three mechanisms have been found to be influential for the catenary and Hyperloop systems, but do not influence the response of the model representative of the railway track. The reason is that in the system representative of the railway track, the variation in support stiffness as felt by the moving load is not as strong as it is in the other two scenarios. Consequently, for investigations focused on transition zones and response amplification at low frequencies (e.g., not valid when studying noise emission), the periodicity of the railway track can be successfully approximated by the equivalent continuously supported one without neglecting amplification mechanisms. Thus, for the remainder of the thesis, the continuously supported system is considered.

Finally, the amplification of stresses and displacements in the transition zones can lead to numerous fatigue and wear problems in the catenary system and in the energy collector of the train. Moreover, accounting for the low (mean) contact force between wires

and carbon strip, the dynamic response of the system can also lead to force fluctuations that are large enough to cause arching (occurs when the contact force is too low) or loss of contact. For the Hyperloop, over time, the amplification can lead to increased degradation of the structure as well as discomfort for passengers. Generally, the influence of all three mechanisms diminishes with increased damping; therefore, if the designed system does not have sufficient inherent damping, additional passive or active damping measures may be needed. The three investigated mechanisms can be considered as additional constraints for the design parameters at transition zones such that amplifications are avoided, especially because all three mechanisms occur in the range of operational train speeds (for the catenary system) and at envisioned operational velocities of the Hyperloop vehicles.

6

Investigating the permanent deformation caused by the response amplification at transition zones

I learned very early the difference between knowing the name of something and knowing *something*.

Richard P. Feynman

A multitude of studies investigating the dynamic response of railway tracks consider the behaviour of the supporting structure to be linear, assumption that is adopted in all models formulated in the previous chapters of this thesis. This approximation is sufficient for many applications and it allows for greater complexity in other modelling aspects (e.g., accurate geometry of the problem). Nonetheless, the influence of the foundation's nonlinearity on the response of a railway track was experimentally shown to be significant by Dahlberg [101], concluding that it should not be overlooked. Furthermore, the fact that settlement is observed in railway tracks is a clear indication that the behaviour of the supporting structure is actually nonlinear. By investigating the settlement of open railway tracks (i.e., not at transition zones), researchers [e.g., 10] observed a rapid settlement in the first cycles, which is governed by the settlement of ballast [102]; after a number of cycles, the ballast reaches its maximum compaction for a given load amplitude [102]. Subsequently, the settlement is governed by the layers beneath the ballast, but the rate of this settlement is low and increases almost linearly with increasing number of cycles, as represented in track

settlement models [10, 103, 104]. Since this thesis focuses on the initiation phase of the degradation, as discussed in the Introduction, the investigation in this chapter is restricted to the settlement originating from the ballast compaction.

The amount of studies that include the nonlinear behaviour of the supporting structure in moving-load problems is low, especially compared to the number of studies of railway-related topics. This indicates, to some degree, the difficulty of accounting for the nonlinear behaviour of the supporting structure. When it comes to systems without transition zones, Metrikin [105, 106] was among the first to introduce springs with cubic nonlinearity to represent the nonlinear behaviour of the supporting structure. To also account for the flexural rigidity, the steady-state response of a beam on a homogeneous and nonlinear elastic foundation subjected to a moving load has been analysed, considering finite [107–109] and infinite [110–112] systems. In addition, Hoang et al. [93] studied the steady-state response of an infinite beam with periodic nonlinear elastic supports.

When it comes to transition radiation, it has also been addressed in systems with nonlinear supporting structure. Castro Jorge et al. [19] used a nonlinear elastic foundation to analyse the effect of the nonlinearity on the maximum displacements in a finite and piecewise-homogeneous system. In addition, Varandas et al. [30, 113] considered nonlinear elastic behaviour of the supporting structure in a 3-D finite-element model of a transition zone. However, to study the degradation in a transition zone, the employed model should incorporate plastic behaviour of the foundation. To this end, Varandas et al. [10] developed a finite 1-D model describing the accumulated permanent deformation in a transition zone using a phenomenological model for the cyclic degradation of the supports. Moreover, Gallego Giner et al. [114] used a elastic-perfectly plastic model (i.e., Drucker–Prager) for the supporting structure in his study of a transition zone using a 3-D finite-element model. More recently, de Oliveira Barbosa et al. [26] incorporated a nonlinear lattice model that can capture the ballast settlement caused by moving loads at transition zones.

Detailed 3-D models of finite and inhomogeneous systems that incorporate nonlinear behaviour of the foundation are available in the literature, as shown previously. However, simplified models of transition zones in infinite systems with nonlinear elasto-plastic foundation behaviour are not available in the literature. This motivates the aim of the current chapter, which is to formulate a 1-D model of an infinite Euler-Bernoulli beam on a smoothly inhomogeneous and nonlinear elasto-plastic Winkler foundation, subjected to a moving load, and study the effect of the nonlinear behaviour on the transition radiation and the degradation in the transition zone.

The novelty of the current chapter is twofold. Firstly, a computationally efficient solution method for an infinite system which locally exhibits nonlinear behaviour is presented. Secondly, the influence of the foundation's nonlinear behaviour on the generated waves (i.e., transition radiation), and the resulting plastic deformation is studied. The model presented here can be used for preliminary designs of transition zones in railway tracks by assessing the potential damage (i.e., plastic deformation) occurring in the transition zone as

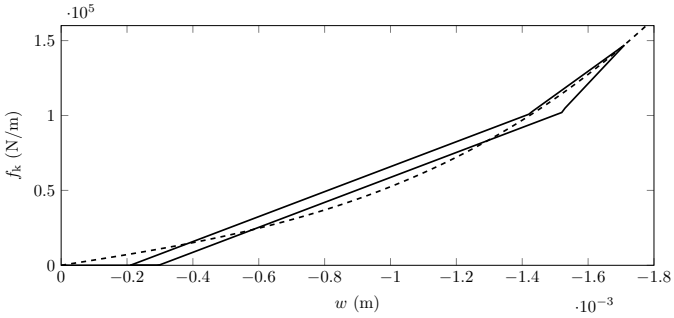

Figure 6.1: Piecewise-linear approximation (solid line) of the cubic constitutive model (dashed line); $f_k = -k_l\, w - k_{nl}\, w^3$ for the cubic model with $k_{lin} = 35.03 \cdot 10^6 (N/m^2)$ and $k_{nl} = 1.74 \cdot 10^{13} (N/m^4)$ [110, 111]

a function of the smoothness of the transition (i.e., length of the transition), of the moving load velocity, of the system's damping and of the stiffness dissimilarity. Furthermore, the results presented here offer insight into the physical mechanisms leading to degradation in the supporting structure.*

6.1. Nonlinear constitutive model of the supporting structure

A variety of models have been used to represent the supporting structure in 1-D systems for railway applications (e.g., linear elastic, bilinear elastic, cubic elastic, etc.); a good overview of models for the foundations in 1-D systems can be found in [115]. One of the most used nonlinear elastic models is the cubic one [e.g., 19, 105, 106, 109–112]. It assumes that the foundation springs exert a reaction force (visualized in Fig. 6.1) proportional to the displacement, through a linear stiffness term k_{lin}, and one proportional to the displacement cubed, through a nonlinear stiffness term k_{nl}. In this chapter, the constitutive relation of the Winkler foundation is based on the cubic model, but also incorporates the possibility of plastic deformation by imposing a different unloading path than that of the loading, as seen in Fig. 6.2.

The loading path of the chosen constitutive relation approximates the cubic model through a piecewise-linear profile (Fig. 6.1) to accommodate the solution method presented in Section 6.2.2. Firstly, k_d^A is assumed to be equal to the stiffness of the equivalent linear model [116]. This assumption is based on the ballast being relatively well compacted at the start of the simulation, represented in Fig. 6.1 through the nonzero displacement at zero force in the piecewise-linear approximation. This implies that the initial soft response of the foundation, as sometimes encountered, is excluded. Furthermore, assuming that the compaction is uniform along the track, the compacted configuration is taken as reference (zero displacement for zero force in Fig. 6.2). Secondly, the steady-state eigenfield is assumed

*This chapter is based on one of the author's publications [77] and it presents few alterations to the original publication.

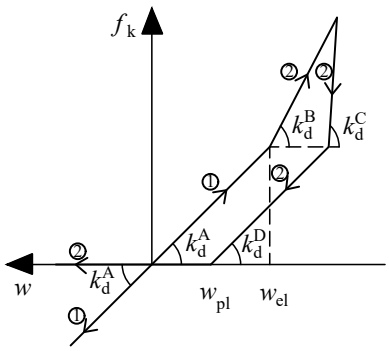

Figure 6.2: Piecewise-linear constitutive law of the foundation. Path (1) represents the loading/unloading path for the linear parts of the computational domain while path (2) represents the first loading/unloading cycle for the nonlinear parts of the computational domain.

to be in the linear regime. This assumption is based on the fact that in the homogeneous parts of the railway track, the steady-state displacement field induced by a train does not lead to significant degradation of the supporting structure. Thirdly, the elastic displacement limit w_{el} is chosen relative to the eigenfield's maximum displacement w^e_{max} in the soft part of the computational domain, where the ratio w_{el}/w^e_{max} is larger than 1. If w_{el} is not exceeded during the simulation, the system remains in the linear regime (branch (1) in Fig. 6.2). At locations where w_{el} is exceeded, the corresponding part of the foundation enters the second loading branch k_d^B. The value of k_d^B is chosen such that it approximates the cubic model (Fig. 6.1).

The parameters of the cubic model which is approximated are chosen as similar to the ones used in other publications [i.e., 110, 111]. However, the parameters for the unloading path, k_d^C and k_d^D, are not well known. For the moment, the parameters are chosen such that the overall constitutive relation resembles the results of cyclic loading experiments on granular material [i.e., 117], but specific additional experiments or 3-D modelling might be needed in order to choose these parameters realistically. Although this thesis focuses on the initiation phase in the ballast compaction, the model developed in this chapter can incorporate cyclic behaviour and the parameters of the constitutive relation can be modified for each cycle to accommodate the behaviour as observed in literature: changing stiffness with increasing cycle number, as well as a changing area (energy dissipation) [26]. However, the computational time required for the simulation of thousands of trains passages can make this approach unfeasible.

The constitutive model incorporates the possibility of separation between the rail and the supporting structure (Fig. 6.2). When the displacement of the beam is larger than the plastic deformation w_{pl} ($w > w_{pl}$; note that w_{pl} has a negative value), the beam looses contact with the foundation. This results in a zero foundation force f_k as depicted in Fig. 6.2. However, this is only allowed at the location where the plastic deformation has been activated; in the

parts of the computational domain with no plastic deformation, the beam is in permanent contact with the supporting structure. In case of separation, besides the foundation stiffness, also the foundation damping is modified. Consequently, the foundation damping reads

$$c_{\mathrm{d}}(x,w)=\begin{cases} c_{\mathrm{d}}(x), & w\le w_{\mathrm{pl}} \text{ or } w_{\mathrm{pl}}=0,\\ 0, & w>w_{\mathrm{pl}} \text{ and } w_{\mathrm{pl}}\neq 0. \end{cases} \tag{6.1}$$

The parameters of the constitutive relation presented in Fig. 6.2 are not only functions of the displacement, but also functions of space, due to the transition zone. To study the influence of the transition smoothness on the plastic deformation in the transition zone and on the radiated wave field, the spatial profile of the foundation stiffness is chosen as the one in Chapter 4, namely Eq. (4.39) and can be visualized in Fig. 4.2. The damping is expressed through the ratio ζ which is defined similar to that of a single-degree-of-freedom system, as given in Eq. (2.27). Therefore, by maintaining a constant damping ratio ζ throughout the system, the spatial variation of the foundation damping is proportional to the square root of that of the stiffness (branch A), except for the parts of the beam which have lost contact with the foundation.

6.2. Model and solution

6.2.1. Problem statement

In this section, a 1-D model is formulated, consisting of an infinite Euler-Bernoulli beam resting on a smoothly inhomogeneous and nonlinear Kelvin foundation, subjected to a constant moving load (Fig. 6.3). In view of practical relevance (degradation is encountered at the transition zone), the nonlinear behaviour of the supporting structure is restricted to the transition zone and its vicinity; this domain is referred to as the *computational domain*. The computational domain is connected at the boundaries to two linear and homogeneous semi-infinite domains to accommodate the infinite extent of the railway track. The equations of motion for the three domains read

$$EI\frac{\tilde{\partial}^4 w}{\tilde{\partial}x^4}+\rho\frac{\tilde{\partial}^2 w}{\tilde{\partial}t^2}+c_{\mathrm{d}}(x)\frac{\tilde{\partial}w}{\tilde{\partial}t}+f_{\mathrm{k}}(x,w)=-F_0\,\delta(x-x_{\mathrm{e}}-vt),\qquad \forall x,\forall t, \tag{6.2}$$

$$w(x,t)=\begin{cases} w_{\mathrm{l}}(x,t), & x\le 0,\\ w_{\mathrm{c}}(x,t), & 0\le x\le L,\\ w_{\mathrm{r}}(x,t), & x\ge L, \end{cases} \qquad c_{\mathrm{d}}(x)=\begin{cases} c_{\mathrm{d,l}}, & x\le 0,\\ c_{\mathrm{d,c}}(x), & 0\le x\le L,\\ c_{\mathrm{d,r}}, & x\ge L, \end{cases}$$

$$f_{\mathrm{k}}(x,w)=\begin{cases} k_{\mathrm{d,l}}w_{\mathrm{l}}, & x\le 0,\\ f_{\mathrm{k,c}}(x,w), & 0\le x\le L,\\ k_{\mathrm{d,r}}w_{\mathrm{r}}, & x\ge L, \end{cases}$$

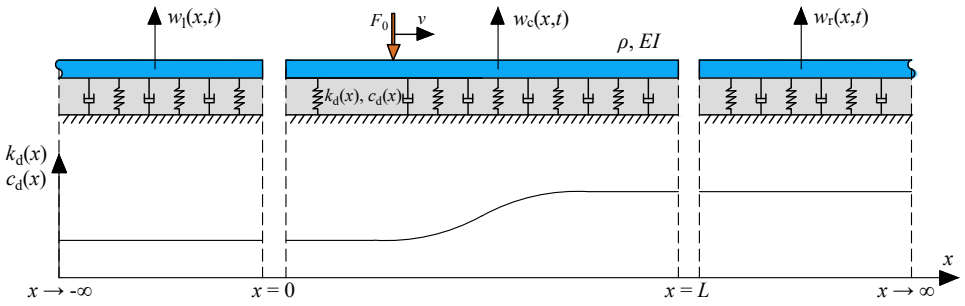

Figure 6.3: Model schematics: infinite Euler-Bernoulli beam supported by an inhomogeneous and nonlinear Kelvin foundation, subjected to a moving constant load.

where $f_k(x, w)$ is the force exerted by the foundation (only the part related to stiffness and not to damping), which is described in detail in Section 6.1, and x_e is the location of the moving load at $t = 0$ (in all previous chapters this was assumed to be zero); all other parameters and variables are introduced in Section 4.1.

As interface conditions between the domains, continuity in displacement and slope, as well as in shear force and bending moment is imposed. The set of boundary conditions is completed by imposing that, due to the presence of damping, the displacements of the left and right domains are zero as x tends to negative and positive infinity, respectively. The interface and boundary conditions are given in Eqs. (4.4)–(4.8).

For computational efficiency, the simulation is performed for the time interval when the moving load is close to and inside the transition zone. Therefore, the choice of initial conditions is crucial for ensuring that the infinite extent of the model is respected. Assuming that the system is initially in the linear regime ($w(x, t = 0) < w_{el}$), the input initial conditions are based on the eigenfield of the approaching load, as done in Chapter 4. In this section, these initial conditions are referred to as the *input* initial conditions w^{in} and $\dot{w}^{in}$, to differentiate them from other initial conditions that will become clear in the next sections. The input initial conditions are given in Eqs. (4.9)–(4.11). With these input initial conditions, the system reaches the steady-state regime instantly at the start of the computation.

In the next section, the solution method is presented.

6.2.2. Locally inhomogeneous and nonlinear system–solution method

Several time-domain methods are available for obtaining the solution to a system representing a railway track with nonlinear behaviour of the foundation [e.g., 25, 30, 107, 114]. These methods are suitable for systems that exhibit nonlinear behaviour continuously throughout the simulation. An alternative method is using the Laplace transform sequentially, as shown by Hoving and Metrikine [118]. The main condition for this method to be applicable is that the system's behaviour is piecewise linear, implying that the system behaves linearly between the moments at which its parameters, being functions of the field variables (displacements,

velocities, etc.), change abruptly (i.e., nonlinear events). This method has the potential of being computationally efficient for systems that have a limited number of nonlinear events.

In this section, the foundation's constitutive law is assumed to be bilinear elastic to allow for a clear and simple derivation. Nonetheless, for the results presented in this chapter (Section 6.3), the constitutive relation discussed in Section 6.1 is adopted. According to the bilinear elastic relation, the force provided by the springs in the Kelvin foundation is given by

$$f_{\mathrm{k,c}}(x,w) = \begin{cases} k^{\mathrm{A}}_{\mathrm{d,c}}(x)\, w_{\mathrm{c}}, & w_{\mathrm{c}} \le w_{\mathrm{el}}, \\ k^{\mathrm{B}}_{\mathrm{d,c}}(x)\, w_{\mathrm{c}} - \Delta k_{\mathrm{d,c}}(x)\, w_{\mathrm{el}}, & w_{\mathrm{c}} > w_{\mathrm{el}}, \end{cases} \tag{6.3}$$

where $k^{\mathrm{A}}_{\mathrm{d,c}}(x)$ and $k^{\mathrm{B}}_{\mathrm{d,c}}(x)$ represent the foundation stiffness related to the first and second branches of the bilinear constitutive law (see Fig. 6.2, considering just branches A and B for both loading and unloading), $\Delta k_{\mathrm{d,c}}(x) = k^{\mathrm{B}}_{\mathrm{d,c}}(x) - k^{\mathrm{A}}_{\mathrm{d,c}}(x)$ is the stiffness difference between the two branches, and w_{el} represents the *elastic displacement limit* at which the stiffness changes from branch A to branch B. Note that, due to the inhomogeneity, both stiffness parameters $k^{\mathrm{A}}_{\mathrm{d,c}}(x)$ and $k^{\mathrm{B}}_{\mathrm{d,c}}(x)$ are functions of space; however, the elastic displacement limit w_{el} is independent of the spatial coordinate.

Assuming that the system is in the linear regime at the start of the simulation and applying the Laplace transform over time to Eq. (6.2), the Laplace-domain equation of motion valid in the computational domain reads

$$EI\,\hat{w}''''_{\mathrm{c},1} + \left(\rho\, s^2 + c_{\mathrm{d,c}}(x)\, s + k^{\mathrm{A}}_{\mathrm{d,c}}(x)\right) \hat{w}_{\mathrm{c},1} = \hat{f}^{\mathrm{IC}}_1 + \hat{f}^{\mathrm{ML}}_1, \tag{6.4}$$

where $\hat{w}_{\mathrm{c},1}$ represents the unknown displacement of the computational domain in the Laplace domain; $s = \sigma + \mathrm{i}\omega$ is the Laplace variable, where σ is a small and positive real number and ω represents the angular frequency. Subscript 1 represents that the analysis is performed for the system before the elastic displacement limit w_{el} is exceeded for the first time. Furthermore, $\hat{f}^{\mathrm{ML}}_1$ represents the Laplace-domain force exerted by the moving load and $\hat{f}^{\mathrm{IC}}_1$ represents the forcing induced by the input initial conditions, and read

$$\hat{f}^{\mathrm{ML}}_1 = -\frac{F_0}{v}\, \mathrm{e}^{-s\frac{x-x_{\mathrm{e}}}{v}}, \tag{6.5}$$

$$\hat{f}^{\mathrm{IC}}_1 = \rho\left(s\, w^{\mathrm{in}}_{\mathrm{c}} + \dot{w}^{\mathrm{in}}_{\mathrm{c}}\right) + c_{\mathrm{d,c}}(x)\, w^{\mathrm{in}}_{\mathrm{c}}. \tag{6.6}$$

Because of the spatial variation of the foundation stiffness and damping, Eq. (6.4) cannot be solved analytically for all stiffness and damping profiles. Therefore, the fourth-order spatial derivative is approximated using the Finite Difference Method. A central difference scheme of order $O(\Delta x^6)$ is used inside the domain, and a hybrid between a central and a forward/backward scheme is used at the boundaries. The coefficients used for the Finite Difference discretization are given in Appendix D. As boundary conditions for the computational domain, the reaction forces delivered by the semi-infinite domains, namely the

bending moment (Eq. (4.6)) and the shear force (Eq. (4.7)), are employed. These reaction forces are derived in Section 6.2.3 by imposing the displacement (Eq. (4.4)) and slope (Eq. (4.5)) of the computational domain as boundary conditions for the semi-infinite domains. Note that for the non-reflective boundaries derived in Section 6.2.3 to be correct, the computational domain must behave linearly at the boundaries. Therefore, the length of the computational domain must be chosen such that the expected nonlinear behaviour is located between its boundaries. After applying the Finite Difference Method to discretise the computational domain, the Laplace-domain equation of motion reads

$$\left[K_{ij} + (\rho\, s^2 + c_{\mathrm{d,c},i}\, s + k_{\mathrm{d,c},1,i})\, I_{ij}\right] \hat{w}_{\mathrm{c},1,j} = \hat{f}^{\mathrm{IC}}_{1,i} + \hat{f}^{\mathrm{ML}}_{1,i} + \hat{f}^{\mathrm{B}}_{1,i}\,, \tag{6.7}$$

where K_{ij} represents the bending-stiffness matrix of the beam incorporating the contribution of the boundary conditions which is proportional to the unknown displacement, while $\hat{f}^{\mathrm{B}}_{1,i}$ represents the contribution of the boundary conditions independent of the unknown displacement, which is regarded as an external forcing (see Section 6.2.3); I_{ij} is the identity matrix. The Laplace-domain displacement $\hat{w}_{\mathrm{c},1,j}$ is obtained by left-multiplying Eq. (6.7) by the inverse of the dynamic stiffness matrix (i.e., the term in the square brackets). Then, the inverse Laplace transform is numerically evaluated to obtain the solution in the time domain. Making use of the symmetry properties of the imaginary and real parts of the Laplace-domain spectrum, only positive frequencies are considered. For the results presented in this thesis, the trapezoidal rule is used to evaluate the integral numerically.

The obtained time-domain solution is correct until the first nonlinear event, defined as the moment in time at which the solution exceeds the elastic limit w_{el} at a certain location inside the computational domain. To obtain the correct solution after the first nonlinear event (i.e., time moment τ_1), the equation of motion of the computational domain, Eq. (6.2), is changed as follows:

- The foundation stiffness profile is modified by assigning the adequate stiffness to the nodes where the elastic limit has been exceeded.
- A new time variable is introduced, namely $t_2 = t - \overline{\tau}_1$ for $t \geq \overline{\tau}_1$. Note that time t represents the global time. Furthermore, for clarity, the time moment of a nonlinear event in the global time axis t is represented with an overbar ($\overline{\tau}_n$), while in the local time axes t_n, this moment is indicated without the overbar (τ_n). Fig. 6.4 offers a graphical representation of the different time axes and nonlinear events.
- To ensure continuity, the displacement and velocity of the previous system at τ_1 are prescribed as initial conditions for the new system:

$$w_{\mathrm{c},2}(x, t_2 = 0) = w_{\mathrm{c},1}(x, t = \tau_1), \tag{6.8}$$

$$\dot{w}_{\mathrm{c},2}(x, t_2 = 0) = \dot{w}_{\mathrm{c},1}(x, t = \tau_1). \tag{6.9}$$

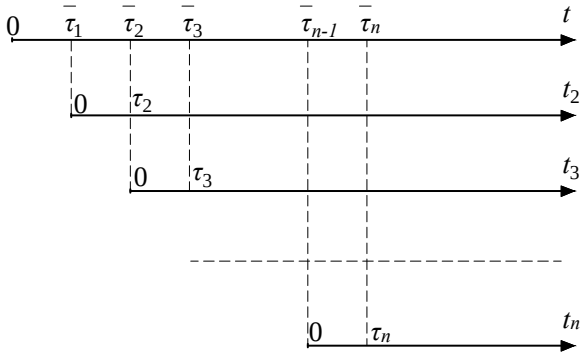

Figure 6.4: Definition of the time intervals and the local and global (overbar) nonlinear events.

Note that these initial conditions differ from the input initial conditions defined in Section 6.2.1.

- The boundary conditions are updated, as shown in Section 6.2.3.
- The position of the moving load is updated accordingly.

The updated system behaves again linearly until the next nonlinear event. Therefore, the forward Laplace transform is applied with respect to the new time variable t_2. The Laplace-domain equation of motion of the new system reads

$$\left[K_{ij} + (\rho\, s_2^2 + c_{\mathrm{d,c},2,i}\, s_2 + k_{\mathrm{d,c},2,i}) I_{ij}\right] \hat{w}_{\mathrm{c},2,j} = \hat{f}_{2,i}^{\mathrm{IC}} + \hat{f}_{2,i}^{\mathrm{ML}} + \hat{f}_{2,i}^{\mathrm{NL}} + \hat{f}_{2,i}^{\mathrm{B}}, \tag{6.10}$$

where s_2 represents the Laplace variable associated with the new time variable t_2, $\hat{w}_{\mathrm{c},2}$ is the unknown Laplace-domain displacement of the new system and subscript 2 represents that the analysis is performed for the system in the second time interval. The term $\hat{f}_{2,i}^{\mathrm{ML}}$ is associated with the moving load acting on the new system, while the initial conditions for the new time interval are accounted through $\hat{f}_{2,i}^{\mathrm{IC}}$; their expressions are given in the following:

$$\hat{f}_{2,i}^{\mathrm{ML}} = -\frac{F_0}{v}\, \mathrm{e}^{-s_2\left(\frac{x_i - x_{\mathrm{e}}}{v} - \overline{\tau}_1\right)}\, H\!\left(\frac{x_i - x_{\mathrm{e}}}{v} - \overline{\tau}_1\right), \tag{6.11}$$

$$\hat{f}_{2,i}^{\mathrm{IC}} = \rho\left(s_2\, w_{\mathrm{c},1,i}(\tau_1) + \dot{w}_{\mathrm{c},1,i}(\tau_1)\right) + c_{\mathrm{d,c},i}\, w_{\mathrm{c},1,i}(\tau_1). \tag{6.12}$$

The Laplace-domain force exerted by the foundation is split into its contribution proportional to the unknown displacement, $k_{\mathrm{d,c},2,i}\, \hat{w}_2$, and the one independent of the unknown displacement, which is accounted for through the external force $\hat{f}_2^{\mathrm{NL}}$, with superscript NL standing for nonlinear:

$$k_{\mathrm{d,c},2,i}\, \hat{w}_{\mathrm{c},2,i} = \begin{cases} k_{\mathrm{d,c},i}^{\mathrm{A}}\, \hat{w}_{\mathrm{c},2,i}, & w_{\mathrm{c},2,i}(t_2 = 0) \le w_{\mathrm{el}}, \\ k_{\mathrm{d,c},i}^{\mathrm{B}}\, \hat{w}_{\mathrm{c},2,i}, & w_{\mathrm{c},2,i}(t_2 = 0) > w_{\mathrm{el}}, \end{cases} \tag{6.13}$$

$$\hat{f}_{2,i}^{\mathrm{NL}} = \begin{cases} 0, & w_{\mathrm{c},2,i}(t_2 = 0) \leq w_{\mathrm{el}}, \\ \frac{\Delta k_{\mathrm{d,c},i}\, w_{\mathrm{el}}}{s_2}, & w_{\mathrm{c},2,i}(t_2 = 0) > w_{\mathrm{el}}. \end{cases} \tag{6.14}$$

The solution of the new system is obtained in the same manner as for the previous one. Moreover, the procedure of searching for the next nonlinear event, modifying the system and then solving it using the Laplace transform, is repeated. To this end, the procedure is generalized. The Laplace-domain equation of motion for the n-th time interval reads

$$\left[K_{ij} + (\rho\, s_n^2 + c_{\mathrm{d,c},i}\, s_n + k_{\mathrm{d,c},n,i})\, I_{ij}\right] \hat{w}_{\mathrm{c},n,j} = \hat{f}_{n,i}^{\mathrm{IC}} + \hat{f}_{n,i}^{\mathrm{ML}} + \hat{f}_{n,i}^{\mathrm{NL}} + \hat{f}_{n,i}^{\mathrm{B}}, \tag{6.15}$$

where the generalized moving-load and initial-conditions forces are given as

$$\hat{f}_{n,i}^{\mathrm{ML}} = -\frac{F_0}{v}\, \mathrm{e}^{-s_n\left(\frac{x_i - x_{\mathrm{e}}}{v} - \overline{\tau}_{n-1}\right)}\, H\!\left(\frac{x_i - x_{\mathrm{e}}}{v} - \overline{\tau}_{n-1}\right), \tag{6.16}$$

$$\hat{f}_{n,i}^{\mathrm{IC}} = \rho\left(s_n\, w_{\mathrm{c},n-1,i}(\tau_{n-1}) + \dot{w}_{\mathrm{c},n-1,i}(\tau_{n-1})\right) + c_{\mathrm{d,c},i}\, w_{\mathrm{c},n-1,i}(\tau_{n-1}). \tag{6.17}$$

The described procedure is repeated until the whole solution is obtained in the time domain. The discretised displacement of the computational domain thus becomes

$$w_{\mathrm{c},j}(t) = \left[w_{\mathrm{c},1,j}(0, ..., \tau_1 - \Delta t),\ w_{\mathrm{c},2,j}(0, ..., \tau_2 - \Delta t), \ldots, w_{\mathrm{c},N,j}(0, ..., t_{\max} - \overline{\tau}_{N-1})\right], \tag{6.18}$$

where Δt is the time spacing, N is the index of the last time interval and $t_{\max}$ is the final moment in time of the simulation.

To obtain correct results, the continuity of displacements and velocities at the nonlinear events is of crucial importance. However, the Laplace-domain spectra of the two quantities exhibit a poor decay due to the applied initial conditions. Consequently, the numerical integration must be performed up to very high frequencies leading to a significant computational effort. In the following section, a method of incorporating the high frequencies without increasing the computational effort is presented.

Improvement of the frequency-spectra decay

The high-frequency regime of the Laplace-domain displacement, obtained from Eq. (6.15), is dominated by the initial conditions as follows:

$$\hat{w}_{\mathrm{c},n,j} \sim \frac{w_{\mathrm{c},n-1,j}(\tau_{n-1})}{\sigma + \mathrm{i}\omega_n} + \frac{\dot{w}_{\mathrm{c},n-1,j}(\tau_{n-1})}{(\sigma + \mathrm{i}\omega_n)^2}, \quad \omega_n \to \infty. \tag{6.19}$$

Similarly, the Laplace-domain velocity $\hat{v}_{\mathrm{c},n,j}$ in the high-frequency regime reads

$$\hat{v}_{\mathrm{c},n,j} \sim \frac{\dot{w}_{\mathrm{c},n-1,j}(\tau_{n-1})}{\sigma + \mathrm{i}\omega_n} + \frac{\ddot{w}_{\mathrm{c},n-1,j}(\tau_{n-1})}{(\sigma + \mathrm{i}\omega_n)^2}, \quad \omega_n \to \infty. \tag{6.20}$$

The initial displacement, velocity and acceleration in the numerators of Eqs. (6.19) and (6.20) are clearly independent of frequency. Therefore, the Laplace-domain spectra are dominated by the expressions in the denominator, exhibiting the slow decay proportional to $1/\omega_n$.

To incorporate the high frequencies without the need to integrate numerically up to very high frequencies, the *high-frequency approximations*, Eqs. (6.19) and (6.20), could be subtracted from $\hat{w}_{\mathrm{c},n,j}$ and $\hat{v}_{\mathrm{c},n,j}$, respectively. However, in doing so, a high peak is introduced in the remaining frequency spectra close to $\omega_n = 0$, which would require a very small step in frequency for obtaining accurate results. To overcome this issue, the high-frequency approximations are only subtracted over part of the frequency axis $\omega_n \geq \omega_{\mathrm{A}}$. The only criteria for choosing ω_{A} is that it is sufficiently distant from the origin $\omega_n = 0$ to ensure that the resulting spectrum does not exhibit a high peak. The Laplace-domain displacement and velocity can now be expressed as

$$\hat{w}_{\mathrm{c},n,j} = \hat{w}^{\mathrm{imp}}_{\mathrm{c},n,j} + \frac{w_{\mathrm{c},n-1,j}(\tau_{n-1})}{\sigma + \mathrm{i}\omega_n} H(\omega_n - \omega_{\mathrm{A}}) + \frac{\dot{w}_{\mathrm{c},n-1,j}(\tau_{n-1})}{(\sigma + \mathrm{i}\omega_n)^2} H(\omega_n - \omega_{\mathrm{A}}), \tag{6.21}$$

$$\hat{v}_{\mathrm{c},n,j} = \hat{v}^{\mathrm{imp}}_{\mathrm{c},n,j} + \frac{\dot{w}_{\mathrm{c},n-1,j}(\tau_{n-1})}{\sigma + \mathrm{i}\omega_n} H(\omega_n - \omega_{\mathrm{A}}) + \frac{\ddot{w}_{\mathrm{c},n-1,j}(\tau_{n-1})}{(\sigma + \mathrm{i}\omega_n)^2} H(\omega_n - \omega_{\mathrm{A}}), \tag{6.22}$$

where $\hat{w}^{\mathrm{imp}}_{\mathrm{c},n,j}$ and $\hat{v}^{\mathrm{imp}}_{\mathrm{c},n,j}$ represent the improved (i.e., with strong decay) Laplace-domain domain expressions of the displacement and velocity, respectively. To obtain the time-domain response, the inverse Laplace transform is evaluated numerically for the improved expressions, and analytically for the high-frequency approximations, as follows:

$$w_{\mathrm{c},n,j} = \frac{1}{\pi}\int_0^{\omega_{\max}} \mathrm{Re}\left(\hat{w}^{\mathrm{imp}}_{\mathrm{c},n,j}\, \mathrm{e}^{s_n t_n}\right) \mathrm{d}\omega_n + w_{\mathrm{c},n-1,j}(\tau_{n-1})\, I_{\mathrm{a}}(t_n) + \dot{w}_{\mathrm{c},n-1,j}(\tau_{n-1})\, I_{\mathrm{b}}(t_n), \tag{6.23}$$

$$\dot{w}_{\mathrm{c},n,j} = \frac{1}{\pi}\int_0^{\omega_{\max}} \mathrm{Re}\left(\hat{v}^{\mathrm{imp}}_{\mathrm{c},n,j}\, \mathrm{e}^{s_n t_n}\right) \mathrm{d}\omega_n + \dot{w}_{\mathrm{c},n-1,j}(\tau_{n-1})\, I_{\mathrm{a}}(t_n) + \ddot{w}_{\mathrm{c},n-1,j}(\tau_{n-1})\, I_{\mathrm{b}}(t_n), \tag{6.24}$$

where $\omega_{\max}$ represents the maximum frequency of integration, while $I_{\mathrm{a}}(t_n)$ and $I_{\mathrm{b}}(t_n)$ represent the time-domain images of the high-frequency approximations divided by the corresponding initial-condition terms. Their expressions are not presented here for brevity; however, they can be easily computed using a symbolic mathematics tool (e.g., Maple).

By evaluating the inverse Laplace transform analytically for the high-frequency approximations, frequencies up to infinity are actually included, which represents an improvement not just in computational time, but also in accuracy (although the results are still approximations since $\hat{w}^{\mathrm{imp}}_{\mathrm{c},n,j}$ and $\hat{v}^{\mathrm{imp}}_{\mathrm{c},n,j}$ are not completely zero at $\omega_{\max}$). Using the improvement presented in this section, the solution obeys the continuity conditions (i.e., displacement and velocity) imposed at nonlinear events. The input initial conditions and the non-reflective boundary conditions are derived in the next section.

6.2.3. Non-reflective boundary conditions

In Section 6.2.2, the boundary conditions for the computational domain, imposed bending moment (Eq. (4.6)) and shear force (Eq. (4.7)), are kept general. In this section, the reaction forces of the semi-infinite domains at the interfaces with the computational domain are derived. When these forces are prescribed as boundary conditions of the computational domain, the finite system will behave exactly as the infinite one. Therefore, these interface reaction forces constitute non-reflective boundary conditions for the computational domain. The goal is to express the interface reaction forces (bending moment and shear force) of the left and right domains as functions of the unknown displacement and slope of the computational domain at the corresponding interfaces. The procedure is similar to the one in Section 4.2.3, but the application of the Laplace transform sequentially causes some differences in the approach, which is explained in the following.

The forward Laplace transform is applied over time t_n to the equation of motion of the left and right semi-infinite domains (Eq. (6.2)):

$$\hat{w}''''_{h,n} - k_h^4\, \hat{w}_{h,n} = \tfrac{1}{EI}\left(\hat{f}^{\mathrm{IC}}_{h,n} + \hat{f}^{\mathrm{ML}}_{h,n}\right), \qquad h = \{\mathrm{l}, \mathrm{r}\}, \tag{6.25}$$

where $\hat{w}_{\mathrm{l},n}$ and $\hat{w}_{\mathrm{r},n}$ represent the unknown Laplace-domain displacements of the left and right semi-infinite domains, respectively, for the n-th time interval, and $\hat{f}^{\mathrm{ML}}_{h,n}$ represents the Laplace-domain moving load given by Eq. (6.16), but with a continuous spatial coordinate x. Note that $\hat{f}^{\mathrm{ML}}_{h,n}$ is non-zero only if the moving load is acting on the corresponding domain. k_{l} and k_{r} represent the wavenumbers of the two semi-infinite domains and their expressions are given in Eq. (4.30). Furthermore, $\hat{f}^{\mathrm{IC}}_{h,n}$ represents the Laplace-domain initial-conditions forces given by

$$\hat{f}^{\mathrm{IC}}_{h,n}(x, s_n) = (\rho s_n + c_{\mathrm{d},h})\, w_h(x, \overline{\tau}_{n-1}) + \rho\, \dot{w}_h(x, \overline{\tau}_{n-1}), \quad h = \{\mathrm{l}, \mathrm{r}\}. \tag{6.26}$$

At infinity, the condition of zero displacements (Eq. (4.8)) is imposed, while at the interfaces the unknown Laplace-domain displacement and slope of the computational domain are prescribed:

$$\hat{w}_{\mathrm{l},n}(0, s_n) = \hat{w}_n(0, s_n), \qquad \hat{w}_{\mathrm{r},n}(L, s_n) = \hat{w}(L, s_n), \tag{6.27}$$

$$\hat{w}'_{\mathrm{l},n}(0, s_n) = \hat{w}'_n(0, s_n), \qquad \hat{w}'_{\mathrm{r},n}(L, s_n) = \hat{w}'_n(L, s_n). \tag{6.28}$$

The Laplace-domain displacement of the two semi-infinite domains can be obtained by solving Eq. (6.25) with the above discussed boundary conditions. By taking the second- and third-order derivatives with respect to space and evaluating them at the interfaces, the reaction forces of the two semi-infinite domains are expressed as functions of the displacement and slope of the computational domain prescribed at the corresponding

interfaces:

$$\begin{pmatrix} \hat{w}'''_{\mathrm{l},n}(0,s_n) \\ \hat{w}''_{\mathrm{l},n}(0,s_n) \end{pmatrix} = \begin{pmatrix} \hat{k}_{\mathrm{l,V}\upsilon} & \hat{k}_{\mathrm{l,V}\phi} \\ \hat{k}_{\mathrm{l,M}\upsilon} & \hat{k}_{\mathrm{l,M}\phi} \end{pmatrix} \begin{pmatrix} \hat{w}_n(0,s_n) \\ \hat{w}'_n(0,s_n) \end{pmatrix} - \hat{\mathbf{b}}^{\mathrm{IC}}_{\mathrm{l},n} - \hat{\mathbf{b}}^{\mathrm{ML}}_{\mathrm{l},n}, \tag{6.29}$$

$$\begin{pmatrix} \hat{w}'''_{\mathrm{r},n}(L,s_n) \\ \hat{w}''_{\mathrm{r},n}(L,s_n) \end{pmatrix} = \begin{pmatrix} \hat{k}_{\mathrm{r,V}\upsilon} & \hat{k}_{\mathrm{r,V}\phi} \\ \hat{k}_{\mathrm{r,M}\upsilon} & \hat{k}_{\mathrm{r,M}\phi} \end{pmatrix} \begin{pmatrix} \hat{w}_n(L,s_n) \\ \hat{w}'_n(L,s_n) \end{pmatrix} - \hat{\mathbf{b}}^{\mathrm{IC}}_{\mathrm{r},n} - \hat{\mathbf{b}}^{\mathrm{ML}}_{\mathrm{r},n}, \tag{6.30}$$

where the entries of the matrices represent the dynamic stiffness coefficients giving rise to the boundary forces proportional to the unknown displacement and slope at the boundary; subscript V stands for shear force, M for bending moment, υ for translation and ϕ for rotation. The coefficients are given by Eqs. (4.33) and (4.34).

In addition, $\hat{\mathbf{b}}^{\mathrm{IC}}_{\mathrm{l},n}$ and $\hat{\mathbf{b}}^{\mathrm{IC}}_{\mathrm{r},n}$ are vectors containing the influence of the initial conditions (Eq. (6.26)) on the reaction forces, giving rise to boundary forces independent of the unknown displacement and slope of the computational domain. The two vectors are given by the following expressions:

$$\hat{\mathbf{b}}^{\mathrm{IC}}_{\mathrm{l},n} = \begin{pmatrix} \hat{w}'''_{\mathrm{l},n,\mathrm{p}}(0,s_n) \\ \hat{w}''_{\mathrm{l},n,\mathrm{p}}(0,s_n) \end{pmatrix} + \begin{pmatrix} \hat{k}_{\mathrm{l,V}\upsilon} & \hat{k}_{\mathrm{l,V}\phi} \\ \hat{k}_{\mathrm{l,M}\upsilon} & \hat{k}_{\mathrm{l,M}\phi} \end{pmatrix} \begin{pmatrix} \hat{w}_{\mathrm{l},n,\mathrm{p}}(0,s_n) \\ \hat{w}'_{\mathrm{l},n,\mathrm{p}}(0,s_n) \end{pmatrix}, \tag{6.31}$$

$$\hat{\mathbf{b}}^{\mathrm{IC}}_{\mathrm{r},n} = \begin{pmatrix} \hat{w}'''_{\mathrm{r},n,\mathrm{p}}(L,s_n) \\ \hat{w}''_{\mathrm{r},n,\mathrm{p}}(L,s_n) \end{pmatrix} + \begin{pmatrix} \hat{k}_{\mathrm{r,V}\upsilon} & \hat{k}_{\mathrm{r,V}\phi} \\ \hat{k}_{\mathrm{r,M}\upsilon} & \hat{k}_{\mathrm{r,M}\phi} \end{pmatrix} \begin{pmatrix} \hat{w}_{\mathrm{r},n,\mathrm{p}}(L,s_n) \\ \hat{w}'_{\mathrm{r},n,\mathrm{p}}(L,s_n) \end{pmatrix}, \qquad \overline{\tau}_{n-1} \leq \frac{L-x_\mathrm{e}}{\upsilon}, \tag{6.32}$$

where $\hat{w}_{\mathrm{l},n,\mathrm{p}}(0,s_n)$ and $\hat{w}_{\mathrm{r},n,\mathrm{p}}(L,s_n)$ are the particular solutions that account for the initial-conditions forcing in Eq. (6.25).

Similar to $\hat{\mathbf{b}}^{\mathrm{IC}}_{\mathrm{l},n}$ and $\hat{\mathbf{b}}^{\mathrm{IC}}_{\mathrm{r},n}$, vectors $\hat{\mathbf{b}}^{\mathrm{ML}}_{\mathrm{l},n}$ and $\hat{\mathbf{b}}^{\mathrm{ML}}_{\mathrm{r},n}$ contain the contribution of the moving load to the reaction forces (they are non-zero only when the moving load is present in the corresponding domain), and they read

$$\hat{\mathbf{b}}^{\mathrm{ML}}_{\mathrm{l},n} = \begin{pmatrix} \hat{V}^0(s) \\ \hat{M}^0(s) \end{pmatrix}, \qquad \hat{\mathbf{b}}^{\mathrm{ML}}_{\mathrm{r},n} = \begin{pmatrix} \hat{V}^{\mathrm{L}}(s) \\ \hat{M}^{\mathrm{L}}(s) \end{pmatrix}, \tag{6.33}$$

$$\hat{V}^{\mathrm{L}}_n(s_n) = \frac{\mathrm{i}F_0\big(s_n + (1+\mathrm{i})k_\mathrm{r}\upsilon\big)}{EI(k_\mathrm{r}\upsilon + s_n)(k_\mathrm{r}\upsilon - \mathrm{i}s_n)}\,\mathrm{e}^{-s_n\left(\frac{L-x_\mathrm{e}}{\upsilon} - \overline{\tau}_{n-1}\right)}, \qquad \overline{\tau}_{n-1} \leq \frac{L-x_\mathrm{e}}{\upsilon}, \tag{6.34}$$

$$\hat{M}^{\mathrm{L}}_n(s_n) = \frac{-\mathrm{i}F_0\upsilon}{EI(k_\mathrm{r}\upsilon + s_n)(k_\mathrm{r}\upsilon - \mathrm{i}s_n)}\,\mathrm{e}^{-s_n\left(\frac{L-x_\mathrm{e}}{\upsilon} - \overline{\tau}_{n-1}\right)}, \qquad \overline{\tau}_{n-1} \leq \frac{L-x_\mathrm{e}}{\upsilon}, \tag{6.35}$$

where $\hat{V}^{\mathrm{L}}_n$ and $\hat{M}^{\mathrm{L}}_n$ are the shear force and bending moment, respectively, exerted by the moving load on the right boundary after it has entered the right semi-infinite domain. Note that $\hat{\mathbf{b}}^{\mathrm{IC}}_{\mathrm{r},n}$, $\hat{V}^{\mathrm{L}}_n$ and $\hat{M}^{\mathrm{L}}_n$ as given in Eqs. (6.32) to (6.35), respectively, are valid for $\overline{\tau}_{n-1} \leq \frac{L-x_\mathrm{e}}{\upsilon}$, meaning that the nonlinear events occur while the moving load is inside the computational domain (they still correctly describe the dynamics when the load is in the right domain, up to the moment a nonlinear event occurs). When nonlinear events occur while the moving

load is in the right domain, this is divided into two domains, one behind the load and one in front, rendering the expressions for $\hat{\mathbf{b}}^{\mathrm{IC}}_{\mathrm{r},n}$, $\hat{V}^{\mathrm{L}}_n$ and $\hat{M}^{\mathrm{L}}_n$ lengthy for $\overline{\tau}_{n-1} > \frac{L-x_{\mathrm{e}}}{v}$. Therefore, these expressions are given in Appendix E. In all scenarios considered in this chapter $x_{\mathrm{e}} = 0$, implying that $\hat{V}^0 = 0$ and $\hat{M}^0 = 0$. In other situations, they can be obtained following the same procedure explained in Appendix E for $\hat{V}^{\mathrm{L}}$ and $\hat{M}^{\mathrm{L}}$.

To obtain the particular solutions in Eqs. (6.31) and (6.32), the Green's-function approach is used as follows:

$$\hat{w}_{\mathrm{l},n,\mathrm{p}}(x, s_n) = \int_{-\infty}^{0} \hat{g}_{\mathrm{l}}(x-\xi, s_n)\, \hat{f}^{\mathrm{IC}}_{\mathrm{l},n}(\xi, s_n)\, \mathrm{d}\xi, \tag{6.36}$$

$$\hat{w}_{\mathrm{r},n,\mathrm{p}}(x, s_n) = \int_{L}^{\infty} \hat{g}_{\mathrm{r}}(x-\xi, s_n)\, \hat{f}^{\mathrm{IC}}_{\mathrm{r},n}(\xi, s_n)\, \mathrm{d}\xi, \tag{6.37}$$

where $\hat{g}_{\mathrm{l}}(x-\xi, s_n)$ and $\hat{g}_{\mathrm{r}}(x-\xi, s_n)$ are the Laplace-domain Green's functions of two infinite domains having the same properties as the corresponding semi-infinite ones. The particular solutions are needed only at the interfaces, as seen in Eqs. (6.31) and (6.32). Therefore, excitation variable ξ is smaller than or equal to the observation point $x = 0$ for the left domain and ξ is larger than or equal to $x = L$ for the right domain. Consequently, the Green's functions are given by [50]

$$\hat{g}_{\mathrm{l}}(x-\xi, s_n) = -\frac{1}{k_{\mathrm{l}}^3}\left(\mathrm{i}\mathrm{e}^{-\mathrm{i}k_{\mathrm{l}}(x-\xi)} + \mathrm{e}^{-k_{\mathrm{l}}(x-\xi)}\right), \tag{6.38}$$

$$\hat{g}_{\mathrm{r}}(x-\xi, s_n) = -\frac{1}{k_{\mathrm{r}}^3}\left(\mathrm{i}\mathrm{e}^{-\mathrm{i}k_{\mathrm{r}}(\xi-x)} + \mathrm{e}^{-k_{\mathrm{r}}(\xi-x)}\right). \tag{6.39}$$

Now, the only unknowns left for deriving the non-reflective boundary conditions are the initial conditions of the two semi-infinite domains in Eq. (6.26). The state (i.e., displacement field and velocity field) of the two domains at time moment $\overline{\tau}_{n-1}$ consists of a superposition of the eigenfield and the waves generated inside the computational domain which have propagated to the two semi-infinite domains, referred to as the *free field* w^{f}. The eigenfield's contribution can be evaluated analytically by equating global time t to $\overline{\tau}_{n-1}$ in Eq. (2.19) and in its time derivative, and inserting the relevant medium parameters. The state of the two domains as induced by the free field can be obtained by solving two boundary-value problems for the two domains with the time history of the free-field displacement and slope of the computational domain observed at the boundaries prescribed as boundary conditions (Fig. 6.5). The free-field displacement at the boundaries is obtained by subtracting the eigenfield from the displacement of the computational domain (Eq. (6.18)), which is known until time moment $\overline{\tau}_{n-1}$:

$$w^{\mathrm{f}}_{\mathrm{c}}(0; t = 0, \ldots, \overline{\tau}_{n-1}) = w_{\mathrm{c}}(0; t = 0, \ldots, \overline{\tau}_{n-1}) - w^{\mathrm{e}}(0; t = 0, \ldots, \overline{\tau}_{n-1}), \tag{6.40}$$

$$w^{\mathrm{f}}_{\mathrm{c}}(L; t = 0, \ldots, \overline{\tau}_{n-1}) = w_{\mathrm{c}}(L; t = 0, \ldots, \overline{\tau}_{n-1}) - w^{\mathrm{e}}(L; t = 0, \ldots, \overline{\tau}_{n-1}). \tag{6.41}$$

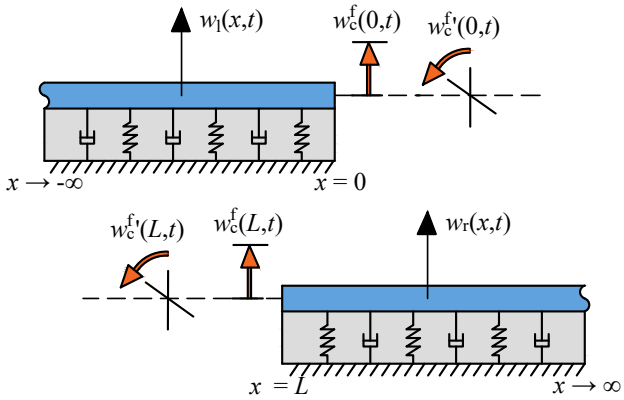

Figure 6.5: Time-domain boundary value problems to be solved for obtaining the initial states of the left and right domains due to the free-field at time moment $t = \overline{\tau}_{n-1}$.

After computing the free-field slopes numerically, the boundary-value problems needed to determine the state of the left and right domains (Fig. 6.5) are solved using the Laplace transform over global time t. Note that $w_c^f(0, t > \overline{\tau}_{n-1})$ and $w_c^f(L, t > \overline{\tau}_{n-1})$ are still unknown and by default equal to zero. Consequently, the discontinuity in the free-field displacements and slopes at $\overline{\tau}_{n-1}$ introduces high-frequency content in its Laplace-domain counterparts. To avoid this, an artificial smooth continuation is imposed on the free-field displacements and slopes for $t > \overline{\tau}_{n-1}$, which does not affect the response for $t \le \overline{\tau}_{n-1}$. Then, the Laplace-domain free-field displacements are given as follows:

$$\hat{w}_l^f(x,s) = C_l\, e^{ik_l x} + D_l\, e^{k_l x}, \tag{6.42}$$

$$\hat{w}_r^f(x,s) = C_r\, e^{-ik_r x} + D_r\, e^{-k_r x}, \tag{6.43}$$

where C_l, D_l, C_r and D_r represent complex-valued amplitudes which read

$$C_l = \frac{1+i}{2k_l}[k_l\, \hat{w}_c^f(0,s) - \hat{w}_c^{f\prime}(0,s)], \qquad D_l = \frac{1-i}{2k_l}[k_l\, \hat{w}_c^f(0,s) + i\hat{w}_c^{f\prime}(0,s)], \tag{6.44}$$

$$C_r = \frac{1+i}{2k_r}[k_r\, \hat{w}_c^f(L,s) - \hat{w}_c^{f\prime}(L,s)]\, e^{ik_r L}, \qquad D_r = \frac{1-i}{2k_r}[k_r\, \hat{w}_c^f(L,s) - i\hat{w}_c^{f\prime}(L,s)]\, e^{k_r L}. \tag{6.45}$$

Note that the forward Laplace transform is applied with respect to the time variable t because the displacement and slope imposed as boundary conditions act from the time moment $t = 0$ until $t = \overline{\tau}_{n-1}$. Therefore, $\hat{w}_c^f(0,s)$ and $\hat{w}_c^f(L,s)$ represent Laplace-domain history contributions for the new system and need to be computed for each nonlinear event.

To obtain the time-domain displacement and velocity of the two semi-infinite domains needed in Eq. (6.26) and thus for the derivation of the non-reflective boundary conditions, the inverse Laplace transform is applied to Eqs. (6.42), (6.43) and the corresponding velocities,

and is evaluated at $\overline{\tau}_{n-1}$:

$$w_{\mathrm{l}}(x,\overline{\tau}_{n-1}) = \frac{1}{2\pi \mathrm{i}} \int_{\sigma-\mathrm{i}\infty}^{\sigma+\mathrm{i}\infty} \hat{w}_{\mathrm{l}}^{\mathrm{f}}(x,s)\, \mathrm{e}^{s\overline{\tau}_{n-1}} \mathrm{d}s + w^{\mathrm{e}}(x,\overline{\tau}_{n-1}), \tag{6.46}$$

$$\dot{w}_{\mathrm{l}}(x,\overline{\tau}_{n-1}) = \frac{1}{2\pi \mathrm{i}} \int_{\sigma-\mathrm{i}\infty}^{\sigma+\mathrm{i}\infty} s\, \hat{w}_{\mathrm{l}}^{\mathrm{f}}(x,s)\, \mathrm{e}^{s\overline{\tau}_{n-1}} \mathrm{d}s + \dot{w}^{\mathrm{e}}(x,\overline{\tau}_{n-1}), \tag{6.47}$$

$$w_{\mathrm{r}}(x,\overline{\tau}_{n-1}) = \frac{1}{2\pi \mathrm{i}} \int_{\sigma-\mathrm{i}\infty}^{\sigma+\mathrm{i}\infty} \hat{w}_{\mathrm{r}}^{\mathrm{f}}(x,s)\, \mathrm{e}^{s\overline{\tau}_{n-1}} \mathrm{d}s + w^{\mathrm{e}}(x,\overline{\tau}_{n-1}), \tag{6.48}$$

$$\dot{w}_{\mathrm{r}}(x,\overline{\tau}_{n-1}) = \frac{1}{2\pi \mathrm{i}} \int_{\sigma-\mathrm{i}\infty}^{\sigma+\mathrm{i}\infty} s\, \hat{w}_{\mathrm{r}}^{\mathrm{f}}(x,s)\, \mathrm{e}^{s\overline{\tau}_{n-1}} \mathrm{d}s + \dot{w}^{\mathrm{e}}(x,\overline{\tau}_{n-1}). \tag{6.49}$$

The particular solutions are now obtained by substituting Eqs. (6.46) to (6.49) in Eq. (6.26), and Eq. (6.26) in Eqs. (6.36) and (6.37), and then changing the order of integration:

$$\begin{aligned}\hat{w}_{\mathrm{l},n,\mathrm{p}}(x,s_n) = &\frac{1}{2\pi \mathrm{i}} \int_{\sigma-\mathrm{i}\infty}^{\sigma+\mathrm{i}\infty} (\rho s_n + c_{\mathrm{d,l}} + \rho s)\, \mathrm{e}^{s\overline{\tau}_{n-1}} \cdot \int_{-\infty}^{0} \hat{g}_{\mathrm{l}}(x-\xi,s_n)\, \hat{w}_{\mathrm{l}}^{\mathrm{f}}(\xi,s)\, \mathrm{d}\xi \mathrm{d}s \\ &+ \hat{w}_{\mathrm{l},n,\mathrm{p}}^{\mathrm{e}}(x,s_n),\end{aligned} \tag{6.50}$$

$$\begin{aligned}\hat{w}_{\mathrm{r},n,\mathrm{p}}(x,s_n) = &\frac{1}{2\pi \mathrm{i}} \int_{\sigma-\mathrm{i}\infty}^{\sigma+\mathrm{i}\infty} (\rho s_n + c_{\mathrm{d,r}} + \rho s)\, \mathrm{e}^{s\overline{\tau}_{n-1}} \cdot \int_{L}^{\infty} \hat{g}_{\mathrm{r}}(x-\xi,s_n)\, \hat{w}_{\mathrm{r}}^{\mathrm{f}}(\xi,s)\, \mathrm{d}\xi\, \mathrm{d}s \\ &+ \hat{w}_{\mathrm{r},n,\mathrm{p}}^{\mathrm{e}}(x,s_n),\end{aligned} \tag{6.51}$$

where $\hat{w}_{\mathrm{l},n,\mathrm{p}}^{\mathrm{e}}(x,s_n)$ and $\hat{w}_{\mathrm{r},n,\mathrm{p}}^{\mathrm{e}}(x,s_n)$ represent the particular solutions accounting for the parts of the eigenfield in the left and right domains, respectively, at $\overline{\tau}_{n-1}$. The integration over ξ can be performed analytically, while the inverse Laplace transform evaluated at $\overline{\tau}_{n-1}$ should be performed numerically. Moreover, the spatial derivatives needed in Eqs. (6.31) and (6.32) can be evaluated analytically.

The non-reflective boundary conditions for the computational domain, Eqs. (6.29) and (6.30) are now fully determined. The contribution of the boundary conditions which is proportional to the yet unknown displacement and slope is incorporated into the beam's bending stiffness matrix K_{ij} (see Eq. (6.15)), while the contribution which is independent of the unknown displacement and slope is accounted for through the boundary-forcing vector $\tilde{f}_{n,i}^{\mathrm{B}}$. As can be seen, the beam's bending stiffness matrix does not change from one system to the other; however, the boundary-forcing vector needs to be updated at each system change.

Although the obtained non-reflective boundary conditions have been derived for the moving-load problem, the same procedure can be applied for any arbitrary loading. Next, the Winkler foundation model used for the results presented in this chapter is described.

6.3. Results and discussion

Here, the proposed model is first verified by considering a limit case and comparing the obtained results to a semi-analytical solution. Then, the time-domain displacement field

Table 6.1: Values of the system parameters used to compute results in Chapter 6.

Parameter	Symbol	Value	Unit
Bending stiffness	EI	$6.42{\cdot}10^6$	Nm^2
Mass per unit length	ρ	268.33	kg/m
Moving-load magnitude	F_0	$80 \cdot 10^3$	N
Loading stiffness	$k^{\mathrm{A}}_{\mathrm{d,l}}$	$83.33{\cdot}10^6$	$\mathrm{N/m}^2$
Loading stiffness	$k^{\mathrm{B}}_{\mathrm{d,l}}$	$158.33 \cdot 10^6$	$\mathrm{N/m}^2$
Unloading stiffness	$k^{\mathrm{C}}_{\mathrm{d,l}}$	$233.33 \cdot 10^6$	$\mathrm{N/m}^2$
Unloading stiffness	$k^{\mathrm{D}}_{\mathrm{d,l}}$	$83.33{\cdot}10^6$	$\mathrm{N/m}^2$
Stiff-soft stiffness ratio	p	5	
Elastic displacement limit ratio	$w_{\mathrm{el}}/w^{\mathrm{e}}_{\mathrm{max}}$	1.1	
Moving load at $t = 0$	x_{e}	0	m

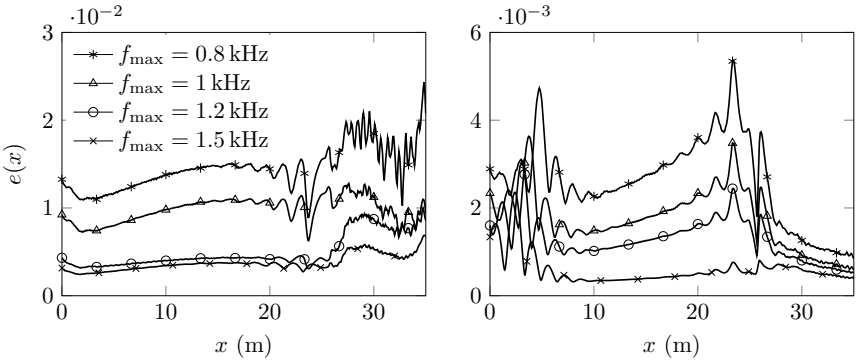

Figure 6.6: Error versus space for the linear limit case with imposed artificial nonlinear events (left panel) and without (right panel); $x_{\mathrm{tc}} = 25$ m, $v = 0.95\, c_{\mathrm{cr,l}}$, $\zeta = 0.05$.

is presented for two specific cases and the influence of the nonlinear foundation on the transition radiation is highlighted. Afterwards, the influence of the transition length, load velocity and stiffness ratio on the plastic deformation is assessed through a parametric study. Finally, the influence of the nonlinear foundation on the radiated energy and on the energy input is discussed. The parameters which are kept constant throughout the presented results are given in Table 6.1, while the ones which are varied are mentioned for each case individually.

6.3.1. Verification and convergence

To validate the solution derived in Section 6.2, a limit case is considered, in which the foundation is piecewise homogeneous and behaves linearly, but for which *artificial* nonlinear events are introduced in the solution. To this end, a soft-to-stiff case is considered where the foundation-stiffness coefficients $k^{\mathrm{B}}_{\mathrm{d,l}}$, $k^{\mathrm{C}}_{\mathrm{d,l}}$, $k^{\mathrm{D}}_{\mathrm{d,l}}$ (described in Section 6.1) are set equal to

$k^{\mathrm{A}}_{\mathrm{d,l}}$. The same is done for the stiff domain, the stiffness coefficients being equal to $k^{\mathrm{A}}_{\mathrm{d,r}}$. To validate the solution, 100 artificial nonlinear events are introduced in the solution, which is comparable to the total number of nonlinear events in the most intensive computations encountered.

The limit-case solution is compared to the semi-analytical transient solution derived in Section 2.3. The error $e(x)$ presented in Fig. 6.6 is defined as the summed-over-time absolute value of the difference between the limit-case solution w_{lin} and the benchmark solution w_{bench}, divided by the summation of the absolute value of the benchmark solution over time:

$$e(x) = \frac{\sum_{t=0}^{t_{\max}} |w_{\mathrm{bench}}(x,t) - w_{\mathrm{lin}}(x,t)|}{\sum_{t=0}^{t_{\max}} |w_{\mathrm{bench}}(x,t)|}. \tag{6.52}$$

This error is caused by two main factors, namely the sequential application of the Laplace transform and the Finite Difference discretization (the left panel of Fig. 6.6 presents the total error). To isolate the error caused by the Finite Difference discretization, the case with no artificial nonlinear events is presented in the right panel of Fig. 6.6. To test the convergence of the derived solution, the maximum frequency has been varied (also done in the numerical integration for the benchmark solution). Note that by changing the maximum frequency, according to the Nyquist sampling rule, the time stepping also changes.

Fig. 6.6 shows that the solution derived in Section 6.2 converges to the correct one as the maximum frequency increases. The higher relative error in the stiffer part of the computational domain can be explained by the smaller displacements. A higher maximum frequency leads to smaller error; however, the computational effort increases significantly. For the rest of the results presented in this section, the maximum frequency was chosen as 1 kHz.

6.3.2. Displacement field in the time domain

To study the effect of the nonlinear foundation on the wave field excited during the transition-radiation process, a relatively severe case is presented. The load velocity is chosen as 95% of the critical velocity in the soft part of the computational domain ($c_{\mathrm{cr,l}}$), and the transition length l_{t} is chosen as 0.1 m, which is close to the piecewise-homogeneous case. To ensure that the initial displacement and velocity fields do not interact with the inhomogeneity, the centre of the transition zone x_{tc} is positioned at 35 m. The influence of the nonlinearity is highlighted by comparing the response to the linear case, as seen in Fig. 6.7.

The plastic deformation close to the transition zone is a result of constructive interference of the approaching eigenfield and the waves generated in the transition zone, the same mechanism that causes response amplification. As in the linear case, the eigenfield interacts with the transition zone, generating waves which mostly propagate towards the softer medium. By constructively interfering, the displacement under the load exceeds the elastic displacement limit (indicated by the grey line in Fig. 6.7) giving rise to permanent deformation in the foundation to the left of the transition zone.

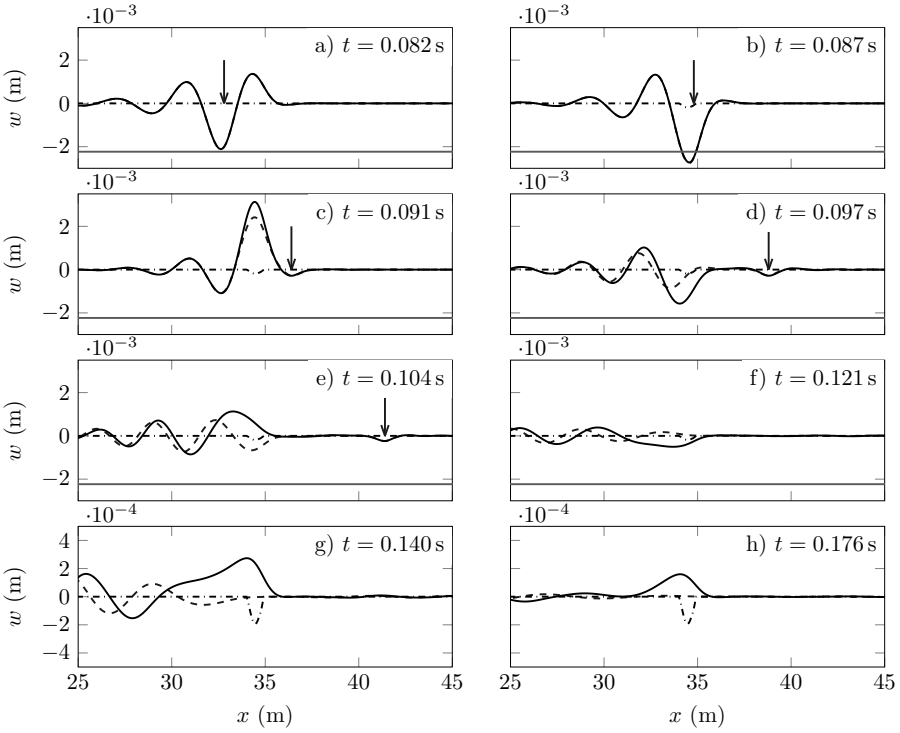

Figure 6.7: Time-domain displacement field for the nonlinear system (solid line), for the linear system (dashed line), the plastic deformation (dash-dot line) and the elastic displacement limit (light grey; given in Table 6.1) for the soft-to-stiff case; $l_\mathrm{t} = 0.1\,\mathrm{m}$, $x_\mathrm{tc} = 35\,\mathrm{m}$, $v = 0.95\,c_{\mathrm{cr},1}$, $\zeta = 0.05$; the arrow indicates the position of the load. Note that panels g) and h) have a different vertical-axis scale for clarity.

In the nonlinear system, the free field has both larger amplitude and is sustained for a much longer period of time compared to the linear one. This can clearly be seen in Fig. 6.7. Both the larger amplitude and longer duration are consequences of the beam's separation from the foundation. In case the separation is not included in the constitutive model (e.g., if the settlement is small), then the difference between the transient responses of the linear and nonlinear models is small (result is not presented here for brevity). The loss of contact leads to larger upward displacement which in turn affects the wave field in areas without loss of contact. The loss of contact also causes the loss of external damping which results in the longer duration of the vibration. Moreover, the shape of the radiated waves is also changed. In the nonlinear case, the contact loss leads to a slight increase in the wavelength of the free field (Fig. 6.7 panels d), e) and f)). This is in accordance with the findings in Section 6.3.4.

In the stiff-to-soft scenario, the displacement field does not exceed the elastic displacement limit (at all), meaning that plastic deformation does not develop, as seen in Fig. 6.8. As shown in Chapter 2 (Fig. 2.7), in the stiff-to-soft scenario both the free field and eigenfield move in the same direction causing the response amplification to occur further away from

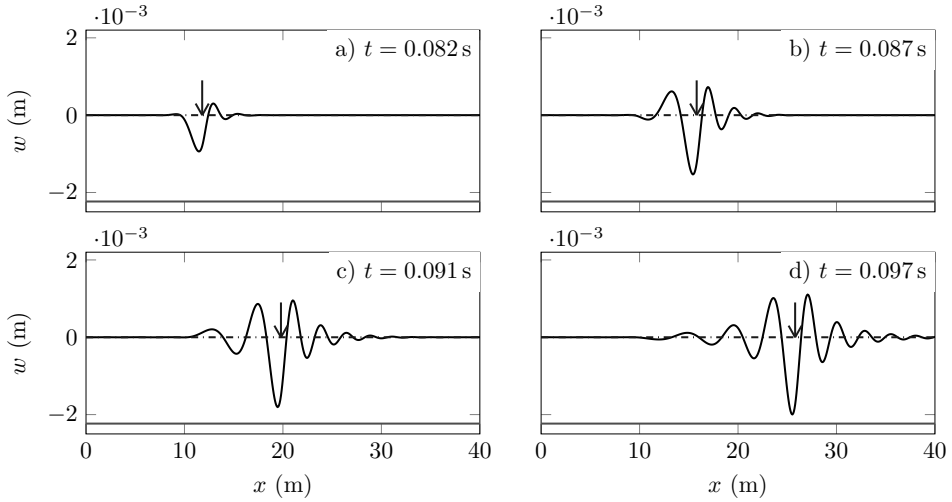

Figure 6.8: Time-domain displacement field for the nonlinear system (solid line), the plastic deformation (dash-dot line) and the elastic displacement limit (light grey; given in Table 6.1) for the stiff-to-soft case; $l_t = 0.1\,\mathrm{m}$, $x_{tc} = 10\,\mathrm{m}$, $v = 0.95\,c_{cr,r}$, $\zeta = 0.05$; the arrow indicates the position of the load.

the transition. However, due to the presence in this chapter of a reasonable amount of damping, the free field decays before a significant amplification can occur. Consequently, in the remainder of this chapter, only the soft-to-stiff case is presented. Nonetheless, if the load travelled super-critically (in the soft medium or in both media) for the stiff-to-soft case, it would move faster than the critical velocity of the free waves, probably leading to more pronounced constructive interference, which could induce plastic deformation to the right of the transition zone. However, this scenario is outside the scope of the analysis done in this chapter.

6.3.3. Parametric study

In this section, the damage occurring in the supporting structure is addressed as a function of the load velocity, the transition length and the stiffness ratio p through a parametric study. The area of the plastic deformation, $A_{pl} = \int w_{pl}(x)\,\mathrm{d}x$, is chosen as the quantifier for the damage in the supporting structure. The three parameters chosen to be varied influence the transition radiation phenomenon most. Furthermore, these parameters can be adjusted in the design stage of railway tracks to minimize damage in the supporting structure.

The plastic deformation area versus varying transition length is presented in Fig. 6.9 for different load velocities and damping ratios. The plastic deformation area decreases as the transition length increases, as could be expected, and the decreasing trend is quasi-monotonic for all load velocities and damping ratios. For the damping ratio $\zeta = 0.05$ (left panel in Fig. 6.9), the transition-length range in which plastic deformation occurs increases with increasing velocity until the critical velocity, beyond which it decreases. However, for

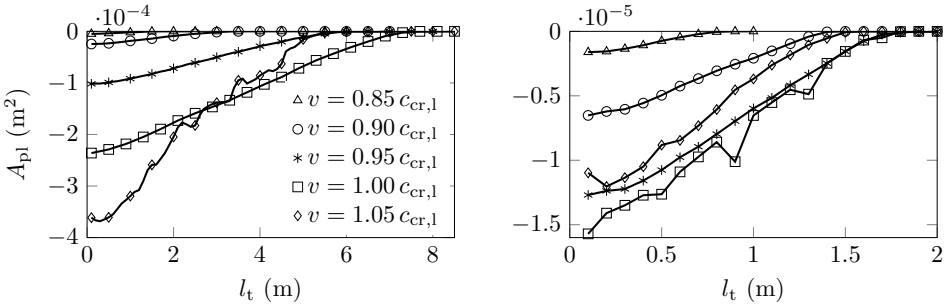

Figure 6.9: Plastic deformation area versus transition length for different load velocities; $\zeta = 0.05$ (left panel), $\zeta = 0.20$ (right panel) and $p = 5$.

the super-critical case ($v = 1.05\, c_{\mathrm{cr,l}}$) and small transition lengths ($l_{\mathrm{t}} = 0, ..., 3$ m), the plastic deformation is still larger than for the critical case ($v = 1.00\, c_{\mathrm{cr,l}}$), which makes the two lines intersect. This larger plastic deformation is caused by the fact that parts of the foundation experience additional plastic deformation produced in the second loading-unloading cycle. This is not the case for larger transition lengths ($l_{\mathrm{t}} = 4, ..., 6$ m), and because the displacement of the eigenfield under the load is smaller in the super-critical case than in the critical case, a smaller plastic deformation area results, which explains the intersection of the two lines. Furthermore, for $\zeta = 0.20$ (right panel in Fig. 6.9), additional plastic deformation is not produced in the second loading-unloading cycle for any of the transition lengths due to the higher damping ratio, and the range as well as the plastic deformation area just decrease as the velocity increases beyond the critical velocity.

Furthermore, the analysis shows that it is not just the *duration of passage* $t_{\mathrm{p}} = \frac{l_{\mathrm{t}}}{v}$ that governs the resulting plastic deformation (which could be intuited), but also the absolute values of the transition length l_{t} and load velocity v separately. It can clearly be seen in Fig. 6.9 that for the same duration of passage, significantly different plastic-deformation values are observed for different load velocities.

In Fig. 6.10, the plastic deformation area is presented as a function of the velocity of the moving load for different transition lengths and damping ratios. The plastic deformation area increases with increasing velocity until close to the critical velocity, beyond which it decreases. For $\zeta = 0.05$ (left panel in Fig. 6.10), the critical velocity appears to be around $1.05\, c_{\mathrm{cr,l}}$ for $l_{\mathrm{t}} = 0.1$ m, and its value decreases with increasing transition length reaching $1.00\, c_{\mathrm{cr,l}}$ for $l_{\mathrm{t}} = 4$ m. This shows that the critical velocity for the plastic deformation area is dependent on the transition length. Moreover, the increasing trend (sub-critical velocities) and the decreasing trend (super-critical velocities) have different slopes, which is explained by the fact that in the super-critical cases parts of the foundation experience additional plastic deformation caused in the second loading-unloading cycle. For $\zeta = 0.20$ (right panel in Fig. 6.10), a similar behaviour to the case of $\zeta = 0.05$ is observed. However, the magnitude of the plastic deformation area is smaller and the slopes of the increasing and decreasing

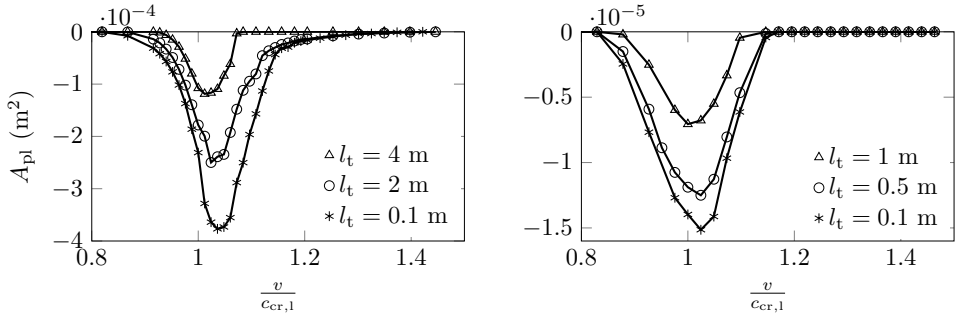

Figure 6.10: Plastic deformation area versus velocity of the moving load for different transition lengths; $\zeta = 0.05$ (left panel), $\zeta = 0.20$ (right panel) and $p = 5$.

trends (left and right of the critical velocity) are almost identical because the foundation does not experience additional plastic deformation caused in the second loading-unloading cycle.

The plastic deformation area as a function of the stiffness ratio p is presented in Fig. 6.11 for different load velocities and transition lengths. The plastic deformation area increases with increasing stiffness ratio for all velocities and transition lengths presented, as could be expected. The increasing trends tend to constant values, which could be obtained in the limit case of the stiff domain being infinitely stiff. It is clear from the trends that the maximum sensitivity of the plastic deformation area occurs at small stiffness ratios. Therefore, the maximum gain in decreasing the damage of the supporting structure can be obtained at small stiffness ratios. For small stiffness ratio, the maximum plastic deformation area is observed for a load velocity $v = 1.00\, c_{\mathrm{cr,1}}$, but for larger stiffness ratio the maximum plastic deformation area is obtained for a load velocity $v = 1.05\, c_{\mathrm{cr,1}}$. This shows that the critical velocity, when it comes to the plastic deformation area, is dependent also on the stiffness ratio (next to transition length).

To conclude, studying the influence of the transition length, load velocity and stiffness ratio on the plastic deformation area provides valuable information about the value ranges of these parameters where the initial design of transition zones should aim at so as to minimize the damage in the supporting structure. Next, the transition radiation phenomenon is studied from an energy point of view.

6.3.4. Energy radiation

In this section, the influence of the nonlinearity on the transition radiation is studied from an energy perspective, which gives additional insight into the properties of the radiated field. To investigate the energy radiation solely due to the transition radiation phenomenon, the study is restricted to sub-critical load velocities. Based on the solution derived in Section 6.2.2, the energy flux through cross-sections of the beam to the left and right of the transition

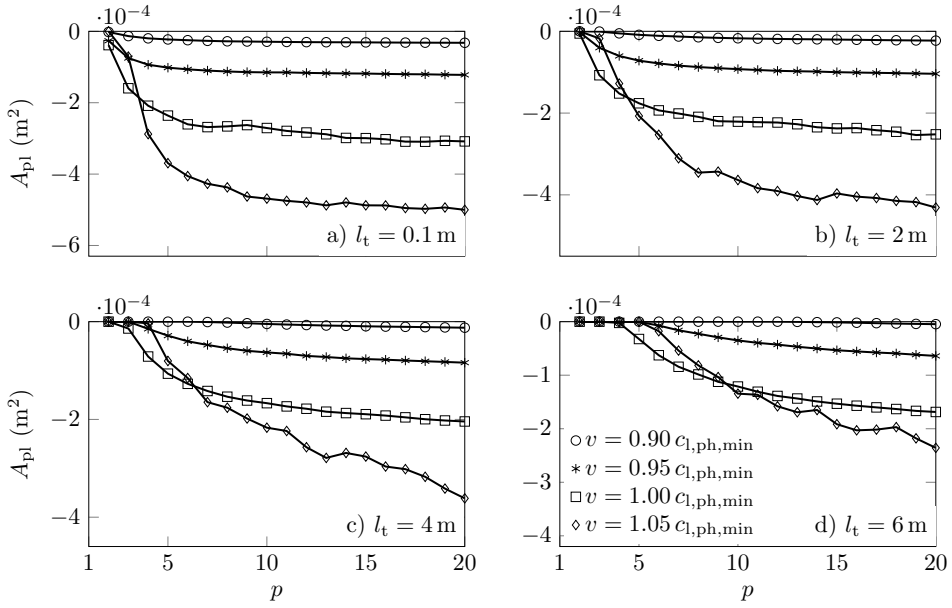

Figure 6.11: Plastic deformation area versus stiffness ratio for different velocities and transition lengths; $\zeta = 0.05$.

zone can be computed as shown in Chapter 2 (Eqs. (2.35) and (2.36)). Also, to visualize the spectral energy density corresponding to the radiation, Eq. (2.39) is used.

In the expressions of the energy radiation and spectral energy density from Chapter 2, the response quantities are evaluated at $x \to \pm\infty$; this is not possible for the response quantities in this chapter because the response is obtained only in the computational domain ($x \in [0, L]$) and the foundation has damping causing the response at infinite distance from the moving load to be zero. Consequently, the quantities at the boundaries of the computational domain are used to determine the energy radiation and the corresponding spectra. Moreover, to focus on the radiation solely and eliminate the energy flux corresponding to the eigenfield entering and exiting the computational domain, only the free field part of the response is considered. It must be emphasized that the computed energy does not represent the total free-field energy because part of it is absorbed by the foundation before reaching the considered cross-sections left and right of the transition. Furthermore, due to the spatial variation of the foundation damping, the energy propagating in the stiff domain is damped more than that propagating in the soft domain. To avoid the last issue, for the computations performed in this section, the spatial damping profile is maintained constant throughout the computational domain (where ζ is defined with respect to the soft domain), except for the parts where the beam-foundation separation occurs (Eq. (6.1)).

The influence of the transition length on the free-field energy is now addressed through a parametric study. The energy associated with the leftward-propagating free field $E_{\mathrm{l}}^{\mathrm{rad}}$,

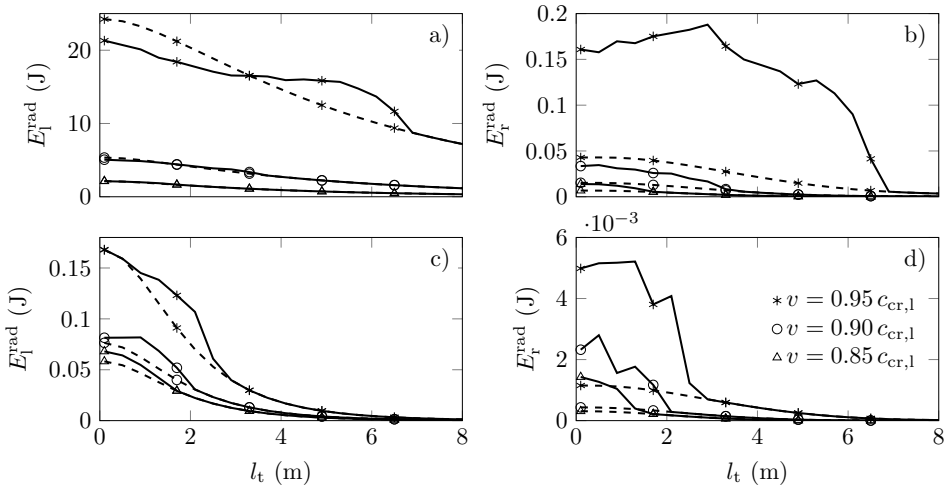

Figure 6.12: Total energy flux leftward $E_{\mathrm{l}}^{\mathrm{rad}}$ (left panels) and rightward $E_{\mathrm{r}}^{\mathrm{rad}}$ (right panels) for the nonlinear system (solid line) and linear system (dashed line) versus transition length; the cross-sections were chosen 10 m left and right of the transition centre; $\zeta = 0.05$ (top panels) and $\zeta = 0.20$ (bottom panels).

presented in the left panels of Fig. 6.12, decreases with increasing transition length, as could be intuited. However, for small transition lengths, $E_{\mathrm{l}}^{\mathrm{rad}}$ in the lightly-damped case (panel a in Fig. 6.12) is smaller in the nonlinear system as compared to that in the linear one. This can be explained by the fact that part of the energy is consumed to plastically deform the foundation, but also by stronger radiation in the rightward direction (panel b in Fig. 6.12). Furthermore, although $E_{\mathrm{l}}^{\mathrm{rad}}$ decreases with increasing transition length, the decrease rate is smaller in the nonlinear case as compared to that in the linear one. Consequently, for some values of the transition length ($l_{\mathrm{t}} \approx 3, \ldots, 7\,\mathrm{m}$ in panel a of Fig. 6.12), $E_{\mathrm{l}}^{\mathrm{rad}}$ is larger in the nonlinear case. However, the behaviour described above is not general. The bottom-left panel in Fig. 6.12 shows that in the system with higher damping ratio ($\zeta = 0.20$), $E_{\mathrm{l}}^{\mathrm{rad}}$ is higher in the nonlinear system than in the linear one for all transition lengths. Finally, it is important to emphasize that the observed differences between the energies in the linear and nonlinear systems mainly stems from the separation between the beam and foundation; if the separation is not allowed, the differences are negligible (the results are not presented here for brevity). This final conclusion is also supported by the findings in Section 6.3.5 where the difference in energy input is negligible because the energy input is not strongly affected by the beam-foundation separation.

Furthermore, the energy associated with the rightward propagating free field $E_{\mathrm{r}}^{\mathrm{rad}}$ (presented in the right panels of Fig. 6.12) is significantly higher in the nonlinear case as compared to that in the linear one. Moreover, $E_{\mathrm{r}}^{\mathrm{rad}}$ is not largest for the shortest transition length, but for a transition length $l_{\mathrm{t}} \approx 0.5, \ldots, 2.5\,\mathrm{m}$ (depends on the load velocity). This is specific to the nonlinear case since for all the linear cases considered, the free-field energy

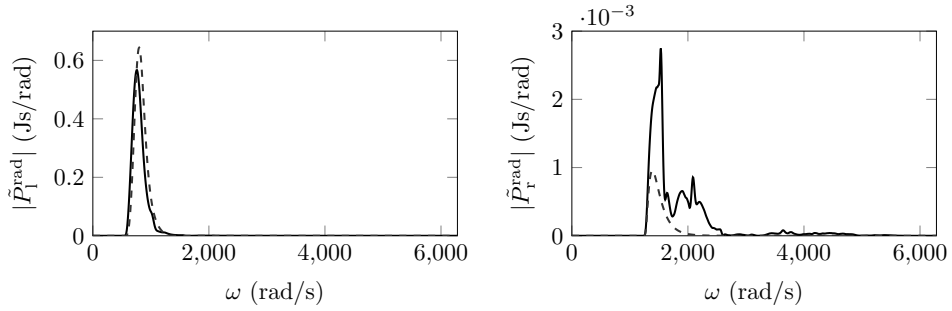

Figure 6.13: Power spectral density leftward $\tilde{P}_{\mathrm{l}}^{\mathrm{rad}}$ (left panel) and rightward $\tilde{P}_{\mathrm{r}}^{\mathrm{rad}}$ (right panel) for the nonlinear system (solid line) and linear system (dashed line); the cross-sections were chosen 10 m left and right of the transition centre; $v = 0.95\, c_{\mathrm{cr,l}}$, $l_{\mathrm{t}} = 0.1\,\mathrm{m}$ and $\zeta = 0.05$.

decreases with increasing transition length. In addition, for the considered cases, $E_{\mathrm{r}}^{\mathrm{rad}}$ is clearly smaller than $E_{\mathrm{l}}^{\mathrm{rad}}$, implying that the free field radiated into the soft part of the system carries most energy, although this is not a necessity as shown in [20].

The power spectral density $\tilde{P}^{\mathrm{rad}}$ for the same system as in Fig. 6.7 ($l_{\mathrm{t}} = 0.1\,\mathrm{m}$, $v = 0.95\, c_{\mathrm{cr,l}}$ and $\zeta = 0.05$) is presented in Fig. 6.13. The leftward-propagating power $\tilde{P}_{\mathrm{l}}^{\mathrm{rad}}$ for the nonlinear system exhibits a small shift towards the lower frequencies as well as a decrease in energy in the nonlinear case, when compared to the linear system. The lower frequencies of the radiated waves in the nonlinear system can also be observed in the time-domain response (Fig. 6.7, panels d), e) and f)) through the larger wavelengths of the left-propagating waves. Furthermore, the energy propagating rightward $\tilde{P}_{\mathrm{r}}^{\mathrm{rad}}$ in the nonlinear system has, next to a higher magnitude (as already observed in the right panel of Fig. 6.13), also higher-frequency content as compared to the linear system.

6.3.5. Energy input

Besides the influence of the nonlinear foundation on the energy radiation, presented in the previous sub-section, its influence on the energy input from the moving load could also offer valuable insight. While the energy radiation refers to the far field, the energy input offers information about the near field, as it relates to the contact point between the moving load and the beam. More energy input leads to more energy radiated and/or more energy dissipated into the foundation, the latter leading to damage. Therefore, the energy input or the maximum power input could represent a good indicator of the potential damage occurring in the foundation, as identified in Chapter 4. To investigate the energy input solely due to the transition radiation phenomenon, the study is restricted to sub-critical load velocities.

The energy input is defined as the power input integrated over time. Due to the damping present in the structure, the power input P^{in} is non-zero over the whole time axis (i.e., even when the load is not in the vicinity of the transition zone), and therefore the energy input

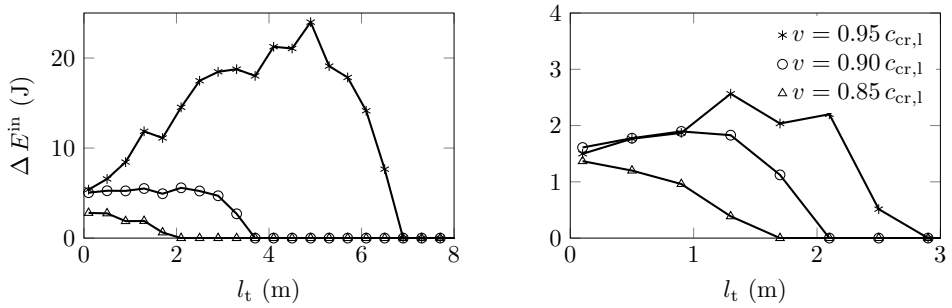

Figure 6.14: Difference in energy input between the linear and nonlinear cases for varying transition length; $\zeta = 0.05$ (left panel) and $\zeta = 0.20$ (right panel).

is infinite. Consequently, the difference in energy input between the linear and nonlinear cases is presented instead. The difference in energy input ΔE^{in} is given by the following expression:

$$\Delta E^{\mathrm{in}} = \int_{-\infty}^{\infty} \left(P^{\mathrm{in}}(t) - P^{\mathrm{in}}_{\mathrm{lin}}(t)\right) \mathrm{d}t = F_0 \int_{-\infty}^{\infty} \left(\dot{w}_{\mathrm{c}}\Big|_{x=vt} - \dot{w}_{\mathrm{lin}}\Big|_{x=vt} \right) \mathrm{d}t, \tag{6.53}$$

where $P^{\mathrm{in}}_{\mathrm{lin}}$ and $\dot{w}_{\mathrm{lin}}$ represent the power input and velocity at the contact point, respectively, of the linear case.

Fig. 6.14 presents the difference in energy input ΔE^{in} as a function of the transition length for different velocities and damping ratios. It can be observed that the maximum difference in energy input does not occur at the smallest transition zone, reinforcing the findings in the energy radiation study (right panels in Fig. 6.12). Furthermore, the difference in energy input increases with increasing velocity, but the difference is smaller in the higher-damping case (right panel in Fig. 6.14).

The normalized maximum power input $P^{\mathrm{in}}_{\mathrm{max}}$ is presented in Fig. 6.15 as a function of the transition length for different velocities and damping ratios. The maximum power input is normalized by the steady-state power input in the soft domain $P^{\mathrm{in}}_{\mathrm{soft}}$. It can be observed that the maximum power input decreases with increasing transition length and decreasing velocity of the moving load. Moreover, the maximum power input in the transition zone can be a factor 1.8 larger than the one in the steady state.

To investigate how much of this additional power input causes damage in the supporting structure, the difference between the linear and the nonlinear cases (for the first passage of the moving load) is presented in Fig. 6.15. It can be seen that the difference is small and can barely be seen, even though the difference in total energy input can be significant (Fig. 6.14). However, the increase is much more drastic for the second passage of the moving load (i.e., of the system that has already been deformed plastically) as can be seen in Fig. 6.16. Both the maximum power input (left panel in Fig. 6.16) and the difference in energy input (right

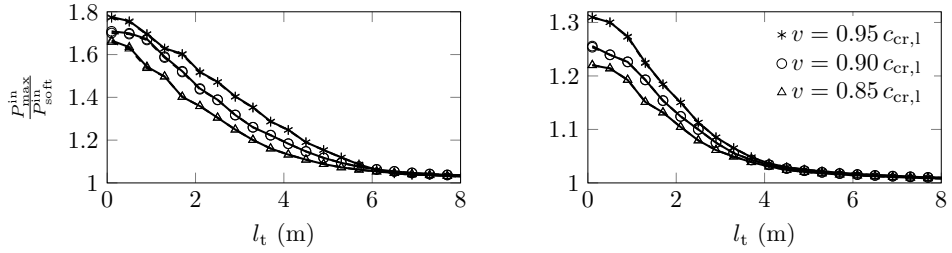

Figure 6.15: Maximum power input for the linear case (dashed line) and nonlinear case (solid line) against varying transition length; $\zeta = 0.05$ (left panel) and $\zeta = 0.20$ (right panel).

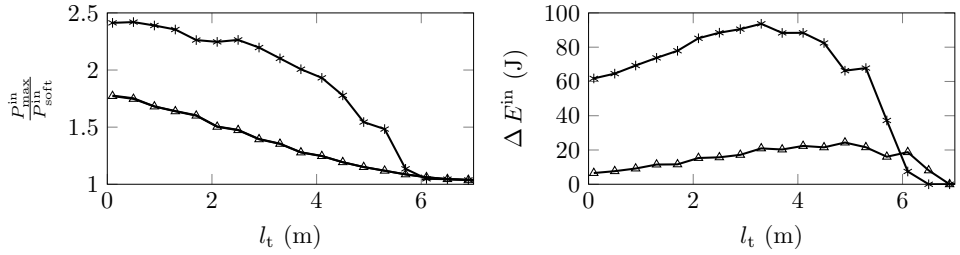

Figure 6.16: Maximum power input (left panel) and difference of energy input between the linear and nonlinear cases (right panel) for the first load passage (triangle) and for the second load passage (asterisk) against transition length; $v = 0.95\, c_{\text{cr,l}}$ and $\zeta = 0.05$.

panel in Fig. 6.16) exhibit a considerable increase compared to the first load passage. The maximum power input and the energy input have the potential to be good indicators of the damage occurring in the foundation of the railway track. However, more extensive research into these two indicators needs to be performed in order to justify this.

6.4. Conclusions

In this chapter, the influence of the foundation's nonlinear behaviour on the waves generated by a moving load crossing an inhomogeneity in the foundation, as well as the resulting plastic deformation has been studied. To this end, a 1-D model has been formulated, consisting of an infinite Euler-Bernoulli beam resting on a locally inhomogeneous and nonlinear Winkler foundation, subjected to a moving load. The reaction of the Winkler foundation has been characterized by a piecewise-linear (in displacements) constitutive relation which accounts for permanent deformations. The foundation's piecewise-linear behaviour allows to obtain the solution by sequentially applying the Laplace transform over time, while the Finite Difference Method has been used for the spatial discretization. The infinite extent of the system has been accounted for through a set of non-reflective boundary conditions, derived by replacing the semi-infinite domains by their response at the interfaces, and through the

input initial conditions based on the steady-state response of a beam with homogeneous foundation subject to the moving load. The solution has been validated for the limit case of a linear and piecewise-homogeneous foundation against a semi-analytical benchmark solution.

Results show that the plastic deformation originates from the response amplification that is typically observed at transition zones (caused by constructive interference between the waves excited at the transition and the response to the load's deadweight). Furthermore, through a parametric study conducted for the soft-to-stiff transition, it has been found that the plastic deformation decreases quasi-monotonically with increasing transition length, and that the decrease rate depends on the velocity of the load and on the magnitude of the foundation damping. Moreover, for super-critical velocities, additional plastic deformation is generated in the second loading-unloading cycle of the foundation for small transition lengths and/or large stiffness dissimilarities. The critical velocity related to the plastic deformation area, which was chosen to quantify the damage in the supporting structure, was observed to be dependent on the transition length and on the stiffness ratio. In addition, the resulting plastic deformation area has been observed to be influenced not only by the time of passage of the transition zone, defined as the transition-zone length divided by the load's velocity, but also by these quantities individually. Finally, the influence of the nonlinear foundation on the transient response mainly stems from the beam-foundation separation; if this is prohibited (e.g., small settlement), then the nonlinearity has a negligible influence on the transient response.

The influence of the foundation's nonlinear behaviour on the radiated field has also been studied from the energy point of view, by considering the energy flux associated with the free field through cross-sections left and right of the transition zone. Results have shown that in the nonlinear system, the maximum rightward-propagating energy flux does not occur at the smallest transition length, but at a larger one, a finding which is reinforced by the difference in energy input between the linear and nonlinear case. This feature is specific to the nonlinear system since in the linear case, the energy flux has been observed to always decrease with increasing transition length. Furthermore, the spectral energy densities have not only shown that the nonlinearity redistributes the energy between frequencies, but have also highlighted the redistribution between the soft and stiff media. Moreover, it has been observed that the maximum power input and the difference in energy input between the linear and nonlinear case drastically increases for the second passage of the moving load (i.e., of the system that has already been deformed plastically). This suggests the use of these energy quantities as possible indicators of the damage in the supporting structure.

Although 1-D models are not able to model all phenomena, they are useful for initial assessments. The model presented here can be used for preliminary designs of transition zones in railway tracks. Given the stiffness ratio and/or the magnitude of the initial plastic deformation, the optimum length of the transition zone and the maximum velocity of the train can be obtained such that the damage in the railway track is minimized.

7

Comparison of solution methods for the nonlinear system

The saddest aspect of life right now is that
science gathers knowledge faster than society gathers wisdom.

Isaac Asimov

To better understand the behaviour of transition zones in railway tracks and propose successful mitigation measures, engineers and researchers have developed a multitude of models to describe and predict the response of the track at these locations. As discussed in the previous chapter, a small amount of these models include the nonlinear behaviour of the supporting structures. One of the main reasons for not accounting for the nonlinear behaviour is the high computational costs that such models require, especially the ones that include multiple dimensions (i.e., 2-D and 3-D). To overcome the high computational costs, generally 1-D models are used, as done in the previous chapter. However, 1-D models have considerable limitations compared to multi-dimensional models (limitations which are discussed in detail in Chapter 8). Consequently, if one wants to overcome the limitations posed by 1-D models, it seems difficult to avoid high computational costs. To this end, this chapter aims to investigate several solution methods for obtaining the response of such systems to ensure that the computational costs are as low as possible.

In their studies of transition radiation, Vesnitskii and Metrikin [16, 38] used the method of images solely or in combination with the Fourier transform over space to determine the response. Later on, the problem of a beam resting on a piecewise-homogeneous Winkler

foundation and subjected to a moving load was solved using modal expansion techniques [18, 40]. To study wave propagation in the ground caused by transition radiation, 2-D models of a piecewise-homogeneous continuum were analysed using the Fourier transform [42], and the Fourier transform combined with mode matching [20, 21]. Lately, a combination of the Fourier transform over time and the Fourier expansion over space was used to study transition radiation in a discretely supported Timoshenko beam [23]. Also, transition radiation was studied in a piecewise-linear 1-D system using a sequential Laplace transform method combined with a finite difference discretisation of the spatial dimension [77] (described in Chapter 6). Furthermore, the interaction between a moving oscillator and an inhomogeneous and infinite structure was analysed by means of the Green's function method [64] (described in Chapter 4), which can be considered as a hybrid between an integral-transform method and a time-domain method.

Although at the beginning researchers have mainly used integral-transform methods to study the dynamics of elastic structures subjected to moving loads, the development of computers has lead to a shift towards numerical methods such as the finite element method combined with time-integration methods (e.g., the Newmark method [13, 41, 119]). One advantage of these time-domain methods is that the geometry of the transition zone can be modelled accurately [27, 28, 31, 34, 67, 120]. Another advantage is that the nonlinear behaviour of the foundation or the nonlinear interaction between the vehicle and the structure can easily be handled by time-domain methods [19, 25, 30, 113, 114]. One of the disadvantages of the standard time-domain methods is that the system must be finite to be solved numerically, while the railway track is practically infinite, potentially causing artificial reflections at the boundaries of the finite domain. To overcome this problem, absorbing boundaries (e.g., perfectly-matched layers) have been used in numerous studies [e.g., 121]. Another challenge caused by the structure being finite is that the vehicle's action on the structure is of finite duration causing an unrealistic transient behaviour at the entrance and exit of the vehicle. This has been elegantly solved by analysing the system in the moving reference frame, approach which is sometimes called the *moving element method* [e.g., 35, 122].

As it can be seen, a multitude of methods have been applied by researchers and engineers to investigate transition radiation in railway applications. Most methods fall into three main categories, namely integral-transform methods, time-domain methods, and hybrid methods (i.e., a combination of integral-transform and time-domain methods). The advantages and disadvantages of these methods have partially been discussed for each method independently, but without much direct comparison between them. This chapter aims at comparing three solution methods, one corresponding to each category, for analysing transition radiation in a 1-D model consisting of an infinite Euler-Bernoulli beam resting on an inhomogeneous and piecewise-linear Kelvin foundation subjected to a moving constant load; the model formulation is the same as in Chapter 6. The integral-transform method, namely the sequential Laplace transform method [77] described in Chapter 6, assumes that

the system's behaviour is piecewise linear and deals with the linear parts of the solution in the Laplace domain. To accommodate the inhomogeneity, the finite difference method is used for the spatial discretisation, and non-reflective boundary conditions are imposed to ensure the infinite extent of the structure. The time-domain method is the more conventional approach; the solution is obtained by applying the finite element method for the spatial discretisation, combined with a set of non-reflective boundaries, and the Newmark-β as the time-stepping method. The hybrid method, namely the pseudo-force method [123, 124], treats the nonlinearity and part of the inhomogeneity as external forces resulting in a fictitious linear and piecewise-homogeneous *base* structure. Taking advantage of the linearity, the Green's function of the base structure is obtained (the integral-transform part of the method), and the response is expressed through convolution integrals of the Green's functions and the forces that account for the nonlinearity and part of the inhomogeneity (the time-domain part of the method). Finally, because these forces are state dependent, the relation for the response at each time step is implicit, and it is therefore solved iteratively.

The three solution methods are compared in terms of accuracy, computational efficiency, and feasibility of application to more complex systems. In this chapter, the feasibility of application to more complex systems refers to the feasibility of the methods to deal with frequency-dependent properties of the structure, to deal with a smooth nonlinearity (as opposed to the piecewise-linear one), and to apply the solution methods to 2-D and 3-D models. It must be emphasized that although the 1-D model described is not particularly demanding from the computational point of view, the aim of the comparison is to establish the most suitable method to be applied to multi-dimensional models, where the choice of the proper solution method could lead to significant gains.

The novelty of the current chapter is threefold. Firstly, a thorough and direct comparison between integral-transform, time-domain, and hybrid methods to describe the behaviour of an infinite and nonlinear system has not been presented in the literature. Such a comparison enables engineers and researchers to choose the most suitable solution method for solving the specific problem they are facing. Secondly, the application of the pseudo-force method to analyse transition radiation in a nonlinear and infinite structure is presented here for the first time. Thirdly, the non-reflective boundary conditions formulated for the time-domain solution method, which enable the finite domain to behave exactly as the infinite one, are derived analytically; to the best of the authors' knowledge, it is for the first time this analytical approach is used to solve a moving load problem containing changes in the foundation properties (see Section 7.1 for more details).

The model used to investigate the solution methods is the one formulated in Chapter 6. The problem statement is described in detail in Section 6.2.1 and is not repeated here. Furthermore, the first solution method, the Laplace transform method, is described thoroughly in Section 6.2.1 and, consequently, is not repeated here. To keep the following derivations concise, as done in Chapter 6, a bilinear elastic constitutive relation is chosen for the foundation (i.e., only branches A and B from Fig. 6.2 are considered with the unloading path

being the same as the loading one). The extension to more than two branches does not pose any difficulties, and thus the bilinear law suffices for the demonstration of the following procedures. The bilinear force exerted by the foundation is given by Eq. (6.3). The remaining two solution methods are presented in the following.*

7.1. Time-domain method

The time-domain method is one of the more conventional approaches to solve the current problem. The spatial dimension is discretised using the finite element method and the Newmark-β time-stepping method is used to solve the discretised system; other methods for the spatial discretisation and the time stepping can also be used, but these are the most common ones. The only difficulty in this approach arises when implementing the non-reflective boundary conditions. Similar to the sequential Laplace transform method, the semi-infinite domains are treated analytically. In the time domain, this is done through convolution integrals, which implies that the relations between displacements and forces at the boundaries are history dependent. Therefore, after spatial discretisation, a system of integro-differential equations has to be solved. The approach followed here differs from those in other works using absorbing boundaries [e.g., 126, 127] in the following ways: i) instead of starting with a finite system and mitigate reflections at the artificial boundaries, the current approach treats the truly infinite system; ii) it does not increase the number of degrees of freedom (like in the case of absorbing layers, that model buffer domains with the intention of attenuating waves); iii) it allows the approach and exit of the load from the modelled domain, thus avoiding transients due to sudden entrance/exit of the load, and in this way it limits the model to the vicinity of the region with support variations and thus further decrease the number of degrees of freedom. The procedure is described in more detail in the following.

The equation of motion for the computational domain after the spatial discretisation reads

$$\mathbf{M}\ddot{\mathbf{x}}(t) + \mathbf{C}\dot{\mathbf{x}}(t) + \left(\mathbf{K}(\mathbf{x}) + \mathbf{K}^{\mathrm{EB}}\right)\mathbf{x}(t) = \mathbf{f}_{\mathrm{c}}^{\mathrm{ML}}(t) + \mathbf{f}_{\mathrm{c}}^{\mathrm{B}}(t) + \mathbf{f}_{\mathrm{c}}^{\mathrm{NL}}(\mathbf{x}), \tag{7.1}$$

where $\mathbf{x} = [w_{\mathrm{c},1}, w'_{\mathrm{c},1}, w_{\mathrm{c},2}, w'_{\mathrm{c},2}, \ldots, w_{\mathrm{c},N_{\mathrm{x}}}, w'_{\mathrm{c},N_{\mathrm{x}}}]^{\mathrm{T}}$ represents the vector of generalized displacements with N_{x} being the number of spatial nodes. The matrices $\mathbf{M}$, $\mathbf{C}$, $\mathbf{K}$, and $\mathbf{K}^{\mathrm{EB}}$ are the mass matrix, Kelvin damping matrix, Kelvin stiffness matrix, and the Euler-Bernoulli bending stiffness matrix, respectively. $\mathbf{K}$ is state-vector dependent because it contains the nonlinear part of the supporting structure that depends on the unknown displacement. Furthermore, the time-dependent vectors $\mathbf{f}_{\mathrm{c}}^{\mathrm{ML}}$, $\mathbf{f}_{\mathrm{c}}^{\mathrm{B}}$, and $\mathbf{f}_{\mathrm{c}}^{\mathrm{NL}}$ represent the moving-load forcing vector, the boundary-forcing vector, and the forcing vector containing the nonlinear part of the supporting structure reaction force that is independent of the unknown displacement (see Eq. (6.3)), respectively. The moving-load forcing vector for a single element $\mathbf{f}_{\mathrm{c},i}^{\mathrm{ML}}$ is

*This chapter is based on one of the author's publications [125] and it presents few alterations to the original publication.

obtained as follows:

$$\mathbf{f}_{\mathrm{c},i}^{\mathrm{ML}}(t) = -F_0 \int_{(i-1)\Delta x}^{i\Delta x} \boldsymbol{\Phi}(x)\delta(x - x_{\mathrm{e}} - vt)\mathrm{d}x = \begin{cases} -F_0\boldsymbol{\Phi}(x_{\mathrm{e}} + vt), & (i-1)\Delta x \le x_{\mathrm{e}} + vt \le i\Delta x, \\ 0, & \text{otherwise}, \end{cases} \tag{7.2}$$

where $\boldsymbol{\Phi}$ is the shape-functions vector. The assembly of the global moving-load vector is done in the traditional way and results in a time-dependent vector which has non-zero entries only at the nodes related to the element where the moving load is acting. Similarly, by assuming a constant nonlinearity force inside one element, the nonlinear-forcing vector corresponding to the bilinear constitutive relation is obtained as follows:

$$\mathbf{f}_{\mathrm{c},i}^{\mathrm{NL}}(t) = \begin{cases} \Delta k_{\mathrm{d,c},i} \int_{(i-1)\Delta x}^{i\Delta x} \boldsymbol{\Phi}(x)\mathrm{d}x, & w_{\mathrm{c},i} < w_{\mathrm{el}}, \\ 0, & w_{\mathrm{c},i} \ge w_{\mathrm{el}}. \end{cases} \tag{7.3}$$

As for the non-reflective boundary conditions, the expressions derived in Section 6.2.3 are valid for this method too. However, they need to be expressed in the time domain. Moreover, the dynamic stiffness coefficients $\big(\hat{k}_{h,\mathrm{V}\upsilon}$, $\hat{k}_{h,\mathrm{V}\phi}$, $\hat{k}_{h,\mathrm{M}\phi}$, and $\hat{k}_{h,\mathrm{M}\upsilon}$ in Eqs. (4.33) and (4.34)$\big)$ increase with increasing frequency, and therefore it is difficult to obtain their counterparts in the time domain. Consequently, for the time-domain method, instead of making use of the dynamic stiffness coefficients (i.e., imposing forces as boundary conditions), the dynamic compliance coefficients are used (i.e., displacement and slope are imposed as boundary conditions), which decay with increasing frequency. By expressing the displacement and slope in terms of the bending moment and shear force in Eqs. (6.29) and (6.30), the dynamic compliance coefficients in the Laplace domain are obtained, and their expressions read

$$\begin{aligned} \hat{c}_{h,\mathrm{V}\upsilon} &= (-1-\mathrm{i})k_h^{-3}, & \hat{c}_{h,\mathrm{M}\upsilon} &= -\mathrm{i}k_h^{-2}, \\ \hat{c}_{h,\mathrm{M}\phi} &= (1-\mathrm{i})k_h^{-1}, & \hat{c}_{h,\mathrm{V}\phi} &= -\mathrm{i}k_h^{-2}, \quad h = \{\mathrm{l},\mathrm{r}\}. \end{aligned} \tag{7.4}$$

where k_h with $h = \{\mathrm{l},\mathrm{r}\}$ are the wavenumbers of the two semi-infinite domains given in Eq. (4.30), and the branches of the complex-valued wavenumbers are chosen such that $\mathrm{Im}(k_h) < 0$ and $\mathrm{Re}(k_h) > 0$.

The time-domain non-reflective boundary conditions are now expressed through convolution integrals. Their expressions are given as follows:

$$\begin{aligned} w_{\mathrm{c}}(d,t) &= w_{\mathrm{V}}(d,t) + w_{\mathrm{M}}(d,t), \\ w'_{\mathrm{c}}(d,t) &= w'_{\mathrm{V}}(d,t) + w'_{\mathrm{M}}(d,t), \qquad d = \{0, L\}, \end{aligned} \tag{7.5}$$

where w_{V} and w_{M} represent the displacements caused by an applied shear force and displacement caused by an applied bending moment, respectively, while w'_{V} and w'_{M} represent

the same quantities for the slope. Furthermore, their expressions read

$$w_{\mathrm{V}}(d,t) = \int_0^t c_{\mathrm{h,V\upsilon}}(t-\tau)\, w_{\mathrm{c}}'''(d,\tau)\mathrm{d}\tau, \qquad w_{\mathrm{M}}(d,t) = \int_0^t c_{\mathrm{h,M\upsilon}}(t-\tau)\, w_{\mathrm{c}}''(d,\tau)\mathrm{d}\tau, \tag{7.6}$$

$$w_{\mathrm{V}}'(d,t) = \int_0^t c_{\mathrm{h,V\phi}}(t-\tau)\, w_{\mathrm{c}}'''(d,\tau)\mathrm{d}\tau, \qquad w_{\mathrm{M}}'(d,t) = \int_0^t c_{\mathrm{h,M\phi}}(t-\tau)\, w_{\mathrm{c}}''(d,\tau)\mathrm{d}\tau, \tag{7.7}$$

where $d = \{0, L\}$ and $h = \{\mathrm{l}, \mathrm{r}\}$, and $h = \mathrm{l}$ for $d = 0$ while $h = \mathrm{r}$ for $d = L$, and where τ represents the running-time variable of integration (should not be mistaken with the variable in Section 6.2 where it indicated the moment of the nonlinear event). The integrals in Eqs. (7.6)–(7.7) are discretised and the forces are assumed to be constant during one time step and equal to the average between the previous and the next time step [128]. The remainder of the procedure is presented only for $w_{\mathrm{V}}(0,t)$ since the procedure is exactly the same for the other terms. The expression for w_{V} now reads

$$w_{\mathrm{V}}(0,t_n) \approx \sum_{\bar{n}=0}^{n-1} \frac{w_{\mathrm{c}}'''(0,t_{\bar{n}}) + w_{\mathrm{c}}'''(0,t_{\bar{n}+1})}{2} \int_{t_{\bar{n}}}^{t_{\bar{n}+1}} c_{\mathrm{l,V\upsilon}}(t_n-\tau)\mathrm{d}\tau, \tag{7.8}$$

where n is the index of the observation time variable while $\bar{n}$ is the index for the running (i.e., integration) time variable. The index n should not be confused with that in Section 6.2 where it specified the time moment of the nth nonlinear event. It can be shown that the remaining integral in Eq. (7.8) is equivalent to

$$\begin{aligned}\int_{t_{\bar{n}}}^{t_{\bar{n}+1}} c_{\mathrm{l,V\upsilon}}(t_n-\tau)\mathrm{d}\tau &= \int_0^{t_{n-\bar{n}}} c_{\mathrm{l,V\upsilon}}(t_{n-\bar{n}}-\tau)\mathrm{d}\tau - \int_0^{t_{n-(\bar{n}+1)}} c_{\mathrm{l,V\upsilon}}(t_{n-(\bar{n}+1)}-\tau)\mathrm{d}\tau \\ &= \mathscr{H}_{\mathrm{l,V\upsilon}}(t_{n-\bar{n}}) - \mathscr{H}_{\mathrm{l,V\upsilon}}\big(t_{n-(\bar{n}+1)}\big),\end{aligned} \tag{7.9}$$

where $\mathscr{H}$ represents the response of the semi-infinite system to a unit step force applied at $t_0 = 0$. The response $\mathscr{H}$ can be obtained with a good accuracy using the inverse Laplace transform as follows:

$$\mathscr{H}_{\mathrm{l,V\upsilon}}(t_{n-\bar{n}}) \approx \frac{\mathrm{e}^{\sigma t_{n-\bar{n}}}}{\pi} \int_0^{\omega_{\max}} \mathrm{Re}\left(\frac{\hat{c}_{\mathrm{l,V\upsilon}}(\omega)}{\sigma + \mathrm{i}\omega} \mathrm{e}^{\mathrm{i}\omega t_{n-\bar{n}}} \right) \mathrm{d}\omega. \tag{7.10}$$

To obtain accurate results without integrating up to very high frequencies, the asymptotic approximation approach described in Section 6.2.2 is used. Substituting Eqs. (7.9) and (7.10) in Eq. (7.8), and rearranging the terms, the displacement w_{V} becomes

$$\begin{aligned} w_{\mathrm{V}}(0,t_n) \approx{}& \frac{1}{2} w_{\mathrm{c}}'''(0,t_1)\big[\mathscr{H}_{\mathrm{l,V\upsilon}}(t_n) - \mathscr{H}_{\mathrm{l,V\upsilon}}(t_{n-1})\big] \\ &+ \sum_{\bar{n}=1}^{n-1} \frac{1}{2} w_{\mathrm{c}}'''(0,t_{\bar{n}})\big[\mathscr{H}_{\mathrm{l,V\upsilon}}(t_{n-\bar{n}+1}) - \mathscr{H}_{\mathrm{l,V\upsilon}}(t_{n-\bar{n}-1})\big] \\ &+ \frac{1}{2} w_{\mathrm{c}}'''(0,t_n)\big[\mathscr{H}_{\mathrm{l,V\upsilon}}(t_1) - \mathscr{H}_{\mathrm{l,V\upsilon}}(t_0)\big]. \end{aligned} \tag{7.11}$$

It is important to note that in Eq. (7.11) and the similar expressions for the other three components w_{M}, w'_{V}, and w'_{M}, the displacement, slope, bending moment, and shear force at time moment t_n are unknown, while all the other components are known (i.e., history terms). Therefore, Eq. (7.11) is divided into a yet unknown *instantaneous* contribution and an already known *history* contribution:

$$w_{\mathrm{V}}(0,t_n) \approx \mathscr{H}^{\mathrm{inst}}_{\mathrm{l,V\upsilon}}\, w'''_{\mathrm{c}}(0,t_n) + w^{\mathrm{hist}}_{\mathrm{V}}(0,t_n), \tag{7.12}$$

$$\mathscr{H}^{\mathrm{inst}}_{\mathrm{l,V\upsilon}} = \frac{1}{2}\Big(\mathscr{H}_{\mathrm{l,V\upsilon}}(t_1) - \mathscr{H}_{\mathrm{l,V\upsilon}}(t_0)\Big). \tag{7.13}$$

After deriving the expressions for the other three components (i.e., w_{M}, w'_{V}, and w'_{M}) and substituting them in Eq. (7.5), the non-reflective boundary conditions become:

$$\begin{pmatrix} w_{\mathrm{c}}(0,t_n) \\ w'_{\mathrm{c}}(0,t_n) \end{pmatrix} = \mathbf{H}^{\mathrm{inst}}_{\mathrm{l}} \begin{pmatrix} w'''_{\mathrm{c}}(0,t_n) \\ w''_{\mathrm{c}}(0,t_n) \end{pmatrix} + \begin{pmatrix} w^{\mathrm{hist}}_{\mathrm{V}}(0,t_n) + w^{\mathrm{hist}}_{\mathrm{M}}(0,t_n) \\ w^{\mathrm{hist}\prime}_{\mathrm{V}}(0,t_n) + w^{\mathrm{hist}\prime}_{\mathrm{M}}(0,t_n) \end{pmatrix}, \tag{7.14}$$

$$\begin{pmatrix} w_{\mathrm{c}}(L,t_n) \\ w'_{\mathrm{c}}(L,t_n) \end{pmatrix} = \mathbf{H}^{\mathrm{inst}}_{\mathrm{r}} \begin{pmatrix} w'''_{\mathrm{c}}(L,t_n) \\ w''_{\mathrm{c}}(L,t_n) \end{pmatrix} + \begin{pmatrix} w^{\mathrm{hist}}_{\mathrm{V}}(L,t_n) + w^{\mathrm{hist}}_{\mathrm{M}}(L,t_n) \\ w^{\mathrm{hist}\prime}_{\mathrm{V}}(L,t_n) + w^{\mathrm{hist}\prime}_{\mathrm{M}}(L,t_n) \end{pmatrix}. \tag{7.15}$$

The force and moment are obtained from Eqs. (7.14) and (7.15) through matrix inversion. Also, to have the complete non-reflective boundary conditions, the effects on the computational domain of the moving load when it acts on the semi-infinite domains and of the non-trivial initial conditions of the left semi-infinite domain need to be superimposed. These contributions are obtained by numerically evaluating the inverse Laplace transform of vectors $\hat{\mathbf{b}}^{\mathrm{ML}}_{\mathrm{l},1}$, $\hat{\mathbf{b}}^{\mathrm{ML}}_{\mathrm{r},1}$, and $\hat{\mathbf{b}}^{\mathrm{IC}}_{\mathrm{l},1}$ from Section 6.2.3. The complete non-reflective boundary conditions now read

$$\begin{pmatrix} w'''_{\mathrm{c}}(0,t_n) \\ w''_{\mathrm{c}}(0,t_n) \end{pmatrix} = \left(\mathbf{H}^{\mathrm{inst}}_{\mathrm{l}}\right)^{-1} \begin{pmatrix} w_{\mathrm{c}}(0,t_n) \\ w'_{\mathrm{c}}(0,t_n) \end{pmatrix} - \mathbf{b}^{\mathrm{hist}}_{\mathrm{l}} - \mathbf{b}^{\mathrm{ML}}_{\mathrm{l}} - \mathbf{b}^{\mathrm{IC}}_{\mathrm{l}}, \tag{7.16}$$

$$\begin{pmatrix} w'''_{\mathrm{c}}(L,t_n) \\ w''_{\mathrm{c}}(L,t_n) \end{pmatrix} = \left(\mathbf{H}^{\mathrm{inst}}_{\mathrm{r}}\right)^{-1} \begin{pmatrix} w_{\mathrm{c}}(L,t_n) \\ w'_{\mathrm{c}}(L,t_n) \end{pmatrix} - \mathbf{b}^{\mathrm{hist}}_{\mathrm{r}} - \mathbf{b}^{\mathrm{ML}}_{\mathrm{r}}. \tag{7.17}$$

where vectors $\mathbf{b}^{\mathrm{hist}}_{\mathrm{l}}$ and $\mathbf{b}^{\mathrm{hist}}_{\mathrm{r}}$ incorporate the history shear forces and bending moments, and read

$$\mathbf{b}^{\mathrm{hist}}_{\mathrm{l}} = \left(\mathbf{H}^{\mathrm{inst}}_{\mathrm{l}}\right)^{-1} \begin{pmatrix} w^{\mathrm{hist}}_{\mathrm{V}}(0,t_n) + w^{\mathrm{hist}}_{\mathrm{M}}(0,t_n) \\ w^{\mathrm{hist}\prime}_{\mathrm{V}}(0,t_n) + w^{\mathrm{hist}\prime}_{\mathrm{M}}(0,t_n) \end{pmatrix}, \tag{7.18}$$

$$\mathbf{b}^{\mathrm{hist}}_{\mathrm{r}} = \left(\mathbf{H}^{\mathrm{inst}}_{\mathrm{r}}\right)^{-1} \begin{pmatrix} w^{\mathrm{hist}}_{\mathrm{V}}(L,t_n) + w^{\mathrm{hist}}_{\mathrm{M}}(L,t_n) \\ w^{\mathrm{hist}\prime}_{\mathrm{V}}(L,t_n) + w^{\mathrm{hist}\prime}_{\mathrm{M}}(L,t_n) \end{pmatrix}. \tag{7.19}$$

The forces expressed in Eqs. (7.16) and (7.17) are imposed at the boundaries of the computational domain (Eq. (7.1)). Consequently, $\left(\mathbf{H}^{\mathrm{inst}}_{\mathrm{l}}\right)^{-1}$ and $\left(\mathbf{H}^{\mathrm{inst}}_{\mathrm{r}}\right)^{-1}$ are added to the Euler-

Bernoulli stiffness matrix $\mathbf{K}^{\mathrm{EB}}$ because they are dependent on the unknown displacement and slope. The remaining terms in Eqs. (7.16) and (7.17) are accounted for in the boundary-forcing vector $\mathbf{f}_{\mathrm{c}}^{\mathrm{B}}$ because they are independent of the unknown displacement and slope, and are thus treated as external forces. Incorporating these boundary conditions (Eqs. (7.16) and (7.17)) ensures that the finite computational domain behaves as an infinite one.

By discretising the convolution integrals, the system of integro-differential equations is approximated by a system of coupled ordinary differential equations with state-dependent coefficients. This system is solved by means of the Newmark-β method [119]. To this end, the generalized displacement vector $\mathbf{x}_{n+1}$ at time moment t_{n+1} is expressed as a function of the displacement $\mathbf{x}_n$, velocity $\dot{\mathbf{x}}_n$, and acceleration $\ddot{\mathbf{x}}_n$ at time moment t_n as follows:

$$\mathbf{x}_{n+1} = \mathbf{Y}_{n+1}^{-1}\mathbf{z}, \tag{7.20}$$

$$\mathbf{Y}_{n+1} = \frac{1}{\beta\Delta t^2}\mathbf{M} + \frac{\gamma}{\beta\Delta t}\mathbf{C} + \mathbf{K}_{n+1} + \mathbf{K}^{\mathrm{EB}}, \tag{7.21}$$

$$\begin{aligned}\mathbf{z} = \left(\mathbf{f}_{\mathrm{c},n+1}^{\mathrm{ML}} + \mathbf{f}_{\mathrm{c},n+1}^{\mathrm{B}} + \mathbf{f}_{\mathrm{c},n+1}^{\mathrm{NL}}\right) + \mathbf{M}\left(\frac{1}{\beta\Delta t^2}\mathbf{x}_n + \frac{1}{\beta\Delta t}\dot{\mathbf{x}}_n + \left(\frac{1}{2\beta} - 1\right)\ddot{\mathbf{x}}_n\right) \\ + \mathbf{C}\left(\frac{\gamma}{\beta\Delta t}\mathbf{x}_n - \left(1 - \frac{\gamma}{\beta}\right)\dot{\mathbf{x}}_n - \Delta t\left(1 - \frac{\gamma}{2\beta}\right)\ddot{\mathbf{x}}_n\right),\end{aligned} \tag{7.22}$$

where γ and β are two parameters that indicate how much of the acceleration at the end of a time interval influences the relations for the velocity and displacement at the end of that interval [119]. The parameters are chosen as $\gamma = \frac{1}{2}$ and $\beta = \frac{1}{4}$, implying that the acceleration is constant over a time step and is equal to the average between the previous and the next time step. This choice is preferred in order to have consistency between the assumed force evolution of the non-reflective boundary conditions (as expressed in Eq. (7.8)) and the assumed force evolution in the time-stepping scheme. After obtaining $\mathbf{x}_{n+1}$, the generalized velocity and acceleration vectors are also computed to be used for obtaining the generalized displacement at the next time moment. Their expressions read

$$\dot{\mathbf{x}}_{n+1} = \frac{\gamma(\mathbf{x}_{n+1} - \mathbf{x}_n)}{\beta\Delta t} + \dot{\mathbf{x}}_n\left(1 - \frac{\gamma}{\beta}\right) + \ddot{\mathbf{x}}_n\Delta t\left(1 - \frac{\gamma}{2\beta}\right), \tag{7.23}$$

$$\ddot{\mathbf{x}}_{n+1} = \frac{\mathbf{x}_{n+1} - \mathbf{x}_n}{\beta\Delta t^2} - \frac{\dot{\mathbf{x}}_n}{\beta\Delta t} - \ddot{\mathbf{x}}_n\left(\frac{1}{2\beta} - 1\right). \tag{7.24}$$

At each time step, the nodes are monitored to check in which branch of the constitutive relation they are, and if they have changed branch, the Kelvin stiffness matrix $\mathbf{K}$ as well as the nonlinear-forcing vector $\mathbf{f}_{\mathrm{c}}^{\mathrm{NL}}$ are updated accordingly. It must be noted that when the nonlinear constitutive relation discussed in the problem statement is adopted, also the Kelvin damping matrix $\mathbf{C}$ becomes state-variable dependent, and thus needs to be updated at each nonlinear event. The time-domain solution method is now fully described. Next, the pseudo-force method is introduced.

7.2. Pseudo-force method

In this section, the problem is solved using the framework of the pseudo-force method [123, 124]. This solution method is based on the response of the linear and piecewise-homogeneous system, which in this work is expressed in terms of the Green's function. The steps of the procedure are as follows. The *base* system is assumed to be linear and piecewise-homogeneous while the nonlinear and the remainder of the inhomogeneity components (the difference between the piecewise-homogeneous profile and the one described by Eq. (4.39)) of the system are accounted for by means of pseudo forces. Basically, the nonlinear and the remainder of the inhomogeneity terms are moved to the right-hand side of the equation of motion and the resulting implicit equation is solved in an iterative manner. It must be noted that the shift-invariant homogeneous system could be chosen as the base system too; however, by doing so, the pseudo forces that account for the inhomogeneity must act on the entire right semi-infinite domain. For the piecewise-homogeneous system, the pseudo forces need to be prescribed only in the transition zone and its vicinity and this is the reason why the piecewise-homogeneous base system is preferred. The procedure on which this solution method is based is explained in detail in [124]. Therefore, only the crucial aspects of the approach are elaborated in the following.

After moving the terms accounting for the nonlinearity and for the remainder of the inhomogeneity to the right-hand side, the equation of motion reads

$$\frac{\tilde{\partial}^4 w}{\tilde{\partial} x^4} + \rho \frac{\tilde{\partial}^2 w}{\tilde{\partial} t^2} + c_{\mathrm{d}}^{\mathrm{PH}}(x) \frac{\tilde{\partial} w}{\tilde{\partial} t} + k_{\mathrm{d}}^{\mathrm{PH}}(x)\, w = f^{\mathrm{ML}} + f^{\mathrm{u}} + f^{\mathrm{v}}, \tag{7.25}$$

where w is the displacement of the entire beam (i.e., $x \in (-\infty, \infty)$), $c_{\mathrm{d}}^{\mathrm{PH}}(x) = c_{\mathrm{d,l}} H(x_{\mathrm{tc}} - x) + c_{\mathrm{d,r}} H(x - x_{\mathrm{tc}})$ and $k_{\mathrm{d}}^{\mathrm{PH}}(x) = k_{\mathrm{d,l}} H(x_{\mathrm{tc}} - x) + k_{\mathrm{d,r}} H(x - x_{\mathrm{tc}})$ are the piecewise-homogeneous damping and stiffness of the Kelvin foundation, respectively, $f^{\mathrm{ML}} = -F_0 \delta(x - x_{\mathrm{e}} - vt)$, and f^{u} and f^{v} are the pseudo forces; f^{u} is proportional to the displacement while f^{v} is proportional to the velocity, and, in the case of the bilinear constitutive relation, they read

$$\begin{aligned} f^{\mathrm{u}}(x, w) &= -\left[k_{\mathrm{d}}^{\mathrm{A}}(x) - k_{\mathrm{d}}^{\mathrm{PH}}(x)\right] w H(w - w_{\mathrm{el}}) - \left[\left(k_{\mathrm{d}}^{\mathrm{B}}(x) - k_{\mathrm{d}}^{\mathrm{PH}}(x)\right) w - \Delta k_{\mathrm{d}}(x)\, w_{\mathrm{el}}\right] H(w_{\mathrm{el}} - w), \\ f^{\mathrm{v}}(x, \dot{w}) &= -\left[c_{\mathrm{d}}(x) - c_{\mathrm{d}}^{\mathrm{PH}}(x)\right] \dot{w}. \end{aligned} \tag{7.26}$$

It must be noted that the part of the nonlinear forcing that is independent of the unknown displacement (denoted by superscript NL in the other two methods), namely $\Delta k_{\mathrm{d}}(x)\, w_{\mathrm{el}} H(w_{\mathrm{el}} - w)$, is incorporated here in f^{u} because in this method both contributions (dependent on or independent of the unknown displacement) are treated as external forces; therefore, the distinction between them is not needed in this method. Additionally, it must be noted that when the nonlinear constitutive relation discussed in the problem statement (Section 6.1) is adopted, the behaviour of the foundation damping becomes piecewise linear too and must be accounted for in Eq. (7.26).

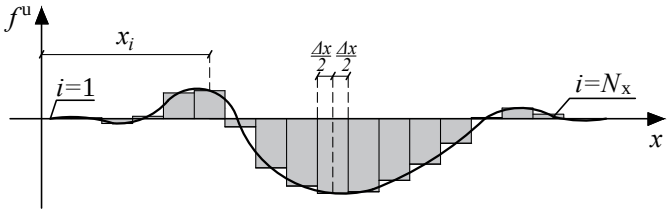

Figure 7.1: The assumed spatial profile of the pseudo forces; the length of the domain should be chosen such that the first ($i = 1$) and last ($i = N_{\mathrm{x}}$) pseudo force are nearly zero.

The solution to Eq. (7.25) can be expressed as a superposition of the response w^{ML} caused by the moving load f^{ML} in the base system and the response to the pseudo forces. Firstly, the response w^{ML} caused by the moving load can be obtained by using the Fourier transform over time. In the Fourier domain, after imposing interface conditions and the condition of zero displacements at infinity, the displacements of the two domains can be obtained analytically [e.g., 20, 49]. To obtain the time-domain solution, the inverse Fourier integral is evaluated numerically. Secondly, the response to the pseudo forces is expressed as a convolution integral of the impulse response of the base system and said forces. For conciseness, the derivation is demonstrated for f^{u} only. The contribution w^{v} caused by the forcing term related to the damping inhomogeneity f^{v} is kept general and is made specific in the final expression (Eq. (7.39)). The response thus reads

$$w(x,t) = w^{\mathrm{ML}}(x,t) + w^{\mathrm{v}}(x,t) + \int_0^L \int_0^t g(x,\xi,t-\tau)\, f^{\mathrm{u}}\big(\xi, w(\xi,\tau)\big)\mathrm{d}\xi\mathrm{d}\tau, \tag{7.27}$$

where g is the time-domain Green's function of the base system.

To evaluate Eq. (7.27), the integrals are discretised. Firstly, the displacement w is assumed to be piecewise constant in space and equal to the value at the centre of each discrete element. Consequently, also the Green's function g is determined with a box-car shaped load in space (see Fig. 7.1), while it assumes a Dirac delta function loading in time. The continuous-in-time and discrete-in-space expression for the displacement reads

$$w_i(t) = w_i^{\mathrm{ML}}(t) + w_i^{\mathrm{v}}(t) + \sum_{\bar{i}=1}^{N_{\mathrm{x}}} \int_0^t g_{i,\bar{i}}(t-\tau)\, f_{\bar{i}}^{\mathrm{u}}\big(w_{\bar{i}}(\tau)\big)\mathrm{d}\tau, \tag{7.28}$$

where i is the index for the observation point in space while $\bar{i}$ is the index for the running (integration) spatial variable, and N_{x} is the number of integration points. Secondly, the forces $f_{\bar{i}}^{\mathrm{u}}$ are assumed to be piecewise linear in time. The displacement thus becomes

$$w_{i,n} = w_{i,n}^{\mathrm{ML}} + w_{i,n}^{\mathrm{v}} + \sum_{\bar{i}=1}^{N_{\mathrm{x}}} \sum_{\bar{n}=1}^{n} \int_{t_{\bar{n}-1}}^{t_{\bar{n}}} g_{i,\bar{i}}(t_n - \tau) \tag{7.29}$$

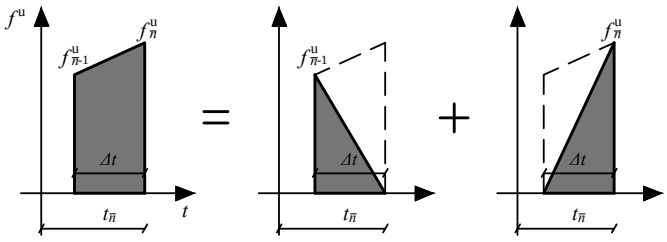

Figure 7.2: The loading applied within a single time step is decomposed into two parts: one proportional to $f^{\mathrm{u}}_{\bar{n}-1}$ and the other proportional to $f^{\mathrm{u}}_{\bar{n}}$.

$$\times \left[f^{\mathrm{u}}_{\bar{i},\bar{n}-1}(w_{\bar{i},\bar{n}-1}) \left(1 - \frac{\tau - t_{\bar{n}-1}}{\Delta t}\right) + f^{\mathrm{u}}_{\bar{i},\bar{n}}(w_{\bar{i},\bar{n}}) \frac{\tau - t_{\bar{n}-1}}{\Delta t} \right] \mathrm{d}\tau, \quad n \geq 1,$$

where n is the index for the observation time variable while $\bar{n}$ is the index for the running (integration) time variable. Eq. (7.2) is valid only for $n \geq 1$ because at $t_0 = 0$, just the response caused by the moving load $\left(\text{i.e., } w_{i,0} = w^{\mathrm{ML}}_{i,0}\right)$ is present, similar to the initial conditions imposed in the other two methods. It can be observed that Eq. (7.2) consists of two terms, one proportional to the force at time moment $t_{\bar{n}-1}$ and one proportional to the force at time moment $t_{\bar{n}}$. Since the two forcing terms are not dependent on the variable of integration τ, they can be taken out of the integral. The equation can therefore be rewritten as follows:

$$w_{i,n} = w^{\mathrm{ML}}_{i,n} + w^{\mathrm{v}}_{i,n} + \sum_{\bar{i}=1}^{N_{\mathrm{x}}} \sum_{\bar{n}=1}^{n} \left[f^{\mathrm{u}}_{\bar{i},\bar{n}-1}(w_{\bar{i},\bar{n}-1}) \mathscr{L}_{i,\bar{i},n-\bar{n}} + f^{\mathrm{u}}_{\bar{i},\bar{n}}(w_{\bar{i},\bar{n}}) \mathscr{R}_{i,\bar{i},n-\bar{n}} \right], \tag{7.30}$$

$$\mathscr{L}_{i,\bar{i},n-\bar{n}} = \int_{t_{\bar{n}-1}}^{t_{\bar{n}}} g_{i,\bar{i}}(t_n - \tau) \left(1 - \frac{\tau - t_{\bar{n}-1}}{\Delta t}\right) \mathrm{d}\tau, \tag{7.31}$$

$$\mathscr{R}_{i,\bar{i},n-\bar{n}} = \int_{t_{\bar{n}-1}}^{t_{\bar{n}}} g_{i,\bar{i}}(t_n - \tau) \frac{\tau - t_{\bar{n}-1}}{\Delta t} \mathrm{d}\tau, \tag{7.32}$$

where $\mathscr{L}$ and $\mathscr{R}$ represent the responses observed at t_n due to triangular pulses lasting between $t_{\bar{n}-1}$ and $t_{\bar{n}}$ (see Fig. 7.2).

The time-domain Green's functions $g_{i,\bar{i}}(t_n - \tau)$ need to be obtained numerically while the integration from $t_{\bar{n}-1}$ to $t_{\bar{n}}$ needs to be performed numerically too, thus introducing two sources of inaccuracy. To increase accuracy, the response associated with a triangular pulse can be obtained directly from the Laplace domain, where only the inverse Laplace transform needs to be evaluated numerically. To this end, the expressions for $\mathscr{L}$ and $\mathscr{R}$ can be rewritten by introducing the variable change $\bar{\tau} = \tau - t_{\bar{n}-1}$:

$$\mathscr{L}_{i,\bar{i},n-\bar{n}} = \int_0^{t_{n-\bar{n}+1}} g_{i,\bar{i}}(t_{n-\bar{n}+1} - \bar{\tau}) \left(1 - \frac{\bar{\tau}}{\Delta t}\right) H(\Delta t - \bar{\tau}) \mathrm{d}\bar{\tau}, \tag{7.33}$$

$$\mathscr{R}_{i,\bar{i},n-\bar{n}} = \int_0^{t_{n-\bar{n}+1}} g_{i,\bar{i}}(t_{n-\bar{n}+1} - \bar{\tau}) \left(\frac{\bar{\tau}}{\Delta t}\right) H(\Delta t - \bar{\tau}) \mathrm{d}\bar{\tau}, \tag{7.34}$$

where $t_{n-\bar{n}+1} = t_n - t_{\bar{n}-1}$. These responses can now be expressed as inverse Laplace transforms as follows:

$$\mathscr{L}_{i,\bar{i},n-\bar{n}} = \frac{\mathrm{e}^{\sigma t_{n-\bar{n}+1}}}{\pi} \int_0^\infty \mathrm{Re}\Big(\hat{g}_{i,\bar{i}}(\sigma + \mathrm{i}\omega)\, \hat{P}_{\mathscr{L}}(\sigma + \mathrm{i}\omega)\, \mathrm{e}^{\mathrm{i}\omega t_{n-\bar{n}+1}}\Big)\mathrm{d}\omega, \tag{7.35}$$

$$\mathscr{R}_{i,\bar{i},n-\bar{n}} = \frac{\mathrm{e}^{\sigma t_{n-\bar{n}+1}}}{\pi} \int_0^\infty \mathrm{Re}\Big(\hat{g}_{i,\bar{i}}(\sigma + \mathrm{i}\omega)\, \hat{P}_{\mathscr{R}}(\sigma + \mathrm{i}\omega)\, \mathrm{e}^{\mathrm{i}\omega t_{n-\bar{n}+1}}\Big)\mathrm{d}\omega, \tag{7.36}$$

where $\hat{g}_{i,\bar{i}}$ is the Laplace-domain Green's function associated with a Dirac delta load in time and a box-car function in space, and $\hat{P}_{\mathscr{L}}$ and $\hat{P}_{\mathscr{R}}$ are given by

$$\hat{P}_{\mathscr{L}}(s) = \frac{1}{s^2 \Delta t}\Big(1 - s\Delta t \mathrm{e}^{-s\Delta t} - \mathrm{e}^{-s\Delta t}\Big), \tag{7.37}$$

$$\hat{P}_{\mathscr{R}}(s) = \frac{1}{s^2 \Delta t}\Big(-1 + s\Delta t + \mathrm{e}^{-s\Delta t}\Big). \tag{7.38}$$

The inverse Laplace transforms are evaluated numerically using a quadratic, nested, adaptive integration scheme.

To express the contribution from the forces proportional to the velocity f^{v} (Eq. (7.26)), one needs to derive an expression for the velocity $\dot{w}_{i,n}$. One could follow the same procedure as for the displacement $w_{i,n}$ and obtain a similar equation to Eq. (7.30). Then, the equations for $w_{i,n}$ (Eq. (7.30)) and $\dot{w}_{i,n}$ could be solved simultaneously. However, the Laplace-domain counterparts of $\mathscr{L}$ and $\mathscr{R}$ that relate applied force to resulting velocity have a poor decay and, consequently, evaluating the inverse Laplace transforms is time consuming. A computationally efficient alternative is to approximate the velocity $\dot{w}_{i,n}$ as a function of the displacement at the previous time moments by using the finite difference method. This makes the force $f^{\mathrm{v}}_{i,n}$ proportional to the displacement (i.e., $f^{\mathrm{v}}_{i,n}(w_{i,n}, w_{i,n-1}, w_{i,n-2})$), so that it can be added to the force f^{u}, together being incorporated in the force $f^{\mathrm{u+v}}_{i,n}$. Note that for conciseness, the force $f^{\mathrm{u+v}}_{i,n}$ is indicated in the following to be dependent on the displacement $w_{i,n}$, while in actual fact it is also dependent on the displacement at the previous time moments. The complete solution now reads

$$w_{i,n} = w^{\mathrm{ML}}_{i,n} + \sum_{\bar{i}=1}^{N_{\mathrm{x}}} \sum_{\bar{n}=1}^{n} \Big[f^{\mathrm{u+v}}_{\bar{i},\bar{n}-1}\big(w_{\bar{i},\bar{n}-1}\big)\mathscr{L}_{i,\bar{i},n-\bar{n}} + f^{\mathrm{u+v}}_{\bar{i},\bar{n}}\big(w_{\bar{i},\bar{n}}\big)\mathscr{R}_{i,\bar{i},n-\bar{n}} \Big]. \tag{7.39}$$

It can be observed that Eq. (7.39) is implicit for $\bar{n} = n$. Therefore, the equation is divided in an yet unknown *instantaneous* contribution and an already known *history* contribution. The equation becomes

$$w_{i,n} = w^{\mathrm{ML}}_{i,n} + w^{\mathrm{hist}}_{i,n} + \sum_{\bar{i}=1}^{N_{\mathrm{x}}} f^{\mathrm{u+v}}_{\bar{i},n}\big(w_{\bar{i},n}\big)\mathscr{R}_{i,\bar{i},0}, \tag{7.40}$$

$$w_{i,n}^{\text{hist}} = \sum_{\bar{i}=1}^{N_{\text{x}}} \sum_{\bar{n}=1}^{n-1} \left[f_{\bar{i},\bar{n}-1}^{\text{u+v}}\left(w_{\bar{i},\bar{n}-1}\right) \mathscr{L}_{i,\bar{i},n-\bar{n}} + f_{\bar{i},\bar{n}}^{\text{u+v}}\left(w_{\bar{i},\bar{n}}\right) \mathscr{R}_{i,\bar{i},n-\bar{n}} \right] + \sum_{\bar{i}=1}^{N_{\text{x}}} f_{\bar{i},\bar{n}-1}^{\text{u+v}}\left(w_{\bar{i},\bar{n}-1}\right) \mathscr{L}_{i,\bar{i},0}. \tag{7.41}$$

In order to advance to the next time step, Eq. (7.40) is solved for $w_{i,n}$ using an iterative scheme. The scheme is defined by the following recursive relation that starts at $j = 0$ (where j indicates the iteration counter):

$$w_{i,n}^{j+1} \approx w_{i,n}^{\text{ML}} + w_{i,n}^{\text{hist}} + \sum_{\bar{i}=1}^{N_{\text{x}}} f_{\bar{i},n}^{\text{u+v}}\left(w_{\bar{i},n}^{j}\right) \mathscr{R}_{i,\bar{i},0}. \tag{7.42}$$

The rate of convergence of this iterative scheme is $\mathscr{R}_{i,\bar{i},0}$ [124]. Iterations continue until specified tolerances are met for all entries of the displacement $w_{i,n}$. No convergence problems were encountered while computing the results for this chapter.

All three solution methods have been presented now. In the following section, the performance of the three solution methods is compared.

7.3. Results and discussion

Here, the proposed solution methods, namely the sequential Laplace transform (SLT) method, the time-domain (TD) method, and the pseudo-force (PF) method, are compared in terms of accuracy, computational efficiency, and feasibility to apply the methods to more complex models. The three methods are assessed for extreme situations. To this end, a relatively high load velocity is chosen, namely 95% of the critical velocity in the soft domain. Also, a relatively low damping ratio ($\zeta = 0.05$) is used to make sure that errors are not damped out. Moreover, a high stiffness ratio between the left and right domain ($p = 5$) is chosen which, combined with an abrupt transition ($l_{\text{t}} = 0.01$ m), leads to strong transition radiation and large plastic deformation. The location of the abrupt transition is at $x_{\text{tc}} = 5$ m for all simulations presented in this section. Also, $x_{\text{e}} = -30$ m for all the results presented in the following to ensure that the eigenfield does not interact with the inhomogeneity at the beginning of the simulation. The parameter values used to compute the results in this section are the same as the ones in Table 6.1, except for the ones given in Table 7.1.

7.3.1. Accuracy

The accuracy assessment of the three methods is based on two types of simulations. Firstly, a linear limit case is considered by setting the parameters $k_{\text{d,c}}^{\text{B}}(x)$, $k_{\text{d,c}}^{\text{C}}(x)$, and $k_{\text{d,c}}^{\text{D}}(x)$ to be equal to the initial stiffness $k_{\text{d,c}}^{\text{A}}(x)$. By doing so, *fictitious* nonlinear events are introduced, but the response should be the same as the response of the linear system. In the second type of simulation, the nonlinear system with the constitutive relation from Section 6.1 is considered.

Table 7.1: Values of the system parameters used for the numerical results.

Parameter	Symbol	Value	Unit
Damping ratio	ζ	0.05	
Stiff-soft stiffness ratio	p	5	
Centre of the transition	x_{tc}	5	m
Transition length	l_{t}	0.01	m
Load position at $t = 0$	x_{e}	-30	m

The linear limit case is compared to the semi-analytical transient solution derived in Section 2.3. This semi-analytical *benchmark* solution is the same as the response w^{ML} of the base system to the moving load in the PF method (Section 7.2). Because the only source of error of this semi-analytical solution is the numerical evaluation of the inverse Fourier transform, a very high maximum frequency (i.e., $f_{\max} = 40$ kHz) and a small frequency step (i.e., $\Delta f = 0.1$ Hz) are adopted to obtain a very high accuracy.

The relative error $e(x)$ used in this section is given in Eq. (6.52). This error formulation where the summation over time is performed in both the numerator and denominator is chosen because at certain locations and time moments, the displacement can be zero or close to zero, which, if the summation over time were not taken, would lead to a huge relative error that has no physical significance. This error relation is also used for the nonlinear case; however, for the nonlinear simulation there is no semi-analytical solution to use as a benchmark, and thus the three methods are compared to each other.

The accuracy is studied for varying sampling parameters Δt and Δx. The three methods have different sensitivities to the two sampling parameters; therefore, when varying one sampling parameter, the other one is chosen such that the resulting error is of the same order for all three methods. For the SLT and TD methods, the frequency spacing $\Delta\omega = 4\pi$ rad/s has been chosen after sensitivity studies, while for the PF method the adaptive algorithm (see Ref. [124]) chooses itself the frequency sampling. Note that for the TD method, the frequency sampling is needed for evaluating the inverse Laplace transforms to obtain the response functions $\mathscr{H}$ (see Eq. (7.10)) and the boundary vectors ($\mathbf{b}_{\mathrm{l}}^{\mathrm{IC}}$, $\mathbf{b}_{\mathrm{l}}^{\mathrm{ML}}$, and $\mathbf{b}_{\mathrm{r}}^{\mathrm{ML}}$). As for the maximum frequency, $f_{\max} = 2$ kHz for the TD method, $f_{\max} = 1/(2\Delta t)$ for the SLT method, and $f_{\max} = 2^{\log_2(2\pi/\Delta t)+2}$ for the PF method, unless specified otherwise. It must be mentioned that $f_{\max}$ for the PF method is set to such a large value (e.g., $f_{\max} \approx 40$ kHz for $\Delta t = 100\,\mu$s) because the adaptive algorithm chooses very few sampling points if the integrand is smooth at high frequencies, therefore leading to almost no additional computational effort.

Linear limit case

The elastic displacement limit ratio $q = w_{\mathrm{el}}/w_{\max}^{\mathrm{e}}$ is chosen to have a value close to unity ($q = 1.01$) such that fictitious nonlinear events occur in abundance. For the TD method, this

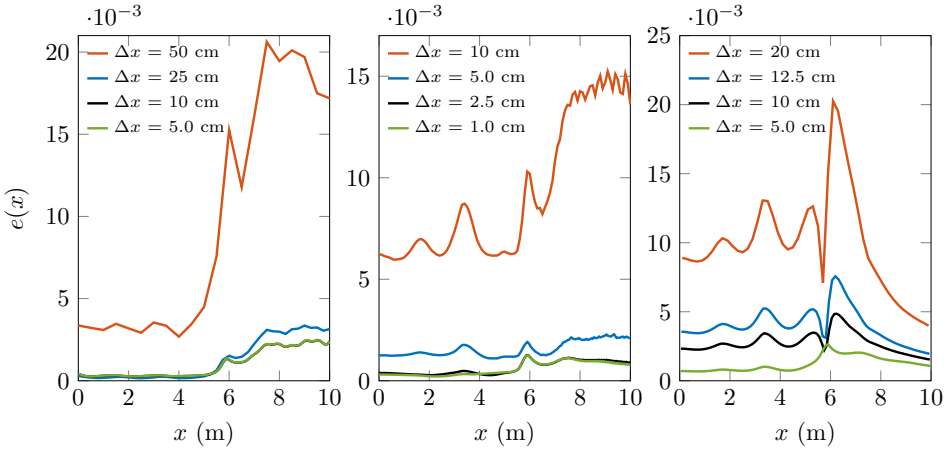

Figure 7.3: Error in the linear limit case for the TD method (left panel; $\Delta t = 20\,\mu s$), the SLT method (middle panel; $f_{max} = 2$ kHz, $\Delta t = 250\,\mu s$), and the PF method (right panel; $\Delta t = 100\,\mu s$).

limit case is the same as a linear case (no fictitious nonlinear events) in terms of accuracy. For the SLT method, this limit case tests all operations, namely solving the system in Eq. (6.15), updating the non-reflective boundaries, and evaluating the inverse Laplace transform. The PF method reduces to computing the response w^{ML} caused by the moving load, which is exactly the same as the benchmark solution; therefore, such a comparison would be superfluous. To also test the PF method, the piecewise-homogeneous base system is prescribed to have the abrupt transition at $x_{tc} = 6$ m while the forces that account for the inhomogeneity need to act such that the system simulates an abrupt transition at $x_{tc} = 5$ m. In this way, the Green's functions and the convolutions are assessed.

Fig. 7.3 shows that the response obtained with all three methods converges to the semi-analytical one as Δx decreases. However, to obtain similar magnitudes of the error, the SLT method requires a smaller Δx than the TD and PF methods. This is because a certain ratio between the maximum frequency f_{max} and Δx must be satisfied in the SLT method. More specifically, the Laplace-domain moving load is harmonic in space $\left(\hat{f}^{ML} = -\frac{F_0}{v}\exp(-s\frac{x-x_e}{v})\right)$; to accurately represent $\hat{f}^{ML}$ at high frequencies, there should be at least five spatial points per wavelength, leading to the requirement that $\Delta x = v/(4f_{max})$. For the parameters in Fig. 7.3, this minimum requirement is $\Delta x = 5$ cm; for this reason, the error is much larger for $\Delta x = 10$ cm while for the remaining values of Δx the error is of similar magnitude. The larger error in the right domain for the SLT and TD methods is caused by the significantly smaller values of the displacement encountered there. The PF method is not so much affected by this because as the transients caused by the transition die out, the solution tends to the semi-analytical baseline response.

The error also decreases with decreasing Δt for all three methods, depicted in Fig. 7.4. Unlike for decreasing Δx, here the TD and PF methods require smaller Δt than the SLT

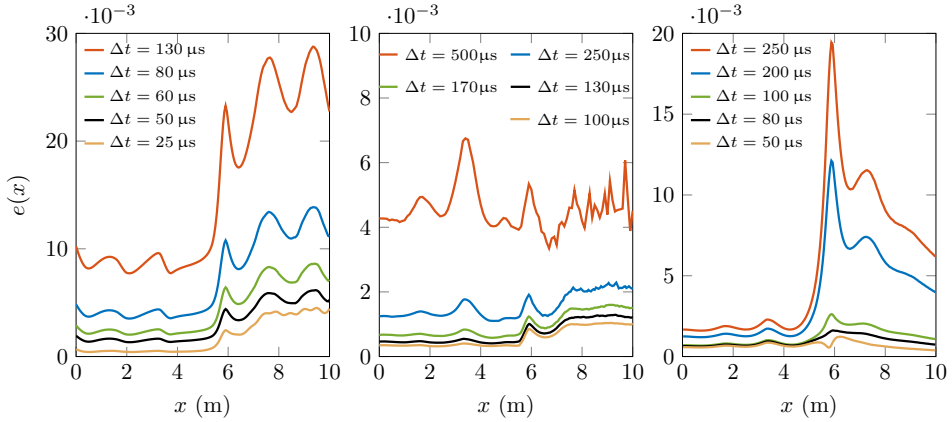

Figure 7.4: Error in the linear limit case for the TD method (left panel; $\Delta x = 5$ cm), the SLT method (middle panel; $\Delta x = v/(4 f_{\max})$), and the PF method (right panel; $\Delta x = 5$ cm).

method to obtain a similar error magnitude. The TD method exhibits a significant error reduction with decreasing Δt, which is to be expected since the Newmark method is a time-stepping method and the smaller the Δt, the more accurate the approximation becomes. For the SLT method, $f_{\max}$ needs to be increased with decreasing Δt to obtain convergent results. More specifically, to satisfy the continuity conditions (see Eqs. (6.8) and (6.9)), the inverse Laplace transform requires a high accuracy close to $t_n = 0$ (here, n refers to the time interval; see Section 6.2). This can be achieved by satisfying the criterion $\Delta t = 1/(2 f_{\max})$ (i.e., the time discretisation should not be more refined than the Nyquist criterion requires). The fact that the spatial discretisation is linked to $f_{\max}$ (as stated in the previous paragraph) leads to the three sampling parameters (i.e., Δx, Δt, and $f_{\max}$) being interdependent for the SLT method. As presented in Section 7.3.2, this leads to significant increase in computational effort when one of them is changed. As for the PF method, the error decreases considerably with decreasing Δt. This is caused by the pseudo forces (acting between $x = 5$–6 m) becoming more accurate; in other words, the approximation of the convolution integrals (see Eq. (7.41)) is improved by decreasing Δt.

Nonlinear case

As there is no semi-analytical solution to test against in the nonlinear case, it is chosen to run a high-resolution simulation using the TD method (i.e., $f_{\max} = 4$ kHz, $\Delta x = 0.5$ cm, $\Delta t = 10$ µs), and perform the accuracy analysis using this result as a benchmark. Therefore, it is important to realize that the error studies presented in this section do not represent errors with respect to a *true* solution, but they are essentially differences between solution methods. For the results presented in this section, the elastic displacement limit ratio is chosen as $q = 1.05$.

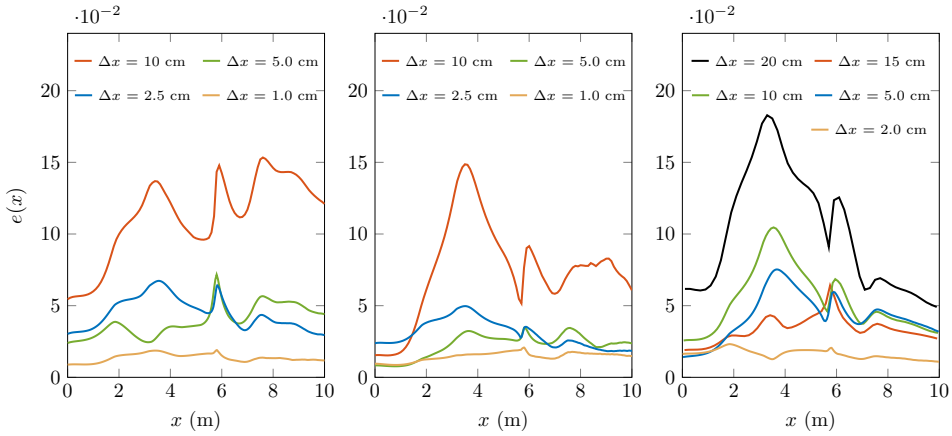

Figure 7.5: Error in the nonlinear case for the TD method (left panel; $\Delta t = 80\,\mu$s), the SLT method (middle panel; $\Delta t = 250\,\mu$s), and the PF method (right panel; $\Delta t = 100\,\mu$s).

One can observe at a first glance of Figs. 7.5 and 7.6 that the error in general is considerably larger than for the linear limit case (Section 7.3.1). The additional error is mainly caused by two factors: the spatial and temporal discretisation of the foundation's nonlinear force (see Eq. (6.3) for the bilinear case), and the combination of non-smooth nonlinearity and separation between the beam and supporting structure only being allowed in the locations where plastic deformation has developed (see Fig. 6.2). To exemplify the latter, assume the minimum displacement at a certain location x_1 computed with the TD method to be $\min\big(w(x_1,t)\big) = w_{\text{el}} + \varepsilon$ (where ε is a very small positive displacement); this location is therefore in the initial stiffness branch $\big(k^{\text{A}}_{\text{d,c}}\big)$ for all time moments. Now, assume the same quantity computed with the SLT method to be $\min\big(w(x_1,t)\big) = w_{\text{el}} - \varepsilon$; this location experiences a small plastic deformation and the separation between the beam and foundation is allowed (i.e., no force is exerted by the foundation for upwards displacement of the beam). As can be seen, a very small difference in the displacement magnitude (2ε) can lead to different behaviour, causing a larger error than in the linear limit case. Nonetheless, the plastic deformation profile and the displacement's time history show that despite the substantial errors, the solutions exhibit the same trend for all three methods (see Figs. 7.7 and 7.8).

Fig. 7.5 shows that all solutions converge to the benchmark by decreasing Δx; however, the convergence is not monotonic for all locations, not even for the TD method despite the benchmark solution being computed with the TD method. The non-monotonic convergence is caused by the several sources of error that may eliminate each other, leading to apparently accurate solutions for certain sampling combinations. Interestingly, the largest error generally does not occur where the plastic deformation develops, but at a location (around $x = 3.5$ m) between two plasticly deformed regions (see Fig. 7.7).

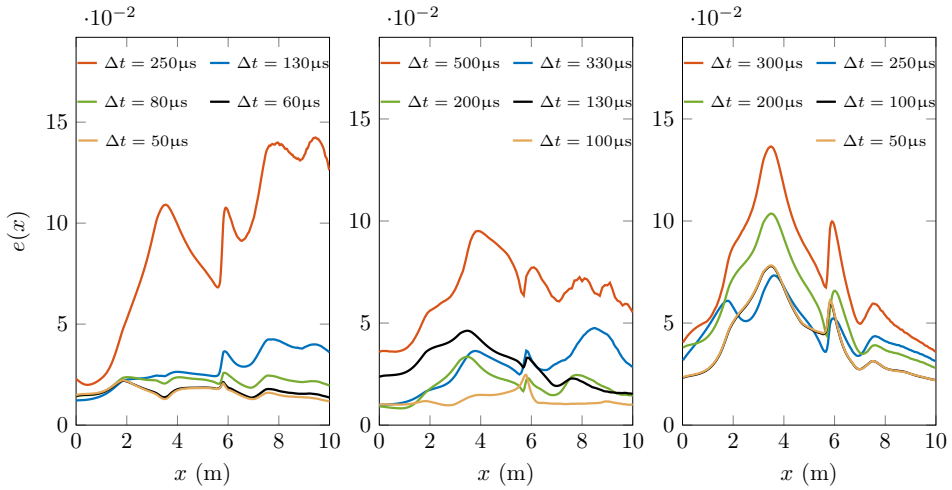

Figure 7.6: Error in the nonlinear case for the TD method (left panel; $\Delta x = 2$ cm), the SLT method (middle panel; $\Delta x = v/(4 f_{\max})$), and the PF method (right panel; $\Delta x = 4$ cm).

One can observe in Fig. 7.6 that the error decreases with decreasing Δt for all three methods, but the decrease is non-monotonic similarly to the error for decreasing Δx, and can be explained in the same manner. The errors obtained with the TD and PF methods seem to converge to a non-zero value because with the decrease in Δt the error introduced by the spatial discretisation starts governing. This is not observed in the SLT method because Δx is decreased with Δt to respect the criterion $\Delta x = v/(4 f_{\max})$ discussed in Section 7.3.1.

To offer a larger picture, Figs. 7.7 and 7.8 present the plastic deformation profile and the displacement's time history at $x = 3.5$ m (the location in the soft domain with the largest error), respectively. Although in some cases the errors may appear to be large (e.g., 2–20 % in Figs. 7.5 and 7.6), all three methods perform well and the differences can hardly be seen.

To conclude, all three methods converge given the appropriate sampling parameters Δx and Δt, and all three can reach similar error magnitudes. Nonetheless, also the computational effort required to achieve the observed accuracy needs to be investigated if one wants to present a complete picture. In this section, the sampling parameters have been chosen such that the error magnitude is similar for the three methods. In the next section, the computational effort to obtain the accuracy discussed in this section is presented and discussed.

7.3.2. Computational efficiency

In this section, the most intensive computational operations are identified for each method. These computational operations are analysed qualitatively as well as quantitatively by presenting a comparison of the computational time required to perform the simulations presented in Section 7.3.1. The computational effort presented in Figs. 7.7 and 7.8 represents

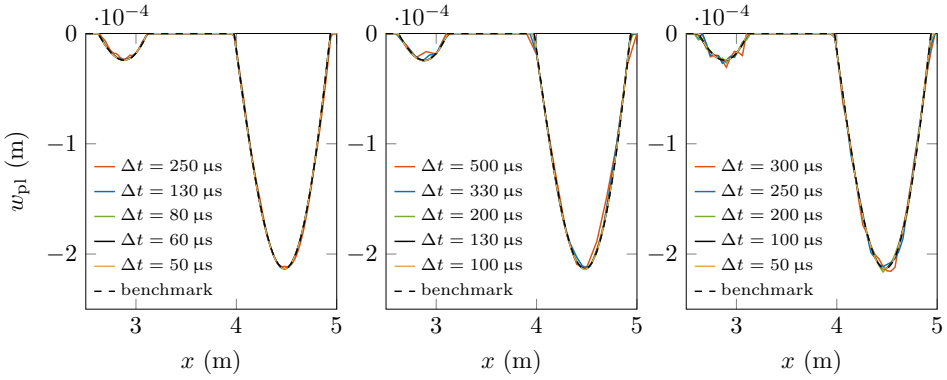

Figure 7.7: Plastic deformation profile for varying Δt for the TD method (left panel; $\Delta x = 2$ cm), the SLT method (middle panel; $\Delta x = v/(4 f_{\max})$), and the PF method (right panel; $\Delta x = 4$ cm).

wall-clock time and the simulations have been performed on a PC with Intel(R) Xeon(R) CPU E5-1630 v3 @ 3.70 GHz processor and 32 GB of RAM memory. It must be emphasized that further optimization of the algorithms is always possible; however, the authors made their best to optimize them and believe that further improvement, although possible, will not lead to significantly different results, especially for the qualitative analysis.

For the TD method, the most computationally demanding processes are numerically solving the system of Eqs. (7.20) to (7.22) and computing the non-reflective boundary conditions. Firstly, determining the solution of the system requires the computation of the matrix inverse $\mathbf{Y}_{n+1}^{-1}$ (the most computationally intensive operation) once at the start of the simulation and recomputed at each nonlinear event due to the change in the properties of the foundation (i.e., $\mathbf{K}$ and $\mathbf{C}$). Alternatively, one can solve the linear system of equations $\mathbf{Y}_{n+1}\mathbf{x}_{n+1} = \mathbf{z}$ using a sparse $\mathbf{Y}$ matrix; this operation is considerably faster than explicitly computing $\mathbf{Y}^{-1}$. However, this operation would need to be computed for each time moment while the matrix inversion needs to be computed only at each nonlinear event. Consequently, for few nonlinear events, the former option is faster while for many nonlinear events, the latter is more efficient. Secondly, the computation of the non-reflective boundary conditions involves numerically evaluating the inverse Laplace transforms to obtain the response functions $\mathscr{H}$ (see Eq. (7.10)) and the boundary vectors ($\mathbf{b}_{\mathrm{l}}^{\mathrm{IC}}$, $\mathbf{b}_{\mathrm{l}}^{\mathrm{ML}}$, and $\mathbf{b}_{\mathrm{r}}^{\mathrm{ML}}$), and evaluating the convolution integrals at the boundaries (see Eq. (7.8)).

For the SLT method, the most computationally intensive operations are solving the linear system of equations (Eq. (6.15)), updating of the non-reflective boundary conditions, and numerically evaluating of the inverse Laplace transform. The linear system of equations (Eq. (6.15)) needs to be solved for each frequency and at each nonlinear event. This is done by using an algorithm to solve linear systems of equations in Matlab (i.e., the *mldivide* routine) where the dynamic stiffness matrix is assembled as sparse. For the results presented here, this is the most computationally intensive part of the SLT method. Next, updating the

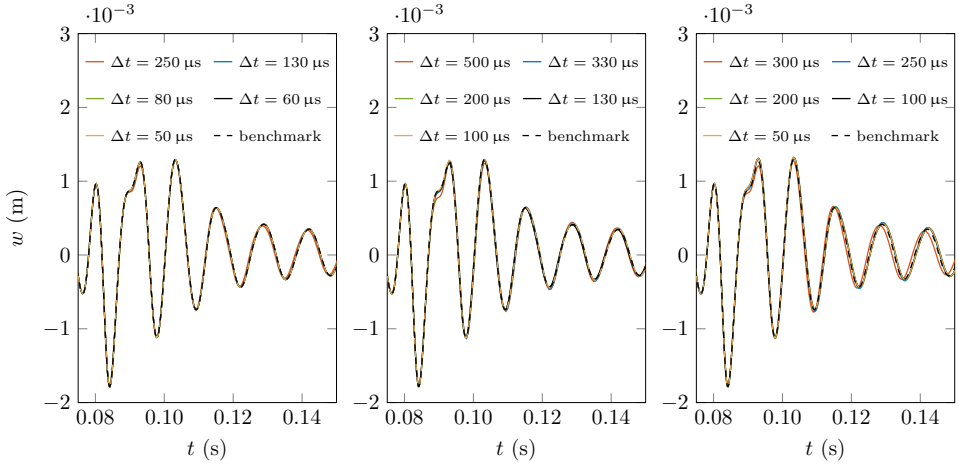

Figure 7.8: Time history of the displacement at $x = 3.5$ m for the TD method (left panel; $\Delta x = 2$ cm), the SLT method (middle panel; $\Delta x = v/(4f_{\max})$), and the PF method (right panel; $\Delta x = 4$ cm).

boundary conditions involves computing the particular solutions of the non-trivial initial conditions in the left and right domains; this implies a numerical evaluation of the inverse Laplace transform for each frequency (see Eqs. (6.50) and (6.50)). Finally, the numerical evaluation of the inverse Laplace transform needs to be performed for each time moment and for each spatial point.

7

For the PF method, the computationally demanding operations are determining the response functions $\mathscr{L}$ and $\mathscr{R}$ in the time domain (i.e., inverse Laplace transforms; see Eqs. (7.35) and (7.36)) and determining the history component $w_{i,n}^{\text{hist}}$ of the response (see Eq. (7.41)). The associated response functions need to be determined for all the excitation points $\xi_{\bar{i}}$ and observation points x_i for all time moments. If the response functions have a strong decay in time, it is sufficient to determine them only for the time moments when the response has a significant amplitude. Determining $w_{i,n}^{\text{hist}}$ involves the evaluation of two convolution integrals (Eq. (7.41)), one over the number of excitation points $\xi_{\bar{i}}$ and one over the time moments smaller than the observation time; this operation needs to be performed for each observation point x_i and observation time t_n.

Fig. 7.9 presents the computational effort C (measured in seconds) needed to reach the accuracy shown in Fig. 7.5. The TD and SLT methods require similar computational times while the PF method appears to be more computationally intensive. This is caused by the fact that with decreasing Δx (i.e., increasing the number N_{x} of excitation $\xi_{\bar{i}}$ and observation x_i points), the number of required response functions $\mathscr{L}$ and $\mathscr{R}$ increases with N_{x}^2. However, once the response functions are determined, a whole parametric study can be conducted (e.g., varying v, l_{t}, types of nonlinearity, etc.) by only performing the convolutions (Eq. (7.40)). For the TD and SLT methods, the computational effort is governed

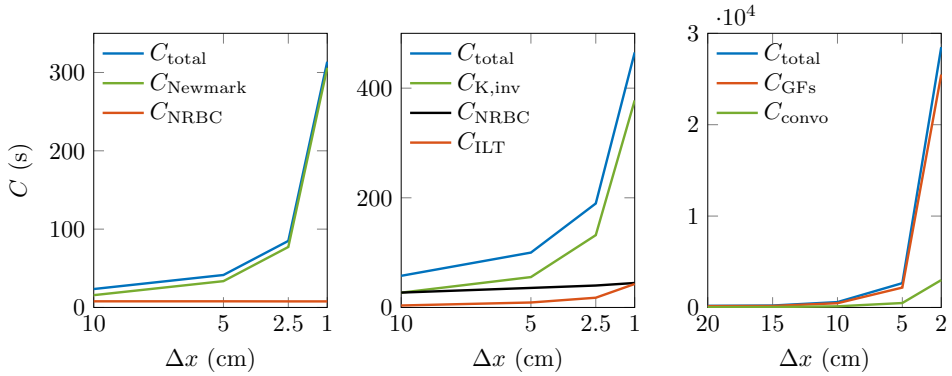

Figure 7.9: Computational effort C in the nonlinear case for the TD method (left panel; $\Delta t = 80\,\mu s$), the SLT method (middle panel; $\Delta t = 250\,\mu s$), and the PF method (right panel; $\Delta t = 100\,\mu s$).

by the matrix inversion operation while updating the non-reflective boundary conditions, as one could expect, is not affected by the change in Δx since they need to be determined only at the boundaries. For the SLT method, the inverse Laplace transform appears to be the least computationally intensive operation.

Fig. 7.10 presents the computational effort C needed to reach the accuracy shown in Fig. 7.6. The computational effort in the TD method is still governed by the inversion of the matrix operation despite Δx being constant because the number of nonlinear events increases with the decreasing Δt (i.e., the number of matrix-inversion operations increases). Also, the computational effort needed to update the non-reflective boundaries appears to be slightly affected by the decrease in Δt. Although the evaluation of the convolution integrals increases almost quadratically, the numerical evaluation of the inverse Laplace transforms increases linearly with decreasing Δt; for $\Delta t = 80$–$250\,\mu s$, the inverse transforms are governing C_{NRBC} for the TD method, while for smaller Δt the convolution integrals start governing. As for the SLT method, the matrix inversion is also still governing the computational time when decreasing Δt because Δx and f_{max} are also varied for these simulations and the number of nonlinear events increases with decreasing Δt. Respecting the convergence criteria for the SLT method leads to a considerable increase in computational effort. For the PF method, C appears to increase less drastically than the other two methods with decreasing Δt. This is because C in the PF method is mainly governed by Δx, which is kept constant here. Also, C for the PF method is not affected by the number of nonlinear events.

Finally, given the accuracy levels presented in Section 7.3.1, the TD method is the most computationally efficient method. However, for certain combinations of Δt and Δx, the SLT method is not far behind while the PF method shows potential for a large number of simulations provided that the associated response functions do not change.

To conclude, it must be mentioned that the above-drawn conclusions can be somewhat different for another choice of parameters (e.g., train velocity, transition length, elastic

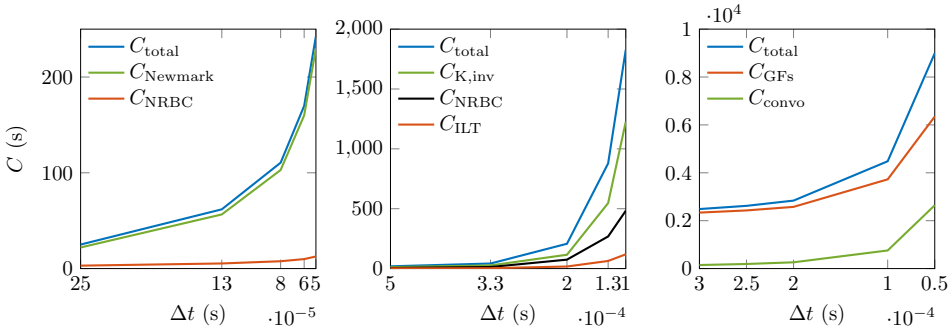

Figure 7.10: Computational effort C in the nonlinear case for the TD method (left panel; $\Delta x = 2$ cm), the SLT method (middle panel; $\Delta x = v/(4f_{\max})$), and the PF method (right panel; $\Delta x = 4$ cm).

displacement limit ratio q, damping ratio, etc.). It is impossible to cover all combinations of parameters, but an indication of how changing these parameters may influence the computational effort is given in the following. The main effects of changing these parameters on the computational effort comparison can be grouped as follows: changes leading to a variation in the number of spatial nodes, changes leading to a variation in the number of time samples, and changes leading to a variation in the number of nonlinear events. Firstly, the number of spatial nodes is affected by the largest real part of the wavenumber of the eigenfield (see Appendix D) and of the generated waves; this is in turn influenced by the load velocity (the higher the load velocity the larger the real part of these wavenumbers). The number of spatial nodes is also affected by the length of the transition zone because the complete nonlinearity and inhomogeneity needs to be incorporated in the computational domain. Secondly, the number of time samples is affected by the maximum frequency of the generated waves (same reasoning as for the maximum wavenumber can be applied here), by the load velocity (i.e., the lower the velocity, the more time moments until the load has passed the transition), and by the damping present in the system (i.e., the higher the damping, the fewer time moments until the waves die out in the computational domain). Thirdly, the number of nonlinear events is affected by the load velocity (the lower the velocity, the less plastic deformation and the fewer nonlinear events), by the length of the transition and the stiffness ratio p (the smoother the transition the fewer nonlinear events), and by the elastic displacement limit ratio q (the larger the ratio the fewer nonlinear events). From the previously drawn conclusions, it can be seen that the PF method is most influenced by the variation in the number of spatial nodes, the TD is most affected by the variation in the number of time samples, and the SLT method is most affected by the number of nonlinear events. (It may seem that also the SLT method is strongly affected by the number of time samples, from Fig. 7.10, but it is mostly the decrease in Δt which leads to an increase in $f_{\max}$ and a decrease in Δx that contributed to this sensitivity; an increase in number of time samples while keeping the Δt fixed does not follow a similar trend in computational

effort increase.) These qualitative observations can give an indication to which method is advantageous for a different choice of parameters.

7.3.3. Feasibility of application to more complex systems

Here, the feasibility for the methods to handle frequency-dependent properties of the structure (e.g., frequency-dependent springs and dashpots) is qualitatively assessed, as well as to handle a smooth nonlinearity (as opposed to the piecewise-linear one), and to apply the solution methods to multi-dimensional models. It must be emphasized that all three methods can be applied in the above-mentioned situations, but one can be more efficient than others, and this is discussed in the following.

Usually when a model reduction is opted for (e.g., going from 2-D to 1-D), the conversion of parameters is done for a specific frequency range of interest. If more frequency ranges are of interest or if the frequency range is broad, then the conversion may lead to frequency-dependent parameters of the reduced-order model. The TD method is inefficient in this case because additional convolution integrals are introduced that are distributed throughout the spatial domain (opposed to the convolution integrals at the boundaries which are local), leading to a significant increase in computational time. For the SLT method, the frequency-dependent parameters can directly be incorporated in the equation of motion with no additional effort since the system is solved in the Laplace domain; therefore, the computational effort in this case is unchanged. For the PF method, the response functions $\mathscr{L}$ and $\mathscr{R}$ are determined from the Laplace domain and can easily incorporate frequency-dependent parameters too; however, the fact that the nonlinearity and part of the inhomogeneity is accounted through the pseudo forces leads to additional convolution integrals throughout the spatial domain, which increases the computational effort of the method. Therefore, the SLT method appears to be most suitable to tackle a system with frequency-dependent properties.

In the problem statement, the reaction of the Kelvin foundation was assumed to be piecewise linear. Although under certain conditions (see Section 6.1) this assumption is reasonable, other analyses might require a smoothly nonlinear constitutive law (e.g., cubic model [111]). The TD method can easily incorporate such behaviour, but with an increase in the computational time because the matrix-inversion operation (see Eq. (7.20)) must be performed at each time moment; however, this operation can be sped up as discussed in Section 7.3.2. The SLT method is very inefficient for such behaviour; the smoothly nonlinear behaviour implies that nonlinear events occur essentially at each time moment leading to a considerable increase in the computational time. The PF method, however, can easily handle such a behaviour. The only increase in the computational time might come from the poorer convergence of the iterative scheme; however, this is unlikely. To present a more quantitative comparison, fictitious nonlinear events are imposed at each time step for one set of sampling parameters ($\Delta x = 5$cm and $\Delta t = 80\mu$s for the TD method, $\Delta x = 5$ cm and $\Delta t = 250\mu$ s for the SLT method, and $\Delta x = 5$ cm and $\Delta t = 100\mu$s for the PF method).

As can be seen in Fig. 7.9, the computational effort for these sampling parameters in the reference case is approximately 40 s for the TD method, 100 s for the SLT method, and 2,660 s for the PF method. When the fictitious nonlinear events are imposed at each time moment, the computational effort is approximately 55 s for the TD method and 550 s for the SLT method, while the one of the PF method remains approximately the same. Thus, by implementing a smoothly nonlinear constitutive law, the TD appears to be most efficient and the PF least efficient, while the computational effort of the SLT method is most affected by such a change.

As for using the methods to analyse a 2-D model, for example, all three methods have advantages and disadvantages. If the nonlinearity and inhomogeneity of the system is considered throughout the depth (i.e., ballast layers as well as the soil layers), then all three methods need to discretise a considerable portion of the vertical direction, leading to a significant increase in the computational time. For such a system, the TD method is likely to be most efficient as the SLT and PF methods become unfeasible for very large systems. More specifically, for the SLT method, the matrix inversion for systems with a very large number of degrees-of-freedom becomes unfeasible when performed for each frequency and each nonlinear event, while for the PF method, the large number of associated response functions to be determined in the time domain renders the method unfeasible. However, if the nonlinearity and inhomogeneity are limited to the surface layers (e.g., nonlinear ballast layer resting on inhomogeneous soil layer supported by a linear half-space), then only the top layers need to be discretised and the others could be included by using frequency-dependent parameters. For such a system, the TD method requires additional spatially distributed convolution integrals to account for the presence of the half-space. The SLT method can exactly replace the half-space by frequency-dependent springs and dashpots, which does not affect its efficiency. Also the PF method can incorporate the half-space with no additional effort (it will already be incorporated in $\mathscr{L}$ and $\mathscr{R}$, which are computed only for the top layers). An example of such a 2-D system has been formulated in Ref. [24] (but with a linear behaviour for all materials), where the ballast and the foundation are modelled as lattices. This model has approximately 60,000 degrees-of-freedom (DOFs) and 40,000 of them are for the foundation. Replacing the foundation by frequency-dependent springs can reduce significantly the amount of DOFs; however, for the SLT method, the dynamic stiffness matrix for the reduced system needs to be inverted for each frequency individually, while for the PF method, obtaining the Green's functions even for this reduced system seems unfeasible. To conclude, even though the SLT appears to have the potential to be more efficient than the TD method for such a system, it difficult to draw a definite conclusion.

7.4. Conclusions

This chapter presents three solution methods to obtain the response of a 1-D model consisting of an infinite Euler-Bernoulli beam resting on a locally inhomogeneous and nonlinear supporting structure subject to a moving constant load. The three methods, namely the

sequential Laplace transform (SLT) method, the time-domain (TD) method, and the pseudo-force (PF) method were chosen from the three main categories of solution methods available in the literature, namely integral-transform methods, time-domain methods, and hybrid methods, respectively. The three methods were compared in terms of accuracy, computational efficiency, and feasibility of application to more complex systems.

Results show that all three methods are able to reach similar accuracy levels, both for a linear limit case and for the nonlinear situation. For the latter case, the combination of non-smooth nonlinearity and separation between the beam and supporting structure only being allowed at the locations where plastic deformation has developed leads to larger relative errors than in the former case and to non-monotonic convergence with decreasing Δx and Δt. Given similar accuracy levels, the TD method is overall the most computationally efficient method. However, for certain sampling combinations, the SLT method is not far behind while the PF method shows potential for a large number of simulations provided that the response functions do not change. As for the feasibility to apply these methods to more complex systems, the SLT method appears to be most efficient in dealing with frequency-dependent parameters while the TD and PF methods in dealing with smooth nonlinearity. For a 2-D system, if the nonlinearity and inhomogeneity is considered throughout the depth, the TD method is likely to be most efficient; however, if the nonlinearity and inhomogeneity are limited to the surface layers (e.g., nonlinear ballast layer resting on inhomogeneous soil layer supported by a linear half-space), the PF and SLT methods have the potential to be more efficient than the TD method.

Based on this study, the adequate solution method to solve more complex systems can be selected depending on the specific characteristics of the model. Although the 1-D model presented in this study has mainly been used to assess the three methods, it can also be used for preliminary designs of transition zones in railway tracks.

8

Transition radiation in a 2-D nonlinear system and the influence of foundation nonlocality

Life would be tragic if it weren't funny.

Stephen Hawking

In all previous chapters, 1-D models have been used to investigate the behaviour of railway tracks. In these models, the supporting structure representing ballast, sub-ballast, soil, etc. was modelled through continuously distributed (Chapters 2–4, 6, and 7) or discrete (Chapter 5) springs and dashpots. Although these 1-D models have been used by researchers for many years due to their simplicity and computational efficiency, they also have drawbacks. Firstly, the Winkler/Kelvin foundation is local by nature, while the ballast-soil foundation is nonlocal; this modelling choice affects the way the supporting structure distributes the load over space. Secondly, closely related to the nonlocality, the reaction of the foundation is frequency-wavenumber dependent in the ballast-soil foundation while the Winkler/Kelvin reaction is independent of frequency and wavenumber. Thirdly, wave propagation (both in vertical and in horizontal directions) is not possible in the Winkler/Kelvin foundation while it does occur in the ballast-soil foundation. Other differences can be mentioned, but these are the most important ones at the low frequencies of interest in the transition radiation problem that this thesis deals with. Naturally, the question arises as to what is the

influence of these effects on the response at transition zones. This chapter aims to answer this question.

The fundamental features of transition radiation in elastic continua (2-D) were first investigated by van Dalen and Metrikine [17] by considering two connected elastic half-spaces, where a moving constant load crosses the interface. More recently, transition radiation was investigated in systems slightly more representative for railway tracks [20, 21]. The above-mentioned studies are mainly focused on investigating fundamental features of the transition radiation phenomenon; consequently, the models used in these studies are simplified ones rendering them suitable for fundamental understanding, but not sufficiently accurate for very specific predictions.

For more practical engineering applications, researchers have developed *predictive* models with a wide focus range to predict the response of railway tracks in the vicinity of transition zones. They range from 2-D FEM models with accurate geometry of the real scenario (e.g., [24, 26–28]), 3-D FEM models [11, 30–32, 67], and hybrid ones [43]. Furthermore, inside each of these categories, researchers focus on a variety of aspects, such as the use of under-sleeper pads for reduction of transition radiation [28], the influence of the foundation nonlinearity on the prediction [26, 129, 130], the influence of accurately modelling ballast behaviour [24, 26, 63, 131], and many more. These predictive models are very important and some of their predictions come very close to the responses measured in practice, especially due to their accurate representation of the geometry and material behaviour. Nonetheless, their complexity makes it difficult to investigate individual mechanisms since there are a multitude at play simultaneously. Therefore, for the purpose of this chapter, a simplified model is preferred.

This chapter has two goals. The first goal is to investigate the response amplification and the corresponding settlement as done in previous chapters for 1-D systems, but now for the 2-D one. The second goal is to investigate the effect of the foundation nonlocality on the response of the system at transition zones in comparison to the 1-D model developed in Chapter 6, and to determine the range of applicability of the 1-D model. To this end, a model is formulated consisting of a linear and homogeneous 2-D continuum layer of finite depth and an Euler–Bernoulli beam connected to the layer through and inhomogeneous and nonlinear Kelvin layer; the beam is acted upon by a moving constant load. This model, actually, consists of the model from Chapter 6 that now rests on a layer of soil. To have the closest comparison possible to the 1-D model, the soil layer is kept homogeneous. Also, the properties of the Kelvin layer are different than in previous chapters because it does not account for the soil any more. The solution is obtained through a pseudo-force method [123–125] that was introduced in a 1-D system in Chapter 7. The novelty of this chapter is contained in the two set goals, with an additional novelty of the application of the pseudo-force method to obtain the response of the current problem.

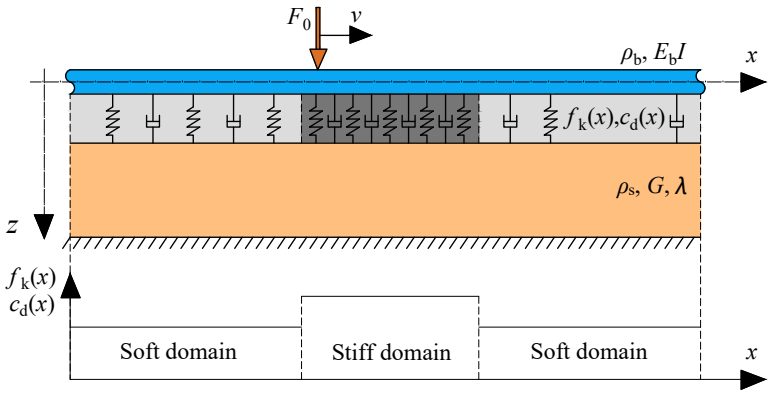

Figure 8.1: Model schematics: infinite Euler-Bernoulli beam connected to an infinite and homogeneous continuum layer through an inhomogeneous and nonlinear layer of springs and dashpots, subjected to a moving constant load acting on the beam.

8.1. Model description

The model formulated in this chapter is representative of a ballasted railway track with a finite inhomogeneous region and it is graphically represented in Fig. 8.1. The model consists of an infinite Euler-Bernoulli beam with mass per unit length ρ_b and bending stiffness EI, and an infinite and homogeneous soil layer with mass density ρ_s, Lamé constants G and λ, and depth Z. The linear mass of the beam includes the mass ρ_r of one rail, the mass ρ_{slp} of half the sleeper distributed along the beam, and the mass ρ_{bal} of half of the layer of ballast. The beam is acted upon by a moving constant load of amplitude F_0 and velocity v. The beam and soil layer are continuously connected by a Kelvin layer of nonlinear springs that provide a restoring force $f_k(x)$ and dashpots with damping coefficient $c_d(x)$. The Kelvin layer effectively accounts for the vertical stiffness and damping of the rail-pads, ballast, and embankment, but no explicit distinction is made between them. The stiffness and damping of the Kelvin layer vary in space in such a way that there is a zone of length l in which the stiffness is p times larger than for the rest of the infinite domain. This region is called the *stiff zone* and represents the source of inhomogeneity in the longitudinal direction. The governing equations of the described system read

$$EIw_{,xxxx} + \rho_b \ddot{w} + c_d(x, \Delta w)\Delta\dot{w} + f_k(x, \Delta w) = -F_0\delta(x - vt), \tag{8.1}$$

$$\rho_s \ddot{u}_x = G(u_{x,xx} + u_{x,zz}) + (\lambda + G)(u_{x,xx} + u_{z,xz}), \tag{8.2}$$

$$\rho_s \ddot{u}_z = G(u_{z,xx} + u_{z,zz}) + (\lambda + G)(u_{z,zz} + u_{x,xz}), \tag{8.3}$$

$$\Delta w = w - u_{z,0}, \qquad \Delta\dot{w} = \dot{w} - \dot{u}_{z,0}, \tag{8.4}$$

$$\sigma_{zx} = 0, \qquad \sigma_{zz} = -c_d(x, \Delta w)\Delta\dot{w} - f_k(x, \Delta w), \qquad z = 0, \tag{8.5}$$

$$u_x = 0, \qquad u_z = 0, \qquad z = Z, \tag{8.6}$$

where overdots denote partial derivatives in time while subscripts , x and , z denote partial derivatives in x- and z-directions, respectively; w is the vertical displacement of the beam while u_x and u_z are the horizontal and vertical displacements of the soil layer, respectively, and $u_{z,0}$ denotes the vertical displacement of the soil layer evaluated at $z = 0$; σ_{zx} and σ_{zz} are the shear and normal stresses, respectively.

As for the nonlinear behaviour of the connecting layer, the constitutive relation presented in Section 6.1 is adopted also here. The only difference in this section is that, due to the fact that the bottom of the springs layer is not fixed (as it is in the 1-D models), the reaction force $f_k(x)$ is governed by the difference in displacement $\Delta w = w - u_{z,0}$, the elastic displacement limit Δw_{el} and the ratio $\Delta w_{el}/\Delta w^e_{max}$. All other characteristics of the nonlinear behaviour of the layer of springs and dashpots of the Kelvin layer is the same as in Section 6.1.

The spatial variation of the stiffness and damping of the Kelvin layer are the same as in Eq. (5.2), which is slightly different than the one presented in Eq. (4.39) and used in Chapters 4, 6, and 7 (i.e., the stiff zone is finite and not semi-infinite). An abrupt change in stiffness is adopted, but any other variation can be implemented without difficulty.

8.2. Solution method

In this section, we present the solution method for obtaining the response of the system described in Section 8.1. Chapter 7 investigated the efficiency of three solution methods (one transform method, one time-domain method, and a hybrid between the two methods) in solving a nonlinear and inhomogeneous 1-D system (in fact, the equivalent problem to the one presented here if the soil layer were infinitely stiff). One conclusion of that study is that the hybrid method (i.e., the pseudo-force method) can be efficient in a 2-D/3-D system where the inhomogeneity and/or nonlinearity is considered along just one line in space. Because in the current study the inhomogeneity and nonlinearity is concentrated in the connecting layer (i.e., at one line at the surface) the pseudo-force is adopted here. The advantages and disadvantages of this method are discussed at the end of the section. The method is presented in the following and is based on the derivations in Chapter 7.

The core principle of the pseudo-force method [123–125] is to consider the inhomogeneity and nonlinearity as external or pseudo forces leading to a linear and homogeneous *base* system. Basically, the nonlinear and the inhomogeneity terms are moved to the right-hand side in the governing equations and the resulting implicit equations are solved in an iterative manner. The solution is obtained by convolving the state-dependent forces (the nonlinearity and inhomogeneity) with the Green's functions of the base system. It must be emphasized that in this section, because the length of the stiff zone is finite, the base system is homogeneous, unlike the one in Chapter 7 where the base system is piecewise-homogeneous. This fact, makes the determination of the Green's functions computationally more efficient.

After moving the terms accounting for the nonlinearity and inhomogeneity to the right-hand side, the governing equations (the equations of motion of the soil as well as the bound-

ary conditions at $z = Z$ remain unchanged) read

$$EIw_{,xxxx} + \rho_b \ddot{w} + c_{d,base}\Delta\dot{w} + k_{d,base}\Delta w = f^{ML} + f^{p}, \tag{8.7}$$

$$\rho_s \ddot{u}_x = G(u_{x,xx} + u_{x,zz}) + (\lambda + G)(u_{x,xx} + u_{z,xz}), \tag{8.8}$$

$$\rho_s \ddot{u}_z = G(u_{z,xx} + u_{z,zz}) + (\lambda + G)(u_{z,zz} + u_{x,xz}), \tag{8.9}$$

$$\sigma_{zx} = 0, \qquad \sigma_{zz} = -c_{d,base}\Delta\dot{w} - k_{d,base}\Delta w - f^{p}, \qquad z = 0, \tag{8.10}$$

$$u_x = 0, \qquad u_z = 0, \qquad z = Z, \tag{8.11}$$

where f^{p} is the pseudo force and f^{ML} is the moving load (the right-hand side of Eq. (8.1)); the pseudo force reads

$$f^{p}(x, \Delta w, \Delta\dot{w}) = -\big(c_d(x, \Delta w) - c_{d,base}\big)\Delta\dot{w} + k_{d,base}\Delta w - f_k(x, \Delta w), \tag{8.12}$$

where $c_d(x, \Delta w)$ is given by Eqs. (6.1) and (2.27) and $f_k(x, \Delta w)$ by Eq. (5.2) and Fig. 6.2. It can be seen that because the inhomogeneity and nonlinearity are limited to the transition zone, the pseudo force acts only inside the transition zone. As can be seen from Eq. (8.12), the pseudo force depends both on displacements Δw and velocities $\Delta\dot{w}$; following a discussion from Chapter 7, for computational efficiency, the velocities in the pseudo force are computed from the displacements at the previous time moments using the finite difference method. This makes the pseudo force f^{p} only dependent on the displacements, albeit on the time history of the displacements. Note that for conciseness, f^{p} is indicated in the following to be dependent on the displacements through Δw, while in actual fact it also depends on the displacement at the previous time moments.

The horizontal displacement u_x, although accounted for, is not investigated further and its derivation is omitted in the following. To simplify the notation, the following is assumed for the remainder of the section:

$$u(x, z, t) = u_z(x, z, t), \tag{8.13}$$

$$u_0(x, t) = u_{z,0}(x, t). \tag{8.14}$$

Also, the vertical displacement of the soil is only determined at the top layer (i.e., u_0). If necessary for certain applications, the solution at other depths can be determined with additional computational effort.

The solutions w and u_0 can be expressed as a superposition of the steady-state responses w^{ML} and u_0^{ML} caused by the moving load f^{ML}, and w^{p} and u_0^{p} caused by the pseudo force f^{p} in the base system, and read

$$w = w^{ML} + w^{p}, \tag{8.15}$$

$$u_0 = u_0^{ML} + u_0^{p}. \tag{8.16}$$

Firstly, the steady-state responses caused by the moving load in the homogeneous and linear base system can be obtained by using the Fourier transform over time and over space in the x-direction, similar to the procedure used by van Dalen et al. [20]. The resulting system of ordinary-differential equations in the frequency-wavenumber domain can be solved by superposition of two wave modes, one travelling in positive and the other in negative z direction. The four unknown wave amplitudes (two for the horizontal displacement and two for the vertical one) are obtained from the boundary conditions (the frequency-wavenumber domain counterparts of Eqs. (8.10)–(8.11), but without the pseudo force). To obtain the time-domain solution, one of the inverse Fourier integrals is evaluated analytically by using the properties of the Dirac-delta function while the other inverse integral is evaluated numerically. The derivation of the steady-state response w^{ML}, described in words above, is not presented here for brevity.

Secondly, the responses of the beam and of the soil to the pseudo force are expressed as convolution integrals of the Green's functions of the base system and the pseudo force. It must be reminded that the governing equations are coupled through the Δw term, and, consequently, the equations need to be solved simultaneously. Nonetheless, for conciseness, the derivation is demonstrated for w^{p} while only the final expression of u_0^{p} is given (the derivation of u_0^{p} is analogous to the one of w^{p}). The response to the pseudo force reads

$$w^{\mathrm{p}}(x,t) = \int_0^L \int_0^t g^{\mathrm{w}}(x-\xi, t-\tau)\, f^{\mathrm{p}}\big(\xi, \Delta w(\xi,\tau)\big)\mathrm{d}\xi\mathrm{d}\tau, \tag{8.17}$$

where g^{w} is the time-domain Green's function of the base system with the impulse excitation acting simultaneously both on the beam and on the soil surface. The derivation of the Green's function is elaborated in Section 8.2.1.

To evaluate Eq. (8.17), the integral is discretised. Firstly, the displacement w^{p} is assumed to be piecewise constant in space and equal to the value at the centre of each discrete element. Consequently, also the Green's function g^{w} is determined with a box-car shaped load in space (see Fig. 7.1), while it assumes a Dirac delta function loading in time. The continuous-in-time and discrete-in-space expression for the displacement reads

$$w_i^{\mathrm{p}}(t) = \sum_{\bar{i}=1}^{N_{\mathrm{x}}} \int_0^t g_{i,\bar{i}}^{\mathrm{w}}(t-\tau)\, f_{\bar{i}}^{\mathrm{p}}\big(\Delta w_{\bar{i}}(\tau)\big)\mathrm{d}\tau, \tag{8.18}$$

where i is the index for the observation point in space while $\bar{i}$ is the index for the running (integration) spatial variable, and N_{x} is the number of integration points. Secondly, the forces $f_{\bar{i}}^{\mathrm{p}}$ are assumed to be piecewise linear in time. The displacement thus becomes

$$w_{i,n}^{\mathrm{p}} = \sum_{\bar{i}=1}^{N_{\mathrm{x}}} \sum_{\bar{n}=1}^{n} \int_{t_{\bar{n}-1}}^{t_{\bar{n}}} g_{i,\bar{i}}^{\mathrm{w}}(t_n-\tau)\left[f_{\bar{i},\bar{n}-1}^{\mathrm{p}}(\Delta w_{\bar{i},\bar{n}-1})\left(1-\frac{\tau-t_{\bar{n}-1}}{\Delta t}\right) + f_{\bar{i},\bar{n}}^{\mathrm{p}}(\Delta w_{\bar{i},\bar{n}})\frac{\tau-t_{\bar{n}-1}}{\Delta t}\right]\mathrm{d}\tau, \quad n \geq 1, \tag{8.19}$$

where n is the index for the observation time variable while $\bar{n}$ is the index for the running (integration) time variable. Eq. (8.19) is valid only for $n \geq 1$ because the system is assumed to be in the steady-state regime at $t_0 = 0$ and then only the response caused by the moving load is present, so $w^{\mathrm{p}} = 0$ at $n = 0$. It can be observed that Eq. (8.19) consists of two terms, one proportional to the force at time moment $t_{\bar{n}-1}$ and one proportional to the force at time moment $t_{\bar{n}}$. Since the two forcing terms are not dependent on the variable of integration τ, they can be taken out of the integral. The equation can therefore be rewritten as follows:

$$w^{\mathrm{p}}_{i,n} = \sum_{\bar{i}=1}^{N_{\mathrm{x}}} \sum_{\bar{n}=1}^{n} \left[f^{\mathrm{p}}_{\bar{i},\bar{n}-1}(\Delta w_{\bar{i},\bar{n}-1}) \mathscr{L}^{\mathrm{w}}_{i,\bar{i},n-\bar{n}} + f^{\mathrm{p}}_{\bar{i},\bar{n}}(\Delta w_{\bar{i},\bar{n}}) \mathscr{R}^{\mathrm{w}}_{i,\bar{i},n-\bar{n}} \right], \tag{8.20}$$

where $\mathscr{L}$ and $\mathscr{R}$ represent the responses observed at t_n due to triangular pulses lasting between $t_{\bar{n}-1}$ and $t_{\bar{n}}$ (see Fig. 7.2) and are given in the following

$$\mathscr{L}^{\mathrm{w}}_{i,\bar{i},n-\bar{n}} = \int_{t_{\bar{n}-1}}^{t_{\bar{n}}} g^{\mathrm{w}}_{i,\bar{i}}(t_n - \tau) \left(1 - \frac{\tau - t_{\bar{n}-1}}{\Delta t}\right) \mathrm{d}\tau, \tag{8.21}$$

$$\mathscr{R}^{\mathrm{w}}_{i,\bar{i},n-\bar{n}} = \int_{t_{\bar{n}-1}}^{t_{\bar{n}}} g^{\mathrm{w}}_{i,\bar{i}}(t_n - \tau) \frac{\tau - t_{\bar{n}-1}}{\Delta t} \mathrm{d}\tau. \tag{8.22}$$

The time-domain Green's functions $g^{\mathrm{w}}_{i,\bar{i}}(t_n - \tau)$ need to be obtained numerically while the integration from $t_{\bar{n}-1}$ to $t_{\bar{n}}$ needs to be performed numerically too, thus introducing two sources of inaccuracy. To increase accuracy, the response associated with a triangular pulse can be obtained directly from the Fourier domain, where only the inverse Fourier transform needs to be evaluated numerically. To this end, the expressions for $\mathscr{L}$ and $\mathscr{R}$ can be rewritten by introducing the variable change $\bar{\tau} = \tau - t_{\bar{n}-1}$:

$$\mathscr{L}^{\mathrm{w}}_{i,\bar{i},n-\bar{n}} = \int_{0}^{t_{n-\bar{n}+1}} g^{\mathrm{w}}_{i,\bar{i}}(t_{n-\bar{n}+1} - \bar{\tau}) \left(1 - \frac{\bar{\tau}}{\Delta t}\right) H(\Delta t - \bar{\tau}) \mathrm{d}\bar{\tau}, \tag{8.23}$$

$$\mathscr{R}^{\mathrm{w}}_{i,\bar{i},n-\bar{n}} = \int_{0}^{t_{n-\bar{n}+1}} g^{\mathrm{w}}_{i,\bar{i}}(t_{n-\bar{n}+1} - \bar{\tau}) \left(\frac{\bar{\tau}}{\Delta t}\right) H(\Delta t - \bar{\tau}) \mathrm{d}\bar{\tau}, \tag{8.24}$$

where $t_{n-\bar{n}+1} = t_n - t_{\bar{n}-1}$ and $H(\ldots)$ represents the Heaviside function. These responses can now be expressed directly as inverse Fourier transforms as follows:

$$\mathscr{L}^{\mathrm{w}}_{i,\bar{i},n-\bar{n}} = \frac{1}{\pi} \int_{0}^{\infty} \mathrm{Re}\left(\tilde{g}^{\mathrm{w}}_{i,\bar{i}}(\omega)\, \tilde{P}_{\mathscr{L}}(\omega)\, \mathrm{e}^{\mathrm{i}\omega t_{n-\bar{n}+1}} \right) \mathrm{d}\omega, \tag{8.25}$$

$$\mathscr{R}^{\mathrm{w}}_{i,\bar{i},n-\bar{n}} = \frac{1}{\pi} \int_{0}^{\infty} \mathrm{Re}\left(\tilde{g}^{\mathrm{w}}_{i,\bar{i}}(\omega)\, \tilde{P}_{\mathscr{R}}(\omega)\, \mathrm{e}^{\mathrm{i}\omega t_{n-\bar{n}+1}} \right) \mathrm{d}\omega, \tag{8.26}$$

where $\tilde{g}^{\mathrm{w}}_{i,\bar{i}}$ is the Fourier-domain Green's function associated with a Dirac-delta load in time and a box-car function in space, and $\tilde{P}_{\mathscr{L}}$ and $\tilde{P}_{\mathscr{R}}$ are given by

$$\tilde{P}_{\mathscr{L}}(\omega) = \frac{1}{\omega^2 \Delta t} \left(-1 + \mathrm{i}\omega\Delta t \mathrm{e}^{-\mathrm{i}\omega\Delta t} + \mathrm{e}^{-\mathrm{i}\omega\Delta t} \right), \tag{8.27}$$

$$\tilde{P}_{\mathscr{R}}(\omega) = \frac{1}{\omega^2 \Delta t}\left(1 - \mathrm{i}\omega\Delta t - \mathrm{e}^{-\mathrm{i}\omega\Delta t}\right). \tag{8.28}$$

The inverse Fourier transforms are evaluated numerically using a quadratic, nested, adaptive integration scheme [124].

It can be observed that Eq. (8.20) is implicit for $\bar{n} = n$. Therefore, it is divided in a yet unknown instantaneous contribution and an already known history contribution. The equation becomes

$$w^{\mathrm{p}}_{i,n} = w^{\mathrm{p,hist}}_{i,n} + \sum_{\bar{i}=1}^{N_{\mathrm{x}}} f^{\mathrm{p}}_{\bar{i},n}(\Delta w_{\bar{i},n}) \mathscr{R}^{\mathrm{w}}_{i,\bar{i},0}, \tag{8.29}$$

$$w^{\mathrm{p,hist}}_{i,n} = \sum_{\bar{i}=1}^{N_{\mathrm{x}}} \sum_{\bar{n}=1}^{n-1} \left[f^{\mathrm{p}}_{\bar{i},\bar{n}-1}(w_{\bar{i},\bar{n}-1}) \mathscr{L}^{\mathrm{w}}_{i,\bar{i},n-\bar{n}} + f^{\mathrm{p}}_{\bar{i},\bar{n}}(w_{\bar{i},\bar{n}}) \mathscr{R}^{\mathrm{w}}_{i,\bar{i},n-\bar{n}} \right] + \sum_{\bar{i}=1}^{N_{\mathrm{x}}} f^{\mathrm{p}}_{\bar{i},\bar{n}-1}(w_{\bar{i},\bar{n}-1}) \mathscr{L}^{\mathrm{w}}_{i,\bar{i},0}. \tag{8.30}$$

The solution for u^{p}_0, the derivation of which is analogous to the one of w^{p}, reads

$$u^{\mathrm{p}}_{0,i,n} = u^{\mathrm{p,hist}}_{0,i,n} - \sum_{\bar{i}=1}^{N_{\mathrm{x}}} f^{\mathrm{p}}_{\bar{i},n}(\Delta w_{\bar{i},n}) \mathscr{R}^{\mathrm{v}_0}_{i,\bar{i},0}, \tag{8.31}$$

where $u^{\mathrm{p,hist}}_0$, $\mathscr{L}^{\mathrm{u}_0,h}$, and $\mathscr{R}^{\mathrm{u}_0,h}$ are the equivalent quantities for u_0 to Eqs. (8.30), (8.25), and (8.26), respectively. Furthermore, it is important to note that a positive f^{p} acts upwards for the beam and downwards for the soil; therefore, the pseudo force $-f^{\mathrm{p}}$ is acting on the soil and minus signs appear in front of the summation signs in Eq. (8.31) compared to Eq. (8.29).

In order to advance to the next time step, the discretised version of Eqs. (8.15) and (8.16) with $w^{\mathrm{p}}_{i,n}$ and $u^{\mathrm{p}}_{0,i,n}$ given by Eqs. (8.29) and (8.31), respectively, are solved simultaneously for $w_{i,n}$ and $u_{0,i,n}$ using an iterative scheme. The scheme is defined by the following recursive relations that start at $j = 0$ (where j indicates the iteration counter):

$$\begin{aligned} w^{j+1}_{i,n} &\approx w^{\mathrm{ML}}_{i,n} + w^{\mathrm{p,hist}}_{i,n} + \sum_{\bar{i}=1}^{N_{\mathrm{x}}} f^{\mathrm{p}}_{\bar{i},n}(\Delta w^{j}_{\bar{i},n}) \mathscr{R}^{\mathrm{w}}_{i,\bar{i},0}, \\ u^{j+1}_{0,i,n} &\approx u^{\mathrm{ML}}_{0,i,n} + u^{\mathrm{p,hist}}_{0,i,n} - \sum_{\bar{i}=1}^{N_{\mathrm{x}}} f^{\mathrm{p}}_{\bar{i},n}(\Delta w^{j}_{\bar{i},n}) \mathscr{R}^{\mathrm{u}_0}_{i,\bar{i},0}. \end{aligned} \tag{8.32}$$

Iterations continue until specified tolerances are met for all entries of $w_{i,n}$ and $u_{0,i,n}$. No convergence problems were encountered while computing the results for this chapter.

8.2.1. Determination of the Green's functions

The solution given in the previous section (Eq. (8.32)) is completely determined except for the frequency-domain Green's functions $\tilde{g}^{\mathrm{w}}$ and $\tilde{g}^{\mathrm{u}_0}$. Since the base system is homogeneous,

is sufficient to determine these Green's functions for one excitation position only. The governing equations for determining the Green's functions read

$$EIw_{,xxxx} + \rho_\mathrm{b}\ddot{w} + c_{\mathrm{d,base}}\Delta\dot{w} + k_{\mathrm{d,base}}\Delta w = \delta(t)\big[H(x-\xi_\mathrm{l}) - H(x-\xi_\mathrm{r})\big], \tag{8.33}$$

$$\sigma_{zx} = 0, \qquad \sigma_{zz} = -c_{\mathrm{d,base}}\Delta\dot{w} - k_{\mathrm{d,base}}\Delta w, \qquad z = 0, \tag{8.34}$$

where ξ_l and ξ_r represent the left and right boundaries of the box-car loading in space. The rest of the governing equations are the same as in Eqs. (8.8)–(8.11). To obtain the response, the Fourier transform is applied over time and space. Then, the Helmholtz decomposition is used to decouple the frequency-wavenumber counterparts of Eqs. (8.2)–(8.3). The solution u_0 in the frequency-wavenumber domain reads

$$\overline{u_0} = \frac{\partial\overline{\phi}}{\partial z}\Big|_{z=0} + \mathrm{i}k_x\overline{\psi}\big|_{z=0}, \tag{8.35}$$

$$\overline{\phi} = A_1\mathrm{e}^{\mathrm{i}k_{z,\mathrm{P}}z} + B_1\mathrm{e}^{-\mathrm{i}k_{z,\mathrm{P}}z}, \tag{8.36}$$

$$\overline{\psi} = A_2\mathrm{e}^{\mathrm{i}k_{z,\mathrm{S}}z} + B_2\mathrm{e}^{-\mathrm{i}k_{z,\mathrm{S}}z}, \tag{8.37}$$

where the overbar denotes the quantity in the frequency-wavenumber domain, $k_{z,\mathrm{P}} = \mathrm{i}\sqrt{(k_x^2 - k_\mathrm{P}^2)}$ and $k_{z,\mathrm{S}} = \mathrm{i}\sqrt{(k_x^2 - k_\mathrm{S}^2)}$ are the z-components of the wavenumbers corresponding to the compression and shear waves, respectively, $k_\mathrm{P} = \frac{\omega}{c_\mathrm{P}}$ and $k_\mathrm{S} = \frac{\omega}{c_\mathrm{S}}$ are their wavenumbers, while $c_\mathrm{P} = \sqrt{(\lambda + 2G)/\rho_\mathrm{s}}$ and $c_\mathrm{S} = \sqrt{G/\rho_\mathrm{s}}$ are their velocities. Also, k_x is the wavenumber in x-direction and ω is the radial frequency. The solution for the displacement of the beam reads

$$\overline{w} = \frac{\overline{F} + (\mathrm{i}\omega c_{\mathrm{d,base}} + k_{\mathrm{d,base}})\overline{u}_0}{EIk_x^4 - \rho_\mathrm{b}\omega^2 + \mathrm{i}\omega c_{\mathrm{d,base}} + k_{\mathrm{d,base}}}, \tag{8.38}$$

$$\overline{F} = \frac{\mathrm{i}\big(\mathrm{e}^{-\mathrm{i}k_x\xi_\mathrm{l}} - \mathrm{e}^{-\mathrm{i}k_x\xi_\mathrm{r}}\big)}{k_x}. \tag{8.39}$$

Using the four boundary conditions at $z = 0$ and at $z = Z$, the complex-valued amplitudes A_1, B_1, A_2, and B_2 can be determined (their expressions are omitted here for brevity), and with that $\overline{u}_0$ is known. To obtain the responses in the frequency-space domain, the inverse Fourier transform over x needs to be evaluated:

$$\tilde{g}^\mathrm{w} = \tfrac{1}{2\pi}\int_{-\infty}^{\infty}\overline{w}\mathrm{e}^{\mathrm{i}k_x x}\mathrm{d}k_x, \qquad \tilde{g}^{\mathrm{u}_0} = \tfrac{1}{2\pi}\int_{-\infty}^{\infty}\overline{u}_0\mathrm{e}^{\mathrm{i}k_x x}\mathrm{d}k_x. \tag{8.40}$$

The integrals can be evaluated by means of contour integration as done in, for example, in Refs. [132–134] for systems similar to the one treated in this section. In the current work, the integrals are performed numerically using an adaptive scheme (*integrate* routine in MATLAB). The contour integration is the more computationally efficient approach out of the two, but the numerical integration is sufficient for the purpose of this work.

8.2.2. Choosing the values of the parameters

Even though the formulated 2-D model includes additional characteristics of the problem compared to 1-D models, it still is a phenomenological one mainly due to (i) the reduction from 3-D to a 2-D plane-strain problem and (ii) the representation of all the layers between the rail and soil through a continuous Kelvin layer (i.e., springs and dashpots). Therefore, the system parameters do not completely correspond to their 3-D counterparts and need to be selected/tuned such that the response resembles the one of a 3-D model or field observations. It must be emphasized that this chapter, as well as the whole thesis, focuses on qualitative analyses for which the exact parameter values are not of crucial importance. Nonetheless, we want to investigate the system response in a realistic parameter space and this section explains how the parameters are chosen. Furthermore, to offer some degree of generality to the results, a parametric study is presented in Section 8.3.3 in which some of the parameters are varied around the chosen values and the change in behaviour is analysed.

For the results presented in this chapter, the parameter values are selected such that its steady-state response resembles the one of an equivalent 3-D model (see Fig. 8.2 for the comparison and Appendix F for a brief description of the 3-D model). In the following, we first describe the tuning procedure for the soil layer and then the tuning of the Kelvin layer.

If we neglect the railway track for a moment, the reduction of a 3-D soil layer under the action of a moving point load to an equivalent 2-D plane-strain problem assumes that the moving load becomes a line load of infinite dimension in transverse direction. To obtain similar response magnitudes in the two cases, two approaches can be taken: (i) the shear stiffness of the soil layer in the 2-D model is increased, or (ii) the magnitude of the moving load is decreased. While the first approach can lead to good results, the physics of the problem are changed by modifying the wave velocities in the soil. Therefore, we choose to scale down the magnitude of the moving load instead while keeping the soil stiffness the same as in the 3-D model. To obtain similar response magnitudes, a factor of 40% is used to the load applied in the 3-D model (the load in the 3-D model is 45 kN). The soil and moving load parameter values used in the 2-D model can be found in Table 8.1. Additionally, a loss factor $\zeta_s = 0.1$ is chosen to represent both soil damping and radiation damping in z-direction. The loss factor is included in the governing equations by making G complex-valued in the frequency domain $\left(\text{i.e., } G(1+\mathrm{i}\zeta_s)\right)$; keeping ν real-valued leads to λ also becoming complex-valued in the frequency domain. It is important to mention that the chosen soil damping is frequency independent (i.e., not of viscous type) since soil usually exhibits hysteretic and not viscous type of damping.

If one does not have a 3-D model to compare to, the two criteria to choose G, λ, and ρ_s are (i) that the critical velocity of the 2-D model is in the realistic regime and (ii) that the overall displacement magnitude is in the realistic regime. The two criteria are competing with each other because, for example, the lower the G, the lower the critical velocity (reaching realistic values) and the higher the displacement magnitude (overestimating field observations). Nonetheless, a balance between the two needs to be obtained.

Table 8.1: Values of the system parameters used to compute results in Chapter 8.1.

Parameter	Symbol	Value	Unit
Bending stiffness	EI	$6.42{\cdot}10^6$	Nm^2
Rail mass	ρ_r	60	kg/m
Distributed half-sleeper mass	ρ_slp	208.33	kg/m
Half-layer of ballast mass	ρ_bal	810	kg/m
Moving-load magnitude	F_0	$18 \cdot 10^3$	N
Kelvin layer stiffness	k_d	$6.7{\cdot}10^6$	$\mathrm{N/m}^2$
Kelvin damping ratio	ζ_K	0.01	
Soil shear modulus	G	$10 \cdot 10^6$	$\mathrm{N/m}^2$
Soil mass density	ρ_s	1730	$\mathrm{kg/m}^3$
Poisson ratio	ν	0.3	
Soil damping factor	ζ_s	0.1	
Layer depth	Z	3	m
Elastic displacement limit ratio	$\Delta w_\mathrm{el}/\Delta w^\mathrm{e}_\mathrm{max}$	1.02	

The Kelvin layer, theoretically, represents the vertical stiffness and damping of the rail-pads ($k_\mathrm{d,rp}$), the ballast ($k_\mathrm{d,bal}$), and the embankment ($k_\mathrm{d,e}$). However, we do not make an explicit distinction between them and the Kelvin layer was tuned such that, using the previously defined values for the soil and moving load, the magnitude of the responses in the two models are similar (the bending stiffness of the beam is the same as in the 3-D model). As for the damping of the Kelvin layer, a conservative ratio ζ_K of 1% has been chosen since most amount of damping in this system is expected to come from the soil and not from the ballast-embankment layer. Although not presented here for brevity, the effect of increasing ζ_K on the results was investigated and it was minimal. The damping ratio is related to the damping coefficient through Eq. (2.27). Finally, the mass of the ballast ρ_bal (next to the mass of the sleepers ρ_slp and of the rail ρ_r) is included in the linear mass of the beam (i.e., $\rho_\mathrm{b} = \rho_\mathrm{r} + \rho_\mathrm{slp} + \rho_\mathrm{bal}$), as done in Chapter 3.

Fig. 8.2 presents the comparison of the steady-state responses obtained with the equivalent 3-D FE model and the current 2-D model. The 3-D model is formulated in the software package Abaqus®and is described in Appendix F. Although there are some discrepancies, especially at locations where there is an upward displacement, the overall agreement is not great. The responses at the top-soil match very well, while the responses at the rail position show good agreement in magnitude, but the displacement field of the 2-D model is wider than the 3-D one. This can be caused by the local nature of the Kelvin layer, although this should, in principle, lead to a narrower field, not a wider one (see Section 8.4). Alternatively, the wider field can also be caused by the continuous supporting structure in the 2-D one while in the 3-D model, the discrete sleepers are accounted for. Nonetheless, the match is satisfactory, at least when it comes to the steady state. As will be discussed in Section 8.4, a good agreement of the steady-state responses is not sufficient to ensure that the transient

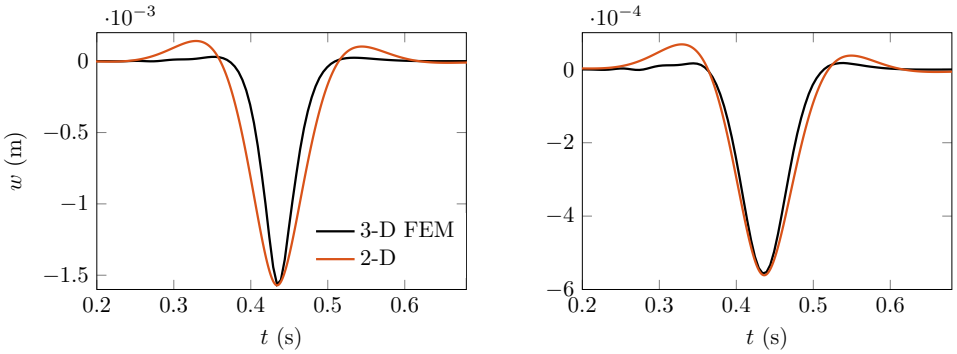

Figure 8.2: Comparison of the steady-state displacement time histories at the rail (left panel) and soil surface (right panel) between a 3-D FE model and the current 2-D model. $v \approx 0.5c_{\mathrm{cr}}$.

response is also well captured. Nevertheless, this tuning is valuable because it ensures that the results obtained with the current model are in the realistic realm.

8.2.3. Verification of the solution method

The solution method described in Section 8.2 is verified by considering a limit case. More specifically, the stiff zone is extended from $x = 0$ to $x = L$ and its stiffness is chosen to be two times larger than in the base system. After the initial transients caused by the jump in stiffness, the solution should be the steady-state one provided that the length of the stiff zone is sufficiently large. This steady-state solution is compared to the semi-analytical one computed similarly to w^{ML}, but with the different stiffness value. Fig. 8.3 presents the error $e(x)$ that is defined as the summed-over-time absolute value of the difference between the limit-case solution w_{lim} (obtained using the solution method presented in this chapter) and the benchmark solution w_{bench}, divided by the summation of the absolute value of the benchmark solution over time; the expression of $e(x)$ is given in Eq. (6.52).

One can see that at the start and end of the stiff zone (note that $L = 40$ m in Fig. 8.3), the error is significant due to the transient behaviour. Nonetheless, the error reduces significantly (around and below 1%) once the response reaches a quasi steady-state regime inside the stiff zone. This shows that the obtained Green's functions are correct, the pseudo forces (and the iterative scheme) work well and that the solution method is correctly implemented. The time and space discretisations for this analysis are $\Delta x = 0.2$ m and $\Delta t = 5 \times 10^{-4}$ s; these parameters have been slightly varied and the error has not changed significantly showing that the error is governed by the transients (the solution not fully reaching steady state) and not by the discretization. It must be emphasized that the large error around $x = 0$ and $x = L$ is not caused by boundary artefacts because the infinite extent of the system is accounted for in an exact manner through the Green's functions; the error is caused by the transition in stiffness and damping which occurs at $x = 0$ and $x = L$.

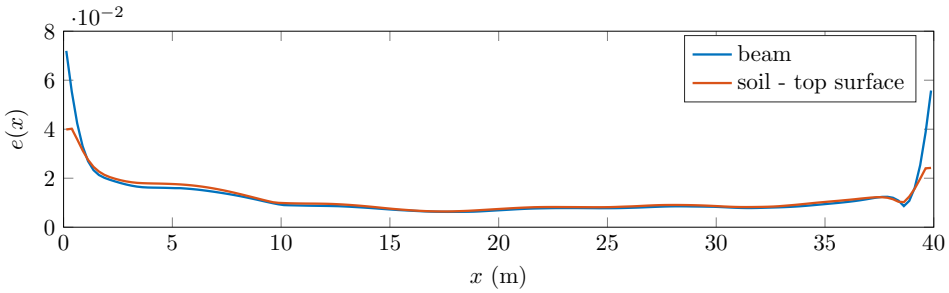

Figure 8.3: The relative errors in the limit case for a load velocity $v = 0.3c_{\mathrm{cr}}$.

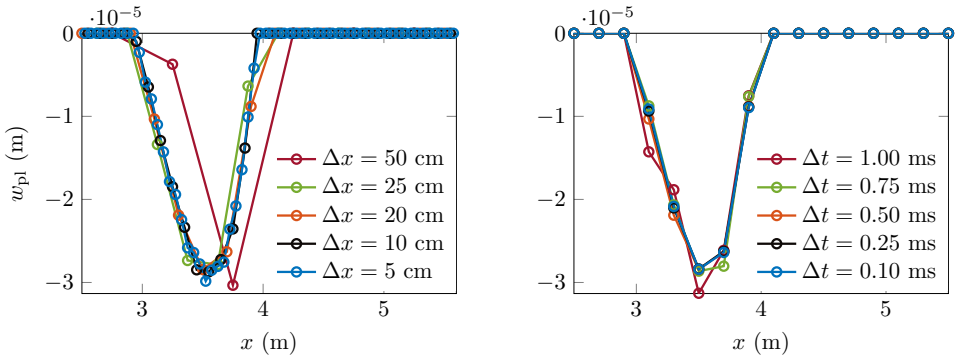

Figure 8.4: The settlement profile for varying Δx (left panel; $\Delta t = 0.5$ ms) and Δt (right panel; $\Delta x = 20$ cm).

The aforementioned limit case verified the correct determination and accuracy of the Green's functions and of the pseudo-forces related to the inhomogeneous nature of the problem. To verify the pseudo-forces related to the nonlinear behaviour of the Kelvin layer, in the absence of a semi-analytical benchmark solution, the convergence of the solution is analysed. The settlement profile is presented in Fig. 8.4 for varying Δx and Δt. It can be seen that when reducing the spatial and temporal steps, the settlement profile converges, giving confidence that the solution to the nonlinear and inhomogeneous problem obtained through the pseudo-force method is correct (although it does not *prove* that the solution is correct since, theoretically, it could converge to an incorrect solution). The convergence analysis also indicates that $\Delta x = 20$ cm and $\Delta t = 0.5$ ms are sufficient for a converged solution.

8.2.4. Advantages and disadvantages of the current solution method

Since the solution method is one of the novelties of the current work, it requires at least some qualitative comparison to the other methods available in the literature. The more common solution method to solve the system under consideration is a FE discretization of

the spatial domain combined with a time-stepping method for the temporal evolution (e.g., Newmark-β, Runge-Kutta, etc.). The advantages of the pseudo-force method are as follows:

- The infinite extent of the system is respected automatically without any additional measures. For example, when using FEM, some type of non-reflective boundaries need to be prescribed (either in the form of boundary elements or perfectly-matched layers). Furthermore, to mitigate the spurious effects from the vehicle suddenly entering the system, special initial conditions need to be imposed in the FEM models or to make the domain large enough such that these effects die out before the vehicle reaches the transition zone. These additional measures increase the complexity of the problem and increase the computational cost.
- Instead of discretising the system, the pseudo-forces are discretised. This means that if one knows a-priori where to expect settlement, the discretisation of the pseudo-forces can be refined only in that region while the response of the rest of the system is very accurate. This also means that the computational cost does not significantly change with increasing depth or multiple layers of the soil, since the depth is not discretised.
- The most expensive computational task of the pseudo-force method is to determine the Green's functions in the time domain. Once these are determined, parametric studies can be performed at a low computational cost. For example, any parameters of the load (velocity or amplitude), of the transition zone (stiffness ratio, location, width, profile, etc.), or of the nonlinear constitutive relation (type, shape, values, etc.) can be varied.

As for any solution method, the pseudo-force method has disadvantages as well, which are presented below:

- The biggest drawback is that the current method is not efficient (or even not feasible) to apply when the soil layer is inhomogeneous or nonlinear. As discussed in Chapter 7, this method can be efficient when the nonlinearity and inhomogeneity is along a line (which is the case in the problem statement). However, in some (or even most) cases the transition zone is characterized primarily by different properties of the soil (e.g., going from soft soil to a bridge founded on piles). The solution to such a scenario cannot be efficiently obtained with the current method.
- Related to the previous point, the solution to a model that accurately represents the geometry of the transition zone cannot be directly obtained using this solution method. The inhomogeneity is introduced in the current model through the pseudo-forces that act along a line (interface between rail and soil). To model the geometry of the problem accurately, the inhomogeneity (man-made structure) needs to be distributed through the depth of the ballast, embankment, and soil layers, leading

to the number of Green's functions required to be unfeasible to determine. A way to indirectly account for the accurate geometry of the man-made structure in the current model is to determine its equivalent stiffness, damping, and mass from a FE analysis. These equivalent quantities can then be introduced in the Kelvin layer. The extent of validity of such an approximation needs to be investigated.

- Since the beam is not discretised, it is difficult to simulate a spatial variation of the bending stiffness (e.g., auxiliary rails imposed only in the transition zone).

Based on the aforementioned advantages and disadvantages, it becomes clear that the pseudo-force method is not ideal for models focused on quantitative predictions for scenarios where the problem's geometry is of importance. Nonetheless, the pseudo-force method is more suitable for simplified models focused on qualitative analyses targeted at understanding the behaviour of more simplified problems. Also, its efficiency in making parametric studies can be useful for preliminary quantitative predictions to reduce the parameter space to be investigated using FE models.

8.3. Response of the 2-D model

This section tackles the first goal of the chapter which is to investigate the response amplification and the corresponding settlement in the 2-D system. Two slightly different scenarios, presented in Fig. 8.5, are investigated. Scenario A (left panel of Fig. 8.5) consists of the original system formulated in Section 8.1; in this scenario, the stiff zone rests directly on the soil layer and is qualitatively representative of a railway crossing where the concrete slab rests directly on the soil. Scenario B (right panel of Fig. 8.5), unlike scenario A, has an additional layer of stiff springs at the bottom of the stiff zone. This scenario is qualitatively representative of a structure (e.g., culvert) supported by stiff and slender piles. Note that the actual piles are not modelled, but their effect is considered through the stiffening of the base (i.e., surface of the soil) in the stiff zone. The inhomogeneity introduced by the piles in the soil is neglected together with potential reflections; we considered that for slender piles (i.e., diameter much smaller than the width of the structure) this effect can be neglected.

This section is divided in three parts. Firstly, to get a fundamental understanding of the system under consideration, its dispersion characteristics are investigated. Then, a reference case is considered and analysed in-depth. Finally, to offer a more comprehensive picture of the system's behaviour, a parametric analysis is performed.

8.3.1. Dispersion characteristics

To better understand the behaviour of the 2-D system at hand, we can first investigate the dispersion characteristics of the homogeneous and linear system (since there is no transition zone, there is no distinction between scenarios A and B). The dispersion equation of the 2-D system can be obtained in a number of ways; here, we use the equivalent stiffness approach of the soil layer, as used by Dieterman and Metrikine [132]. Although they determined the

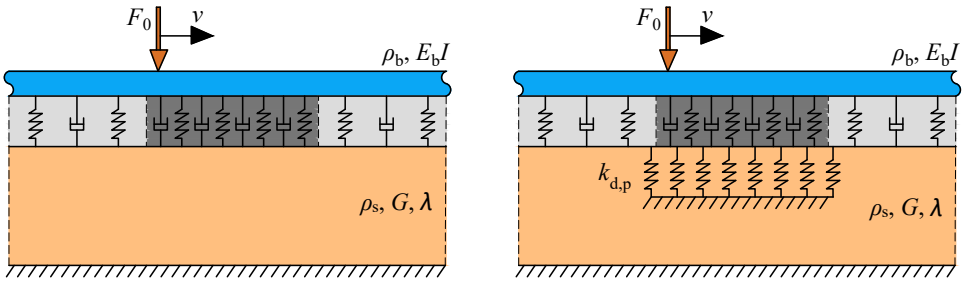

Figure 8.5: Two configurations of the original model: scenario A (left panel) represents the stiff zone resting directly on the soil layer while in scenario B (right panel), the stiff zone rests on stiff and slender piles.

equivalent stiffness of a 3-D half-space, the same approach can be used to determine the equivalent stiffness χ_s of the 2-D soil layer. Then, the equivalent stiffness of the two layers of springs in series (the layer connecting the beam and soil, and the equivalent stiffness of the soil layer) can be expressed straightforwardly. The remaining system is a beam resting on a layer of springs, the dispersion equation of which reads (for a system without damping)

$$E_b I k_x^4 - \rho_b \omega^2 + \frac{k_{d,base}\chi_s(\omega, k_x)}{k_{d,base} + \chi_s(\omega, k_x)} = 0. \tag{8.41}$$

In an undamped 3-D half-space, three types of waves can propagate in x-direction, namely the compressional, the shear and the Rayleigh (surface) waves. When a beam (or plate with finite width) is added to the surface of the 3-D half-space, guided waves can propagate along it without attenuation (i.e., *stationary* waves) at phase velocities lower than (or equal to) the velocity c_R of the Rayleigh wave (see Ref. [132]). Stationary guided waves cannot propagate at velocities larger than c_R because Rayleigh waves are then radiated, thus attenuating the guided wave travelling along the beam; such a wave is usually called a *leaky* wave.

In an undamped 2-D half-space, the same waves as in the 3-D half-space are present, where the Rayleigh wave propagates without amplitude attenuation (i.e., it is a stationary wave) because energy spreading in y (transversal) direction is not possible due to the plane-strain assumption. When a beam is added to the surface of the half-space, due to the two-dimensionality (which implicitly assumes that the beam extends to infinity in the transversal direction), Rayleigh waves can not exist because there is no free surface. Therefore, guided waves can propagate in x-direction without attenuation even at higher phase velocities than c_R of the soil layer. This can be seen in Fig. 8.6 where the purely real-valued k_x curve (i.e., a stationary wave) is located both below and above the k_R line. The upper bound for guided stationary waves in this 2-D system is the phase velocity of the shear waves c_S, and the real-valued k_x curve can be seen to approach the k_S curve at high frequencies (see Fig. 8.6). This is an important difference and shortcoming of the 2-D model and generated waves

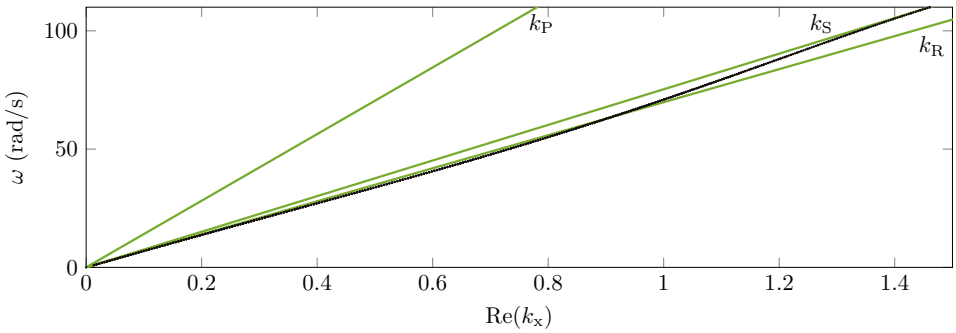

Figure 8.6: Dispersion curves of an undamped 2-D half-space with a beam rigidly connected to its surface. k_P, k_S, and k_R are the compressional, shear, and Rayleigh wavenumbers, respectively.

with a phase velocity larger than c_R (but smaller than c_S) should be treated with care because they would be leaky in a 3-D system. Furthermore, the curve characterising stationary waves initiates at the origin, meaning that even waves of infinite wavelength can propagate in this system. This is because the half-space does not have static stiffness and, thus, allows for rigid body motion.

Fig. 8.7 presents the dispersion curves of the homogeneous and finite-depth 2-D system with properties of the soft domain. To describe the dispersion curves of the system under consideration in a clear manner, the system complexity is gradually increased as follows. We first consider the layer with a free surface (top row), then the beam is rigidly connected to the top of the layer (second row), after which the Winkler layer is inserted between the beam and the surface (third row), and finally the mass layer is added to the top of the layer (forth row). This way, we can investigate the changes to the dispersion curves introduced by each modification. The left column presents the real- and imaginary-valued wavenumbers (i.e., stationary and evanescent waves, respectively), while the right column presents the complex-valued ones. Since the curves are determined numerically using a complex-valued root finder, not all roots are found (especially in the bottom panels) and, consequently, some points are missing in the figure; nonetheless, the figure captures well the main curves and is sufficient for the discussion here.

When a finite-depth layer is considered instead of a half-space, infinitely many additional dispersion curves appear, as can be seen in the top panels of Fig. 8.7 (only a finite amount of them appear in the limited frequency-wavenumber range presented here). The additional curves describe guided waves that are travelling in x-direction and standing in z-direction; their infinite amount originates from infinitely many standing waves modes in a finite layer continuum. One of this dispersion branches highlighted in blue (top left panel), is evanescent up to a certain frequency after which it becomes stationary; this frequency is the cut-off frequency. The wave described by this branch becomes a surface wave at high frequencies (i.e., it approaches k_R). The other branches have a complex behaviour that is

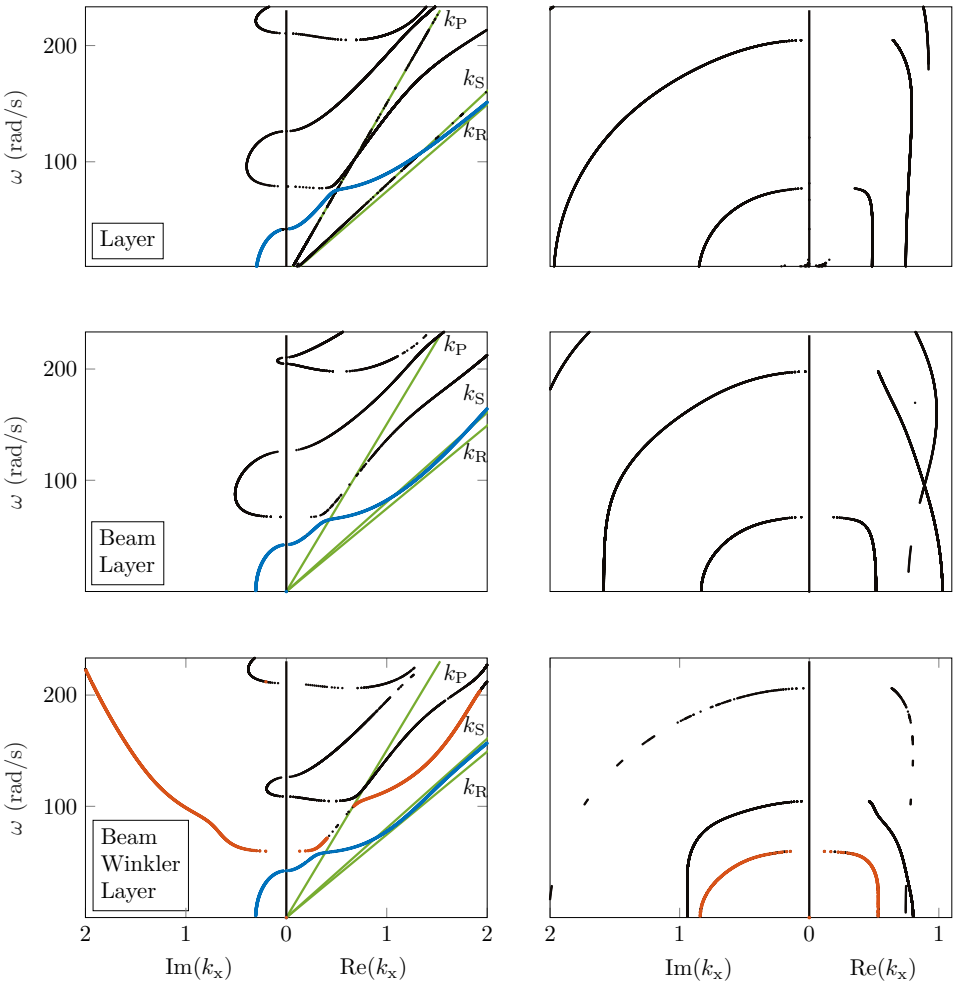

Figure 8.7: Dispersion curves of an undamped 2-D layer with rigid bottom and different boundary conditions at the surface: free surface (top row), beam rigidly connected to its surface (second row), Winkler layer connecting the beam and its surface (third row) and with an additional mass layer (system under consideration in this chapter; bottom row). The left panels present the purely real- and imaginary-valued wavenumbers while the right panels present the complex-valued wavenumbers. k_P, k_S, and k_R are the compressional, shear, and Rayleigh wavenumbers, respectively.

qualitatively very well explained by Mindlin [135] (Fig. 23 and corresponding discussion), Achenbach [136] (Fig. 6.12 and corresponding discussion), and Graff [50] (Fig. 8.10 and corresponding discussion); important to note is that all of them become stationary waves above certain frequencies and that all of them have phase velocities larger than c_S. Finally, unlike the half-space, it can be seen that the finite-depth layer has non-zero cut-off frequencies due to it having a rigid bottom and, consequently, non-zero static stiffness.

Adding a beam to the surface of the layer leads to small qualitative changes in the dispersion curves. As aforementioned, Rayleigh waves cannot exist in this system configuration because there is no free surface. Consequently, the lowest real-valued curve (blue line in the second row of Fig. 8.7) does not tend to k_R at high frequencies any more. Apart from this change, the dispersion curves are the same with the ones of the layer with free surface, but with small quantitative changes. For a more in-depth discussion about the dispersion curves of a system similar to this one, see the study by Metrikine and Vrouwenvelder [137]. With the addition of the Winkler layer connecting the beam and the soil layer, significant qualitative changes occur. Namely, two different guided wave types are introduced (see orange lines in the third row of Fig. 8.7) because, unlike in the previous configuration, the beam has its own degrees of freedom here. These guided waves are complex-valued below the cut-off frequency, after which one becomes stationary and the other one evanescent. These guided waves resemble very closely the two wave types in a beam on Winkler foundation. Finally, adding the mass layer introduces only quantitative changes in the dispersion curves, lowering the lowest real-valued branch. This causes the critical velocity (i.e., the minimum phase velocity) of the system to be considerably lower than c_R of the soil layer, which is usually taken as the critical velocity by engineers. This discrepancy and its practical implications have been touched upon by Metrikine and Vrouwenvelder [137].

To conclude this section, it becomes clear that the transient process in the 2-D system is much more complex compared to the one in the 1-D system due to the infinitely many waves being present. Although the addition of damping will lead to some of the waves to have a negligible contribution to the response far away from transition zones, in their vicinity, where the settlement occurs, some of the additional waves present in the 2-D system can have a significant contribution to the response of the system. This is discussed in more detail in Section 8.4.

8.3.2. Reference case

In this section, the response of the two system configurations (A and B) are analysed for one set of parameters. The values of the parameters used for the results are given in Table 8.1. The stiffness (i.e., $k_{d,p} = 19 \times 10^6$ N/m^2) of the additional springs under the stiff zone is chosen such that the quasi-static stiffness ratio between the stiff and soft zones is approximately three (see next paragraph and Fig. 8.8), as was chosen in most of the previous chapters (note that while the stiffness ratio of five was used in most previous chapters, this lead to a track stiffness ratio as experienced by the moving load of approximately three; see Section 4.3.1

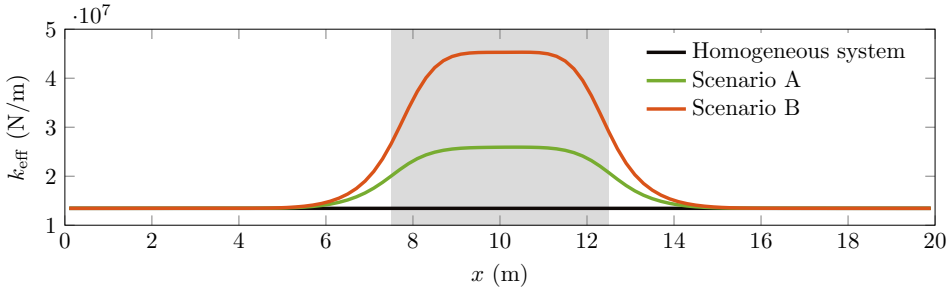

Figure 8.8: The effective stiffness of the track as felt by the load in the quasi-static regime for the homogeneous system, scenario A, and scenario B ($v \approx 0.1c_{\text{cr}}$).

for the relation between foundation stiffness and track stiffness). The stiff zone is located between $x = 7.5$ m and $x = 12.5$ m, in which the stiffness of the Kelvin layer is ten times higher than in the open track; the damping of the Kelvin layer follows from Eq. (2.27). In this reference case, a load velocity $v \approx 0.75c_{\text{cr}}$ is chosen to investigate the response in a realistic regime.

The elastic displacement limit $\Delta w_{\text{el}} = 1.02\Delta w^{\text{e}}_{\text{max}}$ is chosen throughout this chapter. The reason for choosing a smaller ratio compared to Chapter 6 (where 1.05 was chosen) is that, as we shall see in Section 8.4, the settlement predicted by the 2-D model is smaller than the one obtained in the 1-D model. So, to obtain a smooth settlement profile, the ratio has been reduced in this chapter. The exact value of the ratio, although important for specific predictions (in which case it needs to be determined experimentally), is not so important for comparing different scenarios and for parametric analyses provided that it is kept unchanged and that it allows for settlement profile to be somewhat smooth (i.e., not caused by numerical inaccuracy).

The quasi-static stiffness of the track (i.e., as experienced by a very slowly moving load) for both scenarios is presented in Fig. 8.8. Scenario A exhibits a stiffness ratio between the stiff and soft domains of approximately two. The perceived stiffness ratio is this low despite the spring stiffness being ten times larger because the flexibility of the soil layer is governing here. In actual fact, the flexibility of the soil layer, compared to the flexibility of the ballast-embankment structure, is governing in most cases. In scenario B, the quasi-static stiffness of the track (Fig. 8.8) exhibits a ratio between the stiff and soft domains of approximately three (as aforementioned); this is higher than in scenario A due to the presence of the stiff base.

Fig. 8.9 presents the transient response of the system in scenario A; the steady-state response is also presented for comparison. The displacement fields are presented for different time moments in the left column while Δw is presented in the right columns to demonstrate when the settlement occurs. Note that the displacement field of the soil surface is shifted downwards by 1.5 mm such that the two fields do not overlap each other; in this

system there is no actual distance between the beam and the soil surface. As explained in previous chapters, the interference between the eigenfield approaching the stiff zone and the free waves generated due to the inhomogeneity causes the response amplification, which leads to settlement occurring. Note that the settlement in Fig. 8.9 is up-scaled by a factor 50 to be clearly visible because the settlement from one wheel passage is, in fact, very small. In this scenario for the reference case, the settlement only develops at the right of the transition (i.e., in the stiff-to-soft transition). This is caused by the relatively small stiffness ratio between the stiff and soft zones. As argued in Chapter 2 (Fig. 2.8), for small stiffness ratios and high load velocities, the energy of the free-field propagating in negative x-direction is small leading to weak wave interference at the left of the transition zone. On the other hand, there is a significant amount of energy in the free-field propagating in positive x-direction leading to a relatively strong wave interference at the right of the transition zone. The stronger response amplification at the right of the transition zone is observed for most cases investigated when the stiff zone rests directly on the soil.

Fig. 8.10 presents the transient response of the system in scenario B. Like in scenario A, the settlement develops only at the right of the transition, but it is much more pronounced. We can verify that, for a larger relative velocity, the settlement develops also at the left of the transition and it becomes more pronounced as the velocity of the load approaches the critical one (see the following section as well as Chapter 2, Fig. 2.8 and the corresponding discussion). It can also be seen, especially in the third and forth rows of Fig. 8.9, that the wave radiation is stronger compared to scenario A, mainly due to the larger stiffness ratio. The response amplification in the stiff-to-soft transition investigated in Chapter 2 (see Fig. 2.10 and corresponding discussion) showed that the evanescent wave was responsible for a relatively small amplification close to the stiff zone while the propagating wave was causing a relatively large amplification further away. Even though the transition process in the current 2-D model generates more waves compared to the 1-D model in Chapter 2, the settlement profile in scenario B resembles the aforementioned findings.

Fig. 8.11 shows the power input by the moving load in the transition zone for both scenarios; the power input in the steady state (non-zero due to the presence of damping) is also presented for comparison. The peaks, both positive and negative, of the power input are larger in scenario B than in scenario A, as could be expected due to the larger inhomogeneity. It can also be seen that the energy exchange between the load and foundation occurs over a larger distance at the right of the stiff zone, as also seen in Chapter 2. Interestingly, the settlement does not occur at the locations of the peaks in the power input, but at the transition from positive (energy goes from the load to the foundation) to negative (energy goes from the foundation to the load) values. It seems that the larger the difference between positive and negative power input and the steeper the slope, the larger the settlement. Furthermore, it seems that the transition from negative to positive power input is not accompanied by settlement. This insight could be used for indirect identification of settlement, although large amounts of data are needed to prove such a relation.

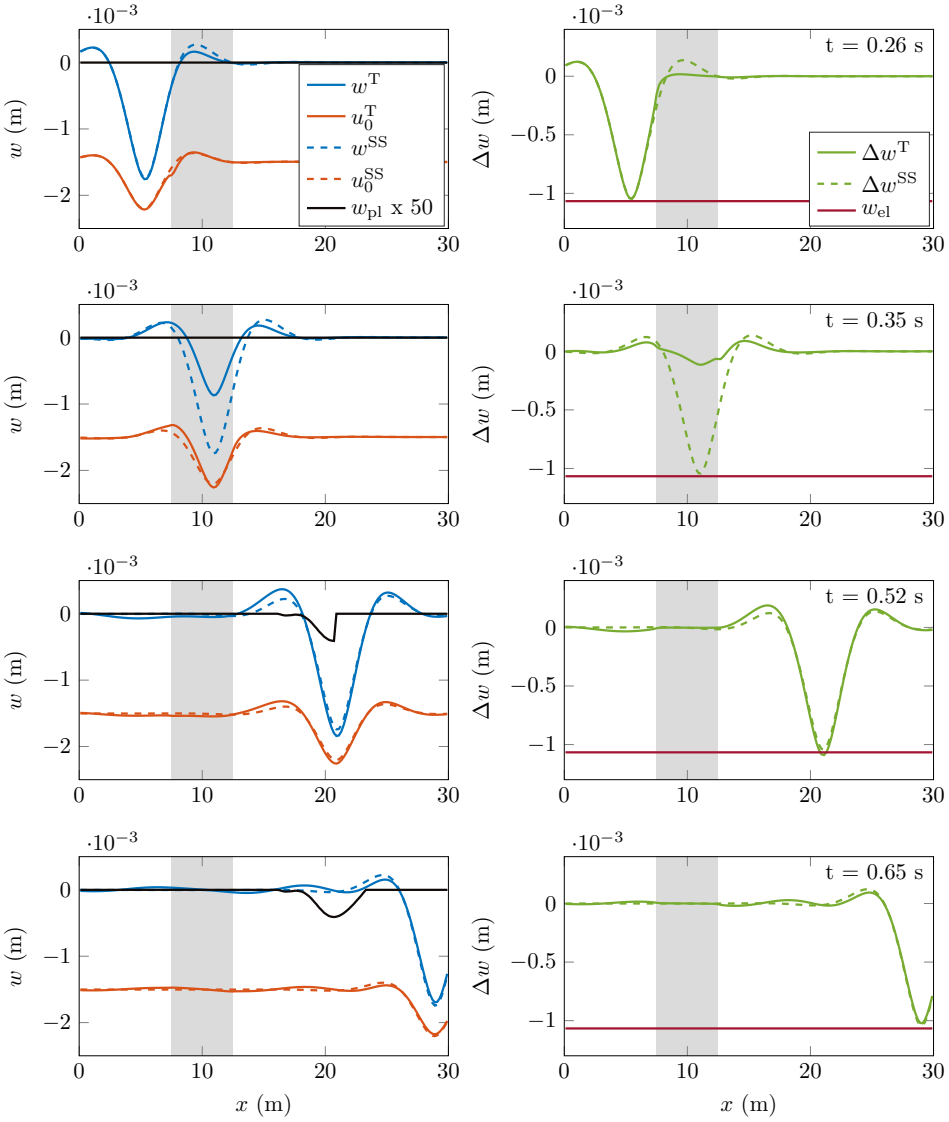

Figure 8.9: Displacement fields in scenario A of the beam (blue lines) and soil surface (orange lines) in the steady-state (dashed lines) and transient (solid lines) regimes and the settlement (black line) at different time moments (left panels). The displacement difference (green lines) in the steady-state (dashed lines) and transient (solid lines) regimes and the elastic displacement limit (Δw_{el}) at the same time moments as the displacement fields (right panels). The stiff zone is represented through the grey background.

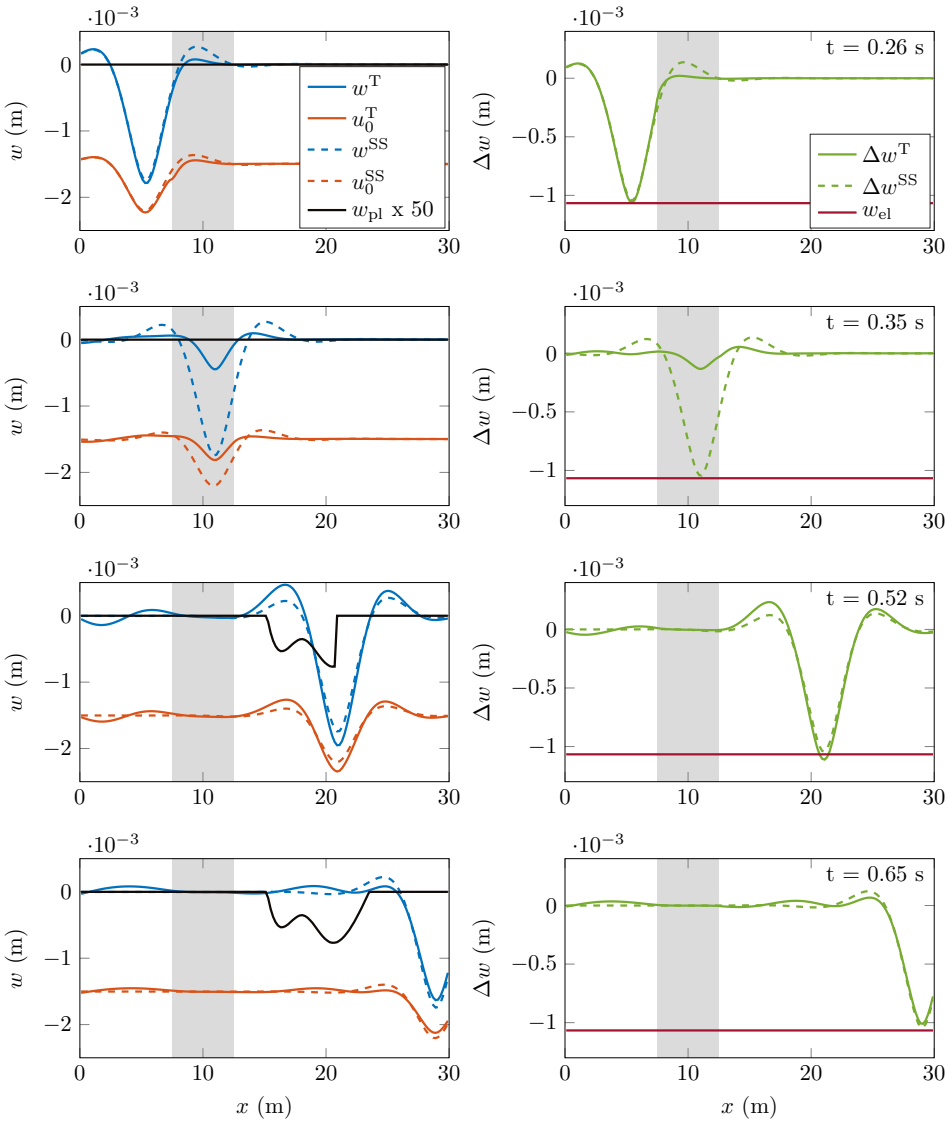

Figure 8.10: Displacement fields in scenario B of the beam (blue lines) and soil surface (orange lines) in the steady-state (dashed lines) and transient (solid lines) regimes and the settlement (black line) at different time moments (left panels). The displacement difference (green lines) in the steady-state (dashed lines) and transient (solid lines) regimes and the elastic displacement limit (Δw_{el}) at the same time moments as the displacement fields (right panels). The stiff zone is represented through the grey background.

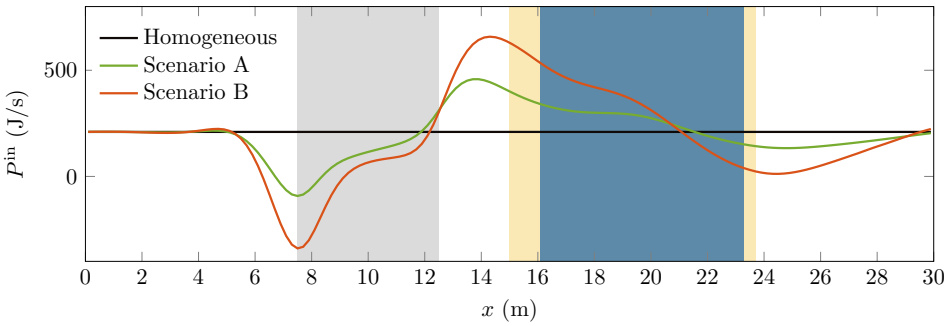

Figure 8.11: The power input by the moving load in the reference case for both scenarios A and B. The grey background indicates the location of the stiff zone, while the blue and yellow backgrounds indicate the settlement locations in scenario A and B, respectively.

8.3.3. Parametric analysis

The previous section analysed in depth one particular case and highlighted the important characteristics of the response. To offer a more general picture of the response, a parametric study is performed here. To keep the section concise, it investigates only the settlement predicted by the model for different system parameters. More specifically, we compare the area (i.e., $A_{\text{pl}} = \int w_{\text{pl}}(x, t_{\text{end}})\text{d}x$) under the settlement profile after one load passage. It must be noted that the area of the settlement profile is not the only important characteristic; to offer a larger picture, also the slope of the settlement profile should be investigated because that is the one dictating the *differential* part of the settlement. However, this is not presented here for conciseness. The parameters that are varied are the load velocity, the stiffness E_{s} of the soil layer, and the length of the stiff zone. The ratio between the Kelvin stiffness in the stiff and soft zones (chosen as ten throughout the chapter) is not varied here because the overall change in track stiffness as felt by the moving load is inherently varied by studying both scenarios A (stiff zone resting directly on soil) and B (stiff zone resting on piles) as well as by varying E_{s}. Other parameters can also be varied (e.g., Poisson ratio ν, soil layer depth Z, etc.), but the ones chosen are most representative for parameters that vary between different types of transition zones.

Fig. 8.12 presents the settlement area versus relative velocity for both scenarios A and B. These results show that the observation made in the previous section, namely that the settlement in scenario B is larger than in scenario A, holds for all load velocities. When it comes to the settlement at the left of the stiff zone (left panel), it can be seen that it only develops at relatively large velocities, confirming the findings in Chapter 6. At the right of the stiff zone (right panel), settlement develops also at relatively low velocities and there is no settlement at velocities close to the critical one. This is to be expected based on the results from Chapter 2, Fig. 2.8. It can also be seen that the settlement area is generally much larger in the stiff-to-soft transition; it is caused by the low frequency oscillation under the moving load (see Fig. 2.6). When comparing the settlements at the left and right, we

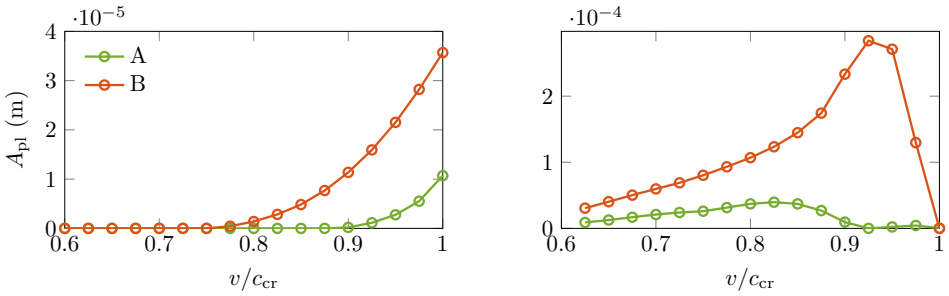

Figure 8.12: The area under the settlement profile versus relative velocity at the left (left panel) and right (right panel) of the stiff zone. Scenario A represents the stiff zone resting on soil and scenario B is the stiff zone resting on piles. Note that the limits of the axis is the same in both panels.

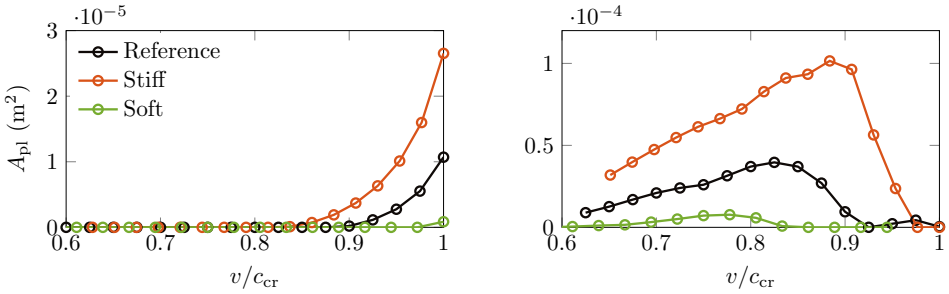

Figure 8.13: The area under the settlement profile versus relative velocity at the left (left panel) and right (right panel) of the stiff zone in scenario A (the stiff zone resting on soil) for different soil stiffness: E_{s} in the reference case is given in Table 8.1 while E_{s} is 50% lower in the soft case and 50% higher in the stiff one. The critical velocity in the x-axis is different for each curve.

can conclude that the settlement at velocities close to the critical one is more pronounced in the soft-to-stiff transition while the opposite is true for the lower velocities.

Fig. 8.13 presents the settlement area for scenario A in which the soil stiffness E_{s} is varied. Two values are chosen for E_{s}, namely 25% lower (soft case) and 25% higher (stiff case) than the reference case. Note that the critical velocity changes with changing E_{s} and Fig. 8.13 presents the results in terms of relative velocity; this means that for the same relative velocity, the load velocity is different for the three cases (reference, soft, and stiff). It is shown that decreasing E_{s} leads to a significant decrease in the settlement both at the left (left panel) and right (right panel) of the stiff zone. This is caused by two factors. The first is that the flexibility of the system comes mainly from the soil and, consequently, there is little variation in the differential displacement Δw between the beam and soil. Secondly, the stiffness ratio between the soft and stiff zones decreases with decreasing E_{s}, leading to a weaker free field and, consequently, to a lower response amplification. By increasing E_{s}, the opposite (to the soft case) is occurring and the settlement area increases; the same aforementioned reasoning can be used to explain it.

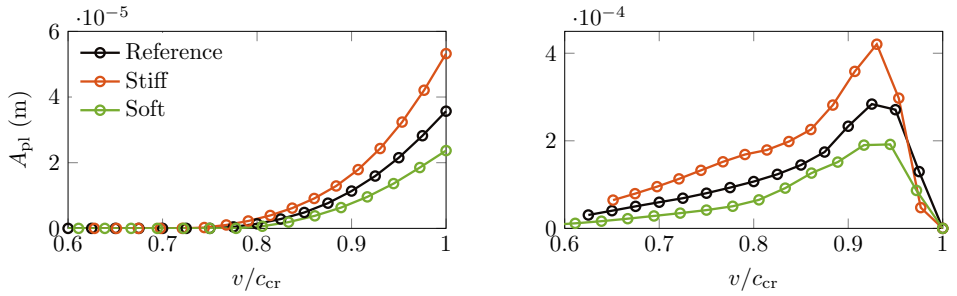

Figure 8.14: The area under the settlement profile versus relative velocity at the left (left panel) and right (right panel) of the stiff zone in scenario B (stiff zone resting on piles) for different soil stiffness: E_{s} in the reference case is given in Table 8.1 while E_{s} is 25% lower in the soft case and 25% higher in the stiff one. The critical velocity in the x-axis is different for each case.

Fig. 8.14 presents the settlement area for scenario B in which E_{s} is varied. The trend of the settlement area with increasing relative velocity is very similar for all three cases, and just the magnitude differs; the stiffer the soil, the larger the settlement area, as also seen in scenario A. Unlike scenario A, the settlement in the soft case is significant, i.e., just slightly smaller than in the reference case. This suggests that the dominant factor (out of the two mentioned in the previous paragraph) influencing the the settlement area when varying E_{s} is the stiffness ratio between soft and stiff domains. Furthermore, the magnitude of the settlement area can be seen to be considerably larger in scenario B than in scenario A (Fig. 8.13) for both soft and stiff cases, complementing the findings in Fig. 8.12.

When looking at the results in Figs. 8.9 and 8.10, the question naturally arises as to what is the influence of the length of the stiff zone on the settlement. For a very long stiff zone, the soft-to-stiff and stiff-to-soft transitions are completely decoupled and can be treated separately (as done in Chapters 2, 3, 4, 6, and 7). However, as the length of the stiff zone decreases, does the interference of the two transitions (soft-to-stiff and stiff-to-soft) lead to an aggravation or reduction of the settlement?

Fig. 8.15 presents the settlement area in scenario A for different lengths of the stiff zone (i.e., 2.5 m, 5 m, 7.5m, and 10 m). For the settlement at the left of the transition, the length of the stiff zone seems to have an insignificant influence for all transition lengths (there is a small difference for the 2.5 m long transition, but it is insignificant). This could have been expected since the soft-to-stiff transition can hardly be affected by the stiff-to-soft one that occurs at a later time. A very short stiff zone (compared to the width of the eigenfield) could have an influence by allowing energy to leak to the right of the transition before the soft-to-stiff transition ends (similar to the mechanism explained in Section 5.1.4, Fig. 5.8 and the corresponding discussion). As for the settlement at the right of the transition, the length of the stiff zone has a considerable effect. It seems that the longer the stiff zone (i.e., the more decoupled the two transitions), the more pronounced is the settlement. This means

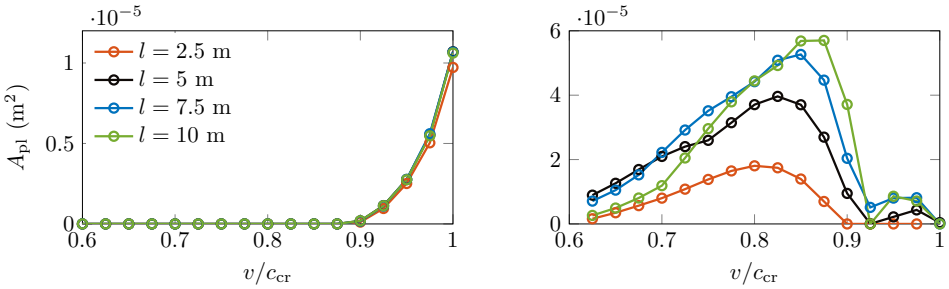

Figure 8.15: The area of the settlement versus relative velocity at the left (left panel) and right (right panel) of the stiff zone in scenario A (stiff zone resting on soil) for the reference case with different lengths of the stiff zone.

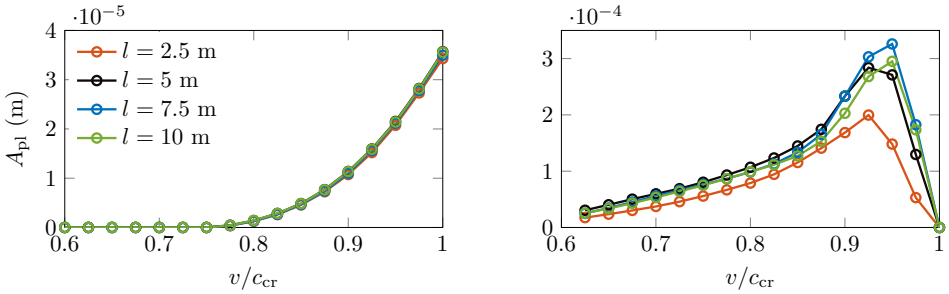

Figure 8.16: The area of the settlement versus relative velocity at the left (left panel) and right (right panel) of the stiff zone in scenario B (stiff zone resting on piles) for the reference case with different lengths of the stiff zone.

that the proximity of the soft-to-stiff transition has a beneficial effect on the settlement at the right of the transition (at least for the scenarios investigated here).

The results for scenario B, presented in Fig. 8.16, are qualitatively similar to the ones in scenario A at the left of the transition. However, at the right of the transition, the influence of the length is considerably less noticeable compared to scenario A. This can be caused by the increased stiffness of the stiff zone leading to most energy at the soft-to-stiff transition to be reflected and not transmitted (see Chapter 2, Fig. 2.16), meaning that it has less influence on the stiff-to-soft transition.

8.4. Influence of the foundation nonlocality

The second aim of this chapter is to analyse the influence of the foundation nonlocality on the response at transition zones. To this end, the response of the 2-D system that includes nonlocality is compared to the 1-D model formulated in Chapter 6. The simplistic geometry of the 2-D system formulated in Section 8.1 is ideal for such a comparison since the only difference between the two models is the addition of the soil layer. The two systems are compared in terms of response fields, both steady state and transient, as well as through

Table 8.2: The tuned values of the parameters of the 1-D model.

Parameter	Symbol	Value	Unit
Beam mass–soft domain	ρ_{l}	1320	kg/m
Kelvin stiffness–soft domain	$k_{\mathrm{d,l}}$	$2.4{\cdot}10^7$	N/m^2
Kelvin damping–soft domain	$c_{\mathrm{d,l}}$	$1.6{\cdot}10^4$	Ns/m^2
Beam mass–stiff domain	ρ_{r}	1968	kg/m
Kelvin stiffness–stiff domain	$k_{\mathrm{d,r}}$	$6.3{\cdot}10^7$	N/m^2
Kelvin damping–stiff domain	$c_{\mathrm{d,r}}$	$4.6{\cdot}10^4$	Ns/m^2

dispersion curves and predicted settlement. This section concludes with the formulation and investigation of an *enhanced* 1-D model that indirectly includes nonlocality in the foundation making it more accurate than the current 1-D model while being more computationally efficient than the 2-D one.

8.4.1. Tuning the 1-D model and comparing the steady-state responses

For a meaningful comparison, the 1-D model needs to be tuned to the 2-D one. Tuning of simplified (1-D) models to more sophisticated models or field measurements is usually performed using the steady-state response in the time domain (e.g., [24, 138]). This procedure is usually done for one velocity and results computed for the same velocity, generally leading to good agreements. The 1-D model essentially has three parameters to tune, namely the mass of the beam and the stiffness and damping of the Kelvin foundation (the bending stiffness of the beam is kept the same as the one in the 2-D model). These three parameters can be tuned in multiple ways depending on the desired outcome.

The system parameters can be tuned such that responses match in the quasi-static velocity regime. However, in this thesis the dynamic velocity regime is of interest and, therefore, the tuning is done to match the responses in dynamic velocity regime. To this end, we impose the criterion that the critical velocity in the two models is the same. This entails that given a fixed stiffness of the foundation, the mass of the beam is determined from Eq. (2.13). Note that Eq. (2.13) is for a system without damping and, consequently, the mass needs a small correction factor such that the critical velocity of the damped systems match.

Two parameters remain now to be tuned, namely the stiffness and damping of the Kelvin layer. Since this chapter is focused on the settlement, and we have seen in the previous chapters that settlement develops under the moving load, a good criterion to tune the stiffness and damping of the foundation is to match the steady-state displacement under the moving load. The expression of the steady-state displacement under the moving load for the 1-D model is known in a closed form (Eq. (2.19) evaluated at $x = vt$ with the wavenumbers corresponding to a damped system) while the response of the 2-D model can be obtained semi-analytically with very little effort. To obtain a best match over a wide range of velocities

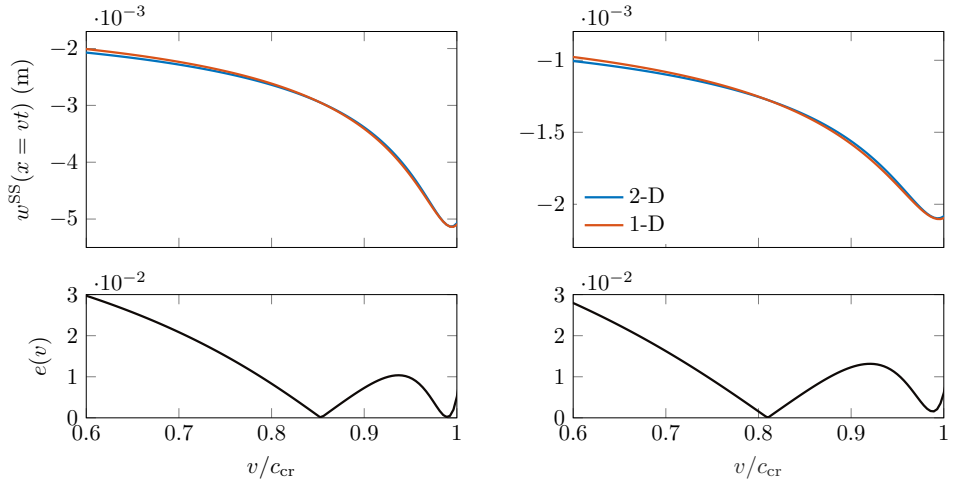

Figure 8.17: Comparison of the steady-state displacement under the moving load versus velocity of the load (top panels) and the relative error (bottom panels) after the tuning of the 1-D model to the 2-D one. The left panels are for the soft region while the right ones are for the stiff region.

(with a focus on the dynamic velocity regime), a least-squares optimization algorithm is used.

The values obtained are given in Table 8.2 and the results are then presented in Figs. 8.17 and 8.18. The mass of the beam is considerably higher than in the previous chapters because here it also accounts for the mass of the ballast and part of the mass of the soil. The stiffness of the foundation is lower than in the previous chapters because the 2-D model is more compliant. Finally, the resulting damping ratio (as defined in Eq. (2.27)) is around 5% for both domains, which is consistent with values chosen in previous chapters.

Fig. 8.17 compares the steady-state displacement under the moving load in both models and presents the associated relative error for the dynamic velocity regime. It can be seen that the responses under the moving load match very well with a maximum relative error of about 3% for both the soft and stiff regions. A better match could be obtained if, for example, the bending stiffness of the beam is tuned as well, but this will not guarantee a better match of the overall displacement profile. Therefore, we decide to keep the same bending stiffness as in the 2-D model.

Fig. 8.18 compares the steady-state displacement fields of the two models for a velocity $v \approx 0.75 c_{\mathrm{cr,l}}$. The match in the soft domain is very good while the match in the stiff domain is satisfactory, but with a more obvious difference. The influence of the foundation nonlocality can already be seen, although just slightly. The foundation nonlocality tends to spread the displacement profile over a larger distance compared to the local foundation. This can be seen in both cases, but is more obvious in the stiff region because there most of the system compliance comes from the soil layer (the Kelvin layer is very stiff). The stiffer the soil layer,

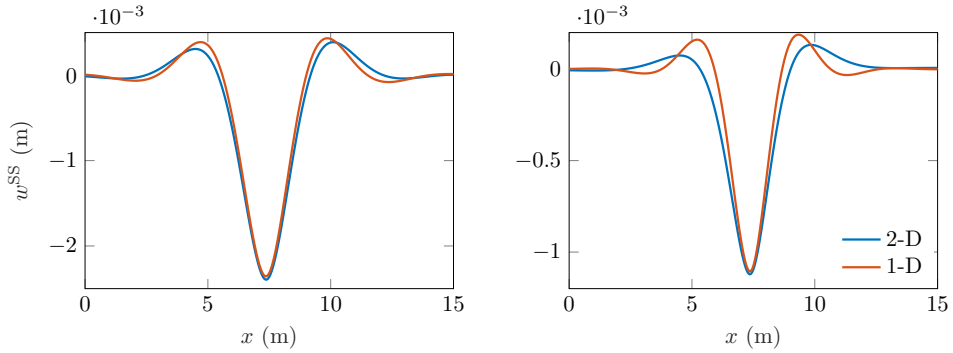

Figure 8.18: Comparison of the steady-state displacement fields in the soft region (left panel) and stiff region (right panel) after the tuning of the 1-D model to the 2-D one; $v \approx 0.75 c_{\mathrm{cr,l}}$.

the less pronounced the effect of the nonlocality becomes because a very stiff soil layer acts as a rigid bottom, practically transforming the 2-D system into a 1-D one with a local foundation. Therefore, the softer the soil, the more important it is to model the nonlocality of the foundation.

8.4.2. Transient response

The fact that the eigenfields of the two systems match well does not mean that the transient responses will also do so. For this reason, the transient responses of the two systems are compared here. The stiff zone is located between $x = 10$ m and $x = 20$ m, in which the stiffness and damping of the Kelvin layer is ten times higher than in the open track. In this reference case, a load velocity $v \approx 0.75 c_{\mathrm{cr,l}}$ is chosen to investigate the response in a realistic regime.

Fig. 8.19 compares the displacement profiles for different time moments. It can be seen that while the eigenfields match well, the free fields show significant differences. More specifically, the free field in the 1-D model seems to be much stronger than in the 2-D one, both to the left and right of the transition. This is even more clear when we look at the frequency spectra of the transient responses presented in Fig. 8.20. It can be seen that the magnitude of the free field is not only overestimated, but it is also located at slightly higher frequencies in the 1-D model.

The reason for the difference in the transient responses can be seen in the difference between the dispersion curves of the two systems, as presented in Fig. 8.21. The dispersion curves of the 2-D system are the same as in Fig. 8.6, but with damping included and without the distributed mass layer (representing embankment). The dispersion curves of the 1-D system are the same as in Chapter 2, but with damping included. The real part of the wavenumbers is presented in the left panel while the imaginary part in the right one. In the left panel, it can be seen that a good match of the dispersion curve that characterizes

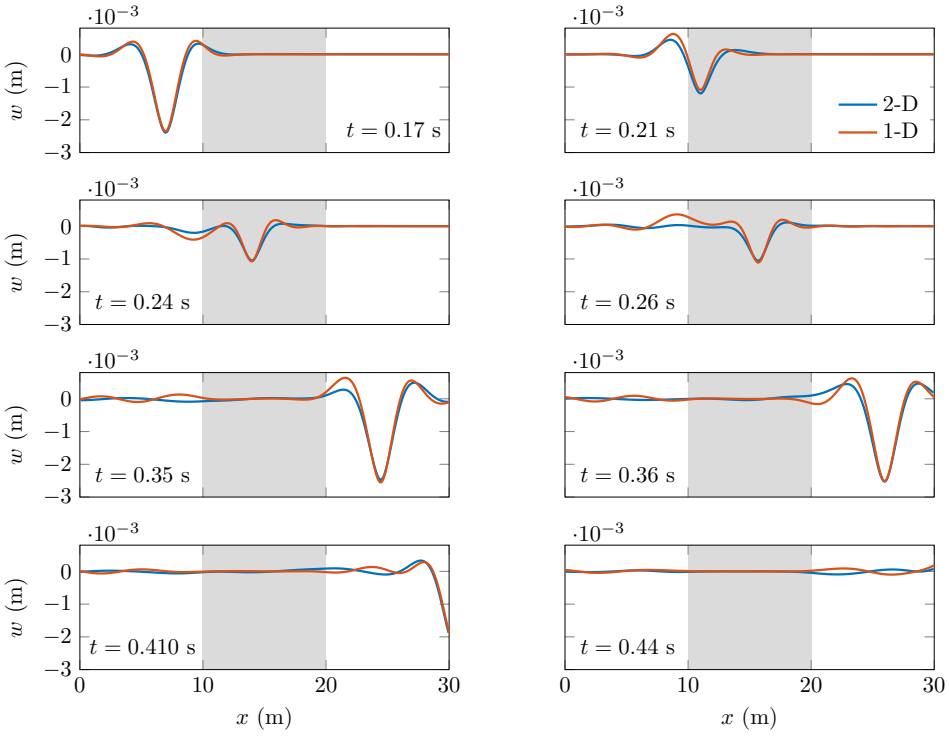

Figure 8.19: Comparison of the transient displacement profile at different time moments. The grey background indicates the location of the stiff zone; $v \approx 0.75 c_{\mathrm{cr},1}$.

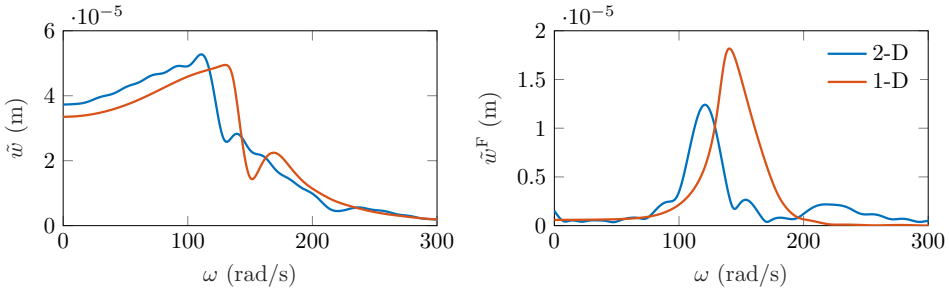

Figure 8.20: Frequency spectra of the transient (left panel) and free-field (right panel) displacement at the left of the stiff zone ($x = 8$ m).

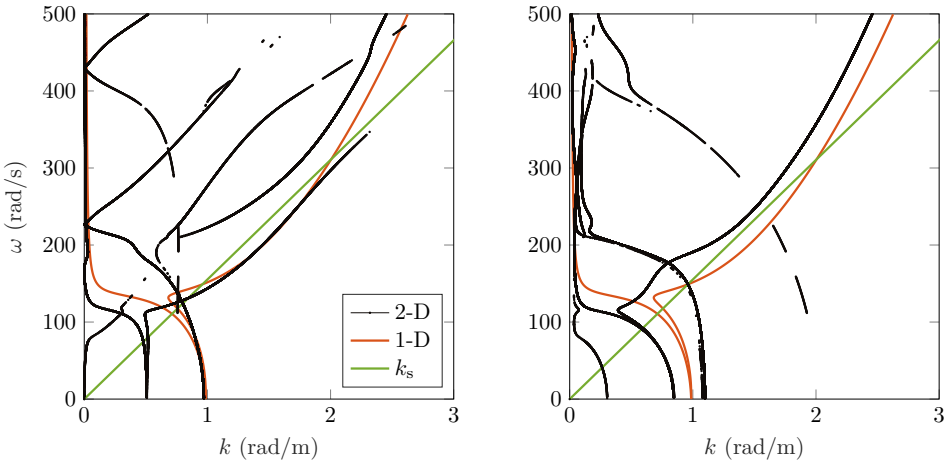

Figure 8.21: Dispersion curves of the 1-D and 2-D systems with damping included; the left panel represents the real part of the wavenumber while the right panel represents its imaginary part. The parameters of the soft domain are used and k_s is the shear wavenumber.

the stationary wave is only in the frequency range of 175–250 Hz, while in the right panel there is a poor agreement. The range in which the dispersion curves match can be adjusted; for example, if the tuning was done for the quasi-static velocity regime, the good match would be at slightly lower frequencies. Nonetheless, a good match over a larger frequency range is not possible due to the locality of the foundation in the 1-D model. Moreover, the 1-D model fails to capture the many different evanescent modes that are present in the 2-D system. These represent two important limitations of this 1-D model and shows that it is difficult, if not impossible, to have a good match of both the eigenfield and of the free field. This conclusion leads to two consequences: (i) the nonlocality seems to be influential in the transient process and, consequently, this 1-D model is not ideal for correctly capturing the transient response, and (ii) if one wants to tune a 1-D model to mimic a 2-D/3-D one, a better strategy is to tune the dispersion curves rather than the steady-state response.

The observed difference in the free field (Fig. 8.19) strongly affects the settlement predicted by the two models. Figure 8.22 presents the settlement profile obtained with both models after one load passage. Results show that the degradation in the 1-D model is significantly larger than in the 2-D model. Furthermore, the 1-D model predicts that settlement occurs both at the left and right of the transition while the 2-D model shows settlement developed only at the right of it. At the right of the transition, the settlement in the 2-D model starts earlier and ends later than the one in the 1-D model. While this fact is caused by the foundation nonlocality (the spread over a larger distance), the reason for the discrepancies in magnitude is different. Namely, the settlement in the 1-D model is based on the displacement of the beam, while in the 2-D model it is dictated by the differential displacement between the beam and the top surface of the soil. Since the soil is considerably

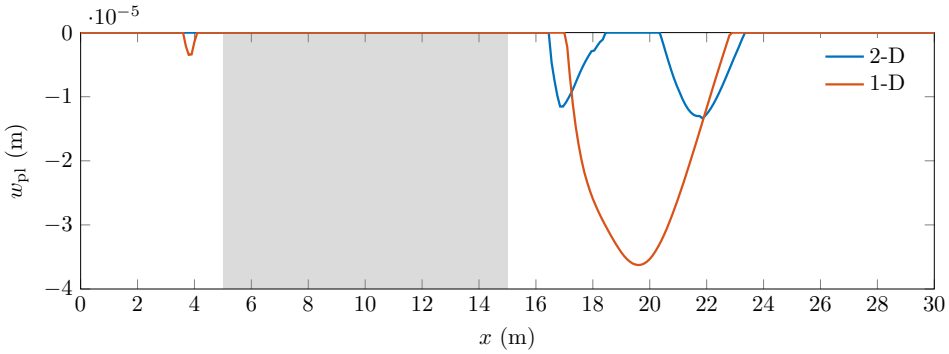

Figure 8.22: The settlement predicted by the two models after one passage of the load in the reference case ($v \approx 0.75c_{\mathrm{cr}}$); the stiff zone is represented through the grey background.

softer than the ballast, the differential settlement between the beam and the top surface of soil is small, leading to a reduced settlement. This shows that if the settlement magnitude is to be correctly predicted, it is more important to account for the flexible bottom of the Kelvin layer than to introduce the foundation nonlocality.

8.4.3. Indirectly introducing nonlocality in the 1-D model

As we have seen in the previous sections, the nonlocality of the 2-D model can be influential and the 1-D model formulated in Chapter 6 fails to accurately capture both the eigenfield and free field. Also, the fact that the bottom of the Kelvin foundation in the 1-D model is fixed causes an overestimation of the settlement compared to the 2-D model. Although these factors render the 1-D model formulated in Chapter 6 inaccurate in predicting the transient response at transition zones and the associated settlement, 1-D models still pose advantages when it comes to computational efficiency. Therefore, this section formulates and analyzes an *enhanced* 1-D model that introduces (i) nonlocality indirectly and (ii) accounts for the flexible bottom of the Kelvin layer that represents the ballast/embankment layers.

The aforementioned 1-D model consists of two beam-Kelvin foundation systems placed in series, similarly to the model introduced in Chapter 3. The top beam and Kelvin layer can be chosen with the exact same properties as the ones in the 2-D model. As for the lower beam and Kelvin layer, they are chosen and tuned to match the response of the 2-D system. The bending stiffness of the lower beam could be neglected, making it a layer of distributed mass as in Chapter 3; this would include property (ii) (i.e., flexible bottom), but it would not incorporate nonlocality. One model that is found in literature used to represent the behaviour of the supporting structure that includes both characteristics (i) and (ii) is the so-called Kerr foundation model [139], which is a generalization of the more well-known Pasternak foundation [140]. This incorporates a shear beam as the lower beam, meaning that it has no flexural rigidity, but it does have shear rigidity. As it has a second-order derivative

Table 8.3: The tuned values of the parameters of the 1-D model with Kerr foundation.

Parameter	Symbol	Value	Unit
Shear beam mass–soft domain	$\rho_{\mathrm{sb,l}}$	2020	kg/m
Shear stiffness–soft domain	$G_{\mathrm{sb,l}}$	$2.68{\cdot}10^7$	N/m^2
Bottom Kelvin stiffness–soft domain	$k_{\mathrm{b,d,l}}$	$6.86{\cdot}10^7$	N/m^2
Bottom Kelvin damping–soft domain	$c_{\mathrm{d,l}}$	$7.8{\cdot}10^4$	Ns/m^2
Shear beam mass–stiff domain	$\rho_{\mathrm{sb,r}}$	2020	kg/m
Shear stiffness–stiff domain	$G_{\mathrm{sb,r}}$	$2.88{\cdot}10^7$	N/m^2
Bottom Kelvin stiffness–stiff domain	$k_{\mathrm{b,d,r}}$	$4.86{\cdot}10^7$	N/m^2
Bottom Kelvin damping–stiff domain	$c_{\mathrm{d,r}}$	$7.2{\cdot}10^4$	Ns/m^2

in space (instead of a fourth-order as in the bending beam model), it potentially can better approximate the behaviour of the soil layer which also has a second-order derivative in space. This model is formulated further.

The equations of motion of such a model read

$$EIw_{,xxxx} + \rho_{\mathrm{b}}\ddot{w} + c_{\mathrm{d}}(x,\Delta w)\Delta\dot{w} + f_{\mathrm{k}}(x,\Delta w) = -F_0\delta(x-vt), \tag{8.42}$$

$$-G_{\mathrm{sb}}u_{,xx} + \rho_{\mathrm{sb}}\ddot{u} - c_{\mathrm{d}}(x,\Delta w)\Delta\dot{w} - f_{\mathrm{k}}(x,\Delta w) + c_{\mathrm{d,b}}\dot{u} + k_{\mathrm{d,b}}u = 0, \tag{8.43}$$

where the first equation of motion is exactly the same as in the 2-D model, while the second one is for the shear beam. G_{sb} and ρ_{sb} are the shear modulus and linear mass of the shear beam while $c_{\mathrm{d,b}}$ and $k_{\mathrm{d,b}}$ are the damping and stiffness of the bottom Kelvin foundation, respectively. The boundary conditions as well as the inhomogeneity and nonlinearity of the top Kelvin layer are exactly the same as for the 2-D model (see Section 8.1).

It must be emphasized that the linear equivalent of two beam model formulated in this section has been used in literature in many variations. It has also been tuned and its response compared to the one of a 3-D model in Ref. [138], showing a good agreement. However, the comparison was only made in the steady-state regime. As we have seen in the previous section, this does not ensure that the transient response is accurately captured. The novelty of this section lies mostly in the in-depth analysis of the transient response in comparison to the 2-D model, in assessing its adequacy of correctly capturing the transient process, and in including the nonlinearity of the foundation and analyzing the accuracy of the settlement prediction.

Tuning the Kerr model

It is chosen that the properties of the top beam and Kelvin layer are kept exactly the same as the ones in the 2-D model. These could also be allowed to vary, but to reduce the complexity of the optimization problem, it is chosen not to. In this case, there are four tuning parameters, the shear modulus and mass of the shear beam, and the damping and stiffness of the lower Kelvin layer. Once again, the mass of the shear beam is chosen such that the critical velocity

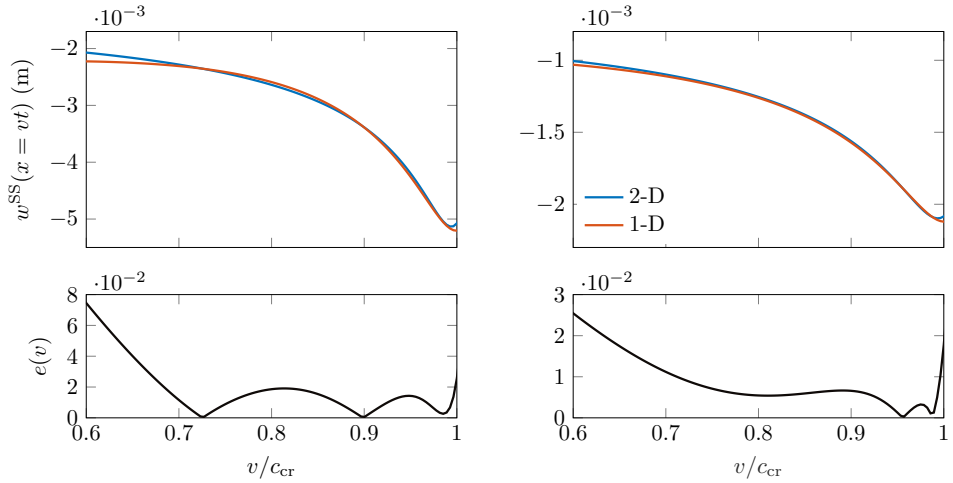

Figure 8.23: Comparison of the steady-state displacement under the moving load versus velocity of the load (top panels) and the relative error (bottom panels) after the tuning of the enhanced 1-D model to the 2-D one. The left panels are for the soft region while the right ones are for the stiff region.

matches the one of the 2-D system. The remaining three parameters are tuned such that the steady-state displacement under the load matches the one of the 2-D system in the dynamic velocity regime, as done in the previous section. Since there is an additional tuning parameter, there are additional parameter combinations that can lead to good agreement between models. Therefore, a second criterion is imposed to select between the different combinations that lead to good results, namely to have a good match in the shape of the steady-state displacement field (not only under the moving load). This criterion is not implemented in the optimization problem, but is checked manually.

The values obtained are given in Table 8.3 and the results are presented in Figs. 8.23 and 8.24. Although the shear beam and bottom Kelvin foundation should, in principle, 'represent' the soil layer which is homogeneous, their parameter values are tuned separately for the soft and stiff domains. This is because the goal is for the whole system to mimic the 2-D system, not individual parts to exhibit similar responses. Nonetheless, the values obtained for the soft and stiff domains are quite similar. Interestingly, the values of the stiffness and damping of the bottom Kelvin layer are smaller in the stiff domain than in the soft (recall that the stiffness difference in the 2-D is in the top Kelvin layer, not to be mistaken with the bottom Kelvin layer). This could be explained that in the stiff domain, most flexibility comes from the soil layer, requiring the bottom Kelvin layer to be slightly more compliant in the stiff region.

Fig. 8.23 shows, at least for the soft domain, that the agreement of the response under the moving load in the dynamic regime is slightly worse than for in the previous section. However, as can be seen in Fig. 8.24, the eigenfields of the two systems match remarkably

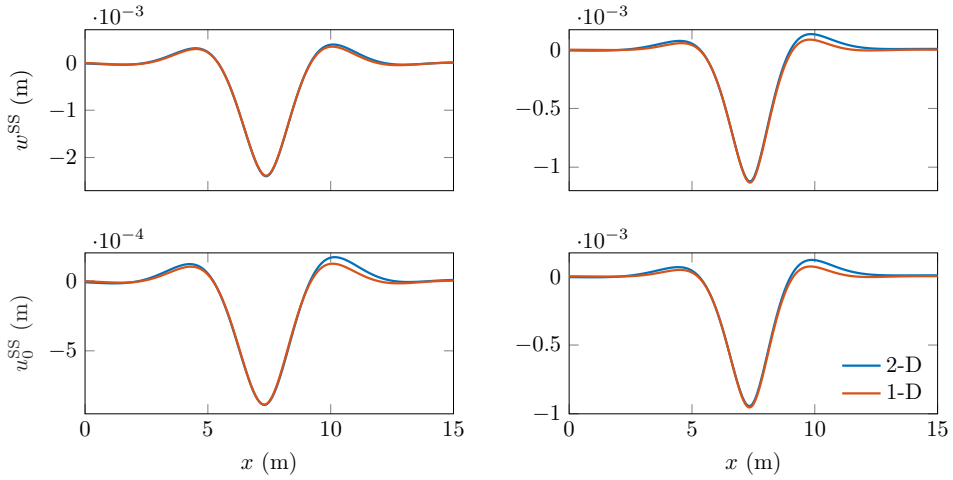

Figure 8.24: Comparison of the steady-state displacement fields at the rail level (top panels) and soil surface/shear beam (bottom panels) in the soft region (left panels) and stiff region (right panels) after the tuning of the enhanced 1-D model to the 2-D one; $v \approx 0.75 c_{\mathrm{cr,l}}$.

well. Both the magnitude of the response as well as the shape (especially the width of the responses) exhibit a considerable improvement compared to the results in the previous section. Mathematically, the better match is attributed to an additional tuning parameter. Physically, indirectly capturing nonlocality through the introduction of the shear beam-Kelvin foundation system is the cause for the better agreement. Furthermore, Fig. 8.24 shows that also the response of the shear beam (in the 1-D model) agrees very well with the response at the soil surface (in the 2-D model).

In the previous section, the two models showed a reasonable agreement in the steady state responses, but a less good agreement in the transient responses. The enhanced 1-D model formulated in this section shows a very good agreement also in the transient responses as shown in Fig. 8.25. This shows that both the eigenfields and the free-fields are captured correctly by the enhanced 1-D model. Although there is a small phase shift in the free-field responses, the magnitudes match remarkably well.

The reason for the good agreement in the transient response can also be seen from the dispersion curves of the two systems. Fig. 8.26 presents the dispersion curves of the enhanced 1-D model in comparison to the ones of the classical 1-D model. The top panels compare the two dispersion curves that exist in both 1-D models, while the bottom panels present the additional dispersion curve that appears in the enhanced model (for comparison, the dispersion curves of the classical 1-D model are presented also in the bottom panels). The dispersion curves of the enhanced model show two important alterations. Firstly, the branch that characterizes propagating waves in the undamped system (blue line in the top left panel) turns from convex (at lower frequencies) to concave (at higher frequencies)

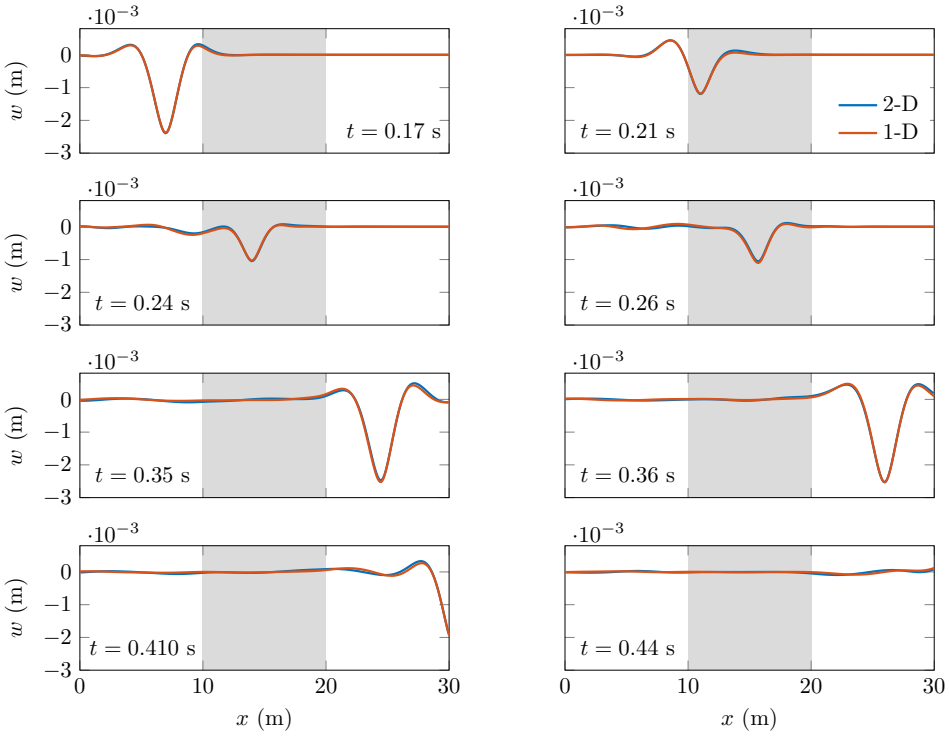

Figure 8.25: Comparison of the transient displacement profile at different time moments. The grey background indicates the location of the stiff zone; $v \approx 0.75 c_{\mathrm{cr,l}}$.

meaning that waves have a finite group velocity, which better resembles the 2-D system. Secondly, an additional dispersion curve (orange lines in the bottom panels) appears in the enhanced model that characterizes an evanescent wave at low frequencies and a stationary one at high frequencies.

The dispersion curve comparison between the three models is presented in Fig. 8.27. For clarity, each individual dispersion curve of the 1-D models is compared to the 2-D ones in separate plots. The branch that characterizes propagating waves in the undamped system (top left panel) shows that a good match occurs over a larger frequency range in the enhanced 1-D model. Also the second dispersion branch (that also exists in the classical 1-D model) characterizing an evanescent wave shows an improved match, in both the real (middle left panel) and imaginary parts (middle right panel). Furthermore, the additional dispersion branch leads to the enhanced model capture more of the evanescent field of the 2-D system. However, even though the free-field response seems to be well captured in the vicinity of the transition zone (where the evanescent modes are restricted to), the enhanced 1-D model can not capture the multitude of evanescent modes present in the 2-D system.

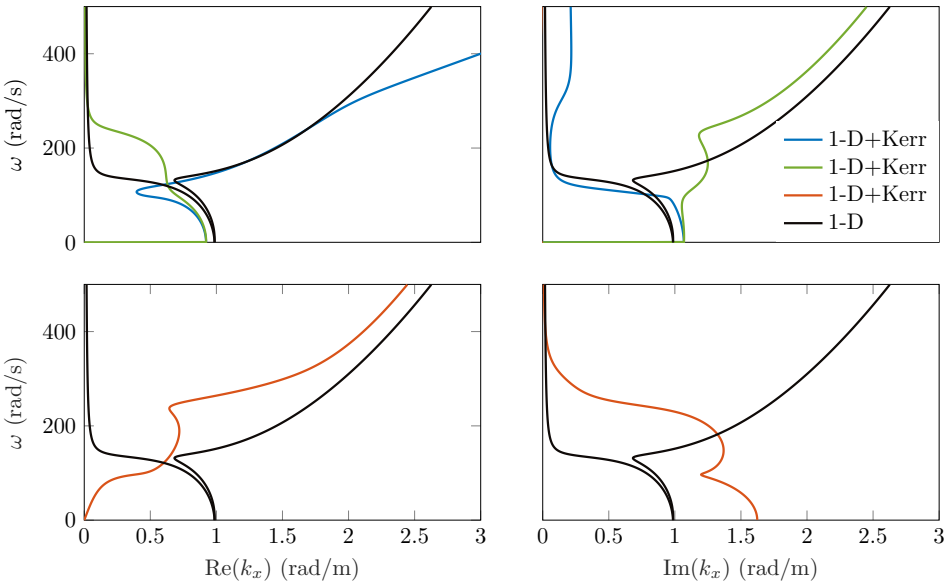

Figure 8.26: Dispersion curves of the classical and enhanced 1-D systems with damping included; the parameters of the soft domain are used.

Figure 8.28 presents the settlement profile obtained with the three models after one load passage. Results show that the settlement predicted by the enhanced 1-D model is closer to the one predicted by the 2-D model (closer than the classical 1-D model). This is caused by (i) the better agreement of both the steady-state and free fields combined with (ii) the incorporation of the flexible bottom of the Kelvin foundation. However, although the magnitude of the settlement agrees very well, the spatial distribution of the settlement does not. This might be caused by the inability of the 1-D model to capture the multitude of evanescent wave modes which are influential in the transition zone. To conclude, although the enhanced 1-D model performs significantly better than the classical 1-D model, it shows the inherent limitations of the 1-D models compared to the 2-D one when it comes to the accurate prediction of the settlement profile.

8.5. Conclusions

The two main goals of this chapter were to (i) investigate the response amplification and the corresponding settlement of a system in which the soil is modelled as a 2-D continuum, and (ii) to analyse the influence of the foundation nonlocality on the response at transition zones. To this end, a 2-D model was formulated consisting of a linear and homogeneous continuum layer of finite depth and an Euler–Bernoulli beam connected to the layer through and inhomogeneous and nonlinear layer of springs and dashpots; the beam is acted upon by a moving constant load. The response of this system was obtained using a novel solution

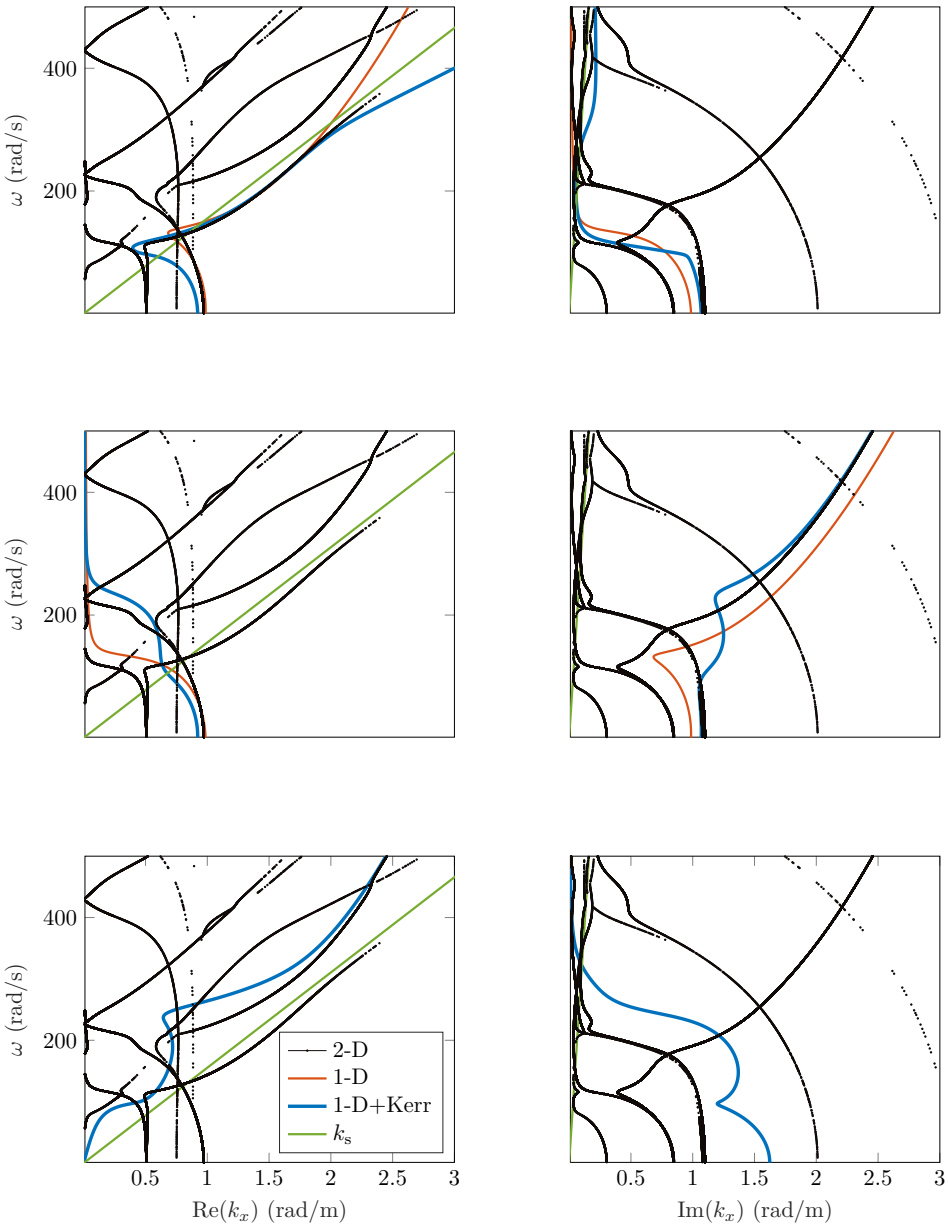

Figure 8.27: Dispersion curves of the 1-D, enhanced 1-D, and 2-D systems with damping included; the left panels represent the real part of the wavenumber while the right panels represent its imaginary part. The parameters of the soft domain are used and k_s is the shear wavenumber.

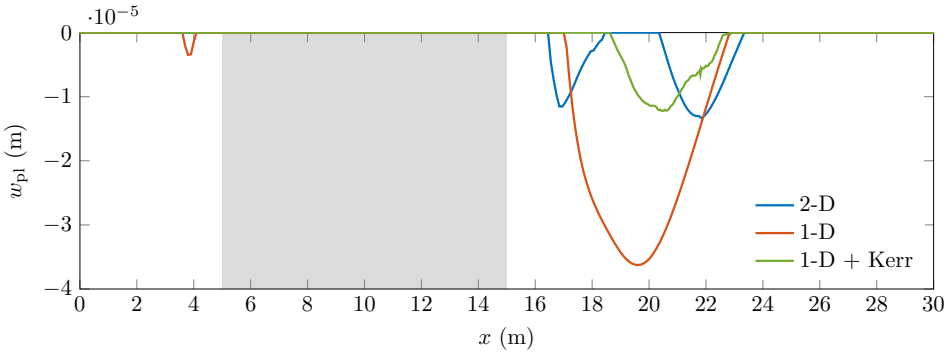

Figure 8.28: The settlement predicted by the three models after one passage of the load in the reference case ($v \approx 0.75 c_{\mathrm{cr}}$); the stiff zone is represented through the grey background.

method, namely the pseudo-force method. The parameter values of the proposed model were tuned such that its steady-state response resembles the one of a 3-D FE model. The purpose of the tuning was not to have the best agreement possible, but to ensure that the response of the proposed model is in the realistic realm. Consequently, even though the agreement between responses was not great, it was satisfactory for the aforementioned purpose. The main novelty of this chapter lies in the two goals set (specified above), especially in the investigation of the foundation nonlocality and its influence on the response of railway tracks at transition zones.

Two configurations of the aforementioned system were analyzed. In scenario A, the stiff zone rests directly on the soil layer and is qualitatively representative of a railway crossing where the concrete slab rests directly on the soil. Scenario B, unlike scenario A, has an additional layer of stiff springs at the bottom of the stiff zone. This scenario is qualitatively representative of a structure (e.g., culvert) supported by stiff and slender piles. Results show that the wave radiation is significantly stronger in scenario B compared to scenario A, mainly due to the larger stiffness ratio. This is the main reason for the larger settlement observed in scenario B compared to scenario A, observation which holds for all load velocities and different values of the soil stiffness. It was also shown that the softer the soil, the lower the settlement predicted at the same relative velocity (load velocity relative to the system's critical velocity), in both scenarios. The two factors causing this are (i) the fact that the system's compliance comes mainly from the soil and, consequently, decreasing the soil stiffness decreases the variation in the differential displacement Δw between the beam and soil, and (ii) the stiffness ratio between the stiff and soft zones decreases with decreasing soil stiffness, leading to a weaker free field and, consequently, to a lower response amplification. Factor (ii) holds for all parameter values in scenario A; for scenario B, it holds for the investigated parameter values, but can be incorrect for a very low soil stiffness. Factor (i) suggests that, at least for the railway tracks founded on soft soils, the soil settlement should be accounted for since the response amplification occurs mostly in the soil. When it comes to the length

of the stiff zone, it was shown that it does not influence the soft-to-stiff transition, but it has an influence for the stiff-to-soft one. More specifically, for scenario A, the shorter the stiff zone the lower the settlement, while for scenario B the influence was much smaller.

The influence of the foundation nonlocality on the response was investigated by comparing the 2-D and 1-D models. For this, the original system presented in Section 8.1 was utilized due to its simplicity and straightforward correspondence to the 1-D model. A simple tuning procedure for the parameter values of the 1-D model leads to a reasonable to good agreement between the steady-state displacement fields of the two models. However, a good agreement for the transient response was not observed mainly because the dispersion curves of the two systems show a good agreement only in a limited frequency range; also, the 1-D model fails to capture the many different evanescent modes that are present in the 2-D system. Therefore, a better approach would be to tune the dispersion characteristics of the simplified model instead of the steady-state response, as is usually done. However, the inaccurate prediction of the transient response combined with the fact that the Kelvin foundation in the 1-D model, unlike in the 2-D one, has a rigid base, causes the settlement prediction to be inaccurate and grossly overestimated. To reconcile the responses of the two systems, an enhanced 1-D model is formulated in which (i) the foundation nonlocality is introduced indirectly and (ii) the compliant base of the Kelvin layer is considered. After tuning its parameters, the response of the enhanced 1-D model presented a much better agreement to the 2-D model in both the steady-state and transient responses. It must be noted that the tuning was performed using the steady-state responses (as done for the classical 1-D system), and that the tuning is not specific to one velocity, but rather to a velocity regime. Moreover, the dispersion curves showed a good agreement over a broader frequency range and one branch that characterizes evanescent waves was also captured. When it comes to the settlement, its magnitude showed a very good agreement to the one predicted by the 2-D model, but the spatial distribution of the settlement was not accurately predicted. This could be caused by the limitation of 1-D models in capturing the multitude of evanescent modes present in the 2-D system.

The investigation in this chapter sheds light on the influence of incorporating the foundation nonlocality and the situations in which this is necessary (e.g., railway tracks on soft soils). This study can help researchers and engineers make informed decisions about modelling approaches depending on the specific problem investigated.

9

Conclusions and recommendations

There are three stages in scientific discovery.
First, people deny that it is true,
then they deny that it is important;
finally, they credit the wrong person.

Bill Bryson

This thesis was concerned with the differential settlements that occur much more frequently at transition zones compared to other parts of the railway track. This issue has been known for a long time, but the mitigation measures designed to cope with this problem have had just limited success. Although the failure of some mitigation measures stems from inadequate design and poor implementation, overall, their lack of efficiency can be attributed to the lack of understanding of the main mechanism(s) that drive(s) the differential settlement. This led to the first and main objective of this thesis, which was to *investigate and advance the understanding of the main mechanisms that lead to railway track degradation at transition zones*.

The settlement mechanisms were studied in this thesis through models rather than in-situ measurements or lab experiments. The majority of previous studies have used models to (i) understand and (ii) predict the response of railway tracks at transition zones. Researchers aiming at (i) have usually used simplified phenomenological models in which system characteristics that are not of interest are excluded. More recently, the models' complexity has increased tremendously by incorporating many system characteristics, making these models ideal for (ii), but less ideal for (i) due to the many mechanisms simultaneously at play. This led to the second objective of this thesis, which is to *investigate the effect of specific*

characteristics of the railway system on the degradation at transition zones. In other words, the second objective entailed improving the simplified models by incorporating additional characteristics and determining which of these characteristics is of importance and which can be neglected.

Naturally, this dissertation could only focus on a few of the many aspects involved in this complex problem, and the two main constraints are presented in the following. Improving the maintenance operations themselves by employing new technologies could lead to a reduction in the maintenance frequency. However, to develop a long-term solution, one should aim at eliminating the root cause. Therefore, this thesis investigated the *initiation* phase of the settlement, and not the *accumulation* phase. Furthermore, this thesis focused on the differential settlement stemming solely from the amplification of stresses and strains that occur at transition zones, which is significant at relatively large train velocities. Consequently, this thesis has not treated other sources of differential settlements, such as the different rates at which autonomous settlement develops in the open-track and at the man-made structure.

9.1. Conclusions

The main high-level conclusions are given in the following and are divided in two categories based on the two goals of this thesis; the first number of each conclusion indicates the corresponding chapter in which the conclusion was reached. For detailed low-level conclusions, the reader is referred to the conclusion section of each individual chapter.

The investigation of mechanisms leading to differential settlements

2.1 The response amplification at transition zones is caused by the interference between the steady-state field (eigenfield) and the free field generated by the transition process. Consequently, the more pronounced the free field compared to the eigenfield, the larger the resulting amplification.

2.2 In the soft-to-stiff transition, the interference leading to response amplification takes place between the rightward travelling eigenfield and the leftward travelling free field, while in the stiff-to-soft transition, both interfering fields are travelling rightward. This causes different amplification profiles in the two scenarios. In the soft-to-stiff case, the amplification develops in a relatively small area close to the stiff zone, but it has a strong spatial variation (i.e., could lead to strong differential settlements). In the stiff-to-soft scenario, the amplification occurs over a much larger area and further away from the stiff zone, but its profile is smoother than in the stiff-to-soft case. Furthermore, the amplification in the soft-to-stiff case is more pronounced the closer the load velocity is to the critical one (i.e., above 75%), while the stiff-to-soft settlement is pronounced at low and medium velocity ranges (e.g., 50-80%).

2.3 Increasing the foundation viscous damping causes a reduction of the response amplification in the stiff-to-soft transition while for the soft-to-stiff one, the reduction occurs only at velocities close to the critical one, and it even leads to an amplification increase for low and medium velocity ranges. This conclusion together with 2.2, strongly suggests the need of different mitigation measure designs for the two types of transition.

2.4 In the absence of damping, results show that the total radiated energy in the transition process is invariant between the soft-to-stiff and stiff-to-soft scenarios. In light of Conclusions 2.2 and 2.3 which emphasized the different behaviour of the two transition types, this finding was unexpected.

2.5 For a large load velocity, quantities evaluated in the far field (e.g., energy flux) can be good indicators of the response amplification because the transition process leads to mostly propagating waves. However, for lower velocities, both propagating and evanescent waves are generated meaning that other quantities (e.g., power input by the load) that include information about the near field should be used as response-amplification indicators.

3.1 The inertia of the supporting structure (ballast, embankment, soil, etc.) does not seem to have a significant qualitative influence on the response amplification at transition zones and on the energy radiated during the transition process.

4.1 The vehicle-structure interaction introduces two additional amplification mechanisms compared to simplified scenario of a moving constant load (i.e., the vehicle does not have its own degrees-of-freedom). Namely, the variation of the vehicle's vertical momentum induced by (i) bending waves excited in the transition process, and (ii) a parametric variation of the system properties as experienced by the moving vehicle (i.e., varying foundation stiffness). Generally, the additional mechanisms lead to a stronger transition radiation.

4.2 The amplification of the wheel-rail contact force caused purely by a change in foundation stiffness and damping (i.e., a track without initial imperfections) can be significant if the vehicle velocity is relatively large and the change in foundation stiffness (and damping) is considerable and not smooth. Previous literature studies concluded the opposite, that the amplification of the contact force due to a change in foundation stiffness is insignificant. However, these studies considered only quasi-static velocities and small effective changes in foundations properties. The findings presented in this thesis, thus, supplement earlier findings to offer a more complete picture.

4.3 For large enough vehicle velocities and stiffness ratios between the stiff and soft domains, loss of contact between the wheel and rail can occur, leading to sharp increases in the contact force when contact is re-established. While in the modelled scenarios this occurs

on the stiff domain where settlement is not considered, the sharp increase in contact force can lead to numerous other fatigue problems in the overall railway system.

5.1 Three response amplification mechanisms have been identified at transition zones in systems that have a periodic nature. The amplification is the product of a system with periodic nature and with a local inhomogeneity, and if one of these characteristics is omitted, the amplification does not occur. While these mechanisms can be influential for the railway over-head wires and for the emerging Hyperloop transportation system, they have a negligible influence in the conventional railway track.

6.1 The development of the initial settlement leads to a redistribution of the energy radiated during the transition not only between between frequencies, but also between the soft and stiff media. This redistribution is mainly attributed to the separation between the beam and foundation at the settlement location. Consequently, if the developed settlement is not large enough to allow for this separation, the influence of the nonlinear foundation on transition radiation is negligible.

8.1 For ballasted tracks founded on soft soils, the vertical stiffness of the ballast layer can be significantly larger than the one of the soil. Consequently, the response amplification at transition zones is more pronounced in the soil layer than in the ballast layer. Results from the 2-D model show that in this situation, soil settlement should be accounted for because the settlement in the ballast is initially minimal.

8.2 The ballast settlement in the 2-D model could be predicted from the power input by the moving load. The larger the negative slope in the power input, the more pronounced the settlement. In other words, the more abrupt the change between energy flowing from structure-to-load to energy flowing from load-to-structure, the stronger the settlement. The power input is a quantity that can more easily be measured than quantities in the ballast/soil. However, more investigation and in-situ measurements are needed to prove such a relation.

The influence of accounting for specific system characteristics

3.a When investigating the response amplification at transition zones using simplified 1-D models, accounting for the inertia of the supporting structure (e.g., ballast) is not necessary for qualitative investigations provided that the vehicle velocity relative to the critical velocity of the system is realistic. However, when investigating the transition radiation energy and its distribution over frequencies, accounting for the inertia of the supporting structure is important for correct quantitative results, but including it as a separate layer is not necessary (i.e., it is sufficient to include the additional mass in the one of the beam).

3.b Above a specific value of the additional mass, incorporating the inertia of the supporting structure through a separate mass layer can lead to an increase (instead of a decrease) of the system's critical velocity, finding which is counter-intuitive.

3.c Incorporating the inertia of the supporting structure through a separate mass layer and neglecting the shear/bending stiffness of this additional layer leads to the steady-state response of the system to a moving constant load to always present at least one propagating wave, which is an artefact.

4.a Accounting for the vehicle-structure interaction leads to a reduction of the maximum response amplification observed at transition zones compared to modelling the vehicle as a moving constant load.

5.a As a consequence of Conclusion 5.1, for investigations focused on transition zones and response amplification at low frequencies, the periodicity of the railway track can be successfully approximated by the equivalent continuously supported one without neglecting influential amplification mechanisms.

5.b Two out of three amplification mechanisms identified in a periodic system with a transition zone could be replicated in a continuously supported system by including harmonic components to the moving load. The solution to the latter system is, in principle, easier to obtain. However, the harmonic components of the moving load must be tuned, and, in principle, are not known before-hand; also, they need to be updated for each change of the system properties, which makes it difficult to use the continuous system in practical situations.

6.a Modelling explicitly the foundation settlement caused by the response amplification at transition zones has a significant effect on the overall response only if the separation between the beam and supporting structure is allowed (i.e., the settlement is large enough for the separation to occur).

7.a For obtaining the response to the nonlinear and inhomogeneous 1-D system (see Chapters 6 and 7), the commonly used time-domain method is overall more computationally efficient than the frequency-domain and hybrid methods. However, when it comes to a 2-D system with the nonlinearity and inhomogeneity limited to the surface layers (e.g., nonlinear and inhomogeneous ballast layer), the frequency-domain and hybrid methods have the potential to be more efficient than the time domain method.

8.a The nonlocality of the soil layer has an increasingly pronounced effect on the steady-state response with its decreasing shear stiffness. Consequently, modelling the nonlocality of the supporting structure can be important for railway tracks founded on soft soils.

8.b The guided waves generated during the transition process in the 2-D system that have a phase velocity between the Rayleigh and shear-wave velocities should be treated with

care because they are stationary in the 2-D model while they would be leaky in a 3-D model.

8.c Comparison of the the responses of the 1-D and 2-D models revealed that while the steady-state responses can show a good agreement, the transient response as well as the predicted settlement are poorly captured with the 1-D model. This fact highlights the importance of the foundation nonlocality on these quantities. Moreover, it was concluded that instead of tuning the 1-D model based on the steady-state displacement fields, an improved strategy would be to aim at matching the dispersion characteristics of the two models.

8.d An enhanced 1-D model, which includes indirectly the foundation nonlocality, shows a good agreement to the 2-D in the steady-state as well as the transient responses. Furthermore, the magnitude of the predicted settlement is well captured, but its spatial distribution is not. Most likely, this cannot be captured irrespective of the tuning and points towards an inherent limitation of 1-D models in accurately capturing behaviour of 2-D or 3-D systems.

9.2. Recommendations

My recommendations for future research related to transition zones in railway tracks are divided into (i) academically oriented and (ii) practically oriented. The academically oriented ones are aimed at expanding the more fundamental knowledge (from an engineering perspective) of transition zone behaviour and do not have a clear practical application. Nonetheless, each of the academically oriented recommendations states its potential long-term implications on transition zone improvement. The practically oriented ones are research directions that can lead to the improvement of transition zone design in the very near future.

Academically oriented recommendations

(1) Chapter 6 introduced in the supporting structure a nonlinear constitutive relation that is representative of ballast and its settlement, and studied its influence on transition radiation. However, the type of nonlinearity introduced is very specific for this application and, consequently, general conclusions cannot be drawn. An academically relevant and challenging research path is to investigate the influence of a general type of nonlinear constitutive law (e.g., cubic stiffening/softening, hyperbolic softening, etc.) on transition radiation. The conclusions of such a study can be relevant for researchers that aim to understand what the influence of complex nonlinear behaviour is on the behaviour of transition zones.

(2) A significant number of mitigation measures at transition zones are trying to reduce the vertical *static* stiffness difference between the soft and stiff domains (e.g., by implementing tuned under-sleeper or rail pads). While this can have a beneficial effect,

the transition zone exhibits, in general, a variation in all properties (i.e., damping, mass, bending/shear stiffness, etc.). Consequently, for the mitigation measure to be efficient, the difference in vertical *dynamic* stiffness should be reduced instead. This could be achieved by placing tuned resonators at the sleeper level. An academically relevant investigation with potentially practical relevance is to study the feasibility of tuned resonators in reducing the dynamic stiffness inhomogeneity at transition zones.

(3) To exclude part of the complexity, this thesis restricted its study to only one wheel travelling on the railway track. An important follow-up research is to investigate the response amplification at transition zones caused by multiple moving loads/oscillators. Although complex models of the whole train have been considered in many previous studies, most of them focused only on predicting the overall response. An in-depth investigation into the wave interference between the steady-state field of the last wheels and the free-field generated by the front wheels—that could lead to a larger response amplification than for only one wheel—was not previously studied, and could improve quantitatively the results obtained in this thesis.

(4) Among others, Chapter 8 found that when tracks are founded on soft soil, the response amplification at transition zones occurs predominantly in the soil layers rather than in the ballast. Therefore, including a settlement mechanism in the soil layers and studying its influence on the transition zone behaviour represents a valuable research direction. The practical outcome of this investigation would be to indicate which component of the supporting structure is most prone to settlement.

(5) Chapter 8 stipulated that tuning a simplified 1-D model to a more complex 2-D/3-D one based on the system dispersion properties could lead to a better representation of the transient response than the current standard procedure which is to base the tuning on the steady-state displacement field. A worthwhile research project would be to investigate this type of tuning procedure. If it leads to improved results, then the 1-D model can be used to investigate aspects which are currently impossible in a 2-D/3-D finite element model due to their computational cost (e.g., settlement at transition zones due to thousands of load passages). In case the results are not satisfactory, then such a study can highlight the importance of problem's multi-dimensionality and an inherent incapability of 1-D models to capture this.

(6) From a mathematical view-point, evaluating some of the inverse transform integrals (e.g., when deriving the time-domain Green's function of a beam on elastic foundation) (semi-)analytically instead of numerically can lead to a significant computational gain and to a broader insight into the solution. Despite the recent increase in computational power, this research direction can generate valuable knowledge for the research community and still prove beneficial to those without access to powerful computers.

Practically oriented recommendations

(a) The amount of available field data at railway transition zones is insufficient to exclude site-specific peculiarities, thus disallowing the generalization of the gained knowledge. To overcome this, field measurements should be performed en masse to generate statistically significant data across multiple transition zones. Such a rich data set combined with computational models that are (to some extent) already available would allow to shed light on the main settlement mechanisms at transition zones.

(b) Related to the previous recommendation, for example, it is not currently clear which of the layers in the railway track experience the most amount of settlement. Many researchers implicitly assume that it is the ballast layer, but there is no statistically significant data to support this because the settlement of the lower layers is largely unknown. As a consequence, it is not clear what a mitigation measure should focus on to increase its efficiency. Therefore, a practically relevant research would be to gather field/laboratory data about the settlement of different railway track layers at transition zones.

Bibliography

References for Chapter 1

[1] *IEA Statistics, https://www.iea.org/data-and-statistics*.

[2] O. Lah. 'The barriers to low-carbon land-transport and policies to overcome them'. In: *European Transport Research Review* 7.1 (2015).

[3] Intergovernmental Panel on Climate Change. *Climate Change 2014 Mitigation of Climate Change*. 2014.

[4] M. J. M. M. Steenbergen. 'Physics of railroad degradation: The role of a varying dynamic stiffness and transition radiation processes'. In: *Computers and Structures* 124 (2013), pp. 102–111.

[5] R. Sañudo, L. Dell'Olio, J. A. Casado, I. A. Carrascal and S. Diego. 'Track transitions in railways: A review'. In: *Construction and Building Materials* 112 (2016), pp. 140–157.

[6] P. Meijers, P. Hölscher and J. Brinkman. *Lasting flat raods and railways/ Literature study of knowledge and experience of transition zones*. Tech. rep. Delft, Netherlands: GeoDelft, 2007.

[7] J. C. Nielsen, E. G. Berggren, A. Hammar, F. Jansson and R. Bolmsvik. 'Degradation of railway track geometry – Correlation between track stiffness gradient and differential settlement'. In: *Proceedings of the Institution of Mechanical Engineers, Part F: Journal of Rail and Rapid Transit* 234.1 (2020), pp. 108–119.

[8] M. Sysyn, M. Przybylowicz, O. Nabochenko and J. Liu. 'Mechanism of sleeper–ballast dynamic impact and residual settlements accumulation in zones with unsupported sleepers'. In: *Sustainability (Switzerland)* 13.14 (2021).

[9] B. Coelho, P. Hölscher, J. Priest, W. Powrie and F. Barends. 'An assessment of transition zone performance'. In: *Proceedings of the Institution of Mechanical Engineers, Part F: Journal of Rail and Rapid Transit* 225.2 (2011), pp. 129–139.

[10] J. N. Varandas, P. Hölscher and M. A. G. Silva. 'Settlement of ballasted track under traffic loading: Application to transition zones'. In: *Proceedings of the Institution of Mechanical Engineers, Part F: Journal of Rail and Rapid Transit* 228.3 (2014), pp. 242–259.

[11] H. Wang and V. Markine. 'Dynamic behaviour of the track in transitions zones considering the differential settlement'. In: *Journal of Sound and Vibration* 459 (2019).

[12] L. Ižvolt and M. Šmalo. 'Historical Development and Applications of Unconventional Structure of Railway Superstructure of the Railway Infrastructure of the Slovak Republic'. In: *Civil and Environmental Engineering* 10.1 (2014), pp. 79–94.

[13] X. Lei and L. Mao. 'Dynamic response analyses of vehicle and track coupled system on track transition of conventional high speed railway'. In: *Journal of Sound and Vibration* 271.3-5 (2004), pp. 1133–1146.

[14] D. Li, D. Otter and G. Carr. 'Railway bridge approaches under heavy axle load traffic: Problems, causes, and remedies'. In: *Proceedings of the Institution of Mechanical Engineers, Part F: Journal of Rail and Rapid Transit* 224.5 (2010), pp. 383–390.

[15] D. Li and D. Davis. 'Transition of Railroad Bridge Approaches'. In: *Journal of Geotechnical and Geoenvironmental Engineering* 131.11 (2005), pp. 1392–1398.

[16] A. I. Vesnitskii and A. V. Metrikin. 'Transition radiation in mechanics'. In: *Physics-Uspekhi* 39.10 (1996), pp. 983–1007.

[17] K. N. Van Dalen and A. V. Metrikine. 'Transition radiation of elastic waves at the interface of two elastic half-planes'. In: *Journal of Sound and Vibration* 310 (2008), pp. 702–717.

[18] Z. Dimitrovová. 'A general procedure for the dynamic analysis of finite and infinite beams on piece-wise homogeneous foundation under moving loads'. In: *Journal of Sound and Vibration* 329.13 (2010), pp. 2635–2653.

[19] P. Castro Jorge, F. M. F. Simões and A. Pinto Da Costa. 'Dynamics of beams on non-uniform nonlinear foundations subjected to moving loads'. In: *Computers and Structures* 148 (2015), pp. 26–34.

[20] K. N. van Dalen, A. Tsouvalas, A. V. Metrikine and J. S. Hoving. 'Transition radiation excited by a surface load that moves over the interface of two elastic layers'. In: *International Journal of Solids and Structures* 73-74 (2015), pp. 99–112.

[21] K. N. van Dalen and M. J. M. M. Steenbergen. 'Modeling of train-induced transitional wavefields'. In: *Proceedings of the Third International Conference on Railway Technology: Research, Development and Maintenance*. Ed. by J. Pombo. Civil-Comp Press, Stirlingshire, UK, Paper 199, 2016.

[22] M. Sadri, T. Lu and M. Steenbergen. 'Railway track degradation: The contribution of a spatially variant support stiffness - Local variation'. In: *Journal of Sound and Vibration* 455 (2019), pp. 203–220.

[23] M. Sadri, T. Lu and M. Steenbergen. 'Railway track degradation: The contribution of a spatially variant support stiffness - Global variation'. In: *Journal of Sound and Vibration* 464 (2019).

[24] J. M. de Oliveira Barbosa, A. B. Fărăgău and K. N. van Dalen. 'A lattice model for transition zones in ballasted railway tracks'. In: *Journal of Sound and Vibration* 494 (2021).

[25] J. N. Varandas, P. Hölscher and M. A. G. Silva. 'Dynamic behaviour of railway tracks on transitions zones'. In: *Computers and Structures* 89.13-14 (2011), pp. 1468–1479.

[26] J. M. de Oliveira Barbosa, A. B. Fărăgău, K. N. van Dalen and M. Steenbergen. 'Modelling ballast via a non-linear lattice to assess its compaction behaviour at railway transition zones'. In: *Journal of Sound and Vibration* 530 (2022), p. 116942.

[27] A. Paixão, E. Fortunato and R. Calçada. 'Transition zones to railway bridges: Track measurements and numerical modelling'. In: *Engineering Structures* 80 (2014), pp. 435–443.

[28] C. Alves Ribeiro, A. Paixão, E. Fortunato and R. Calçada. 'Under sleeper pads in transition zones at railway underpasses: numerical modelling and experimental validation'. In: *Structure and Infrastructure Engineering* 11.11 (2015), pp. 1432–1449.

[29] B. Zuada Coelho and M. A. Hicks. 'Numerical analysis of railway transition zones in soft soil'. In: *Proceedings of the Institution of Mechanical Engineers, Part F: Journal of Rail and Rapid Transit* 230.6 (2016), pp. 1601–1613.

[30] J. N. Varandas, P. Hölscher and M. A. G. Silva. 'Three-dimensional track-ballast interaction model for the study of a culvert transition'. In: *Soil Dynamics and Earthquake Engineering* 89 (2016), pp. 116–127.

[31] M. Germonpré, G. Degrande and G. Lombaert. 'A track model for railway-induced ground vibration resulting from a transition zone'. In: *Proceedings of the Institution of Mechanical Engineers, Part F: Journal of Rail and Rapid Transit* 232.6 (2018), pp. 1703–1717.

[32] H. Wang and V. Markine. 'Modelling of the long-term behaviour of transition zones: Prediction of track settlement'. In: *Engineering Structures* 156.November 2017 (2018), pp. 294–304.

[33] C. Madshus and A. M. Kaynia. 'High-speed railway lines on soft ground: dynamic behaviour at critical train speed'. In: *Journal of Sound and Vibration* 231.3 (2000), pp. 689–701.

[34] B. Zuada Coelho, J. Priest and P. Hölscher. 'Dynamic behaviour of transition zones in soft soils during regular train traffic'. In: *Proceedings of the Institution of Mechanical Engineers, Part F: Journal of Rail and Rapid Transit* 232.3 (2018), pp. 645–662.

[35] K. K. Ang and J. Dai. 'Response analysis of high-speed rail system accounting for abrupt change of foundation stiffness'. In: *Journal of Sound and Vibration* 332.12 (2013), pp. 2954–2970.

[36] V. L. Ginzburg and I. M. Frank. 'Radiation arising from a uniformly moving electron as the electron crosses from one medium into another'. In: *J. Exp. Theoret. Phys.* 16 (1946), pp. 15–30.

[37] V. L. Ginzburg and V. N. Tsytovich. *Transition Radiation and Transition Scattering*. Bristol: Hilger, 1990.

[38] A. I. Vesnitskii and A. V. Metrikin. 'Transition radiation in One-Dimensional Elastic Systems'. In: *Prikladnaya Mekhanika i Tekhnicheskaka Fizika* No. 2 (1992), pp. 62–67.

References for Chapter 2

[4] M. J. M. M. Steenbergen. 'Physics of railroad degradation: The role of a varying dynamic stiffness and transition radiation processes'. In: *Computers and Structures* 124 (2013), pp. 102–111.

[9] B. Coelho, P. Hölscher, J. Priest, W. Powrie and F. Barends. 'An assessment of transition zone performance'. In: *Proceedings of the Institution of Mechanical Engineers, Part F: Journal of Rail and Rapid Transit* 225.2 (2011), pp. 129–139.

[15] D. Li and D. Davis. 'Transition of Railroad Bridge Approaches'. In: *Journal of Geotechnical and Geoenvironmental Engineering* 131.11 (2005), pp. 1392–1398.

[16] A. I. Vesnitskii and A. V. Metrikin. 'Transition radiation in mechanics'. In: *Physics-Uspekhi* 39.10 (1996), pp. 983–1007.

[17] K. N. Van Dalen and A. V. Metrikine. 'Transition radiation of elastic waves at the interface of two elastic half-planes'. In: *Journal of Sound and Vibration* 310 (2008), pp. 702–717.

[18] Z. Dimitrovová. 'A general procedure for the dynamic analysis of finite and infinite beams on piece-wise homogeneous foundation under moving loads'. In: *Journal of Sound and Vibration* 329.13 (2010), pp. 2635–2653.

[20] K. N. van Dalen, A. Tsouvalas, A. V. Metrikine and J. S. Hoving. 'Transition radiation excited by a surface load that moves over the interface of two elastic layers'. In: *International Journal of Solids and Structures* 73-74 (2015), pp. 99–112.

[21] K. N. van Dalen and M. J. M. M. Steenbergen. 'Modeling of train-induced transitional wavefields'. In: *Proceedings of the Third International Conference on Railway Technology: Research, Development and Maintenance*. Ed. by J. Pombo. Civil-Comp Press, Stirlingshire, UK, Paper 199, 2016.

[27] A. Paixão, E. Fortunato and R. Calçada. 'Transition zones to railway bridges: Track measurements and numerical modelling'. In: *Engineering Structures* 80 (2014), pp. 435–443.

[29] B. Zuada Coelho and M. A. Hicks. 'Numerical analysis of railway transition zones in soft soil'. In: *Proceedings of the Institution of Mechanical Engineers, Part F: Journal of Rail and Rapid Transit* 230.6 (2016), pp. 1601–1613.

[30] J. N. Varandas, P. Hölscher and M. A. G. Silva. 'Three-dimensional track-ballast interaction model for the study of a culvert transition'. In: *Soil Dynamics and Earthquake Engineering* 89 (2016), pp. 116–127.

[34] B. Zuada Coelho, J. Priest and P. Hölscher. 'Dynamic behaviour of transition zones in soft soils during regular train traffic'. In: *Proceedings of the Institution of Mechanical Engineers, Part F: Journal of Rail and Rapid Transit* 232.3 (2018), pp. 645–662.

[35] K. K. Ang and J. Dai. 'Response analysis of high-speed rail system accounting for abrupt change of foundation stiffness'. In: *Journal of Sound and Vibration* 332.12 (2013), pp. 2954–2970.

[36] V. L. Ginzburg and I. M. Frank. 'Radiation arising from a uniformly moving electron as the electron crosses from one medium into another'. In: *J. Exp. Theoret. Phys.* 16 (1946), pp. 15–30.

[37] V. L. Ginzburg and V. N. Tsytovich. *Transition Radiation and Transition Scattering*. Bristol: Hilger, 1990.

[38] A. I. Vesnitskii and A. V. Metrikin. 'Transition radiation in One-Dimensional Elastic Systems'. In: *Prikladnaya Mekhanika i Tekhnicheskaka Fizika* No. 2 (1992), pp. 62–67.

[39] V. Pavlov and A. Sukhorukov. 'Transition radiation of acoustic waves'. In: *Usp. Fiz. Nauk.* 1.147 (1985).

[40] Z. Dimitrovová and J. N. Varandas. 'Critical velocity of a load moving on a beam with a sudden change of foundation stiffness: Applications to high-speed trains'. In: *Computers and Structures* 87.19-20 (2009), pp. 1224–1232.

[41] A. S. J. Suiker and C. Esveld. 'Stiffness transition subjected to instantaneous moving load passages'. In: *Sixth International Heavy Haul Railway Conference*. Cape Town, South Africa, 1997.

[42] K. N. van Dalen and A. V. Metrikine. 'Transition radiation of elastic waves at the interface of two elastic half-planes'. In: *Journal of Sound and Vibration* 310.3 (2008), pp. 702–717.

[43] E. Arlaud, S. Costa D'aguar, E. Balmes and G. Faussurier. 'Numerical Study of Railway Track Dynamics : Case of a Transition Zone'. In: *The Third International Conference on Railway Technology: Research, Development and Maintenance, Apr 2016*. Civil-Comp Press. Cagliary, Italy, 2016, pp. 1–20.

[44] M. J. Lighthill. *Introduction to Fourier analysis and generalized functions*. Cambridge University Press, 1958.

[45] S. Timoshenko. 'Methods of analysis of statical and dynamical stresses in rails'. In: *International Congress of Applied Mechanics, Zurich*. 1926, pp. 407–420.

[46] J. Kenney, J. T. 'Steady-State Vibrations of Beam on Elastic Foundation for Moving Load.' In: *ASME. J. Appl. Mech.* 21.4 (1954), pp. 359–364.

[47] P. Matthews. 'Vibrations of a Beam on an elastic foundation'. In: *ZAMM Z. angew. Math. Mech.* 39.1 (1959), pp. 13–19.

[48] S. Krysov. 'Forced Oscillations and Resonance in Elastic Systems with Moving Loads'. In: *GGU, Gor'kii (in Russian)* (1985).

[49] A. R. M. Wolfert. 'Wave effects in one-dimensional elastic systems interacting with moving loads'. PhD thesis. Delft University of Technology, 1999.

[50] K. F. Graff. *Wave Motion in Elastic Solids*. Oxford University Press, 1975.

[51] K. N. van Dalen. 'Ground vibrations induced by a high-speed train running over inhomogeneous subsoil'. MSc thesis. Delft University of Technology, 2006.

References for Chapter 3

[10] J. N. Varandas, P. Hölscher and M. A. G. Silva. 'Settlement of ballasted track under traffic loading: Application to transition zones'. In: *Proceedings of the Institution of Mechanical Engineers, Part F: Journal of Rail and Rapid Transit* 228.3 (2014), pp. 242–259.

[13] X. Lei and L. Mao. 'Dynamic response analyses of vehicle and track coupled system on track transition of conventional high speed railway'. In: *Journal of Sound and Vibration* 271.3-5 (2004), pp. 1133–1146.

[19] P. Castro Jorge, F. M. F. Simões and A. Pinto Da Costa. 'Dynamics of beams on non-uniform nonlinear foundations subjected to moving loads'. In: *Computers and Structures* 148 (2015), pp. 26–34.

[22] M. Sadri, T. Lu and M. Steenbergen. 'Railway track degradation: The contribution of a spatially variant support stiffness - Local variation'. In: *Journal of Sound and Vibration* 455 (2019), pp. 203–220.

[25] J. N. Varandas, P. Hölscher and M. A. G. Silva. 'Dynamic behaviour of railway tracks on transitions zones'. In: *Computers and Structures* 89.13-14 (2011), pp. 1468–1479.

[33] C. Madshus and A. M. Kaynia. 'High-speed railway lines on soft ground: dynamic behaviour at critical train speed'. In: *Journal of Sound and Vibration* 231.3 (2000), pp. 689–701.

[35] K. K. Ang and J. Dai. 'Response analysis of high-speed rail system accounting for abrupt change of foundation stiffness'. In: *Journal of Sound and Vibration* 332.12 (2013), pp. 2954–2970.

[52] D. J. Thompson. *Railway noise and vibration: mechanisms, modelling and means*. 2009.

[53] S. L. Grassie, R. W. Gregory, D. Harrison and K. L. Johnson. 'The dynamic response of railway track to high frequency vertical excitation'. In: *Journal Mechanical Engineering Science* 24.2 (1982), pp. 77–90.

[54] J. C. Nielsen and X. Li. 'Railway track geometry degradation due to differential settlement of ballast/subgrade – Numerical prediction by an iterative procedure'. In: *Journal of Sound and Vibration* 412 (2018), pp. 441–456.

[55] V. V. Krylov. 'Ground vibration boom from high-speed trains'. In: *Journal of Low Frequency Noise Vibration and Active Control* 18.4 (1999), pp. 207–218.

[56] B. Ouchene. 'Including the inertia to a 1-D model-A study on the energy radiation in railway tracks'. PhD thesis. Delft University of Technology, 2021.

[57] V. I. Erofeev, D. A. Kolesov and E. E. Lisenkova. 'Features of wave generation by a source moving along a one-dimensional flexible guide lying on an elastic-inertial foundation'. In: *Acoustical Physics* 62.6 (2016), pp. 643–650.

[58] M. Shamalta and A. V. Metrikine. 'Analytical study of the dynamic response of an embedded railway track to a moving load'. In: *Archive of Applied Mechanics* 73.1-2 (2003), pp. 131–146.

References for Chapter 4

[4] M. J. M. M. Steenbergen. 'Physics of railroad degradation: The role of a varying dynamic stiffness and transition radiation processes'. In: *Computers and Structures* 124 (2013), pp. 102–111.

[10] J. N. Varandas, P. Hölscher and M. A. G. Silva. 'Settlement of ballasted track under traffic loading: Application to transition zones'. In: *Proceedings of the Institution of Mechanical Engineers, Part F: Journal of Rail and Rapid Transit* 228.3 (2014), pp. 242–259.

[13] X. Lei and L. Mao. 'Dynamic response analyses of vehicle and track coupled system on track transition of conventional high speed railway'. In: *Journal of Sound and Vibration* 271.3-5 (2004), pp. 1133–1146.

[15] D. Li and D. Davis. 'Transition of Railroad Bridge Approaches'. In: *Journal of Geotechnical and Geoenvironmental Engineering* 131.11 (2005), pp. 1392–1398.

[23] M. Sadri, T. Lu and M. Steenbergen. 'Railway track degradation: The contribution of a spatially variant support stiffness - Global variation'. In: *Journal of Sound and Vibration* 464 (2019).

[24] J. M. de Oliveira Barbosa, A. B. Fărăgău and K. N. van Dalen. 'A lattice model for transition zones in ballasted railway tracks'. In: *Journal of Sound and Vibration* 494 (2021).

[25] J. N. Varandas, P. Hölscher and M. A. G. Silva. 'Dynamic behaviour of railway tracks on transitions zones'. In: *Computers and Structures* 89.13-14 (2011), pp. 1468–1479.

[26] J. M. de Oliveira Barbosa, A. B. Fărăgău, K. N. van Dalen and M. Steenbergen. 'Modelling ballast via a non-linear lattice to assess its compaction behaviour at railway transition zones'. In: *Journal of Sound and Vibration* 530 (2022), p. 116942.

[27] A. Paixão, E. Fortunato and R. Calçada. 'Transition zones to railway bridges: Track measurements and numerical modelling'. In: *Engineering Structures* 80 (2014), pp. 435–443.

[28] C. Alves Ribeiro, A. Paixão, E. Fortunato and R. Calçada. 'Under sleeper pads in transition zones at railway underpasses: numerical modelling and experimental validation'. In: *Structure and Infrastructure Engineering* 11.11 (2015), pp. 1432–1449.

[31] M. Germonpré, G. Degrande and G. Lombaert. 'A track model for railway-induced ground vibration resulting from a transition zone'. In: *Proceedings of the Institution of Mechanical Engineers, Part F: Journal of Rail and Rapid Transit* 232.6 (2018), pp. 1703–1717.

[33] C. Madshus and A. M. Kaynia. 'High-speed railway lines on soft ground: dynamic behaviour at critical train speed'. In: *Journal of Sound and Vibration* 231.3 (2000), pp. 689–701.

[35] K. K. Ang and J. Dai. 'Response analysis of high-speed rail system accounting for abrupt change of foundation stiffness'. In: *Journal of Sound and Vibration* 332.12 (2013), pp. 2954–2970.

[53] S. L. Grassie, R. W. Gregory, D. Harrison and K. L. Johnson. 'The dynamic response of railway track to high frequency vertical excitation'. In: *Journal Mechanical Engineering Science* 24.2 (1982), pp. 77–90.

[59] A. S. Suiker, A. V. Metrikine and R. De Borst. 'Comparison of wave propagation characteristics of the Cosserat continuum model and corresponding discrete lattice models'. In: *International Journal of Solids and Structures* 38.9 (2001), pp. 1563–1583.

[60] W. M. Zhai, K. Y. Wang and J. H. Lin. 'Modelling and experiment of railway ballast vibrations'. In: *Journal of Sound and Vibration* 270.4-5 (2004), pp. 673–683.

[61] G. Saussine, C. Cholet, P. E. Gautier, F. Dubois, C. Bohatier and J. J. Moreau. 'Modelling ballast behaviour under dynamic loading. Part 1: A 2D polygonal discrete element method approach'. In: *Computer Methods in Applied Mechanics and Engineering* 195.19-22 (2006), pp. 2841–2859.

[62] E. Tutumluer, Y. Qian, Y. M. Hashash, J. Ghaboussi and D. D. Davis. 'Discrete element Modelling of ballasted track deformation Behaviour'. In: *International Journal of Rail Transportation* 1.1 (2013), pp. 57–73.

[63] J. M. de Oliveira Barbosa and K. N. van Dalen. 'Dynamic response of an infinite beam periodically supported by sleepers resting on a regular and infinite lattice: Semi-analytical solution'. In: *Journal of Sound and Vibration* 458 (2019), pp. 276–302.

[64] A. B. Fărăgău, T. Mazilu, A. V. Metrikine, T. Lu and K. N. van Dalen. 'Transition radiation in an infinite one-dimensional structure interacting with a moving oscillator—the Green's function method'. In: *Journal of Sound and Vibration* 492 (2021).

[65] M. Banimahd, P. K. Woodward, J. Kennedy and G. M. Medero. 'Behaviour of train–track interaction in stiffness transitions'. In: *Proceedings of the Institution of Civil Engineers - Transport* 165.3 (2012), pp. 205–214.

[66] X. Lei and B. Zhang. 'Influence of track stiffness distribution on vehicle and track interactions in track transition'. In: *Proceedings of the Institution of Mechanical Engineers, Part F: Journal of Rail and Rapid Transit* 224.6 (2010), pp. 592–604.

[67] P. Galvín, A. Romero and J. Domínguez. 'Fully three-dimensional analysis of high-speed train-track-soil-structure dynamic interaction'. In: *Journal of Sound and Vibration* 329.24 (2010), pp. 5147–5163.

[68] G. G. Denisov, E. K. Kugusheva and V. V. Novikov. 'On the problem of the stability of one-dimensional unbounded elastic systems'. In: *Journal of Applied Mathematics and Mechanics* 49.4 (1985), pp. 533–537.

[69] R. Bogacz, S. Nowakowski and K. Popp. 'On the Stability of a Timoshenko Beam on an Elastic Foundation Under a Moving Spring-Mass System'. In: *Acta Mechanica* 61 (1986), pp. 117–127.

[70] A. I. Vesnitskii and A. V. Metrikin. 'Transient radiation in a periodically nonuniform elastic guide'. In: *Izv. RAN. Mekhanika Tverdogo Tela* 28.6 (1993), pp. 164–168.

[71] A. V. Metrikin. *Unstable lateral oscillations of an object moving uniformly along an elastic guide as a result of an anomalous Doppler effect*. 1994.

[72] T. Mazilu, M. Dumitriu and C. Tudorache. 'On the dynamics of interaction between a moving mass and an infinite one-dimensional elastic structure at the stability limit'. In: *Journal of Sound and Vibration* 330.15 (2011), pp. 3729–3743.

[73] T. Mazilu, M. Dumitriu and C. Tudorache. 'Instability of an oscillator moving along a Timoshenko beam on viscoelastic foundation'. In: *Nonlinear Dynamics* 67.2 (2012), pp. 1273–1293.

[74] T. Mazilu. 'Instability of a train of oscillators moving along a beam on a viscoelastic foundation'. In: *Journal of Sound and Vibration* 332.19 (2013), pp. 4597–4619.

[75] Z. Dimitrovová. 'New semi-analytical solution for a uniformly moving mass on a beam on a two-parameter visco-elastic foundation'. In: *International Journal of Mechanical Sciences* (2016).

[76] T. Mazilu. 'Green's functions for analysis of dynamic response of wheel/rail to vertical excitation'. In: *Journal of Sound and Vibration* 306.1-2 (2007), pp. 31–58.

[77] A. B. Fărăgău, A. V. Metrikine and K. N. van Dalen. 'Transition radiation in a piecewise-linear and infinite one-dimensional structure–a Laplace transform method'. In: *Nonlinear Dynamics* 98 (2019), pp. 2435–2461.

[78] E. Berggren. 'Railway Track Stiffness - Dynamic Measurements and Evaluation for Efficient Maintenance'. PhD thesis. Royal Institute of Technology (KTH), 2009.

[79] E. G. Berggren, Å. Jahlénius, B.-E. Bengtsson and M. Berg. 'Simulation, development and field testing of a track stiffness measurement vehicle'. In: *Proceedings of 8th International Heavy Haul Conference* (2005), pp. 763–772.

[80] E. G. Berggren, A. M. Kaynia and B. Dehlbom. 'Identification of substructure properties of railway tracks by dynamic stiffness measurements and simulations'. In: *Journal of Sound and Vibration* 329.19 (2010), pp. 3999–4016.

[81] D. Stăncioiu, H. Ouyang and J. E. Mottershead. 'Vibration of a beam excited by a moving oscillator considering separation and reattachment'. In: *Journal of Sound and Vibration* 310.4-5 (2008), pp. 1128–1140.

References for Chapter 5

[16] A. I. Vesnitskii and A. V. Metrikin. 'Transition radiation in mechanics'. In: *Physics-Uspekhi* 39.10 (1996), pp. 983–1007.

[22] M. Sadri, T. Lu and M. Steenbergen. 'Railway track degradation: The contribution of a spatially variant support stiffness - Local variation'. In: *Journal of Sound and Vibration* 455 (2019), pp. 203–220.

[24] J. M. de Oliveira Barbosa, A. B. Fărăgău and K. N. van Dalen. 'A lattice model for transition zones in ballasted railway tracks'. In: *Journal of Sound and Vibration* 494 (2021).

[26] J. M. de Oliveira Barbosa, A. B. Fărăgău, K. N. van Dalen and M. Steenbergen. 'Modelling ballast via a non-linear lattice to assess its compaction behaviour at railway transition zones'. In: *Journal of Sound and Vibration* 530 (2022), p. 116942.

[31] M. Germonpré, G. Degrande and G. Lombaert. 'A track model for railway-induced ground vibration resulting from a transition zone'. In: *Proceedings of the Institution of Mechanical Engineers, Part F: Journal of Rail and Rapid Transit* 232.6 (2018), pp. 1703–1717.

[37] V. L. Ginzburg and V. N. Tsytovich. *Transition Radiation and Transition Scattering*. Bristol: Hilger, 1990.

[49] A. R. M. Wolfert. 'Wave effects in one-dimensional elastic systems interacting with moving loads'. PhD thesis. Delft University of Technology, 1999.

[63] J. M. de Oliveira Barbosa and K. N. van Dalen. 'Dynamic response of an infinite beam periodically supported by sleepers resting on a regular and infinite lattice: Semi-analytical solution'. In: *Journal of Sound and Vibration* 458 (2019), pp. 276–302.

[70] A. I. Vesnitskii and A. V. Metrikin. 'Transient radiation in a periodically nonuniform elastic guide'. In: *Izv. RAN. Mekhanika Tverdogo Tela* 28.6 (1993), pp. 164–168.

[76] T. Mazilu. 'Green's functions for analysis of dynamic response of wheel/rail to vertical excitation'. In: *Journal of Sound and Vibration* 306.1-2 (2007), pp. 31–58.

[77] A. B. Fărăgău, A. V. Metrikine and K. N. van Dalen. 'Transition radiation in a piecewise-linear and infinite one-dimensional structure–a Laplace transform method'. In: *Nonlinear Dynamics* 98 (2019), pp. 2435–2461.

[82] A. B. Fărăgău, J. M. de Oliveira Barbosa, A. V. Metrikine and K. N. van Dalen. 'Dynamic amplification in a periodic structure with a transition zone subject to a moving load: three different phenomena'. In: *Mathematics and Mechanics of Solids* 1 (2022), pp. 1–21.

[83] L. Brillouin. *Wave Propagation in Periodic Structures*. II. Dover Publications, Inc., 1953.

[84] L. Rayleigh. 'On the maintenance of vibrations by forces of double frequency, and on the propagation of waves through a medium endowed with a periodic structure'. In: *Philosophical Magazine* XXIV (1887), pp. 145–159.

[85] D. J. Mead. 'Free wave propagation in periodically supported, infinite beams'. In: *Journal of Sound and Vibration* 11.2 (1970), pp. 181–197.

[86] D. J. Mead. 'Vibration and Wave Propagation in Periodic Structures.' In: *Developments in Mechanics* 13.August 1971 (1985), pp. 291–292.

[87] D. J. Mead. 'Wave Propagation in Continuous Periodic Structures : Research Contributions From Southampton'. In: *Journal of Sound and Vibration* 190 (1996), pp. 495–524.

[88] L. Jezequel. 'Response of periodic systems to a moving load'. In: *Journal of Applied Mechanics, Transactions ASME* 48.3 (1981), pp. 613–618.

[89] C. W. Cai, Y. K. Cheung and H. C. Chan. 'Dynamic response of infinite continuous beams subjected to a moving force-An exact method'. In: *Journal of Sound and Vibration* 123.3 (1988), pp. 461–472.

[90] A. Nordborg. 'Vertical rail vibrations: Parametric excitation'. In: *Acustica - acta acustica* 84.December 1997 (1998), pp. 289–300.

[91] A. V. Metrikine and K. Popp. 'Vibration of a periodically supported beam on an elastic half-space'. In: *European Journal of Mechanics, A/Solids* (1999).

[92] X. Sheng, C. J. Jones and D. J. Thompson. 'Responses of infinite periodic structures to moving or stationary harmonic loads'. In: *Journal of Sound and Vibration* 282.1-2 (2005), pp. 125–149.

[93] T. Hoang, D. Duhamel, G. Foret, H. P. Yin and G. Cumunel. 'Response of a periodically supported beam on a nonlinear foundation subjected to moving loads'. In: *Nonlinear Dynamics* 86.2 (2016), pp. 953–961.

[94] M. Botshekan, M. Tootkaboni and A. Louhghalam. 'On the dynamics of periodically restrained flexural structures under moving loads'. In: *International Journal of Solids and Structures* 180-181 (2019), pp. 62–71.

[95] A. V. Metrikine. 'Parametric instability of a moving particle on a periodically supported infinitely long string'. In: *Journal of Applied Mechanics, Transactions ASME* 75.1 (2008), pp. 0110061–0110068.

[96] S. N. Verichev and A. V. Metrikine. 'Instability of vibrations of a mass that moves uniformly along a beam on a periodically inhomogeneous foundation'. In: *Journal of Sound and Vibration* 260.5 (2003), pp. 901–925.

[97] A. V. Metrikine. 'Steady state response of an infinite string on a non-linear visco-elastic foundation to moving point loads'. In: *Journal of Sound and Vibration* 272.3-5 (2004), pp. 1033–1046.

[98] D. Villegas, F. A. Horta-Rangel, T. González, I. Quirós, R. Pérez-Álvarez and F. De León-Pérez. 'Tunneling times in a taut string'. In: *European Journal of Physics* 41.4 (2020).

[99] D. J. Mead. *Waves and modes in finite beams: Application of the phase-closure principle*. 1994.

[100] A. B. Fărăgău, A. V. Metrikine and K. N. van Dalen. 'Dynamic amplification in a periodic structure subject to a moving load passing a transition zone: Hyperloop case study'. In: *Recent Trends in Wave Mechanics and Vibrations*. 2022.

References for Chapter 6

[10] J. N. Varandas, P. Hölscher and M. A. G. Silva. 'Settlement of ballasted track under traffic loading: Application to transition zones'. In: *Proceedings of the Institution of Mechanical Engineers, Part F: Journal of Rail and Rapid Transit* 228.3 (2014), pp. 242–259.

[19] P. Castro Jorge, F. M. F. Simões and A. Pinto Da Costa. 'Dynamics of beams on non-uniform nonlinear foundations subjected to moving loads'. In: *Computers and Structures* 148 (2015), pp. 26–34.

[20] K. N. van Dalen, A. Tsouvalas, A. V. Metrikine and J. S. Hoving. 'Transition radiation excited by a surface load that moves over the interface of two elastic layers'. In: *International Journal of Solids and Structures* 73-74 (2015), pp. 99–112.

[25] J. N. Varandas, P. Hölscher and M. A. G. Silva. 'Dynamic behaviour of railway tracks on transitions zones'. In: *Computers and Structures* 89.13-14 (2011), pp. 1468–1479.

[26] J. M. de Oliveira Barbosa, A. B. Fărăgău, K. N. van Dalen and M. Steenbergen. 'Modelling ballast via a non-linear lattice to assess its compaction behaviour at railway transition zones'. In: *Journal of Sound and Vibration* 530 (2022), p. 116942.

[30] J. N. Varandas, P. Hölscher and M. A. G. Silva. 'Three-dimensional track-ballast interaction model for the study of a culvert transition'. In: *Soil Dynamics and Earthquake Engineering* 89 (2016), pp. 116–127.

[50] K. F. Graff. *Wave Motion in Elastic Solids*. Oxford University Press, 1975.

[77] A. B. Fărăgău, A. V. Metrikine and K. N. van Dalen. 'Transition radiation in a piecewise-linear and infinite one-dimensional structure–a Laplace transform method'. In: *Nonlinear Dynamics* 98 (2019), pp. 2435–2461.

[93] T. Hoang, D. Duhamel, G. Foret, H. P. Yin and G. Cumunel. 'Response of a periodically supported beam on a nonlinear foundation subjected to moving loads'. In: *Nonlinear Dynamics* 86.2 (2016), pp. 953–961.

[101] T. Dahlberg. 'Dynamic interaction between train and non-linear railway track model'. In: *Proc. Fifth Euro. Conf. Struct. Dyn.* Munich, Germany, 2002, pp. 1155–1160.

[102] H. E. Stewart. 'Permanent strains from cyclic variable-amplitude loadings'. In: *J Geotech Eng* 112.6 (1986), pp. 646–660.

[103] M. Shenton. 'Ballast deformation and track deterioration'. In: *Track Technology* (1985), pp. 253–265.

[104] Y. Sato. 'Japanese studies on deterioration of ballasted track'. In: *Veh Sys Dyn: Int J Veh Mech Mob* 24.1 (1995).

[105] A. V. Metrikin. 'Stationary waves in a nonlinear elastic system interacting with a moving load'. In: *Acoustical Physics* 40.4 (1994), pp. 579–576.

[106] A. V. Metrikine. 'Steady state response of an infinite string on a non-linear viscoelastic foundation to moving point loads'. In: *Journal of Sound and Vibration* 272.3-5 (2004), pp. 1033–1046.

[107] P. Jorge Castro, A. Pinto da Costa and F. M. F. Simões. 'Finite element dynamic analysis of finite beams on a bilinear foundation under a moving load'. In: *Journal of Sound and Vibration* 346.1 (2015), pp. 328–344.

[108] D. Froio, E. Rizzi, F. M. F. Simões and A. Pinto Da Costa. 'Critical velocities of a beam on nonlinear elastic foundation under harmonic moving load'. In: *Procedia Engineering* 199.10 (2017), pp. 2585–2590.

[109] C. Rodrigues, F. M. F. Simões, A. Pinto da Costa, D. Froio and E. Rizzi. 'Finite element dynamic analysis of beams on nonlinear elastic foundations under a moving oscillator'. In: *European Journal of Mechanics, A/Solids* 68.October 2017 (2018), pp. 9–24.

[110] H. Ding, K. L. Shi, L. Q. Chen and S. P. Yang. 'Dynamic response of an infinite Timoshenko beam on a nonlinear viscoelastic foundation to a moving load'. In: *Nonlinear Dynamics* 73.1-2 (2013), pp. 285–298.

[111] M. H. Kargarnovin, D. Younesian, D. J. Thompson and C. J. C. Jones. 'Response of beams on nonlinear viscoelastic foundations to harmonic moving loads'. In: *Computers and Structures* 83.23-24 (2005), pp. 1865–1877.

[112] P. Koziol and Z. Hryniewicz. 'Dynamic response of a beam resting on a nonlinear foundation to a moving load: Coiflet-based solution'. In: *Shock and Vibration* 19.5 (2012), pp. 995–1007.

[113] J. N. Varandas, A. Paixão, E. Furtunato, P. Hölscher and R. Calçada. 'Numerical Modelling of Railway Bridge Approaches: Influence of Soil Non-Linearity'. In: *Railway Technology* 3.x (2014).

[114] I. Gallego Giner and A. López Pita. 'Numerical simulation of embankment-structure transition design'. In: *Proceedings of the Institution of Mechanical Engineers, Part F: Journal of Rail and Rapid Transit* 223.4 (2009), pp. 331–343.

[115] D. Froio. 'Structural Dynamics Modelization of One - Dimensional Elements on Elastic Foundations Under Fast Moving Load'. PhD thesis. Universita Degli Studi di Bergamo, 2017.

[116] P. Wang, L. Wang, R. Chen, J. Xu, J. Xu and M. Gao. 'Overview and outlook on railway track stiffness measurement'. In: *Journal of Modern Transportation* 24.2 (2016), pp. 89–102.

[117] A. P. Allaart. 'Design principles for flexible pavements-a computational model for granular bases'. PhD. Delft University of Technology, 1992.

[118] J. S. Hoving and A. V. Metrikine. 'A mixed time-frequency domain method to describe the dynamic behaviour of a discrete medium bounded by a linear continuum'. In: *International Summer School-Conference Advanced Problems in Mechanics, St. Petersburg*. 2015.

References for Chapter 7

[13] X. Lei and L. Mao. 'Dynamic response analyses of vehicle and track coupled system on track transition of conventional high speed railway'. In: *Journal of Sound and Vibration* 271.3-5 (2004), pp. 1133–1146.

[16] A. I. Vesnitskii and A. V. Metrikin. 'Transition radiation in mechanics'. In: *Physics-Uspekhi* 39.10 (1996), pp. 983–1007.

[18] Z. Dimitrovová. 'A general procedure for the dynamic analysis of finite and infinite beams on piece-wise homogeneous foundation under moving loads'. In: *Journal of Sound and Vibration* 329.13 (2010), pp. 2635–2653.

[19] P. Castro Jorge, F. M. F. Simões and A. Pinto Da Costa. 'Dynamics of beams on non-uniform nonlinear foundations subjected to moving loads'. In: *Computers and Structures* 148 (2015), pp. 26–34.

[20] K. N. van Dalen, A. Tsouvalas, A. V. Metrikine and J. S. Hoving. 'Transition radiation excited by a surface load that moves over the interface of two elastic layers'. In: *International Journal of Solids and Structures* 73-74 (2015), pp. 99–112.

[21] K. N. van Dalen and M. J. M. M. Steenbergen. 'Modeling of train-induced transitional wavefields'. In: *Proceedings of the Third International Conference on Railway Technology: Research, Development and Maintenance*. Ed. by J. Pombo. Civil-Comp Press, Stirlingshire, UK, Paper 199, 2016.

[23] M. Sadri, T. Lu and M. Steenbergen. 'Railway track degradation: The contribution of a spatially variant support stiffness - Global variation'. In: *Journal of Sound and Vibration* 464 (2019).

[24] J. M. de Oliveira Barbosa, A. B. Fărăgău and K. N. van Dalen. 'A lattice model for transition zones in ballasted railway tracks'. In: *Journal of Sound and Vibration* 494 (2021).

[25] J. N. Varandas, P. Hölscher and M. A. G. Silva. 'Dynamic behaviour of railway tracks on transitions zones'. In: *Computers and Structures* 89.13-14 (2011), pp. 1468–1479.

[27] A. Paixão, E. Fortunato and R. Calçada. 'Transition zones to railway bridges: Track measurements and numerical modelling'. In: *Engineering Structures* 80 (2014), pp. 435–443.

[28] C. Alves Ribeiro, A. Paixão, E. Fortunato and R. Calçada. 'Under sleeper pads in transition zones at railway underpasses: numerical modelling and experimental validation'. In: *Structure and Infrastructure Engineering* 11.11 (2015), pp. 1432–1449.

[30] J. N. Varandas, P. Hölscher and M. A. G. Silva. 'Three-dimensional track-ballast interaction model for the study of a culvert transition'. In: *Soil Dynamics and Earthquake Engineering* 89 (2016), pp. 116–127.

[31] M. Germonpré, G. Degrande and G. Lombaert. 'A track model for railway-induced ground vibration resulting from a transition zone'. In: *Proceedings of the Institution of Mechanical Engineers, Part F: Journal of Rail and Rapid Transit* 232.6 (2018), pp. 1703–1717.

[34] B. Zuada Coelho, J. Priest and P. Hölscher. 'Dynamic behaviour of transition zones in soft soils during regular train traffic'. In: *Proceedings of the Institution of Mechanical Engineers, Part F: Journal of Rail and Rapid Transit* 232.3 (2018), pp. 645–662.

[35] K. K. Ang and J. Dai. 'Response analysis of high-speed rail system accounting for abrupt change of foundation stiffness'. In: *Journal of Sound and Vibration* 332.12 (2013), pp. 2954–2970.

[38] A. I. Vesnitskii and A. V. Metrikin. 'Transition radiation in One-Dimensional Elastic Systems'. In: *Prikladnaya Mekhanika i Tekhnicheskaka Fizika* No. 2 (1992), pp. 62–67.

[40] Z. Dimitrovová and J. N. Varandas. 'Critical velocity of a load moving on a beam with a sudden change of foundation stiffness: Applications to high-speed trains'. In: *Computers and Structures* 87.19-20 (2009), pp. 1224–1232.

[41] A. S. J. Suiker and C. Esveld. 'Stiffness transition subjected to instantaneous moving load passages'. In: *Sixth International Heavy Haul Railway Conference*. Cape Town, South Africa, 1997.

[42] K. N. van Dalen and A. V. Metrikine. 'Transition radiation of elastic waves at the interface of two elastic half-planes'. In: *Journal of Sound and Vibration* 310.3 (2008), pp. 702–717.

[49] A. R. M. Wolfert. 'Wave effects in one-dimensional elastic systems interacting with moving loads'. PhD thesis. Delft University of Technology, 1999.

[64] A. B. Fărăgău, T. Mazilu, A. V. Metrikine, T. Lu and K. N. van Dalen. 'Transition radiation in an infinite one-dimensional structure interacting with a moving oscillator—the Green's function method'. In: *Journal of Sound and Vibration* 492 (2021).

[67] P. Galvín, A. Romero and J. Domínguez. 'Fully three-dimensional analysis of high-speed train-track-soil-structure dynamic interaction'. In: *Journal of Sound and Vibration* 329.24 (2010), pp. 5147–5163.

[77] A. B. Fărăgău, A. V. Metrikine and K. N. van Dalen. 'Transition radiation in a piecewise-linear and infinite one-dimensional structure–a Laplace transform method'. In: *Nonlinear Dynamics* 98 (2019), pp. 2435–2461.

[111] M. H. Kargarnovin, D. Younesian, D. J. Thompson and C. J. C. Jones. 'Response of beams on nonlinear viscoelastic foundations to harmonic moving loads'. In: *Computers and Structures* 83.23-24 (2005), pp. 1865–1877.

[113] J. N. Varandas, A. Paixão, E. Furtunato, P. Hölscher and R. Calçada. 'Numerical Modelling of Railway Bridge Approaches: Influence of Soil Non-Linearity'. In: *Railway Technology* 3.x (2014).

[114] I. Gallego Giner and A. López Pita. 'Numerical simulation of embankment-structure transition design'. In: *Proceedings of the Institution of Mechanical Engineers, Part F: Journal of Rail and Rapid Transit* 223.4 (2009), pp. 331–343.

[119] N. M. Newmark. 'A method for computation of structural dynamics'. In: *Proc. of the American Society of Civil Engineers*. Vol. 85. 1959, pp. 67–94.

[120] T. Dahlberg. 'Railway Track Stiffness Variations - Consequences and Countermeasures'. In: *International Journal of Civil Engineering* 8.1 (2010).

[121] U. Basu and A. K. Chopra. 'Perfectly matched layers for transient elastodynamics of unbounded domains'. In: *International Journal for Numerical Methods in Engineering* 59.8 (2004), pp. 1039–1074.

[122] S. Krenk, L. Kellezi, N. S.R.K. and P. H. Kirkegaard. 'Finite Elements and Transmitting Boundary Conditions for Moving Loads'. In: *Proceedings of the 4th European Conference on Structural Dynamics, Eurodyn '99, Praha, 7-11 June 1999* January 1999 (1999), pp. 447–452.

[123] A. Aprile, A. Benedetti and T. Trombetti. 'On non-linear dynamic analysis in the frequency domain: algorithms and applications'. In: *Earthquake Engineering and Structural Dynamics* 23 (1994), pp. 363–388.

[124] C. Keijdener, H. Hendrikse and A. Metrikine. 'The effect of hydrodynamics on the bending failure of level ice'. In: *Cold Regions Science and Technology* 153.May (2018), pp. 106–119.

[125] A. B. Fărăgău, C. Keijdener, J. M. de Oliveira Barbosa, A. V. Metrikine and K. N. van Dalen. 'Transition radiation in a nonlinear and infinite one-dimensional structure: a comparison of solution methods'. In: *Nonlinear Dynamics* 103 (2021), pp. 1365–1391.

[126] L. Andersen, S. R. Nielsen and P. H. Kirkegaard. 'Finite element modelling of infinite Euler beams on Kelvin foundations exposed to moving loads in convected co-ordinates'. In: *Journal of Sound and Vibration* 241.4 (2001), pp. 587–604.

[127] V. H. Nguyen and D. Duhamel. 'Finite element procedures for nonlinear structures in moving coordinates. Part II: Infinite beam under moving harmonic loads'. In: *Computers and Structures* 86.21-22 (2008), pp. 2056–2063.

[128] C. Bode, R. Hirschauer and S. A. Savidis. 'Soil-structure interaction in the time domain using halfspace Green's functions'. In: *Soil Dynamics and Earthquake Engineering* 22.4 (2002), pp. 283–295.

References for Chapter 8

[11] H. Wang and V. Markine. 'Dynamic behaviour of the track in transitions zones considering the differential settlement'. In: *Journal of Sound and Vibration* 459 (2019).

[17] K. N. Van Dalen and A. V. Metrikine. 'Transition radiation of elastic waves at the interface of two elastic half-planes'. In: *Journal of Sound and Vibration* 310 (2008), pp. 702–717.

[20] K. N. van Dalen, A. Tsouvalas, A. V. Metrikine and J. S. Hoving. 'Transition radiation excited by a surface load that moves over the interface of two elastic layers'. In: *International Journal of Solids and Structures* 73-74 (2015), pp. 99–112.

[21] K. N. van Dalen and M. J. M. M. Steenbergen. 'Modeling of train-induced transitional wavefields'. In: *Proceedings of the Third International Conference on Railway Technology: Research, Development and Maintenance*. Ed. by J. Pombo. Civil-Comp Press, Stirlingshire, UK, Paper 199, 2016.

[24] J. M. de Oliveira Barbosa, A. B. Fărăgău and K. N. van Dalen. 'A lattice model for transition zones in ballasted railway tracks'. In: *Journal of Sound and Vibration* 494 (2021).

[26] J. M. de Oliveira Barbosa, A. B. Fărăgău, K. N. van Dalen and M. Steenbergen. 'Modelling ballast via a non-linear lattice to assess its compaction behaviour at railway transition zones'. In: *Journal of Sound and Vibration* 530 (2022), p. 116942.

[27] A. Paixão, E. Fortunato and R. Calçada. 'Transition zones to railway bridges: Track measurements and numerical modelling'. In: *Engineering Structures* 80 (2014), pp. 435–443.

[28] C. Alves Ribeiro, A. Paixão, E. Fortunato and R. Calçada. 'Under sleeper pads in transition zones at railway underpasses: numerical modelling and experimental validation'. In: *Structure and Infrastructure Engineering* 11.11 (2015), pp. 1432–1449.

[30] J. N. Varandas, P. Hölscher and M. A. G. Silva. 'Three-dimensional track-ballast interaction model for the study of a culvert transition'. In: *Soil Dynamics and Earthquake Engineering* 89 (2016), pp. 116–127.

[31] M. Germonpré, G. Degrande and G. Lombaert. 'A track model for railway-induced ground vibration resulting from a transition zone'. In: *Proceedings of the Institution of Mechanical Engineers, Part F: Journal of Rail and Rapid Transit* 232.6 (2018), pp. 1703–1717.

[32] H. Wang and V. Markine. 'Modelling of the long-term behaviour of transition zones: Prediction of track settlement'. In: *Engineering Structures* 156.November 2017 (2018), pp. 294–304.

[43] E. Arlaud, S. Costa D'aguar, E. Balmes and G. Faussurier. 'Numerical Study of Railway Track Dynamics : Case of a Transition Zone'. In: *The Third International Conference on Railway Technology: Research, Development and Maintenance, Apr 2016*. Civil-Comp Press. Cagliary, Italy, 2016, pp. 1–20.

[50] K. F. Graff. *Wave Motion in Elastic Solids*. Oxford University Press, 1975.

[63] J. M. de Oliveira Barbosa and K. N. van Dalen. 'Dynamic response of an infinite beam periodically supported by sleepers resting on a regular and infinite lattice: Semi-analytical solution'. In: *Journal of Sound and Vibration* 458 (2019), pp. 276–302.

[67] P. Galvín, A. Romero and J. Domínguez. 'Fully three-dimensional analysis of high-speed train-track-soil-structure dynamic interaction'. In: *Journal of Sound and Vibration* 329.24 (2010), pp. 5147–5163.

[123] A. Aprile, A. Benedetti and T. Trombetti. 'On non-linear dynamic analysis in the frequency domain: algorithms and applications'. In: *Earthquake Engineering and Structural Dynamics* 23 (1994), pp. 363–388.

[124] C. Keijdener, H. Hendrikse and A. Metrikine. 'The effect of hydrodynamics on the bending failure of level ice'. In: *Cold Regions Science and Technology* 153.May (2018), pp. 106–119.

[125] A. B. Fărăgău, C. Keijdener, J. M. de Oliveira Barbosa, A. V. Metrikine and K. N. van Dalen. 'Transition radiation in a nonlinear and infinite one-dimensional structure: a comparison of solution methods'. In: *Nonlinear Dynamics* 103 (2021), pp. 1365–1391.

[129] P. Alves Costa, R. Calçada, A. Silva Cardoso and A. Bodare. 'Influence of soil nonlinearity on the dynamic response of high-speed railway tracks'. In: *Soil Dynamics and Earthquake Engineering* 30.4 (2010), pp. 221–235.

[130] J. N. Varandas, P. Hölscher and M. A. Silva. 'Settlement of ballasted track under traffic loading: Application to transition zones'. In: *Proceedings of the Institution of Mechanical Engineers, Part F: Journal of Rail and Rapid Transit* 228.3 (2014), pp. 242–259.

[131] A. S. Suiker and R. de Borst. 'A numerical model for the cyclic deterioration of railway tracks'. In: *International Journal for Numerical Methods in Engineering* 57.4 (2003), pp. 441–470.

[132] H. A. Dieterman and A. V. Metrikine. 'The equivalent stiffness of a half space interacting with a beam. Critical velocities of a moving load along the beam'. In: *Eur. J. Mech. A/Solids* 15.1 (1996), pp. 67–90.

[133] H. A. Dieterman and A. V. Metrikine. 'Steady-state displacements of a beam on an elastic half-space due to a uniformly moving constant load'. In: *European Journal of Mechanics, A/Solids* 16.2 (1997), pp. 295–306.

[134] T. Lu, A. V. Metrikine and M. J. Steenbergen. 'The equivalent dynamic stiffness of a visco-elastic half-space in interaction with a periodically supported beam under a moving load'. In: *European Journal of Mechanics, A/Solids* 84.July (2020).

[135] R. D. Mindlin. *Waves and vibrations in isotropic elastic plates*. Ed. by J. N. Goodier and N. Hoff. 1960.

[136] J. D. Achenbach. *Wave propagation in elastic solids*. Ed. by H. A. Lauwerier and W. T. Koiter. North-Holland Publishing Company, 1973.

[137] A. V. Metrikine and A. C. Vrouwenvelder. 'Surface ground vibration due to a moving train in a tunnel: two-dimensional model'. In: *Journal of Sound and Vibration* 234.1 (2000), pp. 43–66.

[138] A. F. S. Rodrigues and Z. Dimitrovová. 'Applicability of a Three-Layer Model for the Dynamic Analysis of Ballasted Railway Tracks'. In: *Vibration* 4.1 (2021), pp. 151–174.

[139] A. D. Kerr. 'A study of a new foundation model'. In: *Acta Mechanica* 1.2 (1965), pp. 135–147.

[140] P. L. Pasternak. 'On a new method of analysis of an elastic foundation by means of two foundation constants'. In: *Gosudarstvennoe Izdatelstvo Literaturi po Stroitelstvu i Arkhitekture, Moscow. in Russian* (1954).

A

Dispersion equation and kinematic invariants for a discretely supported string

Here we present a detailed derivation of the dispersion equation (Eq. (5.12)) and of the kinematic invariant (Eq. (5.14)). For simplicity, a system without damping is considered.

Firstly, the dispersion curve is derived. The eigenvalues $\alpha_{1,2}$ are obtained from an eigenvalue analysis of the Floquet matrix. The Floquet matrix $\mathbf{F}$ is obtained by evaluating the right-hand side of Eq. (5.8) (excluding the particular solutions) at $x = (n+1)d$, and reads

$$\mathbf{F} = \begin{pmatrix} \frac{k_\mathrm{s}\sin(\gamma d)}{2T\gamma} + \cos(\gamma d) & \frac{\sin(\gamma d)}{\gamma} - \frac{\cos(\gamma d)k_\mathrm{s}}{2T\gamma^2} + \frac{k_\mathrm{s}}{2T\gamma^2} \\ -\sin(\gamma d)\gamma + \frac{\cos(\gamma d)k_\mathrm{s}}{2T} + \frac{k_\mathrm{s}}{2T} & \frac{k_\mathrm{s}\sin(\gamma d)}{2T\gamma} + \cos(\gamma d) \end{pmatrix}. \tag{A.1}$$

The determinant of $\mathbf{F}$ is 1, and, thus, its eigenvalues read

$$\alpha_{1,2} = B \pm \sqrt{B^2 - 1}, \qquad B = \frac{k_\mathrm{s}\sin(\gamma d)}{2T\gamma} + \cos(\gamma d), \tag{A.2}$$

where B is half the trace of $\mathbf{F}$. The relation between the Floquet wavenumber k^F and the eigenvalue α (we restrict the following derivation to one eigenvalue) is given as follows:

$$\alpha = \mathrm{e}^{\mathrm{i}k^\mathrm{F}d}. \tag{A.3}$$

Depending on the frequency (B is frequency dependent), there are three possible scenarios. The first scenario, $B^2 > 1$, results in real-valued and positive α. From Eq. (A.3), this leads to

purely imaginary k^{F}; the corresponding frequency ranges represent the stop-bands in the dispersion curve. The second scenario, $B^2 = 1$, results in repeated eigenvalues, corresponding to the transition points between the stop and pass bands. The third scenario, $B^2 < 1$, results in complex-valued α and real-valued k^{F} corresponding to the pass-bands in the dispersion curve, in which waves are propagating without attenuation. Consequently, Eq. (A.3) can be rewritten as

$$\alpha = \cos(k^{\mathrm{F}} d) + \mathrm{i}\sin(k^{\mathrm{F}} d). \tag{A.4}$$

This leads to the following set of conditions for the Floquet wavenumber

$$\begin{cases} \cos(k^{\mathrm{F}} d) = B, \\ \sin(k^{\mathrm{F}} d) = \sqrt{B^2 - 1}. \end{cases} \tag{A.5}$$

If one condition in Eq. (A.5) is satisfied, then the other one is also satisfied. Either condition can be selected as the dispersion equation (we chose the first one for its concise form).

Secondly, the kinematic invariants are derived. The kinematic invariants ensure phase equality of the emitted harmonic waves and the load at the contact point [16]. The phase of a harmonic wave with frequency ω and wavenumber k is

$$\phi = \omega t - kx. \tag{A.6}$$

The phase of a harmonic wave is constant for an observer moving together with the wave, resulting in the following relation between frequency and wavenumber: $\omega = k\frac{\mathrm{d}x}{\mathrm{d}t}$. The change of position with time (i.e., $\frac{\mathrm{d}x}{\mathrm{d}t}$) of the moving load is v, and since the kinematic invariant ensures phase equality of the emitted harmonic waves and the load, we have

$$\omega = kv. \tag{A.7}$$

This is the kinematic invariant for a homogeneous system subject to a moving constant load. For the discretely supported systems considered in Chapter 5, a harmonic wave (with phase given by Eq. (A.6)) is not a solution of the equation of motion; the solution is a superposition of harmonic waves that have the following expression for the phase:

$$\phi = \omega t - (k + m\tfrac{2\pi}{d})x, \tag{A.8}$$

where $m = \pm 1, \pm 2, \ldots$. In this case, infinitely many kinematic invariants are necessary to ensure phase equality between the moving load and the infinitely many generated waves. The expression of the kinematic invariants reads

$$\omega = kv + m\tfrac{2\pi v}{d}. \tag{A.9}$$

This expression is analogous to Eq. (5.14).

B

Eigenfield wavenumbers and wave amplitudes

This appendix presents the expressions of the wavenumbers and amplitudes of the waves composing the eigenfield (see Sections 2.2, 4.1). The system with and without damping is considered, consisting of an infinite Euler-Bernoulli beam resting on homogeneous Kelvin or Winkler foundations, respectively, subject to a moving constant load (the system in Section 4.1 has a moving oscillator, but this reduces to a moving constant load in the steady state). The eigenfield for both the systems reads

$$w^{\mathrm{e}}(x,t) = \begin{cases} B_{\mathrm{b}} \mathrm{e}^{-\mathrm{i}k_2^{\mathrm{e}}(x-vt)} + C_{\mathrm{b}} \mathrm{e}^{-\mathrm{i}k_3^{\mathrm{e}}(x-vt)}, & x < vt, \\ A_{\mathrm{f}} \mathrm{e}^{-\mathrm{i}k_1^{\mathrm{e}}(x-vt)} + D_{\mathrm{f}} \mathrm{e}^{-\mathrm{i}k_4^{\mathrm{e}}(x-vt)}, & x \geq vt, \end{cases} \tag{B.1}$$

where k_1^{e}, k_2^{e}, k_3^{e} and k_4^{e} are the eigenfield's wavenumbers, and B_{b}, C_{b}, A_{f}, and D_{f} are the amplitudes of the waves.

The amplitudes of the waves for both systems (Winkler and Kelvin foundations) read

$$B_{\mathrm{b}} = \frac{\mathrm{i}F_0}{(k_2^{\mathrm{e}} - k_1^{\mathrm{e}})(k_2^{\mathrm{e}} - k_3^{\mathrm{e}})(k_2^{\mathrm{e}} - k_4^{\mathrm{e}})}, \qquad C_{\mathrm{b}} = \frac{\mathrm{i}F_0}{(k_3^{\mathrm{e}} - k_1^{\mathrm{e}})(k_3^{\mathrm{e}} - k_2^{\mathrm{e}})(k_3^{\mathrm{e}} - k_4^{\mathrm{e}})}, \tag{B.2}$$

$$A_{\mathrm{f}} = \frac{\mathrm{i}F_0}{(k_1^{\mathrm{e}} - k_2^{\mathrm{e}})(k_1^{\mathrm{e}} - k_3^{\mathrm{e}})(k_1^{\mathrm{e}} - k_4^{\mathrm{e}})}, \qquad D_{\mathrm{f}} = \frac{\mathrm{i}F_0}{(k_4^{\mathrm{e}} - k_1^{\mathrm{e}})(k_4^{\mathrm{e}} - k_2^{\mathrm{e}})(k_4^{\mathrm{e}} - k_3^{\mathrm{e}})}. \tag{B.3}$$

For the system without damping, the wavenumbers are determined from the following dispersion equation (in which the kinematic invariant has been substituted):

$$EIk^4 - \rho k^2 v^2 + k_{\mathrm{d}} = 0. \tag{B.4}$$

The wavenumbers, thus, read [49]

$$k_1^{\mathrm{e}} = (p_2 + \mathrm{i}p_1), \qquad k_2^{\mathrm{e}} = (p_2 - \mathrm{i}p_1), \tag{B.5}$$

$$k_3^{\mathrm{e}} = -k_1^{\mathrm{e}}, \qquad k_4^{\mathrm{e}} = -k_2^{\mathrm{e}}, \tag{B.6}$$

where

$$p_1 = \sqrt{(\beta^2 - \gamma^2 v^2)}, \qquad p_2 = \sqrt{(\beta^2 + \gamma^2 v^2)}, \tag{B.7}$$

$$\beta = \sqrt[4]{\frac{k_{\mathrm{d}}}{4EI}}, \qquad \gamma = \sqrt{\frac{\rho}{4EI}}. \tag{B.8}$$

As for the system with damping, the wavenumbers are determined from the following dispersion equation (in which the kinematic invariant has been substituted):

$$EIk^4 - \rho k^2 v^2 + \mathrm{i}kvc_{\mathrm{d}} + k_{\mathrm{d}} = 0. \tag{B.9}$$

Defining the coefficients of the quartic equation as $c = -\rho v^2$, $d = \mathrm{i}vc_{\mathrm{d,l}}$ and $e = k_{\mathrm{d,l}}$, the complex wavenumbers are expressed as follows:

$$k_1^{\mathrm{e}} = +S + \frac{1}{2}\sqrt{-4S^2 - 2c - \frac{d}{S}}, \qquad k_2^{\mathrm{e}} = +S - \frac{1}{2}\sqrt{-4S^2 - 2c - \frac{d}{S}}, \tag{B.10}$$

$$k_3^{\mathrm{e}} = -S + \frac{1}{2}\sqrt{-4S^2 - 2c + \frac{d}{S}}, \qquad k_4^{\mathrm{e}} = -S - \frac{1}{2}\sqrt{-4S^2 - 2c + \frac{d}{S}}, \tag{B.11}$$

where $S = (2\sqrt{3})^{-1}\sqrt{-2c + U + \Delta_0 U^{-1}}$, $U = 2^{-\frac{1}{3}}\sqrt[3]{\Delta_1 + \sqrt{\Delta_1^2 - 4\Delta_0^3}}$, $\Delta_0 = c^2 + 12e$, and $\Delta_1 = 2c^3 + 27d - 72ce$.

It must be emphasized that the sign of the wavenumbers in both systems (Winkler and Kelvin foundations) is as follows:

$$\mathrm{Re}(k_1^{\mathrm{e}}) > 0, \quad \mathrm{Im}(k_1^{\mathrm{e}}) \leq 0, \tag{B.12}$$

$$\mathrm{Re}(k_2^{\mathrm{e}}) > 0, \quad \mathrm{Im}(k_2^{\mathrm{e}}) \geq 0, \tag{B.13}$$

$$\mathrm{Re}(k_3^{\mathrm{e}}) < 0, \quad \mathrm{Im}(k_3^{\mathrm{e}}) \geq 0, \tag{B.14}$$

$$\mathrm{Re}(k_4^{\mathrm{e}}) < 0, \quad \mathrm{Im}(k_4^{\mathrm{e}}) \leq 0. \tag{B.15}$$

It must be noted that the expressions presented in this appendix are not valid when Eq. (B.9) leads to repeated roots. This situation occurs when there is no viscous damping and $v = c_{\mathrm{cr}}$, or for very high viscous damping. These scenarios are not treated in this thesis.

C

Primary and secondary dispersion curves of a periodically supported string

Here we show why the branch of the dispersion curve of the periodic system closest to the dispersion curve of the unsupported string leads to more energetic waves than the other branches. One might think that all information is just repeated from one Brillouin zone to the next (like for discrete periodic systems), but that is not completely correct for a continuous system. Let us consider a wave field propagating in positive x direction (i.e., the second term in Eq. (5.11) is zero). The normalized state at interface nd would then read

$$\frac{\tilde{\mathbf{w}}_n}{a_1} = \mathrm{e}^{-\mathrm{i}k_1^{\mathrm{F}} nd}\mathbf{u}_1. \tag{C.1}$$

The displacement inside the generic cell can be calculated using Eq. (5.8) without the particular solution, as follows:

$$\frac{\tilde{w}(x,\omega)}{a_1} = \Big(u_{1,1} f_{1,1}(x-nd) + u_{1,2} f_{1,2}(x-nd)\Big)\mathrm{e}^{-\mathrm{i}k_1^{\mathrm{F}} nd}, \quad nd \le x \le (n+1)d, \tag{C.2}$$

where $f_{1,1}(x)$ and $f_{1,2}(x)$ are the functions from Eq. (5.8). Furthermore, $u_{1,1}$ and $u_{1,2}$ represent the first and second entries in the eigenvector $\mathbf{u}_1$, respectively. To see which wavenumbers are present in $\tilde{w}(x,\omega)$, we can take the Fourier transform over space (note that $\overline{k} \in (-\infty,\infty)$ is the Fourier variable), and the scaled response $\hat{w}(\overline{k},\omega)$ in the frequency-wavenumber

domain reads

$$\hat{w}(\overline{k},\omega) = \sum_{n=-\infty}^{\infty} \int_{nd}^{(n+1)d} \frac{\tilde{w}(x,\omega)}{a_1} \mathrm{e}^{-\mathrm{i}\overline{k}x} \mathrm{d}x. \tag{C.3}$$

Provided that the sign of the imaginary part of k_1^{F} is chosen properly (to represent a forward propagating wave), both the integral and the summation in Eq. (C.3) can be performed analytically. The result reads

C

$$\hat{w}(\overline{k},\omega) = A(\gamma,\overline{k}) \frac{1}{\gamma^2 - \overline{k}^2} \frac{\mathrm{e}^{\mathrm{i}d(\overline{k}+k_{1,\mathrm{r}}^{\mathrm{F}})}}{\mathrm{e}^{\mathrm{i}d(\overline{k}+k_{1,\mathrm{r}}^{\mathrm{F}})} - \mathrm{e}^{dk_{1,\mathrm{i}}^{\mathrm{F}}}}, \tag{C.4}$$

where $k_{1,\mathrm{r}}^{\mathrm{F}}$ and $k_{1,\mathrm{i}}^{\mathrm{F}}$ are the real and imaginary parts of k_1^{F}, respectively. Function $A(\gamma,\overline{k})$ contains terms proportional to $(\overline{k}\pm\gamma)$; these terms increase linearly with increasing $\overline{k}$ while the second factor in Eq. (C.4) is inversely proportional to $\overline{k}^2$ for large enough values of $\overline{k}$; this is the reason why the second factor was singled out while the other terms are contained in $A(\gamma,\overline{k})$. The last factor in Eq. (C.4) gives the influence of the Floquet wavenumber (the periodic part of the system) on the response while the second factor gives the influence of the wavenumber of the unsupported string (the continuous part of the system); actually, the denominator of the second factor yields the dispersion curve of the unsupported string (when equated to zero). The last factor exhibits peaks of equal magnitude (infinite magnitude in the case of no damping) at $\overline{k} = -k_{1,\mathrm{r}}^{\mathrm{F}} \pm m\frac{2\pi}{d}$; therefore, this factor associated with the Floquet wavenumbers does not make any distinction between Brillouin zones. The second factor, has a parabolic function in the denominator and decreases as $\overline{k}$ moves away from γ. Therefore, the peaks of $\hat{w}(\overline{k},\omega)$ at $\overline{k} = -k_{1,\mathrm{r}}^{\mathrm{F}} \pm m\frac{2\pi}{d}$ decrease in amplitude as $\overline{k}$ moves away from γ. This is the mathematical reason why the branches closest to the dispersion curve of the unsupported string lead to most energetic waves. From a physical perspective, the energy propagated from cell to cell is governed by the Floquet wavenumbers; however, the propagation inside the cells is governed by the string, which imposes what branches of the dispersion curve lead to more or less energetic waves.

D

Finite difference coefficients

Here, the Finite Difference coefficients used to discretise the beam in Section 6.2.2 are provided. The Finite Difference scheme with 9 nodes is used. The fourth-order derivative reads

$$\begin{aligned}\hat{w}''''_m \approx \frac{1}{\Delta x^4}\Big(&\frac{7}{240}\,\hat{w}_{m-4} - \frac{2}{5}\,\hat{w}_{m-3} + \frac{169}{60}\,\hat{w}_{m-2} - \frac{122}{15}\,\hat{w}_{m-1} + \frac{91}{8}\,\hat{w}_m - \frac{122}{15}\,\hat{w}_{m+1} \\ &+ \frac{169}{60}\,\hat{w}_{m+2} - \frac{2}{5}\,\hat{w}_{m+3} + \frac{7}{240}\,\hat{w}_{m+4}\Big), \qquad m = 3..M-2,\end{aligned} \tag{D.1}$$

where M represents the number of nodes of the computational domain. As can be seen from Equation D.1, this approximation is applied only from node 3 to node $M-2$. This is because there are only two boundary conditions at each boundary, and thus, only two *ghost nodes* can be used. The fourth-order derivative approximations for nodes 1, 2, $M-1$ and M are obtained by using a hybrid between the central scheme and the forward scheme (for nodes 1 and 2) or the backward scheme (for nodes $M-1$ and M). The expressions are given in the following:

$$\begin{aligned}\hat{w}''''_1 \approx \frac{1}{\Delta x^4}\Big(&\frac{127}{240}\,\hat{w}_{-1} - \frac{11}{15}\,\hat{w}_0 - \frac{77}{20}\,\hat{w}_1 + \frac{193}{15}\,\hat{w}_2 - \frac{407}{24}\,\hat{w}_3 \\ &+ \frac{61}{5}\,\hat{w}_4 - \frac{311}{60}\,\hat{w}_5 + \frac{19}{15}\,\hat{w}_6 - \frac{11}{80}\,\hat{w}_7\Big),\end{aligned} \tag{D.2}$$

$$\begin{aligned}\hat{w}''''_2 \approx \frac{1}{\Delta x^4}\Big(&-\frac{11}{80}\,\hat{w}_{-1} + \frac{53}{30}\,\hat{w}_0 - \frac{341}{60}\,\hat{w}_1 + \frac{77}{10}\,\hat{w}_2 - \frac{107}{24}\,\hat{w}_3 \\ &+ \frac{11}{30}\,\hat{w}_4 + \frac{13}{20}\,\hat{w}_5 - \frac{7}{30}\,\hat{w}_6 + \frac{7}{240}\,\hat{w}_7\Big),\end{aligned} \tag{D.3}$$

$$\hat{w}''''_{M-1} \approx \frac{1}{\Delta x^4}\Big(\frac{7}{240}\,\hat{w}_{M-6} - \frac{7}{30}\,\hat{w}_{M-5} + \frac{13}{20}\,\hat{w}_{M-4} + \frac{11}{30}\,\hat{w}_{M-3} - \frac{107}{24}\,\hat{w}_{M-2} + \frac{77}{10}\,\hat{w}_{M-1} - \frac{341}{60}\,\hat{w}_{M} + \frac{53}{30}\,\hat{w}_{M+1} - \frac{11}{80}\,\hat{w}_{M+2}\Big), \tag{D.4}$$

$$\hat{w}''''_{M} \approx \frac{1}{\Delta x^4}\Big(-\frac{11}{80}\,\hat{w}_{M-6} + \frac{19}{15}\,\hat{w}_{M-5} - \frac{311}{60}\,\hat{w}_{M-4} + \frac{61}{5}\,\hat{w}_{M-3} - \frac{407}{24}\,\hat{w}_{M-2} + \frac{193}{15}\,\hat{w}_{M-1} - \frac{77}{20}\,\hat{w}_{M} - \frac{11}{15}\,\hat{w}_{M+1} + \frac{127}{240}\,\hat{w}_{M+2}\Big), \tag{D.5}$$

where the nodes -1, 0, $M+1$ and $M+2$ represent the so-called ghost nodes. These nodes are not part of the computational domain; therefore, the displacements of these nodes ($\hat{w}_{-1}$, $\hat{w}_0$, $\hat{w}_{M+1}$, $\hat{w}_{M+2}$) are expressed in terms of the displacements of the nodes inside the computational domain by using the four non-reflective boundary conditions. The resulting equations are included in Equation (6.15).

E

Additional expressions for the non-reflective boundary conditions

In Section 6.2.3, the expressions for the non-reflective boundary conditions have been derived for the situation in which the nonlinear events occur while the moving load is inside the computational domain. Due to the rail losing and regaining contact with the supporting structure, nonlinear events can still occur while the moving load is in the right domain. In this section, the expressions for the non-reflective boundary conditions at the right are derived for that situation. The aim is to express the reaction forces of the right domain, at the interface with the computational domain, as functions of the displacement and slope of the computational domain at the right boundary. The procedure is similar to the one explained in Section 6.2.3. It must be noted that the non-reflective boundary conditions at the left, derived in Section 6.2.3, remain valid through the simulation.

If a nonlinear event occurs when $\overline{\tau}_{n-1} > \frac{L-x_\mathrm{e}}{v}$, the right semi-infinite domain must be divided in two sub-domains, one sub-domain behind the load (sub-domain A) and the second one in front of it (sub-domain B). The forward Laplace transform is applied to the governing equations, and the solution of the sub-domain behind the moving load $\hat{w}_\mathrm{r}^\mathrm{A}$ and that in front $\hat{w}_r^\mathrm{B}$, already accounting for the condition of vanishing displacement at infinity, are obtained as follows:

$$\hat{w}_{\mathrm{r},n}^\mathrm{A}(x,s_n) = C_1^\mathrm{A}\,\mathrm{e}^{-\mathrm{i}k_\mathrm{r}x} + C_2^\mathrm{A}\,\mathrm{e}^{+\mathrm{i}k_\mathrm{r}x} + C_3^\mathrm{A}\,\mathrm{e}^{+k_\mathrm{r}x} + C_4^\mathrm{A}\,\mathrm{e}^{-k_\mathrm{r}x} + \hat{w}_{\mathrm{r},n,\mathrm{p}}^\mathrm{A}, \qquad L < x < x_\mathrm{P}, \tag{E.1}$$

$$\hat{w}_{\mathrm{r},n}^\mathrm{B}(x,s_n) = C_1^\mathrm{B}\,\mathrm{e}^{-\mathrm{i}k_\mathrm{r}x} + C_4^\mathrm{B}\,\mathrm{e}^{-k_\mathrm{r}x} + \hat{w}_{n,\mathrm{p}}^\mathrm{ML} + \hat{w}_{\mathrm{r},n,\mathrm{p}}^\mathrm{B}, \qquad x > x_\mathrm{P}, \tag{E.2}$$

where $x_\mathrm{P} = x_\mathrm{e} + v\,\overline{\tau}_{n-1}$ is the position of the load at the moment of the nonlinear event, $C_1^\mathrm{A}, C_2^\mathrm{A}, C_3^\mathrm{A}, C_4^\mathrm{A}, C_1^\mathrm{B}$ and C_4^B represent yet unknown complex amplitudes, $\hat{w}_{\mathrm{r},n,\mathrm{p}}^\mathrm{A}$ and $\hat{w}_{\mathrm{r},n,\mathrm{p}}^\mathrm{B}$

represent the particular solutions accounting for the initial state of the two sub-domains, and $\hat{w}_{n,\mathrm{p}}^{\mathrm{ML}}$ represents the particular solution accounting for the moving load which reads:

$$\hat{w}_{n,\mathrm{p}}^{\mathrm{ML}} = -\frac{F_0\, v^3}{s_n^4 - k_\mathrm{r}^4\, v^4}\, \mathrm{e}^{-s_n \frac{x-x_\mathrm{P}}{v}}. \tag{E.3}$$

The six unknown complex amplitudes are obtained by employing the two boundary conditions at $x = L$ given by Equations (6.27) and (6.28), and four interface conditions at $x = x_\mathrm{P}$, namely the continuity of displacement and slope, and the equilibrium of bending moment and shear force. To find the reaction forces of the right domain at the interface with the computational domain, the second and third derivatives of $\hat{w}_{\mathrm{r},n}^{\mathrm{A}}$ with respect to space are taken, and are evaluated at $x = L$:

$$\begin{pmatrix} \hat{w}_{\mathrm{r},n}^{\mathrm{A}'''}(L, s_n) \\ \hat{w}_{\mathrm{r},n}^{\mathrm{A}''}(L, s_n) \end{pmatrix} = \begin{pmatrix} k_{\mathrm{r,V}\upsilon} & k_{\mathrm{r,V}\phi} \\ k_{\mathrm{r,M}\upsilon} & k_{\mathrm{r,M}\phi} \end{pmatrix} \begin{pmatrix} \hat{w}_n(L, s_n) \\ \hat{w}_n'(L, s_n) \end{pmatrix} - \mathbf{D}_{\mathrm{r},n} - \begin{pmatrix} \hat{V}_n^{\mathrm{L}}(s_n) \\ \hat{M}_n^{\mathrm{L}}(s_n) \end{pmatrix}. \tag{E.4}$$

Vector $\mathbf{D}_{\mathrm{r},n}$ now reads

$$\begin{aligned} \mathbf{D}_{\mathrm{r},n} = &\begin{pmatrix} \hat{w}_{\mathrm{r},n,\mathrm{p}}^{\mathrm{A}'''}(L, s_n) \\ \hat{w}_{\mathrm{r},n,\mathrm{p}}^{\mathrm{A}''}(L, s_n) \end{pmatrix} + \begin{pmatrix} k_{\mathrm{r,V}\upsilon} & k_{\mathrm{r,V}\phi} \\ k_{\mathrm{r,M}\upsilon} & k_{\mathrm{r,M}\phi} \end{pmatrix} \begin{pmatrix} \hat{w}_{\mathrm{r},n,\mathrm{p}}^{\mathrm{A}}(L, s_n) \\ \hat{w}_{\mathrm{r},n,\mathrm{p}}^{\mathrm{A}'}(L, s_n) \end{pmatrix} \\ &+ \begin{pmatrix} a_\mathrm{V} & b_\mathrm{V} & c_\mathrm{V} & d_\mathrm{V} \\ a_\mathrm{M} & b_\mathrm{M} & c_\mathrm{M} & d_\mathrm{M} \end{pmatrix} \begin{pmatrix} \Delta\hat{w}_{\mathrm{r},n,\mathrm{p}}(x_\mathrm{P}, s_n) \\ \Delta\hat{w}_{\mathrm{r},n,\mathrm{p}}'(x_\mathrm{P}, s_n) \\ \Delta\hat{w}_{\mathrm{r},n,\mathrm{p}}''(x_\mathrm{P}, s_n) \\ \Delta\hat{w}_{\mathrm{r},n,\mathrm{p}}'''(x_\mathrm{P}, s_n) \end{pmatrix}, \quad \overline{\tau}_{n-1} > \frac{L - x_\mathrm{e}}{v}, \end{aligned} \tag{E.5}$$

where $\Delta\hat{w}_{\mathrm{r},n,\mathrm{p}}(x_\mathrm{P}, s_n) = \hat{w}_{\mathrm{r},n,\mathrm{p}}^{\mathrm{B}}(x_\mathrm{P}, s_n) - \hat{w}_{\mathrm{r},n,\mathrm{p}}^{\mathrm{A}}(x_\mathrm{P}, s_n)$ represents the difference of the particular solutions of the two sub-domains evaluated at $x = x_\mathrm{P}$; a_V, b_V, c_V, d_V, a_M, b_M, c_M and d_M represent complex coefficients which read

$$\begin{aligned} a_\mathrm{V} &= \frac{-1+\mathrm{i}}{2}\, k_\mathrm{r}^3 \big(\mathrm{e}^{\mathrm{i}k_\mathrm{r}(L-x_\mathrm{P})} + \mathrm{e}^{k_\mathrm{r}(L-x_\mathrm{P})}\big), \quad & b_\mathrm{V} &= \frac{1+\mathrm{i}}{2}\, k_\mathrm{r}^2 \big(\mathrm{e}^{\mathrm{i}k_\mathrm{r}(L-x_\mathrm{P})} + \mathrm{i}\mathrm{e}^{k_\mathrm{r}(L-x_\mathrm{P})}\big), \\ c_\mathrm{V} &= \frac{-1+\mathrm{i}}{2}\, k_\mathrm{r} \big(-\mathrm{e}^{\mathrm{i}k_\mathrm{r}(L-x_\mathrm{P})} + \mathrm{e}^{k_\mathrm{r}(L-x_\mathrm{P})}\big), \quad & d_\mathrm{V} &= \frac{1+\mathrm{i}}{2} \big(-\mathrm{e}^{\mathrm{i}k_\mathrm{r}(L-x_\mathrm{P})} + \mathrm{i}\mathrm{e}^{k_\mathrm{r}(L-x_\mathrm{P})}\big), \\ a_\mathrm{M} &= \frac{-1-\mathrm{i}}{2}\, k_\mathrm{r}^2 \big(\mathrm{i}\mathrm{e}^{\mathrm{i}k_\mathrm{r}(L-x_\mathrm{P})} + \mathrm{e}^{k_\mathrm{r}(L-x_\mathrm{P})}\big), \quad & b_\mathrm{M} &= \frac{-1-\mathrm{i}}{2}\, k_\mathrm{r} \big(\mathrm{e}^{\mathrm{i}k_\mathrm{r}(L-x_\mathrm{P})} + \mathrm{e}^{k_\mathrm{r}(L-x_\mathrm{P})}\big), \\ c_\mathrm{M} &= \frac{-1-\mathrm{i}}{2} \big(-\mathrm{i}\mathrm{e}^{\mathrm{i}k_\mathrm{r}(L-x_\mathrm{P})} + \mathrm{e}^{k_\mathrm{r}(L-x_\mathrm{P})}\big), \quad & d_\mathrm{M} &= \frac{-1-\mathrm{i}}{2\,k_\mathrm{r}} \big(-\mathrm{e}^{\mathrm{i}k_\mathrm{r}(L-x_\mathrm{P})} + \mathrm{e}^{k_\mathrm{r}(L-x_\mathrm{P})}\big). \end{aligned} \tag{E.6}$$

The particular solutions $\hat{w}^{\mathrm{A}}_{\mathrm{r},n,\mathrm{p}}(L,s_n)$, $\hat{w}^{\mathrm{A}}_{\mathrm{r},n,\mathrm{p}}(x_\mathrm{P},s_n)$ and $\hat{w}^{\mathrm{B}}_{\mathrm{r},n,\mathrm{p}}(x_\mathrm{P},s_n)$ that account for the non-trivial initial state are obtained as explained in Section 6.2.3 and read

$$\hat{w}^{\mathrm{A}}_{\mathrm{r},n,\mathrm{p}}(L,s_n) = \frac{1}{2\pi\mathrm{i}}\int_{\sigma-\mathrm{i}\infty}^{\sigma+\mathrm{i}\infty}(\rho s_n + c_{\mathrm{d,r}} + \rho s)\,\mathrm{e}^{s\overline{\tau}_{n-1}}\int_L^{x_\mathrm{P}}\hat{g}_\mathrm{r}(x-\xi,s_n)\,\hat{w}^{\mathrm{f}}_\mathrm{r}(\xi,s)\,\mathrm{d}\xi\,\mathrm{d}s + \hat{w}^{\mathrm{e}}_{\mathrm{r},n,\mathrm{p}}(L,s_n), \tag{E.7}$$

$$\hat{w}^{\mathrm{A}}_{\mathrm{r},n,\mathrm{p}}(x_\mathrm{P},s_n) = \frac{1}{2\pi\mathrm{i}}\int_{\sigma-\mathrm{i}\infty}^{\sigma+\mathrm{i}\infty}(\rho s_n + c_{\mathrm{d,r}} + \rho s)\,\mathrm{e}^{s\overline{\tau}_{n-1}}\int_L^{x_\mathrm{P}}\hat{g}_\mathrm{l}(x-\xi,s_n)\,\hat{w}^{\mathrm{f}}_\mathrm{r}(\xi,s)\,\mathrm{d}\xi\,\mathrm{d}s + \hat{w}^{\mathrm{e}}_{\mathrm{r},n,\mathrm{p}}(x_\mathrm{P},s_n), \tag{E.8}$$

$$\hat{w}^{\mathrm{B}}_{\mathrm{r},n,\mathrm{p}}(x_\mathrm{P},s_n) = \frac{1}{2\pi\mathrm{i}}\int_{\sigma-\mathrm{i}\infty}^{\sigma+\mathrm{i}\infty}(\rho s_n + c_{\mathrm{d,r}} + \rho s)\,\mathrm{e}^{s\overline{\tau}_{n-1}}\int_{x_\mathrm{P}}^{\infty}\hat{g}_\mathrm{r}(x-\xi,s_n)\,\hat{w}^{\mathrm{f}}_\mathrm{r}(\xi,s)\,\mathrm{d}\xi\,\mathrm{d}s + \hat{w}^{\mathrm{e}}_{\mathrm{r},n,\mathrm{p}}(x_\mathrm{P},s_n). \tag{E.9}$$

The integration over ξ in Equations (E.7) to (E.9) can be performed analytically, while the integration over s needs to be performed numerically. Furthermore, the contribution from the moving load in the right domain on the reaction forces at $x = L$, namely $\hat{V}^{\mathrm{L}}_n(s_n)$ and $\hat{M}^{\mathrm{L}}_n(s_n)$, also change compared to Equations (6.34) and (6.35) and are given by the following expressions:

$$\hat{V}^{\mathrm{L}}_n(s_n) = \frac{(1-\mathrm{i})\,F_0}{2}\left(\frac{\mathrm{e}^{-\mathrm{i}k_\mathrm{r}(x_\mathrm{P}-L)}}{k_\mathrm{r}v-\mathrm{i}s_n} + \frac{\mathrm{e}^{-k_\mathrm{r}(x_\mathrm{P}-L)}}{k_\mathrm{r}v+s_n}\right), \qquad \overline{\tau}_{n-1} > \frac{L-x_\mathrm{e}}{v}, \tag{E.10}$$

$$\hat{M}^{\mathrm{L}}_n(s_n) = \frac{(1-\mathrm{i})\,F_0}{2\,k_\mathrm{r}}\left(\frac{-\mathrm{e}^{-\mathrm{i}k_\mathrm{r}(x_\mathrm{P}-L)}}{k_\mathrm{r}v-\mathrm{i}s_n} + \mathrm{i}\frac{\mathrm{e}^{-k_\mathrm{r}(x_\mathrm{P}-L)}}{k_\mathrm{r}v+s_n}\right), \qquad \overline{\tau}_{n-1} > \frac{L-x_\mathrm{e}}{v}. \tag{E.11}$$

Together with the expressions in Section 6.2.3, Equations (6.32), (6.34) and (6.35), the non-reflective boundary conditions at the right boundary are now complete.

F

Description of the 3-D finite element model

This appendix briefly describes the 3-D finite element model developed* in Abaqus FEA software and used to tune the 2-D model formulated in Chapter 8. The developed model consists of a ballasted railway track with a length of 60 m. The ballasted track consists of a rail connected to sleepers resting on a three layered foundation composed of ballast, embankment, and subgrade. The ballast layer has a 0.3 m depth, while the other two layers have a 1 m depth each. One moving axle is considered and represented by a moving constant load with magnitude of 90 kN. The mechanical properties of the materials can be found in Table F.1 where α and β represent the Rayleigh damping coefficients, and ν the Poisson ratio.

*This model was developed by my colleague Avni Jain to which I am thankful.

Table F.1: Values of the 3-D model parameters.

Material	E (N/m^2)	ρ (kg/m^3)	ν	α	β
Steel (rail)	$21 \cdot 10^{10}$	7850	0.3	0	0
Concrete (sleepers)	$3.5 \cdot 10^{10}$	2400	0.15	0	0
Ballast	$1.5 \cdot 10^{8}$	1560	0.2	0.0439	0.0091
Sand (embankment)	$8 \cdot 10^{7}$	1810	0.3	8.52	0.0004
Clay (subgrade)	$2.55 \cdot 10^{7}$	1730	0.45	8.52	0.0029
Under sleeper pad	$1 \cdot 10^{6}$	500	0.1	0	0

Curriculum Vitæ

Andrei Bogdan Fărăgău

05-10-1990 Born in Cluj-Napoca, Romania

Education

2010–2014 Bachelor of Science
Technical University of Cluj-Napoca
Thesis: Structural design of an industrial steel hall with adjacent office building
Supervisor: Pavel Alexa

2015–2017 Master of Science (cum laude)
Delft University of Technology
Thesis: Transition radiation in an inhomogeneous and nonlinear one-dimensional system
Supervisors: Karel van Dalen and Andrei Metrikine

2018–2022 Doctor of philosophy research
Delft University of Technology
Dissertation: Understanding degradation mechanisms at railway transition zones using phenomenological models
Promotors: Andrei Metrikine and Karel van Dalen

2022– Post-doctoral researcher
Delft University of Technology
Project: Sustainable Installation of XXL Monopiles (SIMOX)

List of Publications

Journal publications

7. A. B. Fărăgău, J. M. de Oliveira Barbosa, A. V. Metrikine and K. N. van Dalen. 'Dynamic amplification in a periodic structure with a transition zone subject to a moving load: three different phenomena'. In: *Mathematics and Mechanics of Solids* 1 (2022), pp. 1–21
6. J. M. de Oliveira Barbosa, A. B. Fărăgău, K. N. van Dalen and M. Steenbergen. 'Modelling ballast via a non-linear lattice to assess its compaction behaviour at railway transition zones'. In: *Journal of Sound and Vibration* 530 (2022), p. 116942
5. A. B. Fărăgău, C. Keijdener, J. M. de Oliveira Barbosa, A. V. Metrikine and K. N. van Dalen. 'Transition radiation in a nonlinear and infinite one-dimensional structure: a comparison of solution methods'. In: *Nonlinear Dynamics* 103 (2021), pp. 1365–1391
4. J. M. de Oliveira Barbosa, A. B. Fărăgău and K. N. van Dalen. 'A lattice model for transition zones in ballasted railway tracks'. In: *Journal of Sound and Vibration* 494 (2021)
3. J. Zhang, E. Sulollari, A. B. Fărăgău, F. Pisanò, P. van der Male, M. Martinelli, A. V. Metrikine and K. N. van Dalen. 'Harmonic Balance Method for the Stationary Response of Finite and Semi-infinite Nonlinear Dissipative Continua: Three Canonical Problems'. In: *Advanced Structured Materials* 139 (2021), pp. 255–274
2. A. B. Fărăgău, T. Mazilu, A. V. Metrikine, T. Lu and K. N. van Dalen. 'Transition radiation in an infinite one-dimensional structure interacting with a moving oscillator—the Green's function method'. In: *Journal of Sound and Vibration* 492 (2021)
1. A. B. Fărăgău, A. V. Metrikine and K. N. van Dalen. 'Transition radiation in a piecewise-linear and infinite one-dimensional structure–a Laplace transform method'. In: *Nonlinear Dynamics* 98 (2019), pp. 2435–2461

Conference publications

4. A. B. Fărăgău, R. Wang, A. V. Metrikine and K. N. van Dalen. 'The interplay between the electro-magnetic and wave-induced instability mechanisms in the Hyperloop transportation system'. In: *Nodycon2023 Proceedings*. 2023
3. A. B. Fărăgău, A. V. Metrikine and K. N. van Dalen. 'Settlement at transition zones in railway tracks - is modelling the soil as a 2-D continuum important?' In: *EURODYN2023 Proceedings*. 2023

2. A. Bracci, A. B. Fărăgău, A. V. Metrikine, K. N. van Dalen, R. Corradi and E. Vlijm. 'Assessment of the metawedge as a mitigation measure for railway induced ground vibration'. In: *EURODYN2023 Proceedings*. 2023

1. A. B. Fărăgău, A. V. Metrikine and K. N. van Dalen. 'Dynamic amplification in a periodic structure subject to a moving load passing a transition zone: Hyperloop case study'. In: *Recent Trends in Wave Mechanics and Vibrations*. 2022

Nominations

2. Best paper award at 10th International Conference on Wave Mechanics and Vibrations (WMVC 2022) for:

   A. B. Fărăgău, A. V. Metrikine and K. N. van Dalen. 'Dynamic amplification in a periodic structure subject to a moving load passing a transition zone: Hyperloop case study'. In: *Recent Trends in Wave Mechanics and Vibrations*. 2022

1. Best paper award at the First International Nonlinear Dynamics Conference (NODYCON 2019) for:

   A. B. Fărăgău, A. V. Metrikine and K. N. van Dalen. 'Transition radiation in a piecewise-linear and infinite one-dimensional structure–a Laplace transform method'. In: *Nonlinear Dynamics* 98 (2019), pp. 2435–2461

Awards

1. Best paper award at the Third International Nonlinear Dynamics Conference (NODYCON 2023) for:

   A. B. Fărăgău, R. Wang, A. V. Metrikine and K. N. van Dalen. 'The interplay between the electro-magnetic and wave-induced instability mechanisms in the Hyperloop transportation system'. In: *Nodycon2023 Proceedings*. 2023